Laser Induced Fluorescence Studies in the Gas Phase

A Thesis Submitted for the Degree of Doctor of Philosophy

Christopher Guy Atkins

Hertford College, Oxford

Trinity Term 1986

Laser Induced Fluorescence Studies in the Gas Phase

A Thesis Submitted for the Degree of Doctor of Philosophy

Christopher Guy Atkins

Hertford College, Oxford

Trinity Term 1986

ABSTRACT

Laser Induced Fluorescence has been used to study rotational and vibrational energy disposal following gas phase photodissociations and reactions of small molecules. Three distinct systems have been studied.

The rotational and vibrational distributions in the ground and first electronically excited states of the OH radical have been studied following the two and three photon dissociation of water using laser radiation of 266nm and 355nm wavelength respectively. The results have been compared to recent theoretical calculations and experimental investigations at different wavelengths in the same region of the spectrum.

The rotational distribution in vibrational levels of the ground electronic state of the NO molecule following 355nm photodissociation of methyl nitrite have been studied and compared to recent experimental studies of the photodissociation of NO containing molecules. A statistical treatment allowed the vibrational distribution to be determined. A simple model is described which rationalises the process.

Finally, the rotational distributions within vibrational levels of the ground electronic state of the CO molecule, produced via the gas phase reaction between oxygen atoms and the CS radical, are presented. The vibrational distribution resulting from this reaction is well established but, to date, there have been no reports of the rotational distribution. A proposal has been made to employ the system studied in a vacuum ultra violet laser. Some comments are made concerning this proposal.

Acknowledgements

I would like to thank Dr G Hancock for his advice and assistance throughout the time I worked within his research group. In addition thanks are due to Dr Mike Ashfold, Dr Phil Lightfoot, Dr Jim Baggott and Dr Ken McKendrick whose support and advice helped my studies immeasurably.

I appreciate the contribution made by Dr E Gill in preparing the methyl nitrite and the Physical Chemistry Laboratory technical staff in constructing the apparatus.

I would like to thank Dr Keith McLaughlan for his continued interest in my studies and also my parents for their interest and support.

Finally I am indebted to Christine for keeping me sane in the darkest hours of scientific research.

C G Atkins

May 1986

CONTENTS

CHAPTER ONE

1.1 INTRODUCTION

It is generally accepted that the aim of chemical reaction dynamics is the complete specification of the initial and final quantum states of two atomic or molecular species involved in a reactive encounter [1]. It would be unreasonable and time consuming to repeat this for every reaction of interest to man and so it is hoped that, by study of model cases which are also amenable to current theoretical techniques, accurate predictive theories can be developed. Accurate knowledge of the most detailed rate processes in reactive systems would allow the calculation of bulk quantities, such as rate constants, since they are a weighted sum over an appropriate distribution of initial states. Photodissociation [2] [3] has also been included in studies of reaction dynamics and can be considered as a "half collision" in which photon absorption prepares the molecule in an excited state, which can be compared to the transition state of a reaction, followed by the separation into fragments in various quantum states. The complete specification of initial and final quantum states described above includes translational, rotational, vibrational and, where appropriate, electronic energy. It has recently become apparent that orientational and alignment effects are also important [4].

Although the ideal state-to-state reaction, or photodissociation, dynamic experiment is well established in theory there have been no experimental realisations of this ideal to date, although some recent

investigations have approached it closely [5] [6]. This introduction will briefly review the experimental methods used to establish initial reactant conditions and to determine final product energy distributions and then examine the theoretical approaches which attempt to rationalise and, in some cases, predict the outcome of experimental investigations. Finally the work presented in this thesis will be briefly described. Since essentially three distinct dynamic processes are investigated it is not appropriate to review the literature relevant to each one at this stage, and thus this introduction takes the form of a more general review.

1.2 EXPERIMENTAL TECHNIQUES

By far the biggest impact upon chemical dynamics from an experimental point of view have been made by the reactive molecular beam apparatus and the laser [7]. The rigorously collision free conditions of molecular beam apparatus ensures that any effects studied are those due to the reaction dynamics and not distorted by the effects of inter-molecular energy transfer via collisions following a reactive collision. The laser allows both initial quantum state selection and an accurate determination of final state distributions in addition to providing an intense narrow band excitation source for photodissociation studies.

1.2.1 Initial State Selection Effusive ovens were originally employed in molecular beam apparatus resulting in a Maxwell-Boltzmann distribution of velocities. Mechanical selection of a subset of these velocities was achieved by the use of rotating discs, with a resultant

loss in molecular beam flux. More intense narrow velocity distributions can be achieved by the use of a supersonic expansion of the gas through a small orifice into the reaction chamber [8] [9] [10] [11]. The use of a seeded supersonic expansion, in which the reactant molecule is diluted in an inert gas, allows continuous adjustment of the translational energy whilst maintaining a narrow velocity distribution. An additional advantage of the supersonic expansion is that very low rotational levels and predominately the ground vibrational level are populated within the beam. It is not easy to predict the extent of vibrational and rotational cooling effected by the expansion and measurements of the distribution are needed for complete characterisation. Differences in product rotational distributions have been noted when an initial 300K distribution is compared to that produced via supersonic expansion. An example of this is the rotational distribution arising in $NH(a^1\Delta)$ following 248nm photodissociation of NH_3 [9]. An initial 300K sample of NH_3 gave rise to a rotational distribution corresponding to an average energy of $770cm^{-1}$ which was reduced to $470cm^{-1}$ when a supersonic expansion with an estimated initial temperature of 3K was used. Similarly a rotational distribution corresponding to a temperature of $900cm^{-1}$ was observed in $OH(X^2\Pi_i)$ following photodissociation of H_2O at 157nm whilst a markedly non-Boltzmann distribution resulted when a supersonic expansion, corresponding to an initial rotational temperature of 10K in the H_2O, was used [6].

A new, and potentially powerful, alternative method of rotational and vibrational state selection is via the use of infra-red lasers. The

advent of a wide variety of such lasers, and parametric mixing processes, allows the selection of individual vibration-rotation lines in molecules prior to reactive collision. An example of this is the excitation of HF(v"=0) to v"=1 in a molecular beam followed by an investigation of the effect of parent vibrational energy on the reaction with Sr and Ba [12] [13]. More recently a Nd:YAG laser pumped $LiNbO_4$ optical parametric oscillator has been used to excite individual rotational lines in the first excited vibrational level of HF and the subsequent reaction with Ca investigated [14].

When photodissociation rather than reaction is studied it is equally important to specify the initial state but in this case the initial level is in some high lying dissociative, or possibly predissociative, state. When the absorption spectrum is an apparent continuum caused by a congestion of vibrational and rotational states then the supersonic expansion cooling techniques described above can be used to simplify spectral features. This has been done in the case of NO_2 which has a particularly complicated absorption spectrum [15] [16]. Such ground electronic state pre-selection is not necessary if the excited state is sufficiently long lived to support a resolvable rotational structure on the absorption spectrum. This is the case with the $\tilde{C}\ ^1B_1$ excited state of H_2O, discussed in more detail later in this thesis, and also in H_2S [17] and NH_3 [18]. High resolution spectroscopy allows the vibrational and rotational level populated in the excited state to be determined [19].

1.2.2 Final State Determination Whilst the importance of parent state specification has only recently received experimental acknowledgement and investigation, the determination of product energy distributions both as the result of reaction and photodissociation has been, and remains, a popular field of study in chemical dynamics.

Translational energy distributions are commonly measured by mechanical velocity selection using rotating discs or by time-of-flight analysis [20]. Since any collisions will distort the results of a translational energy distribution this determination must be performed in a crossed molecular beam apparatus. An alternative method of determining the translational energy, which relaxes the collisional restriction somewhat, is by measuring the Doppler broadening of the line profile spectroscopically as demonstrated recently by Dixon et al [21]. Angular product distributions are also measured in molecular beam apparatus [22]. Such information is of equal interest when photodissociation is studied when one of the molecular beams is replaced, usually by a laser. More recently, higher resolution time-of-flight detection has been developed allowing vibrational structure on fragment translational energy distributions to be discerned. An example of this is the 266nm photodissociation of O_3 where the vibrational product distribution in $O_2(^1\Delta_g)$ was fully resolved [23].

Vibrational and rotational product energy distributions are most commonly measured by a variety of spectroscopic techniques. Vibrationally excited product molecules may be observed by infra-red chemiluminescence in which the infra-red emission resulting, usually,

from a fast flow of reactants through a reaction vessel is dispersed through a monochromator and detected via a cooled IR detector [24]. The higher pressure found in such an experiment suggests that rotational relaxation and some vibrational relaxational, which is less efficient, would occur. To avoid this the technique of arrested relaxation was developed by Polanyi and co-workers [25]. The essence of this is that the walls of the reaction chamber are cooled to liquid nitrogen temperatures thus trapping any condensable matter which collides with the walls or, hopefully, completely vibrationally deactivating any non-condensable matter thus making it unobservable by IR-chemiluminescence. This method gives rise to vibrational distributions which are partially relaxed but can be corrected for collisional effects thus giving the nascent distribution. Time resolved absorption spectroscopy has also been applied to the determination of the product energy distributions in photodissociation.

By far the most powerful methods of determining the internal energy distribution in the products of reactions and photodissociations are Laser Induced Fluorescence (LIF) and the more recent technique of Resonantly Enhanced Multi-Photon Ionisation (REMPI or MPI). In Laser Induced Fluorescence a narrow band tunable laser, usually a dye laser, is used to excite the various vibrational and rotational levels of product molecule or fragment to a bound electronically excited state. The unresolved fluorescence is monitored and is related to the original ground electronic state population distribution as described in Appendix 1. In Multi-Photon Ionisation the ground state product levels are

excited via an intermediate bound state to some ionic state where they are detected electronically. The absorption to the intermediate state, which may or may not be a multi-photon transition, is usually rate limiting and thus the analysis of Multi-Photon Ionisation spectra is similar to that of Laser Induced Fluorescence spectra.

Laser Induced Fluorescence was first demonstrated on the products of molecular beam reactions of alkaline earth atoms with hydrogen halides [26] and has since been used for the determination of internal energy distributions in a wide variety of experiments. Multi-Photon Ionisation has been employed as a high resolution spectroscopic technique in spectral regions where conventional one photon spectroscopy is experimentally difficult [27], and also as a detection method for the products of photodissociation [28] [29].

Time resolved experiments such as Laser Induced Fluorescence and Multi-Photon Ionisation allow investigation of photodissociation to be carried out in collision free conditions without the use of molecular beam apparatus since timing can be arranged such that no collisions occur between the photodissociation pulse and subsequent probing of the fragments. This allows beam/gas and even bulk gas experiments under collisionless conditions.

Excited electronic states produced as the result of a reaction or, more commonly, a photodissociation can be examined by their resolved emission spectra giving vibrational and rotational populations when corrected for detectivity effects and Franck-Condon factors etc. In

essence this is similar to the chemiluminescence described earlier. Generally, however, the fluorescence lifetime of the electronically excited state is shorter than that of the vibrationally excited states observed in IR chemiluminescence experiments and hence collisional effects are less of a problem. Laser Induced Fluorescence has been reported on an electronically excited state [30] but this is much less common.

In conclusion it can be said that there are a wide range of experimental methods for selecting initial states of species involved in both reactions and photodissociations and for monitoring the energy distribution and partitioning as a result of these processes.

1.3 THEORETICAL APPROACHES

The requirements of initial energy in reactants and the partitioning of available energy in the products are controlled by the potential surface (or surfaces) governing a reactive or photodissociative event [31]. Fig. 1.1 illustrates schematic potential surfaces for the hypothetical exchange reaction:

$$A + BC \rightarrow AB + C \qquad (1.1)$$

under conditions of co-linear geometry. In case (a) the transition state occurs early in the entrance channel of the potential surface and is known as an attractive interaction. Relative translational energy is most effective in overcoming this barrier and results in vibrational energy in the diatomic products as illustrated by the typical trajectory

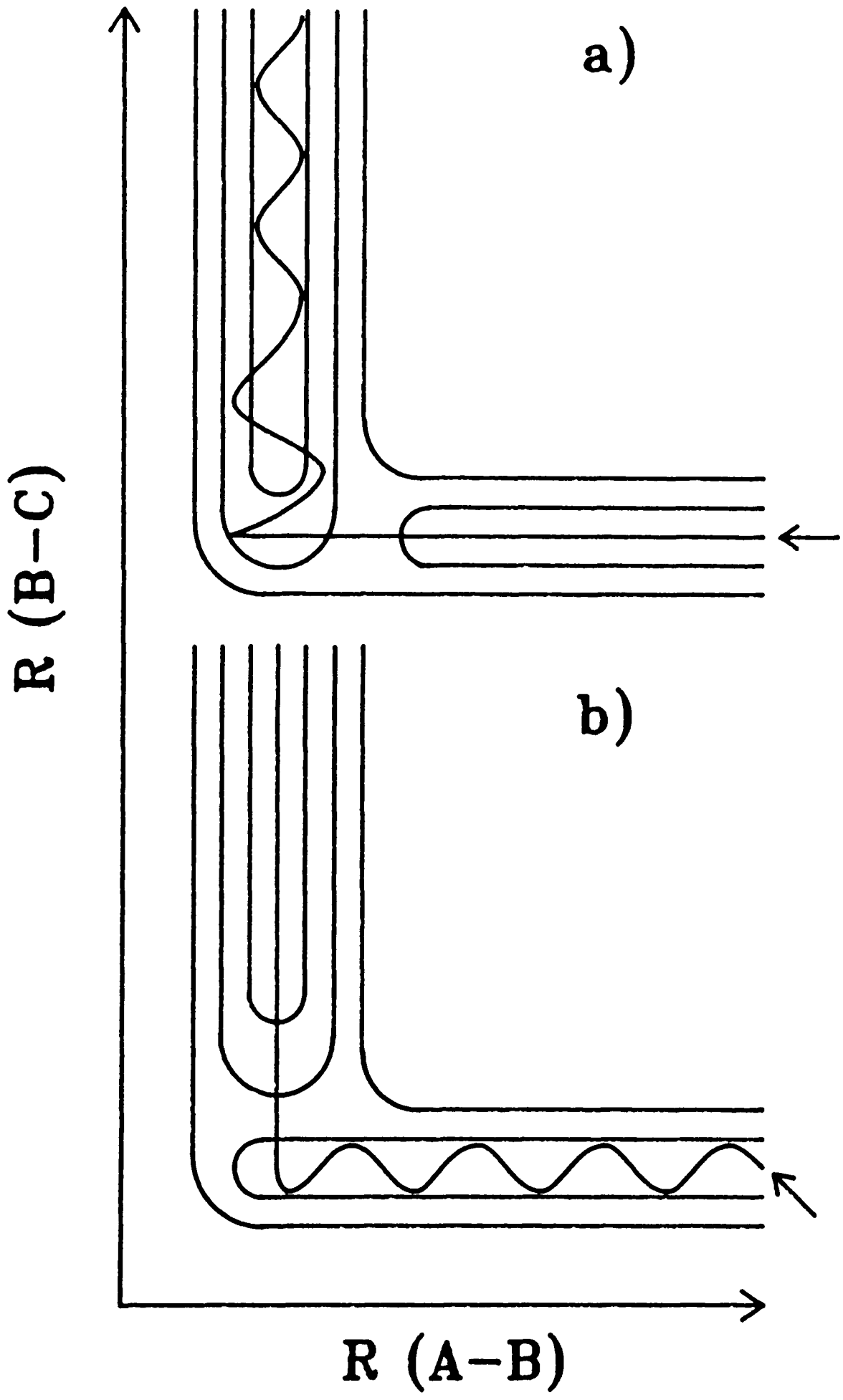

Figure 1. Hypothetical potential surface for colinear reaction A+BC. a) shows an early transitions state in which relative translational energy is effective in surmounting the barrier. b) shows a late transition state in which vibrational energy within BC is effective.

across the surface. In the second case, (b), characterised by a late transition state and known as a repulsive surface, the converse applies, in that initial vibrational energy is most efficient in surmounting the potential barrier, resulting in relative translational energy in the products. Initial translational energy results in a trajectory which does not give rise to reaction. The two idealised situations are related by the principle of microscopic reversibility. The case illustrated in Fig. 1.1 represents a reaction upon a ground state potential surface. In the case of photodissociation this is not usually so. For direct photodissociation, absorption of the excitation radiation places the molecule on an excited repulsive surface which leads to photofragments. In the case of predissociation initial excitation is to a bound excited state and a crossing to a repulsive potential surface occurs leading, finally, to fragments.

For photodissociation, and to a lesser extent reaction, the theoretical aspects can be separated into two major parts. Firstly there is Franck-Condon excitation from the ground state potential to the excited surface. In this region geometric changes in the reactant will occur, governed by the Frank-Condon factors of the two potential surfaces involved. Secondly there are effects due to separation of the fragments, known as the final state interactions, which govern the partitioning of the energy into product degrees of freedom and are influenced by the dissociative potential topology only. In reality interference effects between these two phases must be considered and may lead to changes in the final results. In a reaction rather than

photodissociation the initial stage can be thought of as leading to the formation of the transition state.

1.3.1 Photodissociation One of the earliest models of photodissociation, which concentrated exclusively on final state interactions, was the impulsive model [32], which considered a repulsive force between the atoms which separated during the photodissociation along the line of the breaking bond. The application of the principles of conservation of energy, linear momentum and angular momentum then gave rise to a calculated energy partitioning which was compared to experimental results. This model is considered in more detail later in this thesis. The basic model was later modified to take some account of the initial excitation step [33].

In contrast to this, theories were developed which considered the photo-excitation step to be the most important and final state interactions were thought to play only a minor role in modifying the Franck-Condon dominated effects [34] [35]. This was modified in a series of articles by Freed and co-workers [36] in which the final state interactions were included as a repulsive potential which was varied to give a good fit to experimental results. The theory was extended from linear to bent triatomic parent molecules and predicts both angular and rotational effects some of which are yet to be investigated experimentally.

The pragmatic measure of separating photodissociation into two distinct phases, whilst instructive, is physically unrealistic and

recently some progress has been made in the field of full 3-D quantum mechanical calculations of photodissociation and reaction dynamics. These advances have been reviewed by Shapiro and Bernsohn [37]. The basis of such approaches is the calculation of a more or less ab-initio potential surface or surfaces relevant to the particular case under study. In general, potential curves are calculated for a number of distinct geometries and a full surface is produced by fitting an analytic form or by a spline method [38]. It is important to ensure that such surfaces are consistent with known dissociation channels, symmetry and spectroscopic data. In some cases semi-empirical surfaces which are consistent with a body of experimental data are used, or ab-initio surfaces are modified, to ensure consistency. To date accurate calculations have only proved successful for small systems such as $H+H_2$ [39] [40].

Once a reliable surface has been established then there are essentially three possible methods of calculating the energy disposal in the products or fragments. The first is a quantum method and involves the solution of the Schrodinger equation for the scattering of all initially occupied states on the potential surface giving rise to the product energy distribution as a function of collision energy. The majority of studies have been restricted to one dimensional calculations due to the complexity of such a method. An alternative is the application of semi-classical collision theory which is an approximation to the full quantal procedure described above. Finally a classical trajectory method may be used. In most cases a Monte-Carlo averaging

over initial reactant states is used to obtain the initial trajectories, a sufficient number of which are run on the potential surface to establish the final outcome of the reaction or photodissociation.

In the case of a photodissociation, the initial trajectories are governed by the Franck-Condon area of the excited state potential surface populated by photon absorption. Predissociation, in most cases, is treated as a direct dissociation. This is an area which has received little attention theoretically [41] considering the large number of important predissociative photofragmentations, some of which have received considerable experimental investigation. Some classical trajectory studies on more than one potential surface have been carried out but again for relatively small systems [42].

In principle it should be possible to invert an energy disposal distribution to yield a potential surface but in practice this has not been achieved. A full energy distribution would be required. It is more common for potential surfaces to be modified in the light of experimental results as described previously.

For systems in which there is a relatively long lived intermediate, such as a transition state with a potential well or a long lived predissociative state, it has been found that statistical models can be applied. For reactions, transition state and RRKM [43] type models are used to obtain reaction rates whilst more recent models such as phase space theory [44] and the statistical adiabatic channel model [45] can be applied to predict the product energy distribution. The use of

information theoretic techniques known as surprisal analysis pioneered by Levine and Bernstein [46] has been used to classify energy disposal in the products of reactions and photodissociations. This involves comparing an experimentally determined energy distribution to one which would be expected on the principle of maximal entropy - essentially a statistical distribution. Surprisal analysis is discussed in more detail later in this thesis.

In conclusion it can be seen that there are a variety of theoretical models which have been applied to reaction and photodissociation dynamics. It should also be apparent that there is some discrepancy between experiments performed and theoretical investigations. It is by no means clear whether experimental or theoretical limitations have prevented a more general meeting of minds. It is hoped that this gap will narrow considerably in the near future.

1.4 WORK PRESENTED

This thesis investigates aspects of chemical dynamics concentrating on final product energy distributions in three different systems.

Chapter 3 describes both a two photon and a three photon dissociation of gas phase water molecules using 266nm and 355nm radiation respectively as the excitation source. The photodissociation, which has been well studied in single photon excitation, gives rise to OH radicals in both the ground $OH(X^2\Pi_i)$ and first excited $OH(A^2\Sigma^+)$ states. The rotational distribution arising in the $OH(A^2\Sigma^+)$ state is compared to theoretical predictions based on ab-initio potential

surfaces.

Chapter 4 describes an investigation of the 355nm single photon dissociation of gas phase methyl nitrite molecules. The rotational and vibrational distribution resulting in the $NO(X^2\Pi_i)$ fragment is compared to other experimental results, and to both impulsive and statistical models of dissociation.

In Chapter 5 the gas phase radical reaction between oxygen atoms and the CS radical is studied. This reaction, which is a classic example of one taking place on an attractive potential surface, results in highly vibrationally excited CO molecules with a well known distribution. The rotational distribution, which has not been investigated previously, is presented in this chapter.

CHAPTER TWO

2.1 INTRODUCTION

The ground electronic state species studied in this thesis by Laser Induced Fluorescence (LIF); $OH(X^2\Pi_i)$, $CO(X^1\Sigma^+)$ and $NO(X^2\Pi_i)$ require radiation in the range 280-207nm to promote them to their first electronically excited state. Tunable radiation in this region was obtained by frequency doubling and Raman shifting the output of a tunable dye laser, pumped by the 2nd harmonic of a pulsed Nd:YAG laser. In addition the higher harmonics of the Nd:YAG laser were available to perform the photodissociations.

2.2 THE LASER

The commercial Nd:YAG laser and associated dye laser (JK Lasers Ltd. Hyper-Yag, System 2000L) are shown in Fig. 2.1. The Q-switched Nd:YAG oscillator produced pulses of wavelength 1.064μm = 9397.613cm^{-1} lasting ~20ns and containing ~200mJ pulse^{-1} at a repetition rate of 10Hz. The spatial profile was Gaussian indicating TEM_{00}. A beam expanding telescope (BET) was used to compensate for thermal lensing in the Nd:YAG crystal and to match the oscillator output to the amplifier rod. Amplification raised the pulse energy to ~750mJ.

Non-linear second harmonic generation (frequency doubling) in temperature stabilised, angle tuned KDP gave up to 250mJ pulse^{-1} at 532nm. Following this, either sum frequency mixing of the fundamental wavelength, at 1.064μm, and the second harmonic at 532nm gave up to

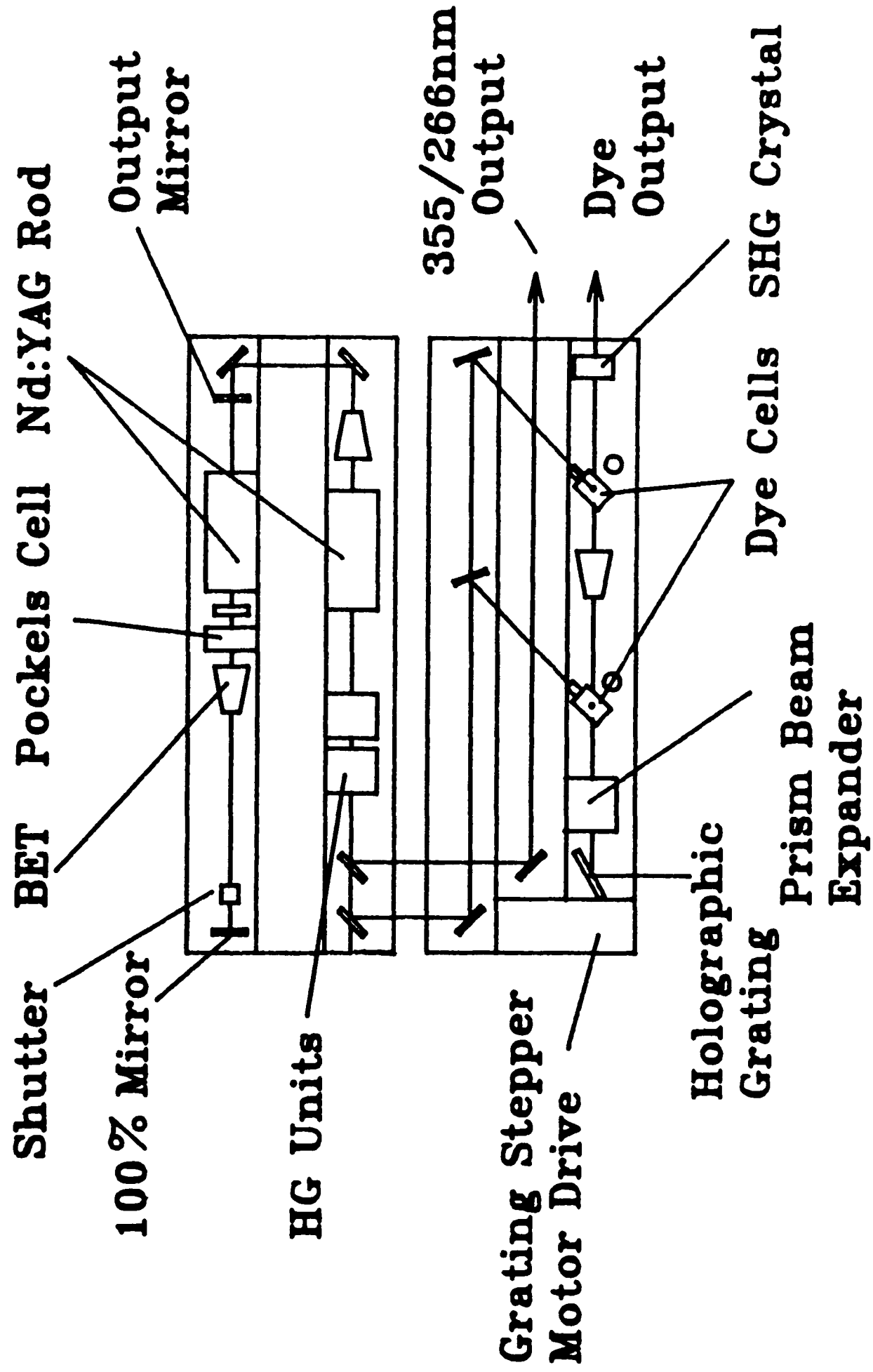

Figure 2.1. Schematic plan view of the laser system showing both pump laser and dye laser.

120mJ pulse^{-1} of the 3rd harmonic at 355nm, or second harmonic generation of the 532nm resulting in 60mJ pulse^{-1} of the fourth harmonic at 266nm was possible. All output beams were highly linearly polarised (>90%).

The second harmonic of the Nd:YAG laser was used to pump the dye laser which comprised an oscillator and single amplification stage. The oscillator consisted of a stepper motor driven holographic grating, prism beam expander, transversely pumped gain medium at Brewster's angle and a 4% reflectivity output coupler. Amplification, following beam expansion via a BET, gave pulses lasting ~10ns and containing up to 35mJ of energy tunable in the region 555-585nm (Rhodamine 6G,B). The bandwidth was ~0.3cm^{-1} and the output horizontally polarised. Frequency doubling in temperature stabilised, angle tuned KD*P, with 20% efficiency gave an ultra-violet tuning range of 277-292nm.

2.3 STIMULATED RAMAN SCATTERING

Several non-linear optical techniques have been proposed to extend the tuning range of frequency doubled dye lasers into the 200nm region and beyond. Of these Stimulated Raman Scattering (SRS), usually employing hydrogen gas as the non-linear medium, has proved efficient and relatively simple [47] [48].

Stimulated Raman Scattering in H_2 results in a series of Stokes and Anti-Stokes output lines, in a similar manner to Spontaneous Raman Scattering but with two important differences. The first of these is that the intensity of the Stimulated Stokes and Anti-Stokes lines are

comparable to that of the pump - indeed considerable pump depletion is observed. Secondly, suceedingly higher order lines do not show anharmonicity, all being separated by $4155cm^{-1}$ in the case of SRS in hydrogen. This is due to the non-linear process by which Stimulated Raman Scattering occurs.

The polarisation of a medium with non-linear susceptibility subject to an electric field, E, can be expressed as an expansion in the field and the susceptibility χ [49]

$$P = E_0 (\chi^{(1)}E + \chi^{(2)}E^2 + \chi^{(3)}E^3 ..) \qquad (2.1)$$

Stimulated Raman Scattering can be expressed as a non-linear interaction involving the 3rd order susceptibility, $\chi^{(3)}$. The depletion of a pump wavelength and the concomitant growth of the Stokes field in the presence of a medium with a non-zero value of $\chi^{(3)}$ is given by: [50]

$$\partial E_p/\partial z = -\omega_p/2cn_p \cdot \chi''_R|E_s|^2 E_p \qquad (2.2)$$

$$\partial E_s/\partial z = \omega_s/2cn_s \cdot \chi''_R|E_p|^2 E_s \qquad (2.3)$$

where χ''_R is the peak Raman susceptibility, n the refractive index, c the velocity of light in vacuo and ω the frequency. The subscripts p and s refer to the pump and Stokes lines respectively. Under steady-state pump conditions the Stokes field grows exponentially. Normally SRS builds up from the Spontaneous Raman noise level so it is more usual to express the Raman gain in terms of the Spontaneous Raman cross-section, $\partial\sigma/\partial\Omega$: [50]

$$g_s = 4\lambda_s^2 N(d\sigma/d\Omega) I_p / n_s^2 \hbar\omega_p \Delta\omega_R \qquad (2.4)$$

where N is the population density, I_p the pump intensity, $\Delta\omega_R$ the FWHM Raman linewidth and λ the Stokes wavelength. Higher order Stokes and Anti-Stokes lines are either stimulated by the Stimulated Raman wave or produced by a non-linear four wave mixing process involving two pump photons and a Stimulated Stokes photon. This is illustrated in Fig. 2.2 for the first Anti-Stokes output line. The phase matching requirements for four wave mixing, also illustrated in Fig. 2.2 results in a conical output of the Stimulated Raman Scattering lines, symmetrically disposed about the pump propagation direction.

The wavelength regions of interest to the present studies accessible with the current apparatus of frequency doubled Rhodamine 6G and B as pump and employing 1st, 2nd and 3rd Anti-Stokes SRS transitions are shown in Fig. 2.3. More sophisticated equipment allows complete coverage of the spectral region 880-185nm with no holes in the tuning range [47].

The high pressure hydrogen cell used for Stimulated Raman Scattering was 38cm in length and was constructed from stainless steel in the Laboratory Workshops. The windows were 5mm thick Spectrosil B. Both fundamental and the second harmonic of the dye laser were focussed into the cell using a 20cm focal length Spectrosil B lens and multi-line output was recollimated using a second 20cm focal length lens. The required line was then selected using a Spectrosil prism arrangement. A parametric study of Stimulated Raman Scattering using this apparatus

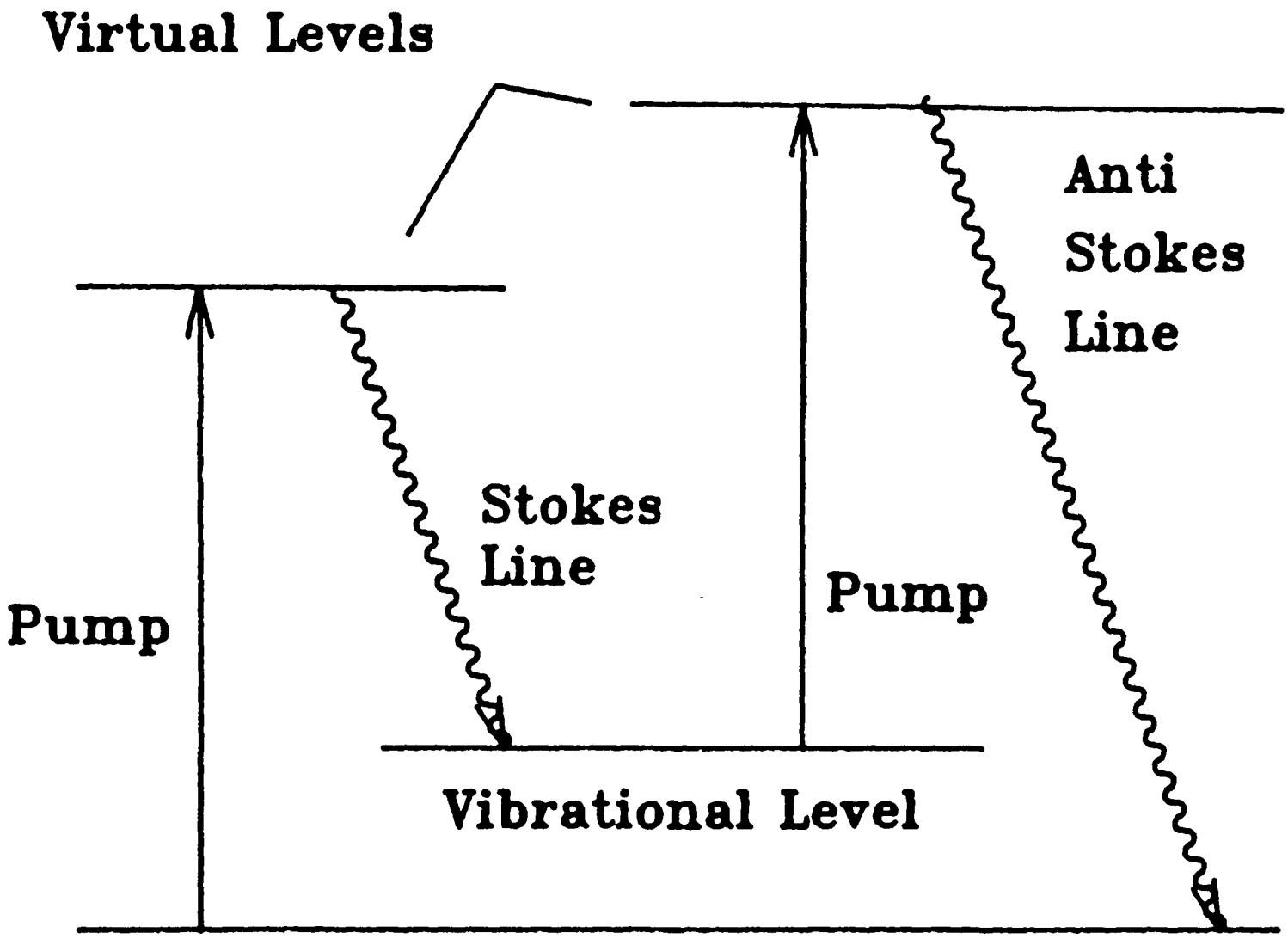

Figure 2.2. Top: Schematic of four wave mixing process giving rise to high order SRS transitions. Bottom: Phase matching requirement leading to conical output of SRS about propagation direction.

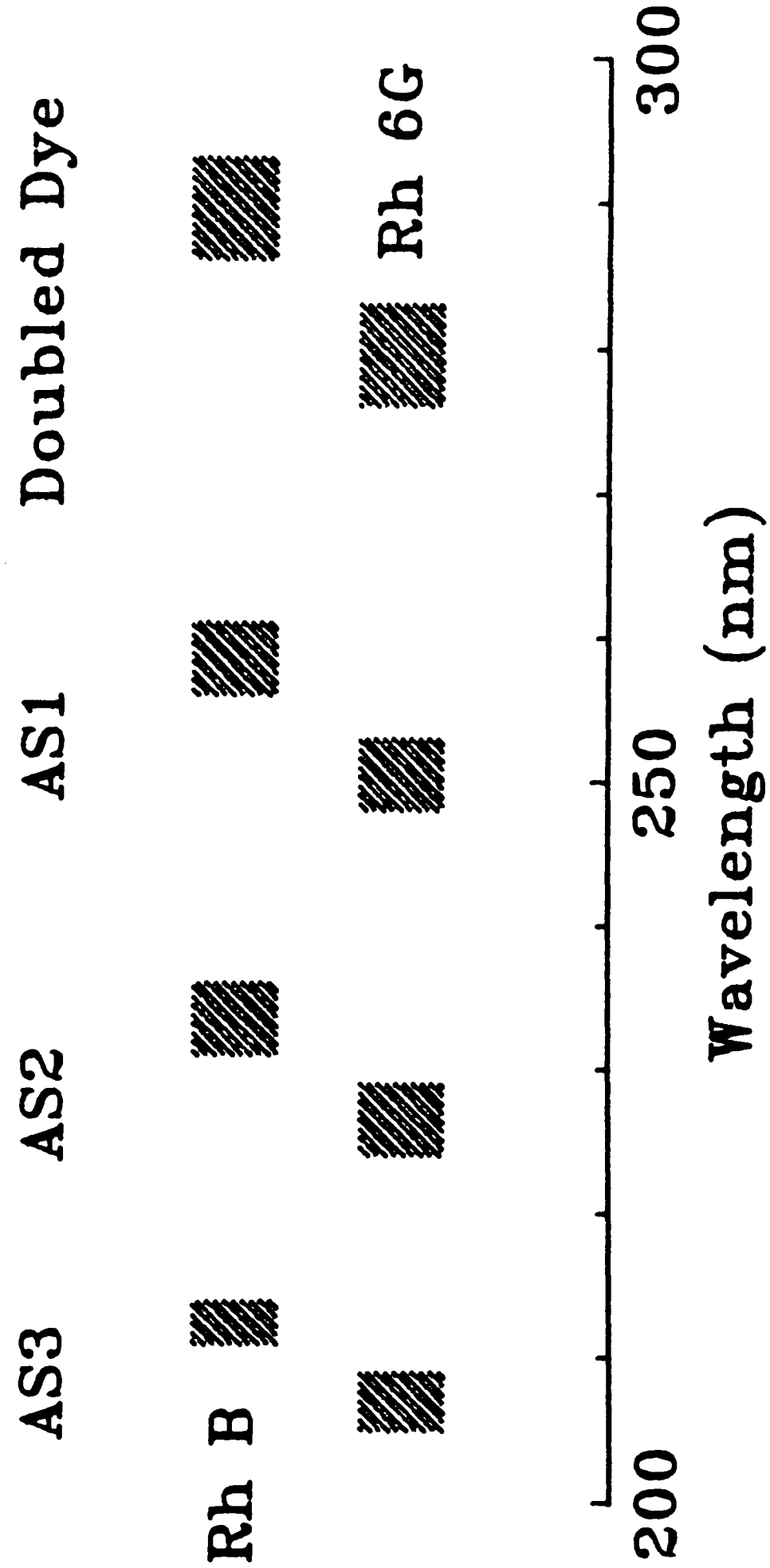

Figure 2.3. Tuning range achieved with laser system, employing SRS of frequency doubled Rhodamine 6G and B.

showed similar operating conditions of pressure dependence and output to those reported in the literature [47]. Typically a pressure of 200psig of hydrogen (BOC commercial grade) was maintained in the cell, this being optimum for the 2nd and 3rd Anti-Stokes transitions which were used in the majority of experiments reported in this thesis.

For a linearly polarised pump theory suggests that the SRS output should also be linearly polarised. The polarisation of the SRS lines was found to depend critically on the optical alignment through the focussing and recollimating lenses, and on the laser beam spatial quality.

2.4 REACTION CELLS

Emission spectra from $OH(A^2\Sigma^+)$ resulting from the two photon dissociation of water were taken in a Pyrex cell with Spectrosil windows [51]. All Laser Induced Fluorescence spectra were recorded in a hexagonal stainless steel cell with a range of windows, baffled arms and gas inlets.

2.4.1 Emission Spectra from Electronically Excited OH The apparatus used is shown schematically in Fig. 2.4. The 4th harmonic of the Nd:YAG laser was focussed, using a 10cm focal length lens through a Spectrosil input window and exited through a second window at Brewster's angle, scattered light being collected by a Wood's horn. Emission from the focal region was viewed at right angles to the beam direction through a smaller Spectrosil window and imaged onto the entrance slit of a 0.5m Czerny-Turner configuration monochromator with a stepper motor

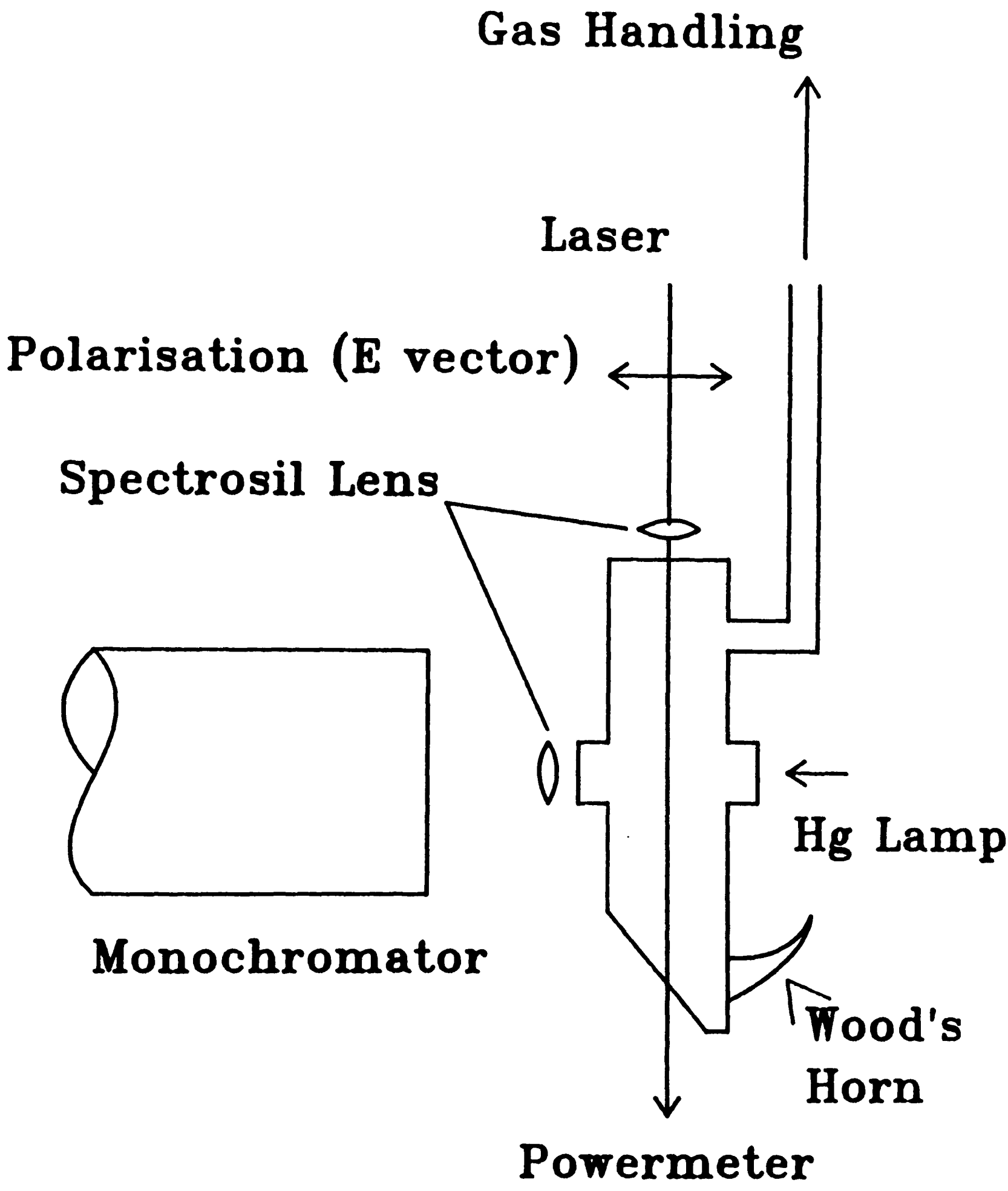

Figure 2.4. Pyrex cell with Spectrosil windows used to observe emission from $OH(A^2\Sigma^+)$.

controlled 1200 line/inch grating blazed at 300nm.

The monochromator wavelength and resolution were calibrated using the 313nm lines from a low pressure Hg lamp. The emission intensity at the exit slit was detected by an EMI 9813, bialkali photocathode, 14 stage photmultiplier. The laser power was monitored after exiting the cell using a Scientech model 364 powermeter.

2.4.2 Laser Induced Fluorescence Spectra Laser Induced Fluorescence spectra were recorded in a hexagonal stainless steel cell constructed in the laboratory workshops. Three basic experiments were performed.

- LIF of $OH(X^2\Pi_i)$ following photodissociation of H_2O using both 266 and 355nm radiation.
- LIF of $NO(X^2\Pi_i)$ following 355nm photodissociation of CH_3ONO.
- LIF of $CO(X^1\Sigma^+)$ following the reaction of the oxygen atom and the CS radical.

The first two of these were pump-probe type experiments for which the experimental arrangement was similar in each case. Fig. 2.5 shows the configuration used for the LIF of $NO(X^2\Pi_i)$. The cell was evacuated through a liquid nitrogen vapour trap by a small oil diffusion pump (Edwards E04), backed by a rotary pump. Pressure within the cell was measured by an ionisation gauge and a capacitance manometer (Baratron 220A). The laser beams entered the cell through Spectrosil B windows, either at Brewster's angle or normal to the beam direction. Baffled entry arms were used where scattered light proved to be a problem.

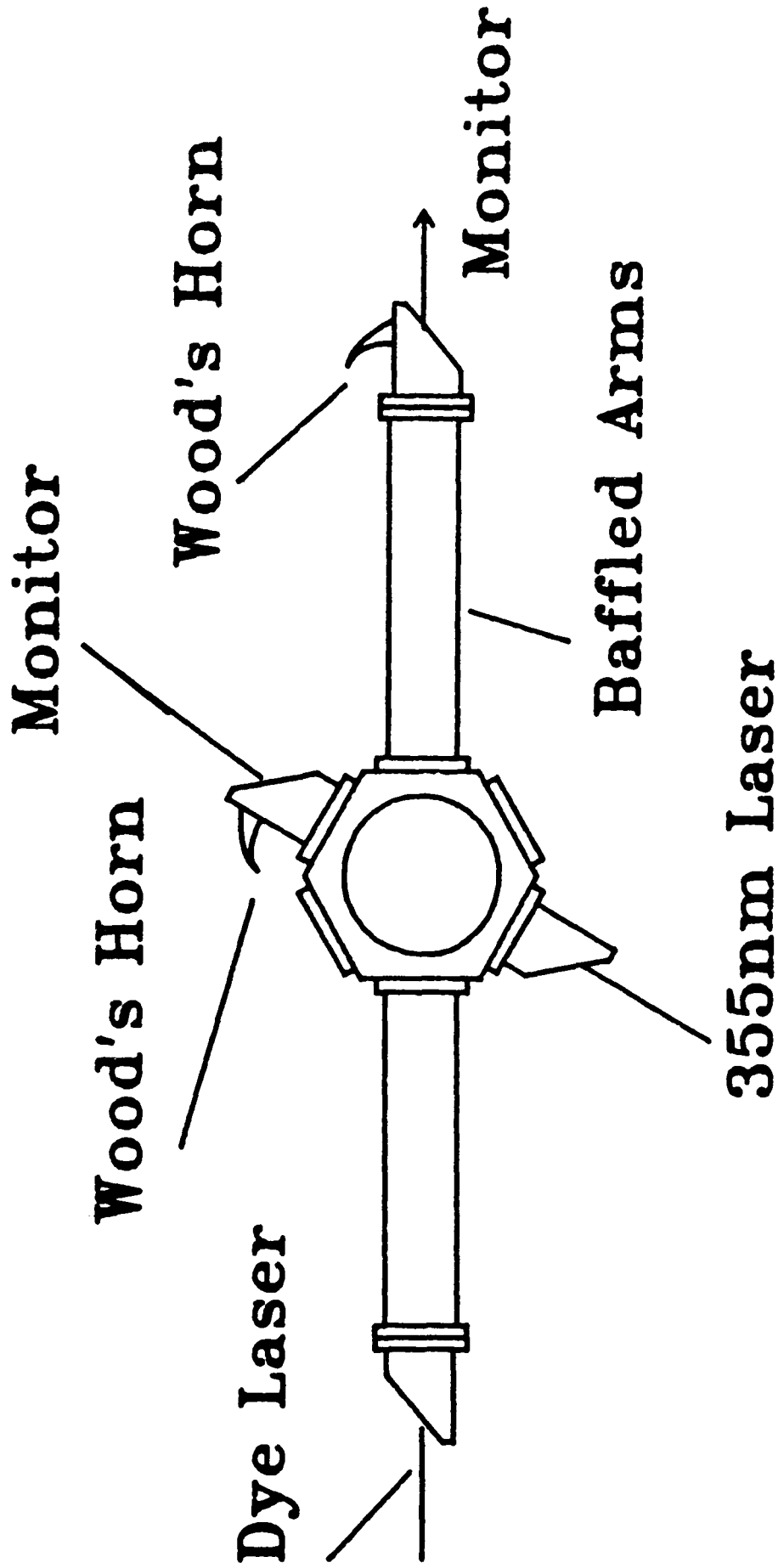

Figure 2.5. Diagram of stainless steel cell used in LIF experiments. Configuration shown was used for the 355nm dissociation of CH_3ONO described in Chapter 4.

Laser power was monitored upon leaving the cell using either a Scientech 364 powermeter or a photodiode/integrating amplifier combination. LIF within the cell was viewed vertically through a MgF_2 window and imaged by a MgF_2 lens onto one of three photomultipliers: EMI 9558 (S20 photocathode) for red emission, EMI 9813 (Bialkali photocathode) for blue/UV emission, and EMI-GENCOM G-26E314LF (CsI photocathode) for vacuum-ultra-violet emission. When the solar blind photomultiplier was used the region between the cell window and the photomultiplier window was flushed with Ar. This was to prevent absorption of the VUV radiation by the atmosphere and to prevent electrical breakdown from the photocathode to earth. Gases were stored in bulbs on a glass vacuum line evacuated by a mercury diffusion pump, backed by a rotary pump, and admitted to the reaction cell via a needle valve and side arm.

For the investigation of the LIF of $CO(X^1\Sigma^+)$ following the reaction of O and CS a different arrangement was used. Both a low pressure and a fast flowrate were required within the cell and the pump described above was replaced by a large, 10 inch diameter, diffusion pump (Edwards Diffstak 160/750) capable of a pumping rate of $700ls^{-1}$ at 10^{-4} Torr and a large rotary pump (Edwards ISC 450B). The design of the microwave discharge units used for the production of atoms and radicals is shown in Fig. 2.6. A precursor gas was mixed with Ar on the glass gas handling vacuum line. The gas mixture, controlled in composition by needle valves, passed through a microwave discharge cavity at 2.45GHz (EMS Microtron 200) The resulting fragments and gases passed into the inlet arm where most were removed by fast rotary pumps (Edwards ES200).

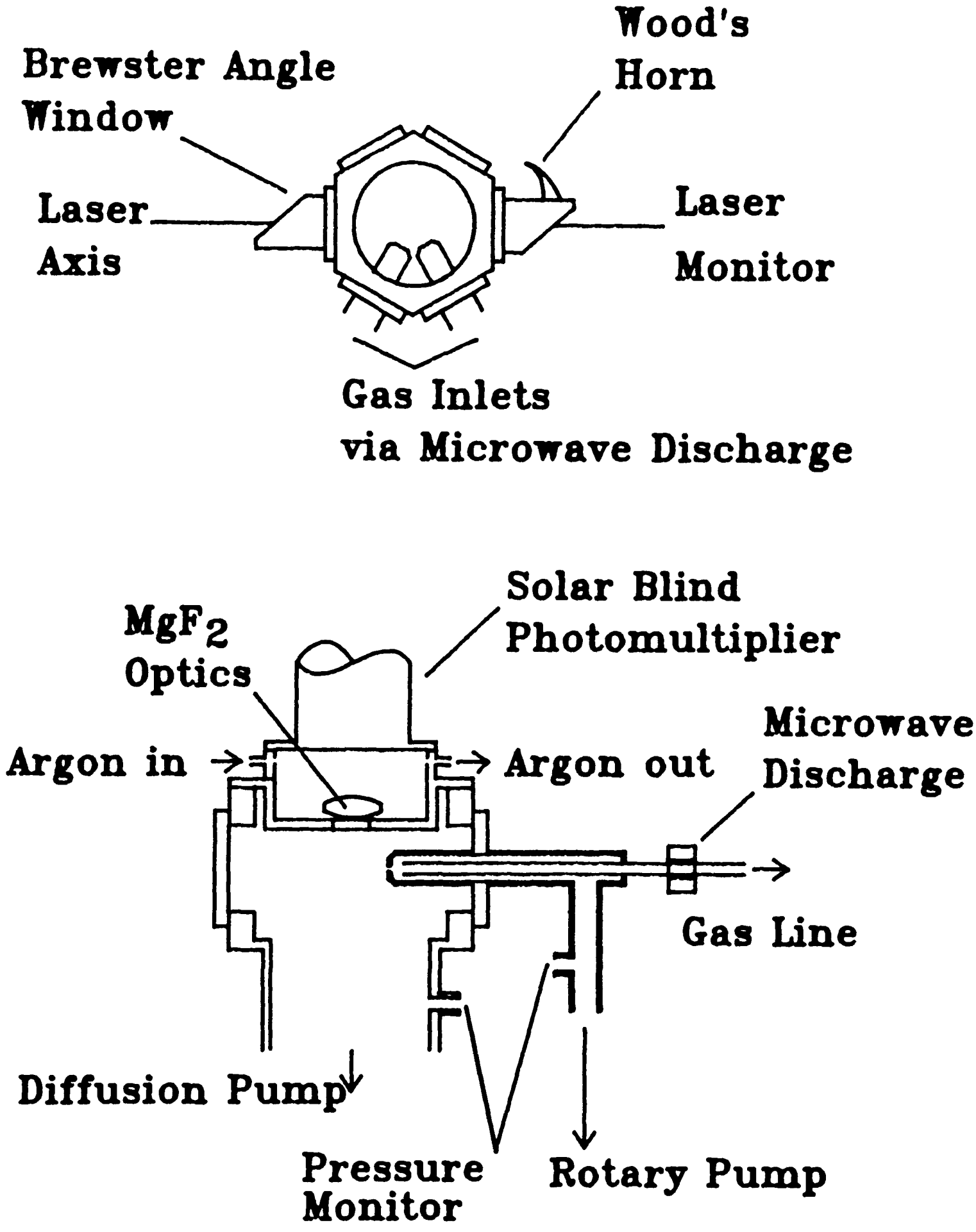

Figure 2.6. Microwave discharge units used for the production of Oxygen atoms and CS radicals used in the experiments described in Chapter 5.

Radical recombination and wall removal were minimised by coating all glass components in ortho-phosphoric acid and all metal components in PTFE. The pressure inside the microwave discharge inlets was monitored via a capacitance manometer (Baratron 221) and was typically maintained at 1 Torr. A small pinhole leak allowed a fraction of the discharge mixture into the main hexagonal cell. The pressure within the cell was controlled by varying the size of the pinhole leak.

2.5 DATA ACQUISITION

Emission spectra from $OH(A^2\Sigma^+)$ and LIF spectra from $OH(X^2\Pi_i)$ were acquired using a boxcar signal averaging system (Ortec Brookdeal models 9415,9425) operating as a linear gate and synchronised to the laser via the pockels cell trigger. A 20μs sampling gate was normally used. The integration time constant depended on the amount of signal: for the weak emission from $OH(A^2\Sigma^+)$ a time constant of 30 s was typically employed with a monochromator scan rate of ~0.05nm/min. Experiments involving LIF gave more signal hence faster scan rates and shorter time constants could be used.

The 4th harmonic of the Nd:YAG laser was monitored, as described previously, with a power meter with a time constant of 10s. The frequency doubled dye laser was monitored via a photodiode/integrating amplifier combination and this was acquired using a second boxcar system. The output from the boxcars and the power meter, as appropriate, were fed to a 3 pen chart recorder (Rikadenki R13) so that corrections for variation in laser energy could be made at a later stage

during analysis.

Time resolved data were obtained using a transient digitiser (Biomation 8100) with a 10ns sampling gate and a maximum sampling rate of 100MHz. In early experiments the data were transferred to a signal averaging system (Nicolet 1070,SD78A Buffer) and then output manually. For later work this was replaced by a microcomputer data acquisition system (Strumech System 19) allowing storage on floppy disc for subsequent analysis.

LIF spectra of $CO(X^1\Sigma^+)$ and $NO(X^2\Pi_i)$, in which Stimulated Raman Scattering of the frequency doubled dye laser was used as excitation source could not be reliably recorded using the boxcar signal averaging system described above due to the large (≥50%) shot-to-shot variation of the UV excitation wavelength. This jitter was due to the large number of non-linear optical processes which gave rise to the desired wavelength radiation, and this difficulty was overcome using the transient digitiser/microcomputer system described above to correct for laser variations on a shot-to-shot basis.

In the non-saturated region of Laser Induced Fluorescence the emission intensity at a fixed wavelength is directly proportional to the excitation laser intensity:

$$S_{lif} = C(\lambda, N_i) I_L \qquad (2.5)$$

where λ is the laser wavelength and N_i molecular properties such as line strength, concentration etc. This implies that the variation in signal

due to laser jitter can be corrected by dividing the signal by the laser intensity at each point in the wavelength region of interest. This correction was performed digitally using the transient recorder in dual channel mode with the signal from the photomultiplier input to one channel and the output of the photodiode/amplifier combination to the other.

As a test of the data acquisition system, LIF spectra of a room temperature sample of $NO(X^2\Pi_i)$ (Matheson, 98%) were found to be reproducible and to yield a rotational distribution corresponding to a 300K thermal sample.

CHAPTER THREE

3.1 INTRODUCTION

In recent years it has been recognised that the experimental difficulties associated with the investigation of the spectroscopy and photochemistry of small molecules in the vacuum-ultra-violet spectral region can be alleviated by employing multi-photon techniques, bringing the excitation wavelength into the more easily accessible visible or near ultra-violet region. In addition, the different selection rules for various multi-photon transitions may allow single-photon forbidden states to be accessed leading to new spectroscopy and photochemistry.

The work described in this chapter concerns the multi-photon disssociation of gas phase H_2O using high intensity radiation from a Nd:YAG laser. The fourth harmonic at 266nm, generated by two stages of frequency doubling of the fundamental, was used in the majority of the studies to cause two photon absorption followed either by dissociation to give the detected OH fragment in both the ground and excited electronic states, or by further absorption of a single photon to produce ions (2+1 Resonance Enhanced Multi-Photon Ionisation, REMPI). Preliminary results are presented for the equivalent proccess resulting from three photon absorption of the third harmonic of the Nd:YAG laser at 355nm.

3.1.1 Spectroscopy The vacuum-ultra-violet absorption spectrum of H_2O, which has been extensively studied and reviewed [52] [53] [27] is shown in Fig. 3.1. A schematic molecular orbital diagram for H_2O is shown in

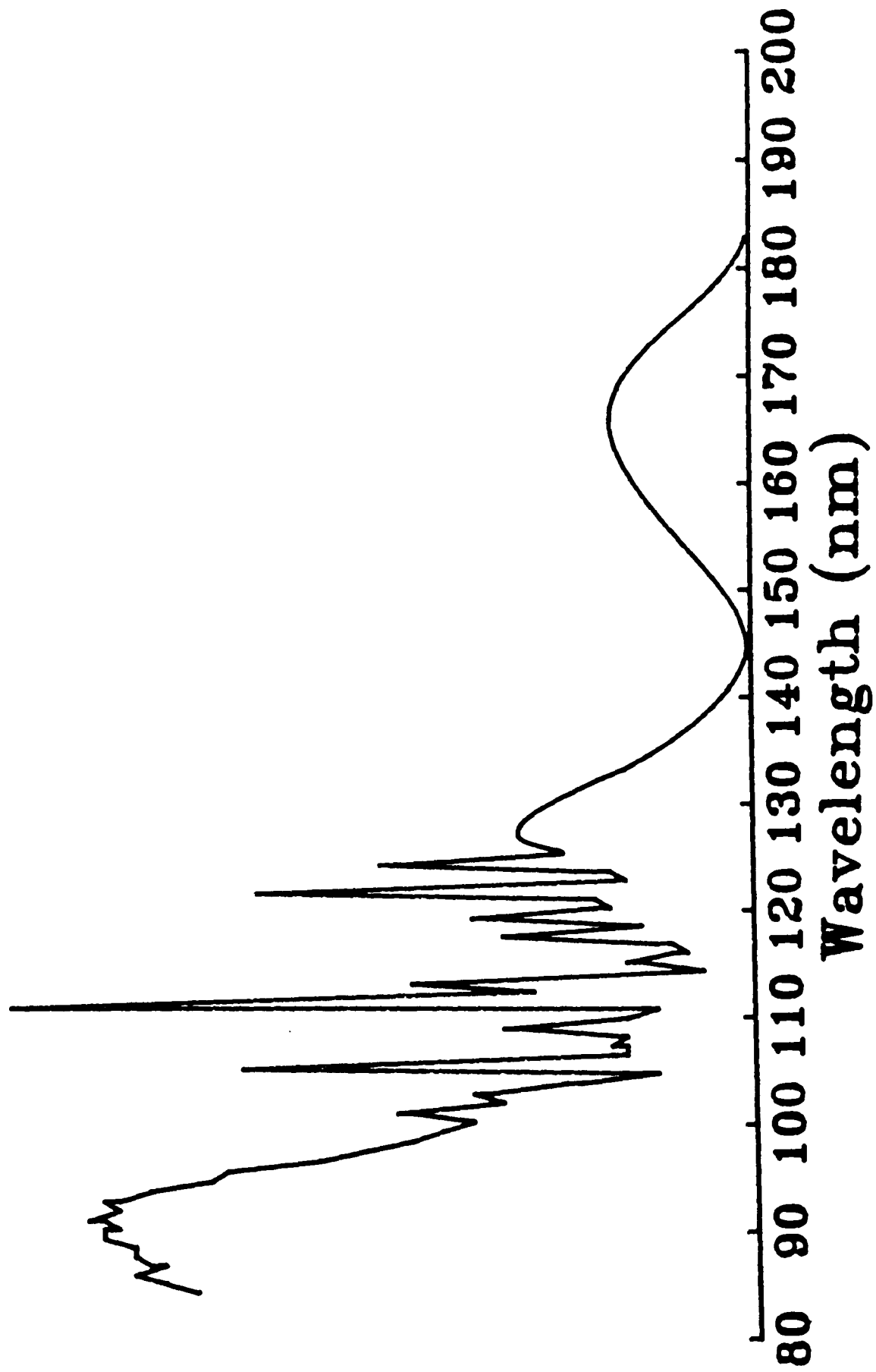

Figure 3.1. Absorption spectrum of H_2O, taken from [52].

Fig. 3.2. The ground state is $(1a_1)^2(2a_1)^2(1b_2)^2(3a_1)^2(1b_1)^2$: $\tilde{X}^1A_1$.

There is little doubt that, in the low lying electronically excited states, the vacated orbitals are the $3a_1$ and $1b_1$; the others being deeply buried in the core. There is, however, considerably more debate upon the nature of the populated orbital, in particular the degree of Rydberg character of some of the final states. Rydberg orbitals are extremely diffuse, resulting in a high sensitivity to external perturbations such as pressure changes and are essentialy non-bonding, resulting in a geometry close to that of the molecular ion. If the vacated orbital is also non-bonding then a sharp atomic-like Rydberg series results. In other cases, geometrical changes broaden the Rydberg transitions. The absorption spectrum of water is complicated because the Rydberg transitions fall at the same energy as the intravalence, molecular, transitions leading to mixed Rydberg/Intravalence orbitals in which the degree of mixing and composition of the orbitals can vary greatly.

The first absorption band of H_2O, centred at 167nm is a diffuse continuum, reflecting rapid predissociation, which shows a poorly defined progression in the bending vibration ν_2'. The raised frequency of this vibration compared to that in the ground state suggests that the terminal orbital is more H-H bonding than the ground state. Both the $4a_1$ molecular and $3sa_1$ Rydberg orbitals satisfy this condition. The differences between this band and the $^2B_1$ cationic state, studied by Photo-Electron Spectroscopy (PES) [54] and which should resemble the Rydberg state suggests considerable intravalence character. This is in

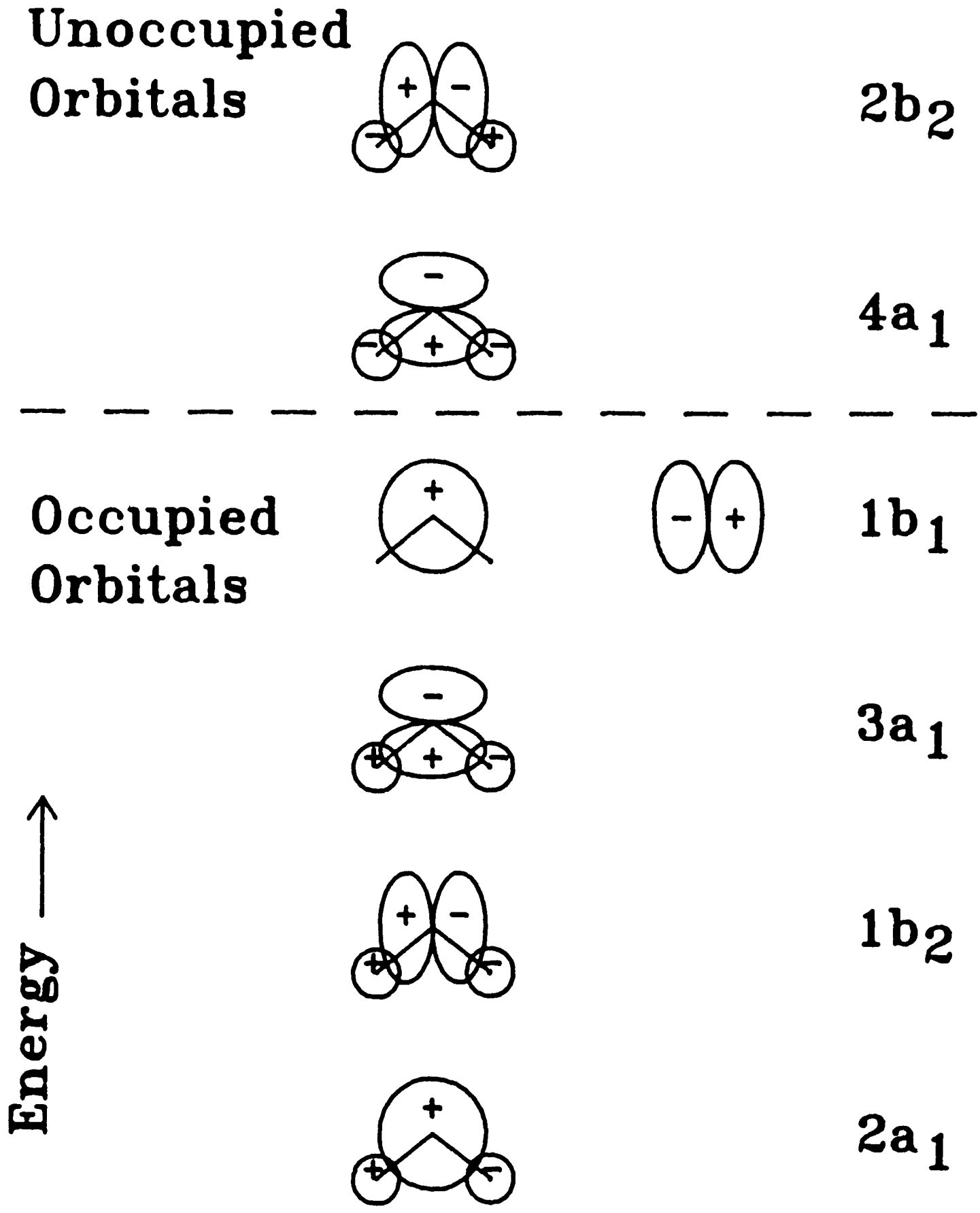

Figure 3.2. Schematic molecular orbital diagram for H_2O showing high occupied and lowest unoccupied orbitals. Two views of the $1b_1$ molecular orbital are shown.

contradiction with calculations [55] [56] which suggest that the state is predominantly $3sa_1$ Rydberg in character. In summary the first absorption continuum has been assigned as involving a mixed Rydberg/Intravalence state $3sa_1/4a_1$ and the state assigned $\tilde{A}^1B_1$.

The second absorption band, centred at 128nm, shows structure which has been asigned to a long progression in $\nu_2' \sim \nu_2''/2$, suggesting considerably less H-H bonding in the excited state compared to the ground state. The similarity to the $\tilde{X}\ ^1A_1 \rightarrow ^2A_1$ PES band suggests that the symmetry of the excited state is $^1A_1$ and that the vacated orbital is the $3sa_1$, which is strongly H-H bonding. Isotopic substitution studies [57] suggest that the excited state is close to linear and quantum defect arguments [58] can be used to show that the state is a Rydberg $3sa_1\ \tilde{B}^1A_1$.

Both the $\tilde{A}^1B_1$ and the $\tilde{B}^1A_1$ states correlate with the $^1\Pi_u$ state in linear geometry and hence should exhibit Renner-Teller splitting. This can be observed as an alternate (ν_2' odd) sharp, (ν_2' even) broad vibrational structure on the 128nm absorption band.

An irregularity in the vibrational structure of the $\tilde{B}^1A_1 \leftarrow \tilde{X}^1A_1$ band is seen at 136.5nm. Wang <u>et al</u> [52] assigned this to a $3sa_1\ ^1B_1$ Rydberg state, on the basis of an assignment of the corresponding $4sa_1\ ^1B_1$ state to a feature at 105.5nm, from quantum defect arguments. However a more recent study [27] has reported a hitherto undiscovered state of H_2O and assigned it as $\tilde{D}'\ ^1B_1\ 4sa_1 \leftarrow \tilde{X}^1A_1\ 1b_1$ thus bringing the earlier assignment into question. A state formed from the $3pb_2\text{-}1b_1$

Rydberg transitions of symmetry $^1A_2$ has been predicted theoretically to lie in this region [59] and it has been suggested [60] that the irregularity is due to this state, accessed by vibronic coupling of the (0,0,1) level of the $^1A_2$ state giving overall $^1B_1$ symmetry which is then allowed in single photon absorption. Polarisation studies, discussed shortly, have also been interpreted as showing evidence for absorption to a state other than $\tilde{B}^1A_1$ in this region with the $^1A_2$ a possible candidate. Detailed quantum mechanical calculations, also discussed later in the chapter, however suggest that the structure is explicable in terms of structure on the $\tilde{B}^1A_1$ potential surface and that no other state need be invoked to explain the irregularity. The $^1A_2$ state in this wavelength region has not been observed in Multi-Photon Ionisation spectroscopy [27], the conditions of which (3 photon excitation to the intermediate state), makes all singlet states allowed under the selection rules. This suggests that the $3pb_2$ $^1A_2$ state dissociates very rapidly, resulting in a very small probability of further absorption leading to ion formation, the method of detection used. The same study [27] however presents evidence for the existence of a state of symmetry $^1A_2$ at an energy below $86257\pm2cm^{-1}$ (115.9nm) since the recently discovered $\tilde{D}$" state of $^1A_2$ symmetry at that energy is homogeneously predissociated (ie predissociated by a state of the same symmetry).

The band at 124nm is the first to show resolvable rotational structure. This structure, arising from a longer lived state, suggests that it is Rydberg in nature and has been assigned as $\tilde{C}^1B_1$ $3pa_1$ ← $\tilde{X}^1A_1$ $1b_1$ [61]. This has been confirmed and the predissociation dynamics

studied by a later investigation employing Multi-Photon Ionisation spectroscopy [62]. Another of the 3p Rydberg states has been attributed to a diffuse feature at 121.nm [63] and has been assigned as $\tilde{D}^1A_1$ $3pb_1$ ← $\tilde{X}^1A_1$. The potential surfaces for the various states of H_2O discussed above are presented in Fig. 3.3, taken from recent theoretical calculations [59] and experimental investigations [27].

3.1.2 Dissociation A correlation diagram for the states of H_2O dissociating to give $O + H_2$, under C_{2v} symmetry, and $OH + H$, under C_s is presented in Fig. 3.4 [64]. The threshold wavelength, based on energetic considerations only, for some of the many possible fragmentation channels are shown below.

H_2O	→	$H_2(X^1\Sigma_g^+)$	+ $O(^3P)$	246nm
		$H(^2S)$	+ $OH(X^2\Pi_i)$	242nm
		$H_2(X^1\Sigma_g^+)$	+ $O(^1D)$	177nm
		$H(^2S)$	+ $OH(A^2\Sigma^+)$	137nm
		$H_2(X^1\Sigma_g^+)$	+ $O(^1S)$	134nm
		$H(^2S)$	+ $O(^3P)$	129nm
		$H(^2S)$	+ $O(^1D)$	108nm
		$H(^2S)$	+ $O(^1S)$	90nm
		$H(^2P)$	+ $OH(X^2\Pi_i)$	81nm

Below the threshold for production of $OH(A^2\Sigma^+)$, it is found that $OH(X^2\Pi_i)$ is the predominant product fragment with less than 1% dissociating into $H_2(X^1\Sigma_g^+) + O(^3P, ^1D)$ [65]. This can be rationalised in terms of a potential barrier to dissociation giving rise to these

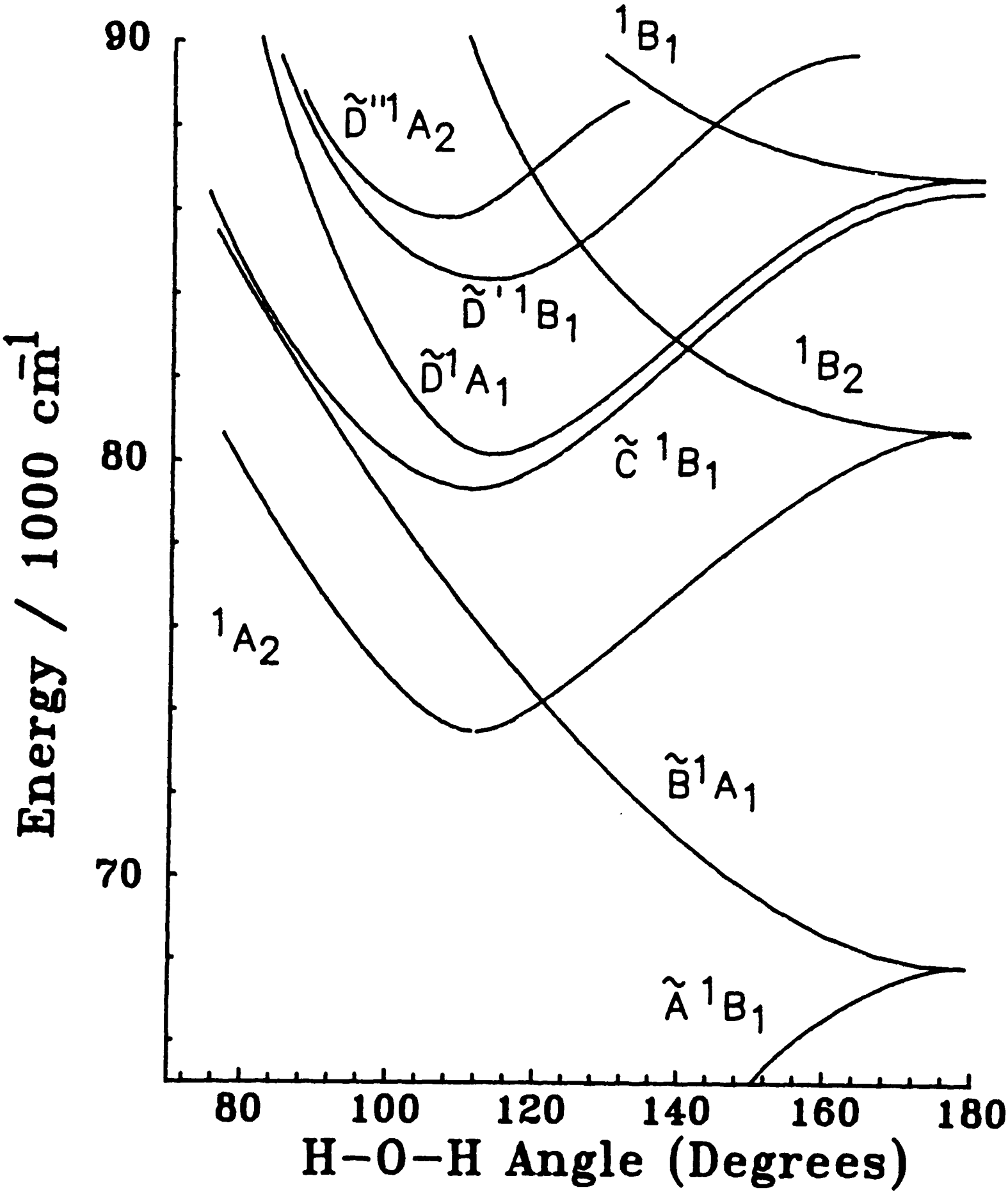

Figure 3.3. Singlet potential surfaces for H_2O as a function of the H-O-H bending angle.

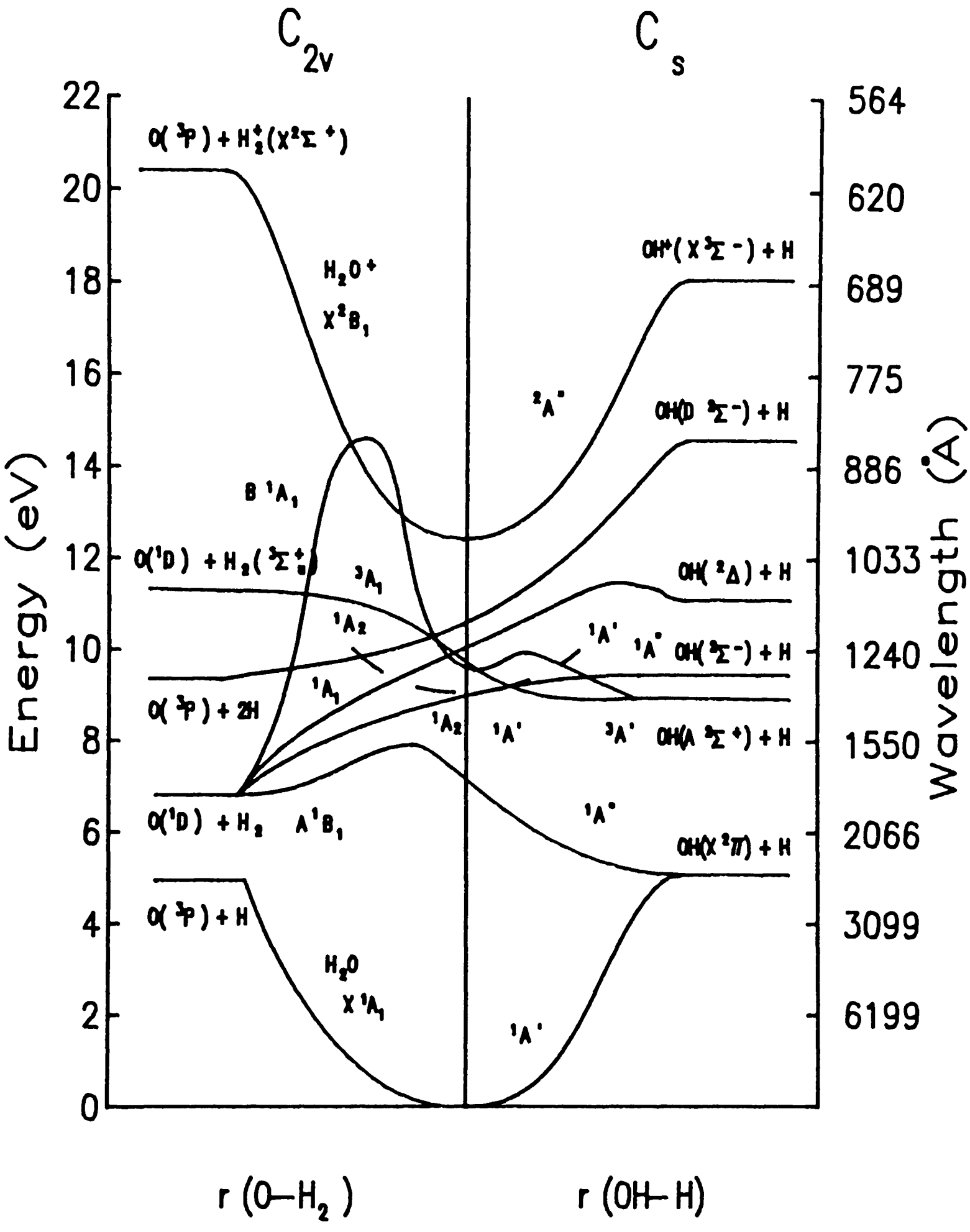

Figure 3.4. Correlation diagram for the dissociation of H_2O into $O + H_2$ and OH + H.

products in the $\tilde{A}^1B_1$ state as seen in Fig. 3.4 and predicted theoretically [56]. An early investigation of the rotational and vibrational distribution arising in $OH(X^2\Pi_i)$ following photoexcitation of H_2O into the first absorption continuum showed a rotational distribution close to that observed in a room temperature sample of $OH(X^2\Pi_i)$, ie 300K, and a cold vibrational distribution, predominantly in v"=0 [66]. The pressure/time combination employed in this experiment suggests that rotational equlibration via collisions was probably causing the observed rotational distribution and a more recent study [6] [67] of the 157nm photodissociation of H_2O shows a rotational distribution differing from a 300K Boltzmann distribution, and which is also strongly dependant on the initial state distribution of the H_2O molecules. For a 300K sample of H_2O a distribution very close to a Boltzmann with a temperature of ~900K was observed for $OH(X^2\Pi_i)$ in both v"=0 and v"=1 whilst a strong deviation from Boltzmann behaviour was apparent when the water was cooled to ~10K via a supersonic nozzle expansion. The vibrational distribution in the observed levels, v"=0,1,2, was 1:1:0.15 respectively with the majority of the available energy, 88.5% partitioned into product translation [6]. In addition the same study showed the spin states of $OH(X^2\Pi_i)$ to be statistically populated but the Λ doublets to be highly inverted. The rotational and vibrational distributions described above can be rationalised qualitatively in terms of the $\tilde{A}^1B_1$ potential surface [6].

Considerably more work has been performed on the dissociation of H_2O into $OH(A^2\Sigma^+)$ + $H(^2S)$. It was recognised in 1934 that the

rotational distribution arising in $OH(A^2\Sigma^+)$ following electrical discharge dissociation was "abnormal" [68]. OH radicals in the ground electronic state still account for the majority of the fragments; >72% in the region 133.6nm-76.0nm [69] with a reported yield of $OH(A^2\Sigma^+)$ of ~5-6% near 130nm [70]. The rotational and vibrational distribution in $OH(A^2\Sigma^+)$ was first investigated by Carrington [71] using dissociation wavelengths of 121.6nm, 123.6nm and 130.2nm. Markedly non-Boltzmann rotational distributions were found in which the highest rotational levels allowed on energetic grounds were most populated; the lowest vibrational level was most populated with the ratio v"=0:1:2 = 1:0.3:≤0.01

The high rotational excitation in $OH(A^2\Sigma^+)$, confirmed by other studies [69] [72], was explained qualitatively by the opening of the H-O-H angle in the excited state, produced by photoexcitation, imparting a torque on the OH fragment as it departed from the H atom: the "spin off" mechanism [73].

Two photon excitation of H_2O has recently become possible with the advent of high power KrF excimer sources, the fundamental wavelength of which, at 248nm, fortuitously overlaps the structured $\tilde{C}^1B_1 \leftarrow \tilde{X}^1A_1$ absorption feature at 124nm. Excitation by broadband KrF radiation [51] [74] [75] and more recently by the line narrowed output ($\Delta\nu$~0.3cm^{-1}) [76] [19] has been achieved with, in the latter studies, full rotational resolution of the emitting $OH(A^2\Sigma^+)$ fragment being possible. Rotational distributions were again found to be similar to those of the one photon case [71] although a slightly broader distribution was observed for

photolysis wavelengths in the continuum absoption region between the prominent $\tilde{C}^1B_1$ state rotational features [76] [19]. A notable feature of these experiments was the lack of OH fluorescence for the $\tilde{C}^1B_1$ state levels with $<J_a^2>=0$, and this was explained by a crossing to the $\tilde{B}^1A_1$ suface (which, in contrast to the $\tilde{C}^1B_1$ state correlates with the formation of $OH(A^2\Sigma^+)$) being allowed only for levels with $<J_a^2> > 0$.

Although energy distributions as discussed above can give partial insight into the various potential energy surfaces upon which the dissociation can take place, a more applicable technique pioneered by Simons and co-workers is that of polarised photofragment fluorescence spectroscopy (PPFS) [77].

Consider a plane polarised beam of light promoting a molecule of H_2O to an excited, predissociating, state. The transition dipole moment must lie in the plane of the molecule or perpendicular to it leading to parallel or perpendicular transitions. Those molecules whose transition dipole moment lies parallel to the electric vector of the incident radiation will be preferentially promoted to the excited state which will, upon initial excitation, consist of an aligned subset of water molecules originally in the ground electronic state. If dissociation occurs on a fast timescale, compared to rotation, then the fragments will also be preferentally aligned and hence the emission from the electronically excited fragments will be polarised. The extent of the polarisation will depend on the nature of the transition dipole moment of both the initial absorption and the emission transition, which for $OH(A^2\Sigma^+)\leftarrow(X^2\Pi_i)$ is known to be perpendicular. The predicted

polarisation that can be observed has been calculated for a variety of cases [78] [4]. Both 1 and 2 photon dissociation processes in H_2O have been investigated by PPFS. In the single photon case [79] [80] photolysis at discrete VUV wavelengths between 121.6-130.4nm using atomic resonance radiation has enabled polarisation to be measured as a function of rotational quantum number N' in the $OH(A^2\Sigma^+)$ fragment. Of particular interest to the present study are measurements at 130.4nm and 129.5nm where absorption is into the $\tilde{B}^1A_1$ continuum. Rotational populations were again found [80] to peak close to but, in contrast with earlier measurements [71], not at the maximum allowed value of N' and the alignment factors, $A_0^{(2)}$, determined from polarisation measurements decreased markedly with decreasing N' from the large negative limiting value expected for dissociation on the $^1A_1$ surface [78] and observed for transitions with high N'. The explanation is consistent with the trapped trajectories, predicted by theory - see later, which lead to a more statistical distribution of the available energy, and hence low rotational excitation in the fragments, resulting in fragments with less memory of the initial parent molecular alignment and hence less polarisation in their emission.

Measurements of unresolved fluorescence polarisation carried out as a function of dissociating wavelength in this region will clearly be affected by the rotational state distributions in the $OH(A^2\Sigma^+)$ fragment. In the region 126-137nm the total polarisation is found to be as expected for a transition to the $\tilde{B}^1A_1$ state [81] but variations are observed, and in particular a marked discontinuity at 134.5nm has been

attributed to the existence of another electronic transition, the most likely candidate being the elusive $^1A_2$ state accessed, as explained previously, in its (0,0,1) level, of $^1B_1$ symmetry. The one photon transitions $\tilde{B}^1A_1 \leftarrow \tilde{X}^1A_1$ and $^1B_1 \leftarrow \tilde{X}^1A_1$ will result in OH fragments of measurably different polarisation [80] [81]. However a polarisation change of the magnitude of that observed experimentally near 134.5nm could be produced by a change in rotational state distribution and thus without such information any conclusions on the involvement of the $^1A_2$ state must remain tentative.

PPFS following two photon absorption at wavelengths near 248nm has also been caried out [76]. Excitation of rotationally resolved H_2O features corresponding to initial absorption into the $\tilde{C}^1B_1$ state leads to low polarisation and this has been attributed to slow predissociation rates from the $\tilde{C}^1B_1$ to the $\tilde{B}^1A_1$ state surface upon which the fragmentation occurs. In the underlying continuum, polarisation is strong and its value has been used to suggest the identity of the absorbing state. The $\tilde{B}^1A_1$ state is clearly a candidate, and so too is the $^1A_2$ state, transitions to both states being allowed for two photon absorption. Mention has already been made of theoretical [59] and experimental [81] evidence reported for the $^1A_2$ state: more pertinently, the rotational energy distribution in $OH(A^2\Sigma^+)$ from broadband 248nm two photon dissociation of H_2O [51] is <u>cooler</u> than that produced by single photon dissociation in this region [71] and this evidence has been used to suggest different decomposition mechanisms in the two cases; absorption to the $^1A_2$ state being involved in the two photon absorption.

In the narrow band 248nm excitation studies, however, Simons et al favour the the $\tilde{B}^1A_1$ state as giving rise to the underlying continuum, as measured alignment factors, $A_0^{(2)}$, are always higher than those predicted for transitions to the $^1A_2$ state [76].

3.1.3 Theortical Studies Potential surfaces for the ground, $\tilde{X}^1A_1$, [82] and excited, $\tilde{B}^1A_1$, [83] states of H_2O have been determined and these will be described first.

The ground state potential of water, $\tilde{X}^1A_1$, has been determined by Sorbie and Murrell [82] by a method which is consistent with both the stable equilibrium configuration, where Taylor expansions in the internal coordinates are valid, and the dissociation limit of fragments, where such an expansion is invalid. It is consistent with the known spectroscopic features of H_2O in the ground electronic state. An ab-initio study of the $\tilde{B}^1A_1$ state of H_2O has been made by Flouquet and Horsley using the LCAO-MO SCF method incorporating configuration interactions where required. They show that the surface correctly predicts, in a qualitative manner, the rotational distribution on the basis that the H-O-H angle increases rapidly as the OH-H distance increases; a rationalisation of the "spin off" mechanism described earlier.

Segev and Shapiro [84] [85] have combined the potential surfaces discussed above in a full three dimensional quantum mechanical scattering calculation for the photodissociation of H_2O at wavelengths around 130nm. Their calculated absorption spectrum is shown in Fig.

3.5. Also indicated are the positions of the diffuse bands in the observed water spectrum. The agreement between theory and experiment is very good. In addition the rotational distribution arising in the $OH(A^2\Sigma^+)$ fragment at a number of different wavelengths is calculated and illustrated in Fig. 3.5. It is apparent that the rotational distribution is highly dependant on the excitation wavelength. In particular, absorption into the resonances gives rise to a "cool" rotational distribution whereas absorption off-resonance gives rise to an inverted or "abnormal" rotational distribution. The different rotational distributions arise from differing trajectories on the $\tilde{B}^1A_1$ excited state potential surface and these are illustrated in Fig. 3.6. Trajectory A corresponds to an increase in bond angle combined with rapid predissociation, ie the "spin off" mechanism, and occurs off-resonance on the calculated absorption spectrum. This can be described as Franck-Condon type dissociation, as discussed in Chapter 1, where dissociation is sufficiently fast that the excited state plays very little part in the dynamics. In trajectory B the molecule executes a number of bending vibrations upon the $\tilde{B}^1A_1$ potential surface. This increases the cross-section due to the increased excited state lifetime and allows some equilibration of the geometry prior to dissociation resulting in a less excited rotational distribution. This is an example in which the excited state potential surface plays a crucial part in the determination of the final state distribution. It is possible that the dissociation at wavelengths between the on and off-resonance cases will lead to a mixture of both types of distribution. Indication of such "bimodal" rotational distributions have been observed in early work [86]

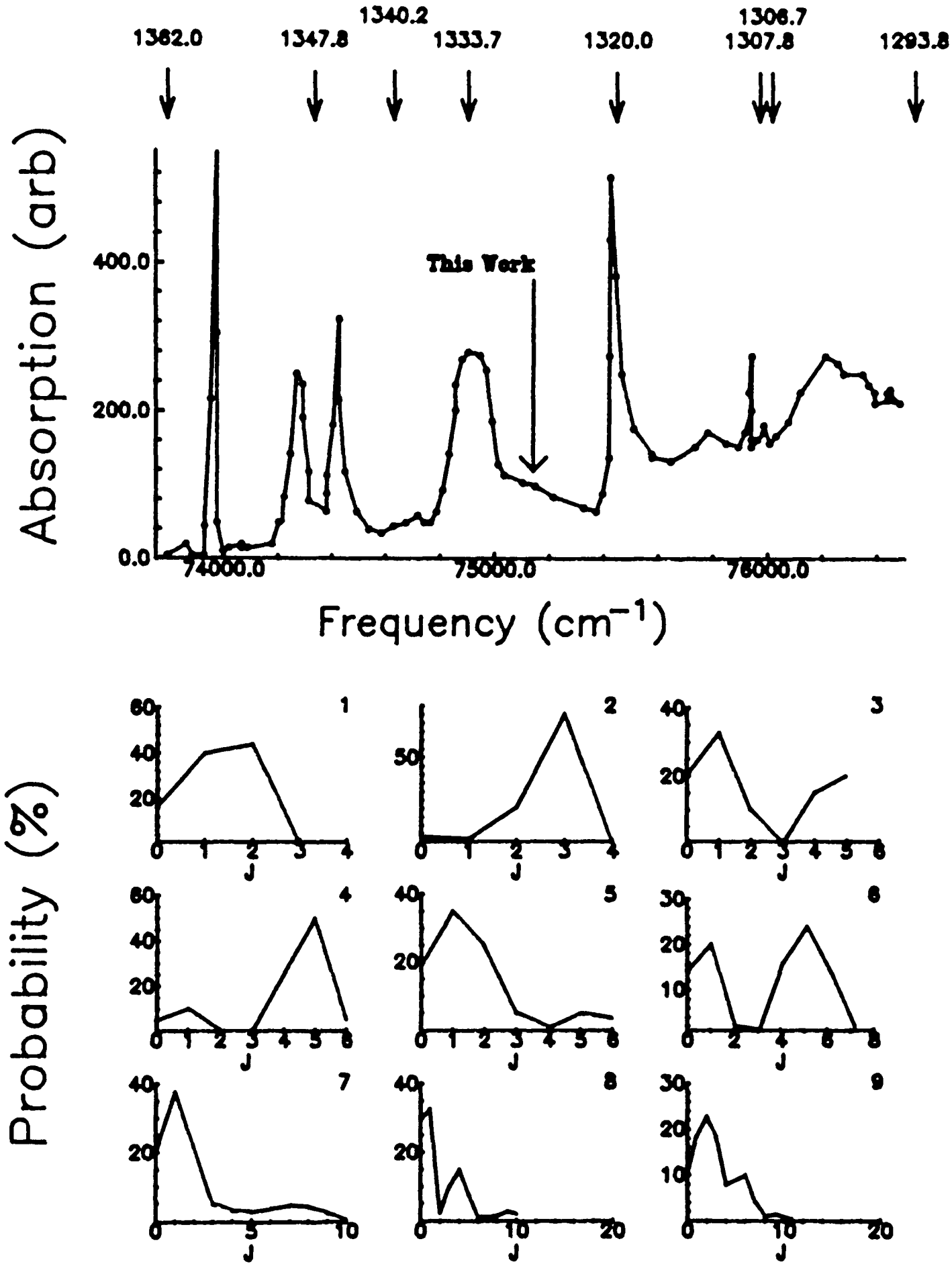

Figure 3.5. Top: Calculated absorption spectrum of H_2O at 0K. Bottom: Rotational distributions expected at dissociation wavelengths shown in the absorption spectrum.

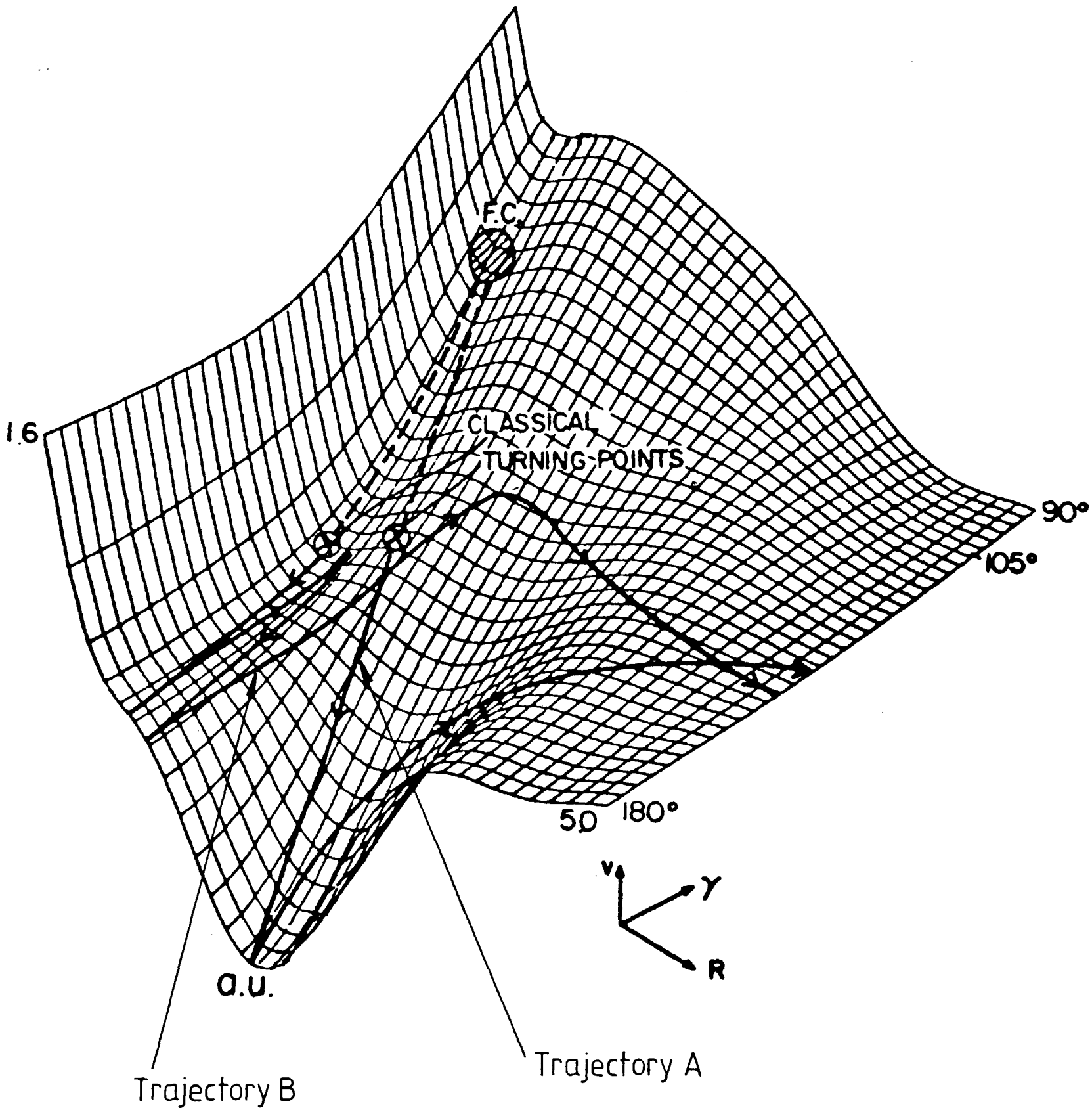

Figure 3.6. $\tilde{B}^1A_1$ state potential surface showing both direct and trapped trajectories leading to rotationally excited and cooler OH fragments respectively.

[69] on the dissociation of H_2O in agreement with the prediction of Segev and Shapiro.

These calculations explain the polarisation measurements of Simons et al following single photon excitation [80] since low rotational excitation in the $OH(A^2\Sigma^+)$ product is expected from transitions which give rise to long lived trajectories, thereby retaining less memory of the excitation anisotropy.

Recently, Dixon [87] has calculated the rates of radiationless transfer from the $\tilde{B}^1A_1$, correlating with $OH(A^2\Sigma^+)$, to the $\tilde{A}^1B_1$ state, which correlates with $OH(X^2\Pi_i)$. His calculations show that the "trapped" trajectories on the $\tilde{B}^1A_1$ state, which give rise to $OH(A^2\Sigma^+)$ with low rotational excitation according to Segev and Shapiro, have a high probability of crossing to the $\tilde{A}^1B_1$ state giving rise to $OH(X^2\Pi_i)$. Rapid dissociative trajectories, which give rise to high rotational excitation in $OH(A^2\Sigma^+)$, are not affected to the same extent. These results explain both the high rotational excitation observed in H_2O photolysis compared to the predictions of Segev and Shapiro and also the generally low quantum yield for production of $OH(A^2\Sigma^+)$ following $\tilde{B}^1A_1$ state excitation of H_2O.

The experiments described in this chapter examine the two and three photon dissociation of H_2O at excitation wavelengths of 266nm and 355nm respectively. The first excitation falls in the $\tilde{B}^1A_1$ single photon absorption region but also near the predicted, but undiscovered, $^1A_2$ state. By comparison with the rotational distributions reported for

single photon absorption into the $\tilde{B}^1A_1$ state and also the underlying continuum near 124nm it is hoped that the ~130nm photodissociation of H_2O can be clarified.

3.2 EXPERIMENTAL RESULTS : 266nm

3.2.1 Identification of Emitting Species Emission in the region 306-314nm was detected when a 400mTorr sample of freeze-pump-thaw degassed, demineralised water was irradiated with 266nm laser light focused with a 20cm focal length spectrosil lens. Figs. 3.7 and 3.8 shows the wavelength resolved fluorescence spectrum in the region 206-215nm taken with the monochromator and signal averaging system described in Chapter 2, together with a more detailed spectrum of the long wavelength components in the region 310-314nm. The form of the spectrum immediately identifies the emitting species as $OH(A^2\Sigma^+ \ v'=0)$ with rotational levels populated for values of N' between 0 and ~9. The identification of the $OH(A^2\Sigma^+)\leftarrow OH(X^2\Pi_i)$ bands is taken from the data of [88] [89] and the spectroscopy is discussed in Appendix 2.

Further confirmation of the identity of the emitting species was obtained by measurement of the decay rate of the fluorescence as a function of pressure and extracting the radiative lifetime and quenching rate constant from these data. The decay rate of the total, unresolved, fluorescence was determined using the transient digitiser; the results being plotted directly onto semi-logarithmic graph paper. Linear regression of the data gave the decay rate at a range of pressures. A plot of the decay rate as a function of pressure is shown in Fig. 3.9.

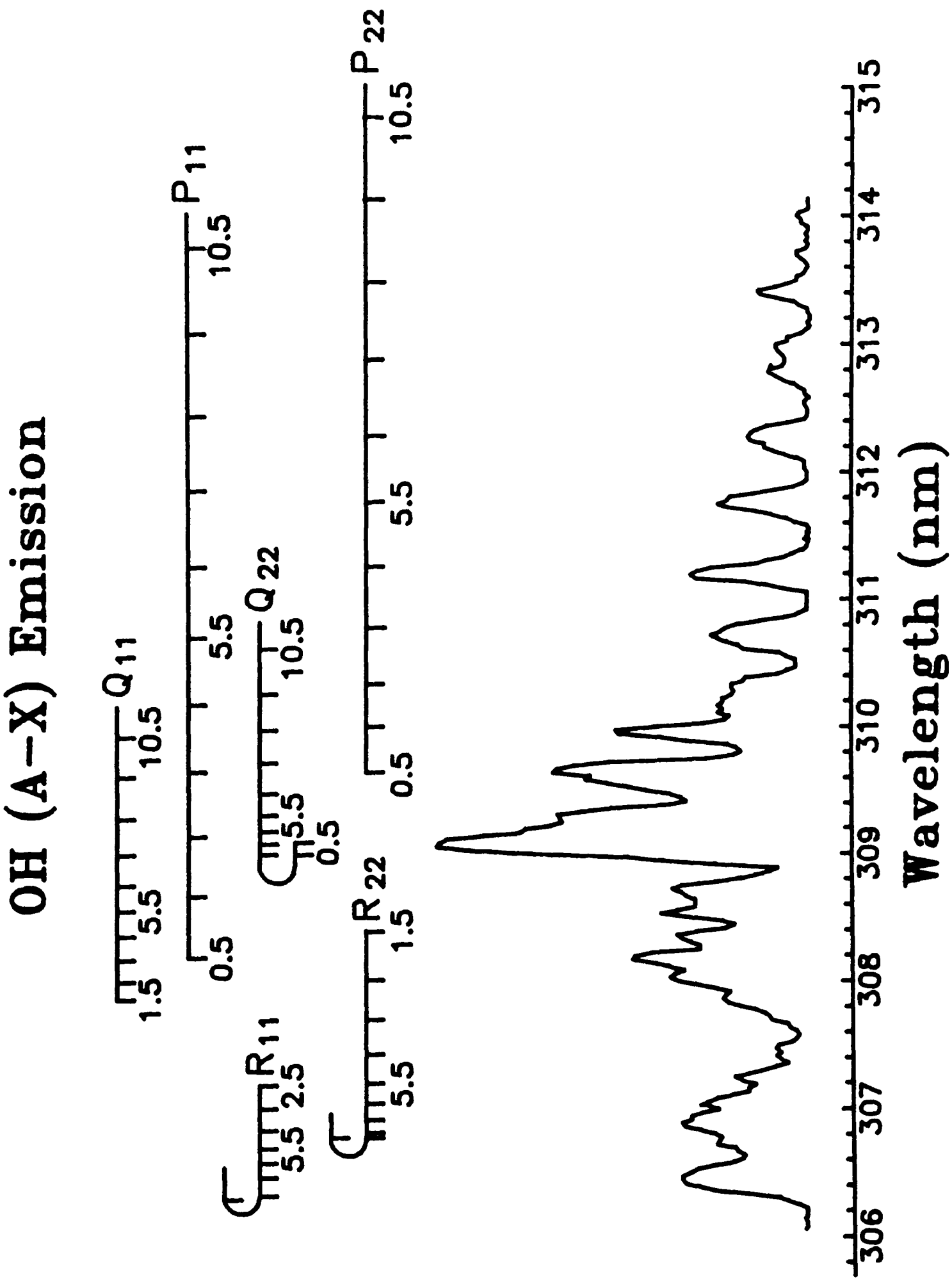

Figure 3.7. Emission spectrum arising from $OH(A^2\Sigma^+)$ following two photon dissociation of H_2O at 266nm.

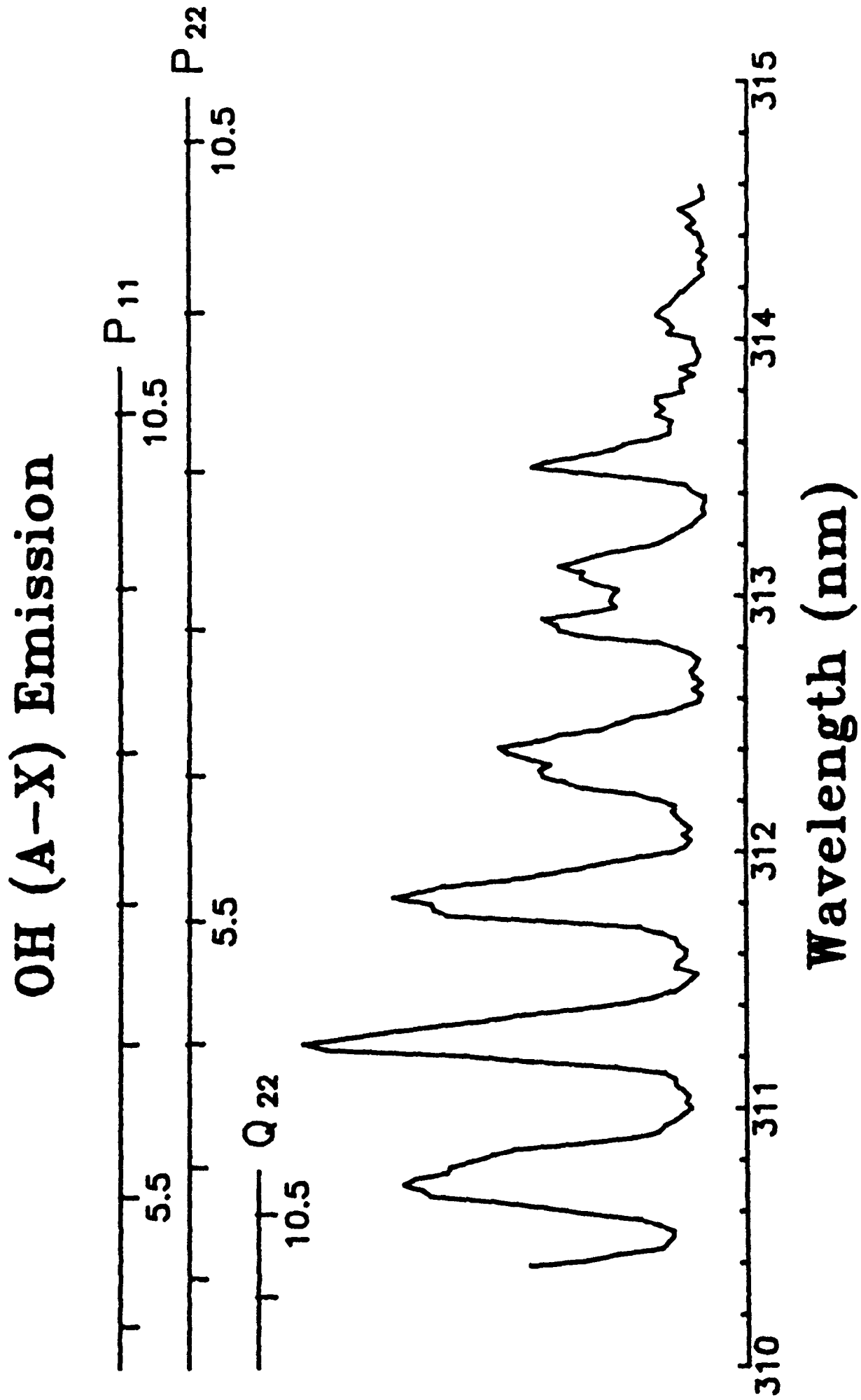

Figure 3.8 Detailed emission spectrum of OH($A^2\Sigma^+$) in the region 310-315nm.

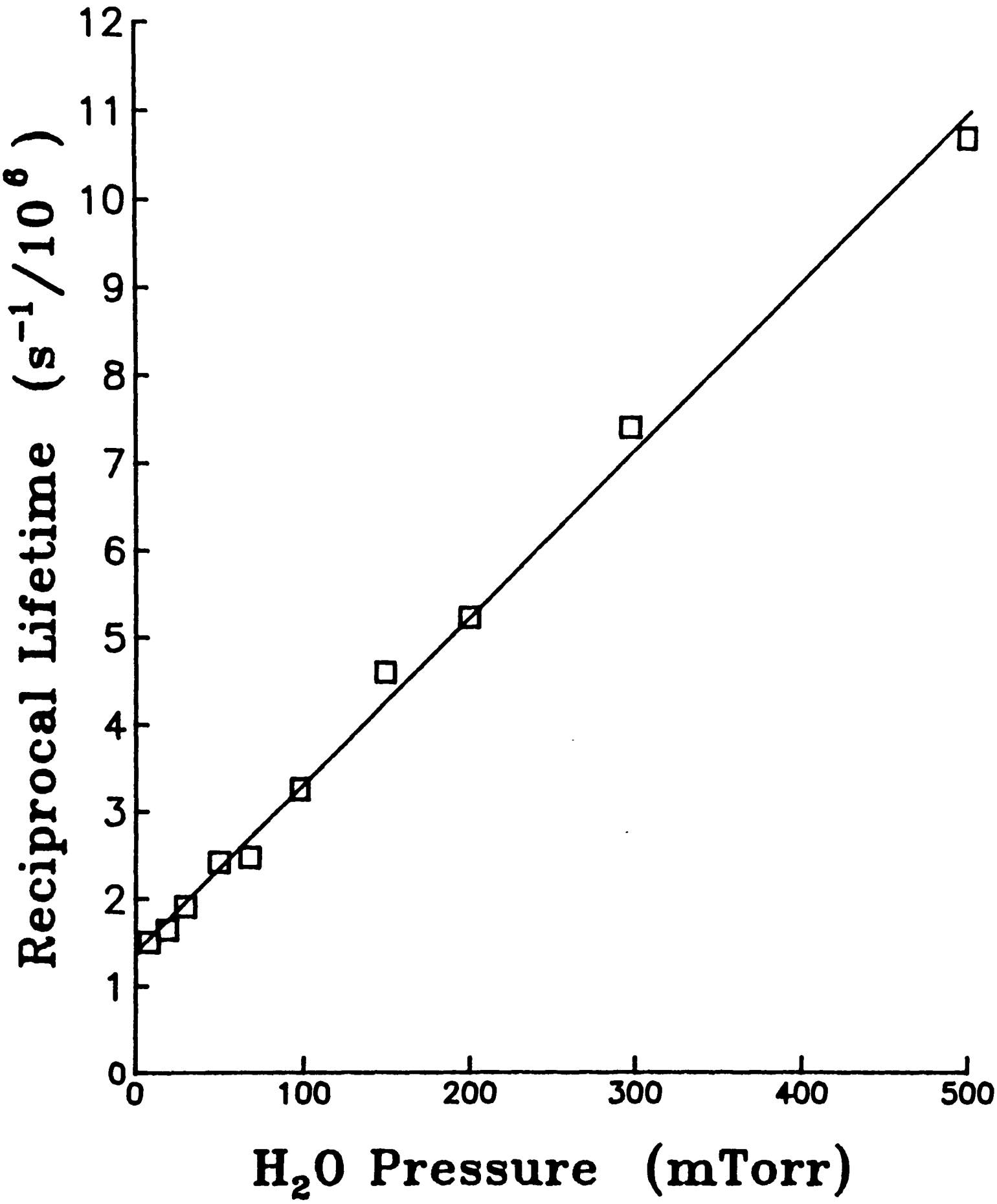

Figure 3.9 Radiative lifetime of emission as a function of total pressure.

Further linear regression gives the intercept and gradient from which the radiative lifetime and the quenching rate constant for $OH(A^2\Sigma^+)$ by H_2O can be obtained. The results are presented in Table 3.1 and compared to literature values.

Source	τ_0/ns	$K_q/10^{-10}cm^3mol^{-1}s^-$
This work	757±92	5.96±0.25
JCP 76 (1982) 1824	721±9	5.67±0.10
Phys Scripta 17 (1978) 507	760± 60	
JCP 62 (1975) 2584	690±9	

Table 3.1

The error in the present determination reflects the small signal levels in the experiments and the results should be regarded as a confirmation of the identity of the emitting fragment rather than an accurate determination of these values. In addition the radiative lifetime of $OH(A^2\Sigma^+)$ is dependant on N', the total angular momentum [90], and will thus change with the rotational distribution within that state.

Measurements of the total fluorescence signal as a function of H_2O pressure were also carried out using the gated detection system described in Chapter 2. As seen in Fig. 3.10, where the results are presented, the signal increased initially linearly with pressure in the region where radiative decay dominates, eventually flattening off to an approximately constant value. Such behaviour is expected for a process

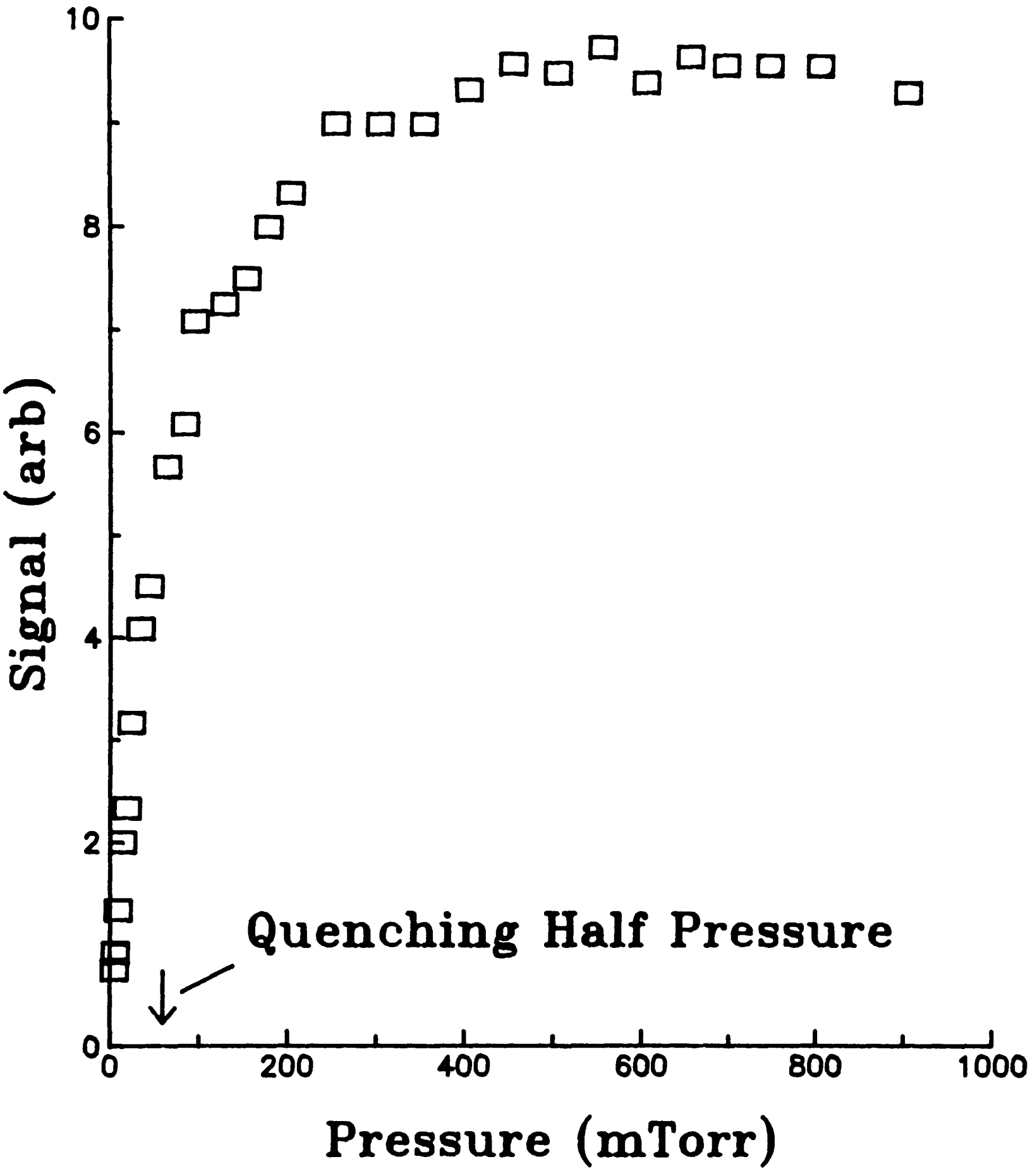

Figure 3.10. Total unresolved emission as a function of total pressure. The quenching half pressure is indicated.

in which both the production rate and collisional quenching rate of the excited species, $OH(A^2\Sigma^+)$, are proportional to the pressure of H_2O. From the data of Table 2.1 the quenching half pressure (where contributions from radiative decay and quenching by H_2O are equal, and the signal is half its maximum value) is expected at a pressure of $1/k_q \equiv \tau_0$=68mTorr, and as Fig. 3.10 shows this is consistent with the observed behaviour.

3.2.2 Intensity Dependance For a true coherent multi-photon transition, involving no intermediate state, of order n (n photons absorbed) then for a collimnated laser beam the production of the excited state will depend on the laser intensity to the power n:

$$S=kI^n \qquad (3.1)$$

The gradient of a log-log plot of the signal due to the excited state vs. the laser intensity will give the order of the multi-photon process. The effect of the focussing geometry commonly employed in multi-photon absorption experiments and the possibility of geometrical saturation of the sample complicate this analysis. This situation has been thoroughly treated in the literature [91] [92] [93] and it can be shown that any multi-photon absorption process of order $n\geq 2$ reduces to a dependance of $I^{3/2}$ in the limit of geometric saturation.

The intensity of the total fluorescence from $OH(A^2\Sigma^+)$ as a function of the laser intensity on a logarithmic scale is presented in Fig. 3.11. The gradient, obtained by linear regression, is 2.05 ± 0.05 which agrees very closely with a two photon absorption. There is no evidence in the

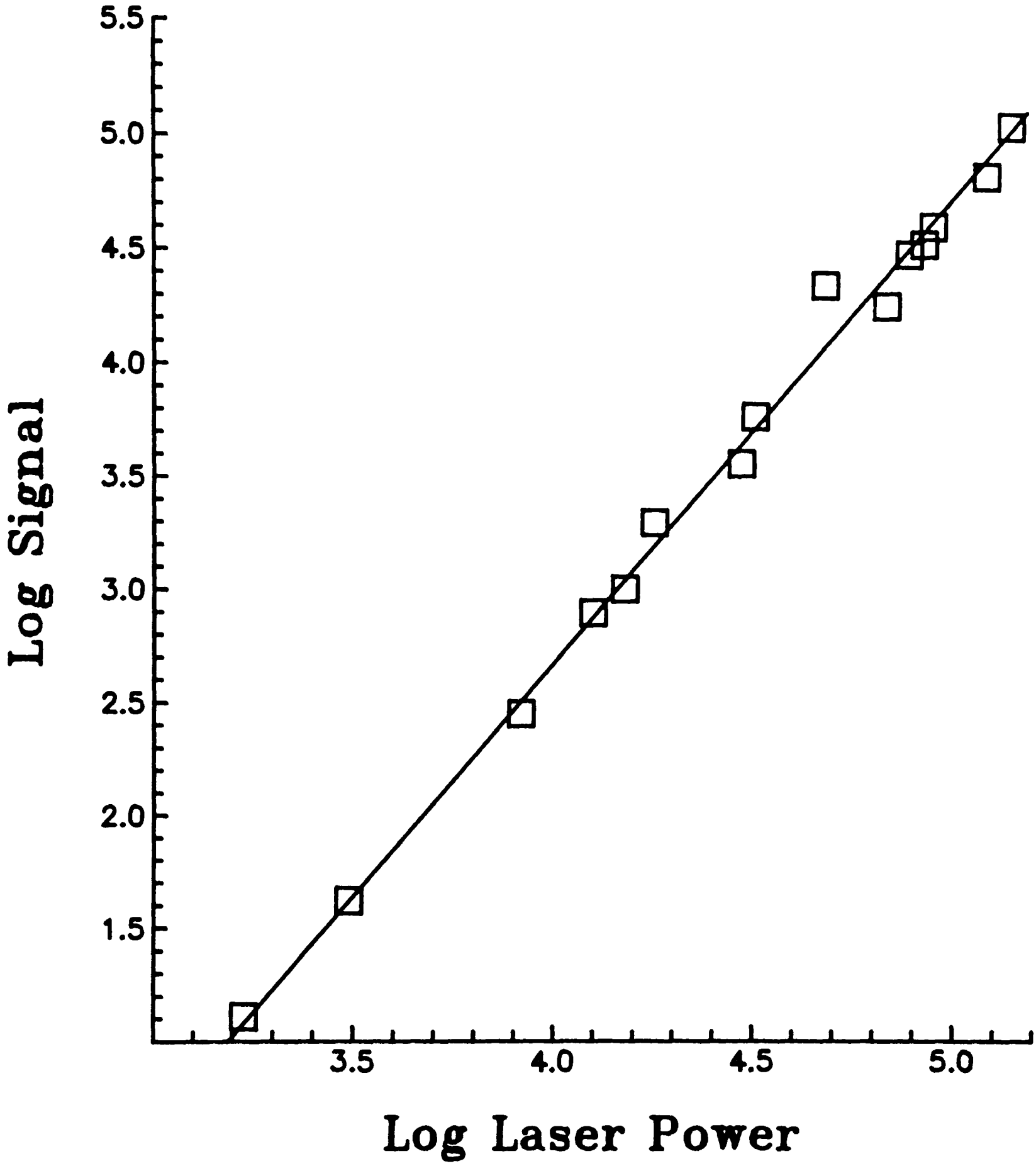

Figure 3.11. Unresolved emission as a function of laser power, both axes on a logarithmic scale.

data for the onset of saturation.

There is a possibility of further photon absorption from the initially populated two photon state leading, probably, to the production of ions, H_2O^+. Indeed this is the basis of Multi-Photon Ionisation spectroscopy which has been used recently to investigate the VUV states of H_2O [27].

The kinetics of the competing two photon dissociation and three photon ionisation are illustrated in Fig. 3.12. The rate of change of population in the initially produced state can be written as:

$$dn_1/dt = k_1 n_0 I^2 - k_p n_1 - k_2 n_1 I^m \qquad (3.2)$$

where m is the order of the (possibly) multi-photon process which produces the ions. Energetically $m \geq 1$ for the case in question. Applying the steady state approximation to n_1 ; $dn_1/dt=0$ and assuming that the steps are not saturated we obtain:

$$n_1 = k_1 n_0 I^2 / (k_p + k_2 I^m) \qquad (3.3)$$

The fluorescence and ion signals are given by

$$S_f = K k_p n_1 \quad : \quad S_i = K' k_2 I^m n_1 \qquad (3.4)$$

where K and K' are constants. This gives:

$$S_f = K k_p k_1 n_0 I^2 / (k_p + k_2 I^m) \qquad (3.5)$$

$$S_i = K' k_2 I^m k_1 n_0 I^2 / (k_p + k_2 I^m) \qquad (3.6)$$

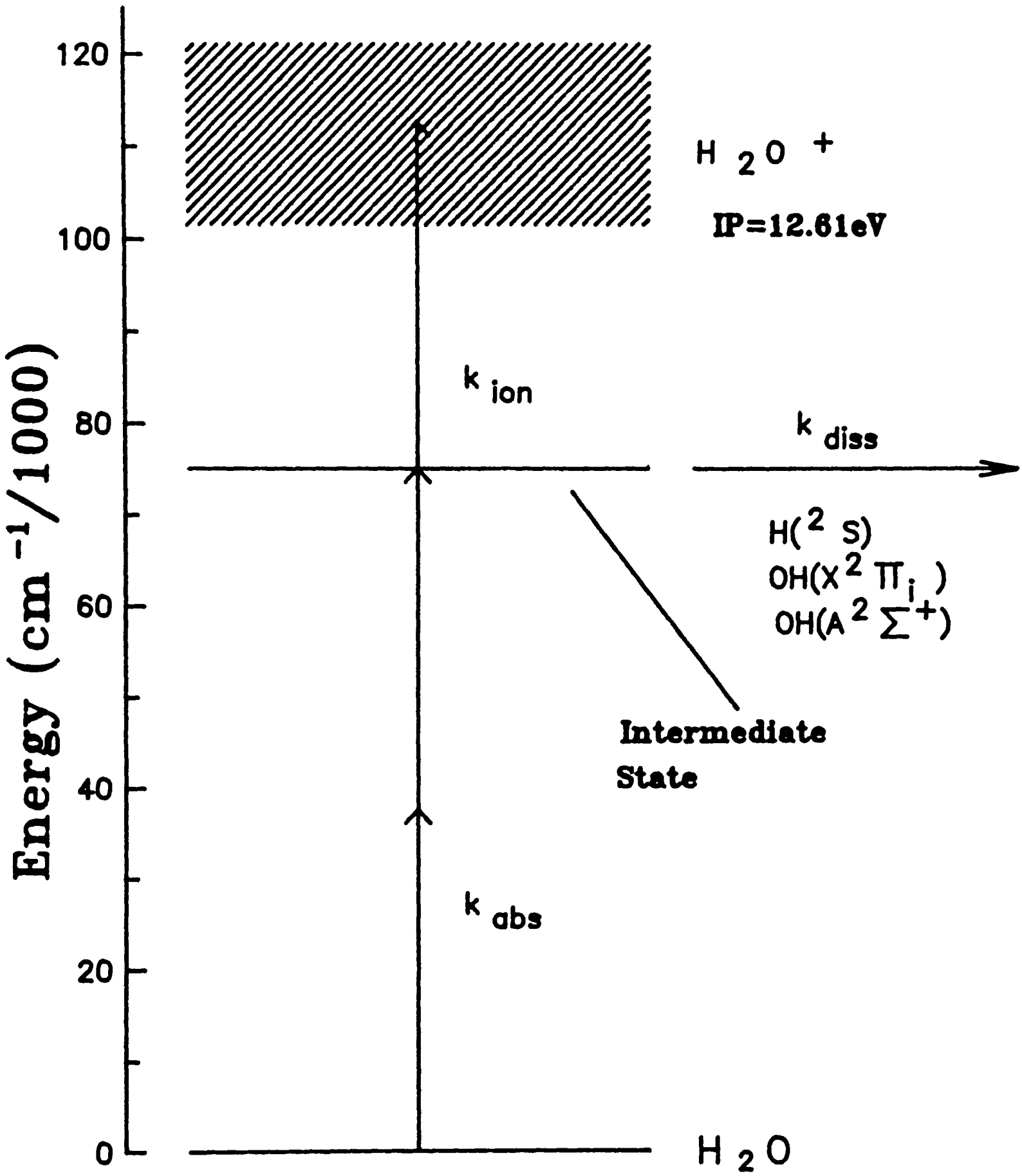

Figure 3.12. Kinetic scheme for two photon dissociation and multi photon ionisation of H_2O at 266nm.

If the predissociation rate, k_p, dominates the denominator then the expression for the fluorescence signal reduces to:

$$S = Kk_1 n_0 I^2 \qquad (3.7)$$

which is the observed behaviour in Fig. 3.11. Should this condition not hold then a decrease in the power dependance of the fluorescence signal should be observed at high intensities. This behaviour also predicts that the predissociation rate dominates the producation of ions and that an ion signal should show a I^{2+m} dependance.

A simple ion detection apparatus consisting of two copper plates spaced by ~3cm and biased at 70-140V followed by a current amplifier with gain of 10^5-$10^7 VA^{-1}$ confirmed the ion production channel. The dependance of the ion signal upon the laser intensity, at a water pressure of 200mTorr is shown in Fig. 3.13, again plotted on a logarithmic scale. The gradient is 1.87 ± 0.05 which is at variance with the notion of a ≥3 photon ionisation step. This phenomenon however is common in Multi-Photon Ionisation spectroscopy and arises from a saturation in the ionisation process such that effectively all molecules reaching the intermediate level (in this case after absorption of two photons) are ionised, the cross section for this step being much larger than that for the initial MPA process. This information gives rise to an interesting question. In the interaction of 266nm radiation with H_2O $OH(A^2\Sigma^+)$ is produced by a 2 photon absorption which does not saturate and ions are produced via a 2 photon intermediate state in a process which does exhibit saturation. One possible explanation is that the two

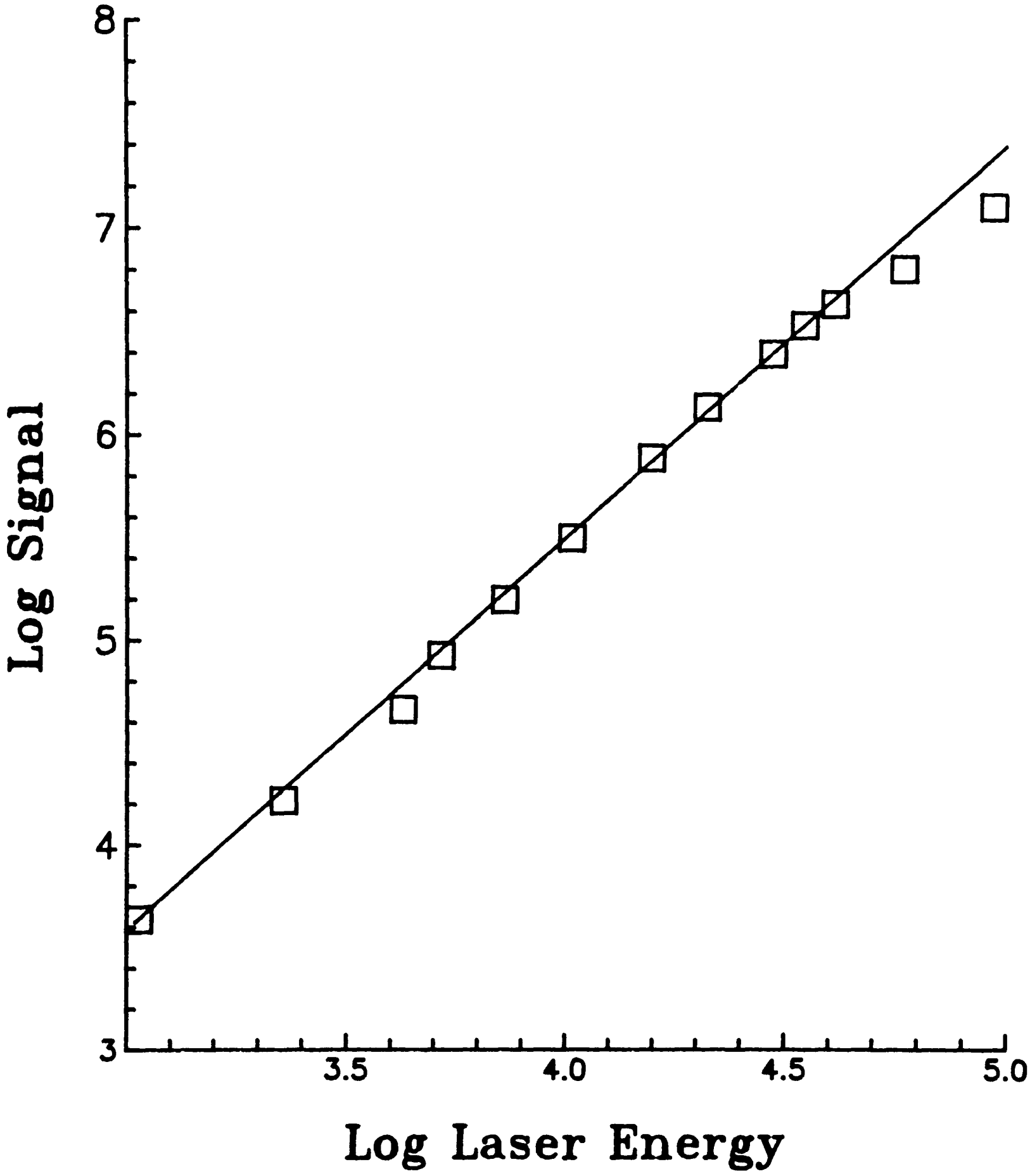

Figure 3.13. Dependance of ion signal upon laser energy. Both axes represented as logarithmic scales.

channels proceed via differant 2 photon intermediate states and the nature of these states will be discussed later in this chapter.

Until now it has been assumed that the ionic species produced are H_2O^+ but this is not neccessarily the case. Several excitation schemes can be envisaged and these are summarised below.

$$H_2O \xrightarrow{2h\nu} H_2O^* \xrightarrow{h\nu} H_2O^+ \qquad (3.8)$$

$$H_2O \xrightarrow{2h\nu} H_2O^* \rightarrow H + OH^* \xrightarrow{2h\nu} OH^+ \qquad (3.9)$$

$$H_2O \xrightarrow{2h\nu} H_2O^* \xrightarrow{2h\nu} H_2O^{+*} \rightarrow OH^+ \qquad (3.10)$$

In the third process the ionisation and dissociation steps may be simultaneous or sequential, both mechanisms having been reported recently for diatomic species [94]. In addition the ionic species may be in their ground electronic state or may be electronically excited. In general terms the first process is most likely to be the dominant one as fewer photons are involved.

An attempt was made to identify, by spectroscopic means, the ionic species present both in emmsion, to detect excited states, and via Laser Induced Fluorescence, to detect ground electronic states. H_2O^+ has been observed in comet tail emission and many of the vibrational bands of the $\tilde{A}^2A_1 \leftarrow \tilde{X}^2B_1$ have been documented following laboratory studies [95]. No emission was observed which could be attributed to either $OH^+(A^3\Pi_i)$ or $H_2O^+(A^2A_1)$. An attempt to pump the $(0,10,0) \leftarrow (0,0,0)$ band of the

$H_2O^+(\tilde{A}^2A_1 \leftarrow \tilde{X}\ ^2B_1)$ system at 560nm, a favourable region for the Nd:YAG pumped dye laser, and observe red shifted fluorescence on the (0,10,0)→(0,2,0) vibrational band proved fruitless as did other less favourable bands. A similar lack of success was encountered when the $OH^+(A^3\Pi_i \leftarrow X^3\Sigma^-)$ band was investigated by LIF at 362nm [96]. In conclusion it can be said that the nature of the ions produced in the photodissociation proccess cannot be identified by spectroscopic means but H_2O^+ is the most likely candidate. Recent investigations of the high lying excited states of H_2O by 3+1 Multi-Photon Ionisation Spectroscopy have not shown any features inconsistent with the production of H_2O^+ [27]. It should be noted that Equation 3.9 could account for the observed intensity dependance if the OH intermediate were the vibrationally excited levels of the $OH(X^2\Pi_i)$ state (which, it will be seen later, are formed in the two photon dissociation process), and that if the two photons required energetically for the ionisation of these levels were absorbed in saturated steps. Absorption of the first 266nm photon from v'=0 in $OH(A^2\Sigma^+)$ could access the $B^2\Sigma^+$ state [96] and the high intensity radiation present may be sufficient to saturate both this and the subsequent single photon ionisation step to give OH^+. Without mass discrimination of the fragment ions such conclusions are speculative.

The nature of the state(s) giving rise to ions and also to $OH(A^2\Sigma^+)$ could also be investigated by monitoring the ion production (or emission intensity) as a function of excitation wavelength near 266nm. Indeed new excited states of H_2O have recently been observed via 3+1 Multi-

Photon Ionisation in this way [27] and the $OH(A^2\Sigma^+)$ intensity and rotational distribution following two photon excitation at tunable wavelengths around 248nm has been reported [76]. An attempt was made to perform this experiment by pumping the dye laser with the third harmonic of the Nd:YAG laser at 355nm and employing Coumarin 152 dye to obtain laser action at 532nm which could be frequency doubled to give a tunable source at 266nm. Unfortunately this process proved unsuccessful, not enough energy being obtained from the laser system to produce any signal.

3.2.3 Resolved Emission Studies - 266nm This section describes measurements of the internal state distribution of $OH(A^2\Sigma^+)$ produced in the 266nm multi-photon dissociation of H_2O. Wavelength resolved emission, Figs. 3.7 and 3.8, was recorded using the monochromator and signal averaging system described in Chapter 2, with the laser power monitored to ensure there was no appreciable drift in experimental conditions. As the emission from the photodissociation products is, in general, expected to be polarised (see earlier) and the polarisation will be dependant upon $|\Delta J|$ in the transition and may depend on the value of J [3], it is clearly desirable to introduce no polarisation dependance in the detection system when total populations are to be measured. In the present experiments the polarisation dependance of the grating in the monochromator was avoided by ensuring that the collected light was unpolarised: this was achieved by observing the emission in a direction parallel to the electric vector, E, of the dissociating radiation, ie such that E pointed directly into (or out of) the

monochromator slit. The unpolarised nature of such emission can be readily verified for a two photon absorption and dissociation from [97].

It is of crucial importance in studies of photodissociation, in which a rotational distribution is used to imply dynamic effects, that the rotational distribution is the nascent one from the dissociation and not resulting from collisional relaxation. To ensure this the resolved emission spectrum was recorded at a range of pressures up to 1 Torr. The appearance of the spectrum did not change over this range, in agreement with previous studies on the photodissociation of H_2O giving rise to $OH(A^2\Sigma^+)$ at pressures similar to these [98] [76]. This has been attributed to the very rapid electronic quenching of $OH(A^2\Sigma^+)$ by H_2O [99] preserving the nascent rotational distribution: any molecule which undergoes a collision will be electronically quenched rather than rotationally relaxed. Independent determinations of the rate of rotational relaxation of $OH(A^2\Sigma^+)$ by H_2O confirm this view [100] [101].

The small signal levels meant that it was not possible to resolve isolated lines of the emission spectrum: the resolution of ~0.9nm resulting from a 120μm slit setting of the monochromator was the best possible whilst maintaining an acceptable signal to noise ratio. The rotational population distribution cannot be deduced directly from the spectrum due to the many blended lines. A computer method was used to obtain the rotational distribution.

In the $OH(A^2\Sigma^+)$ state each rotational level, of quantum number N', is split by spin-rotation doubling into two states, designated F_1

($J'=N'+1/2$) and F_2 ($J'=N'-1/2$). Each spin-rotation doubled level produces 6 lines in emission giving 12 lines for each N′ and, as can be seen from the assignment of Fig. 3.7, many of these form band heads or overlap.

The observed spectrum can be thought of as a convolution of the separate spectra arising from the individual rotational levels in the $OH(A^2\Sigma^+)$ weighted by the population distribution of the various levels giving rise to emission. The signal at a particular wavelength can be written as:

$$S(\lambda) = \sum_i C_i P_i \qquad (3.11)$$

Where C_i is the normalised contribution of the spectrum due to the state i at that wavelength and P_i is the weighting of the population of that state. The summation extends over all states contributing to the spectrum. The expression above can be expanded into a matrix representation of a set of simultaneous equations, in terms of the digitized experimental spectrum, the simulated spectra arising from each contributing level, and the unknown weights. Since the experimental spectrum was digitized into approximately 400 points the set of equations is over-determined: there are more equations than unknown weights. There is no unique solution to this problem but the best approximation can be obtained using the matrix equation [102]:

$$\tilde{x}=(F^TF)^{-1}F^T\,\tilde{g};\quad \text{for } F\tilde{x}=\tilde{g} \qquad (3.12)$$

Essentially this reduces the over-determined system to the best estimate

of the exactly determined system and then solves the matrix equation, in this case by the method of Gaussian reduction [102].

The experimental spectrum was digitized manually from the chart recorder output. The basis set, the spectra arising from individual spin rotation levels, was calcualted using the spectral simulation program described in Appendix 3, taking spectroscopic constants and Einstein emission coefficients from [88] [89]. The number of contributing rotational levels can be calculated on the basis of conservation of energy:

$$E_{avail} = 2h\nu - D_0^0(H\text{-}OH) - \nu_{00}[OH(A\text{-}X)] \qquad (3.13)$$

The fudamental output of the Nd:YAG laser has an energy of $9397.6cm^{-1}$ [103] which gives the two photon excitation energy as $75180.0cm^{-1}$. The dissociation energy, at zero Kelvin (D_0^0) of H_2O giving rise to H + $OH(X^2\Pi_i)$ is $41214.6cm^{-1}$ [104] and the origin of the A-X transition for OH is $32462.3cm^{-1}$ [96]. The combination of these values gives $1503.1cm^{-1}$ for the energy available to be partitioned amongst the rotational levels of the $OH(A^2\Sigma^+)$ state. This suggests that levels with $N' \leq 9$ (F_1 J=9.5, F_2 J=8.5) can be populated on energetic grounds. Examination of the experimental spectrum shows that levels slightly above this energetic limit give rise to emission lines. This can be attributed to some initial thermal energy in the water parent molecules being carried over into the $OH(A^2\Sigma^+)$ fragment, as noted in other studies [76]. The limits of the basis set were adjusted accordingly at a level somewhat above the energetic limit. In principle the spectrum

should be able to be fitted using the minimisation procedure with an arbitrarily large basis set but storage and run-time considerations precluded the use of such a data-base.

The results of the data analyses are shown in Fig. 3.14, where the rotational population distributions for F_1 and F_2 levels are plotted as a function of the rotational angular momentum quantum number, N', and where the experimental spectrum is compared with one simulated using these populations. Table 3.2 lists the populations together with errors derived from the minimisation routine.

N	F1 Population	% Error	F2 Population	% Error
0	0.328	14.9		
1	0.529	10.7	0.346	16.7
2	0.998	6.9	0.348	31.2
3	0.939	7.6	0.364	10.4
4	0.716	4.2	0.779	6.1
5	0.755	5.7	0.895	4.9
6	0.643	5.9	1.000	4.0
7	0.576	7.3	0.850	4.2
8	0.160	10.5	0.723	4.3
9	0.400	5.8	0.640	4.9
10	0.169	12.6	0.050	14.4

Table 3.2

Although the fit is generally satisfactory, the R_{11} bandhead, at low wavelengths, is underestimated: it was found to be impossible to fit

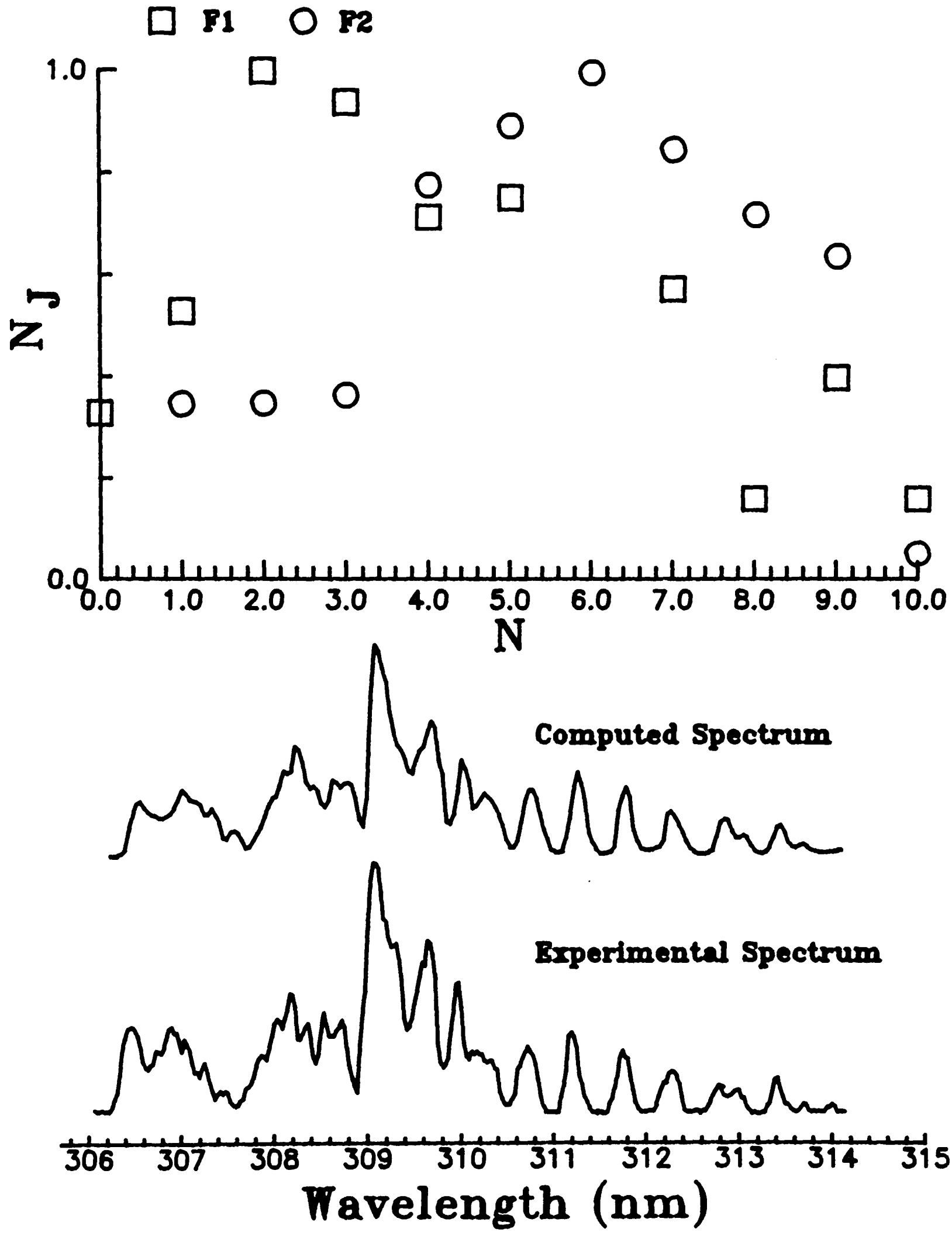

Figure 3.14. Top: Population as a function of quantum number N, J=N±½. Bottom: Comparison of experimental spectrum with spectrum derived from populations obtained by fitting procedure.

this region without seriously degrading the quality of the rest of the fit. The data are represented as a Boltzmann plot in Fig. 3.15, the energetic limit is indicated in both Figures 3.14 and 3.15. The conclusions which can be drawn from these observations are:

- That F_1 and F_2 distributions do not seem to be the same. Although there is considerable experimental error in the data caused by noise from the low signal levels, the observed peaking of F_1 at lower N' levels than F_2 was consistently observed when the basis set was increased or a different fitting procedure (NAG E04JAF) [105] was used. Fits in which the F_1 and F_2 levels were constrained to be equal for the same N' produced less satisfactory fits to the data.

  The errors referred to in the table are the variances in the weights, expressed as a percentage, as derived by the fitting routine.

- Both distributions are broad, peaking at intermediate N' levels. On a Boltzmann plot, which masks the F_1/F_2 differences, the distribution can be approximately represented by a "temperature" of 1100K, with considerably lower populations in the levels observed above the energetic limit.

The form of the distribution is compared with those from other studies in the Discussion below.

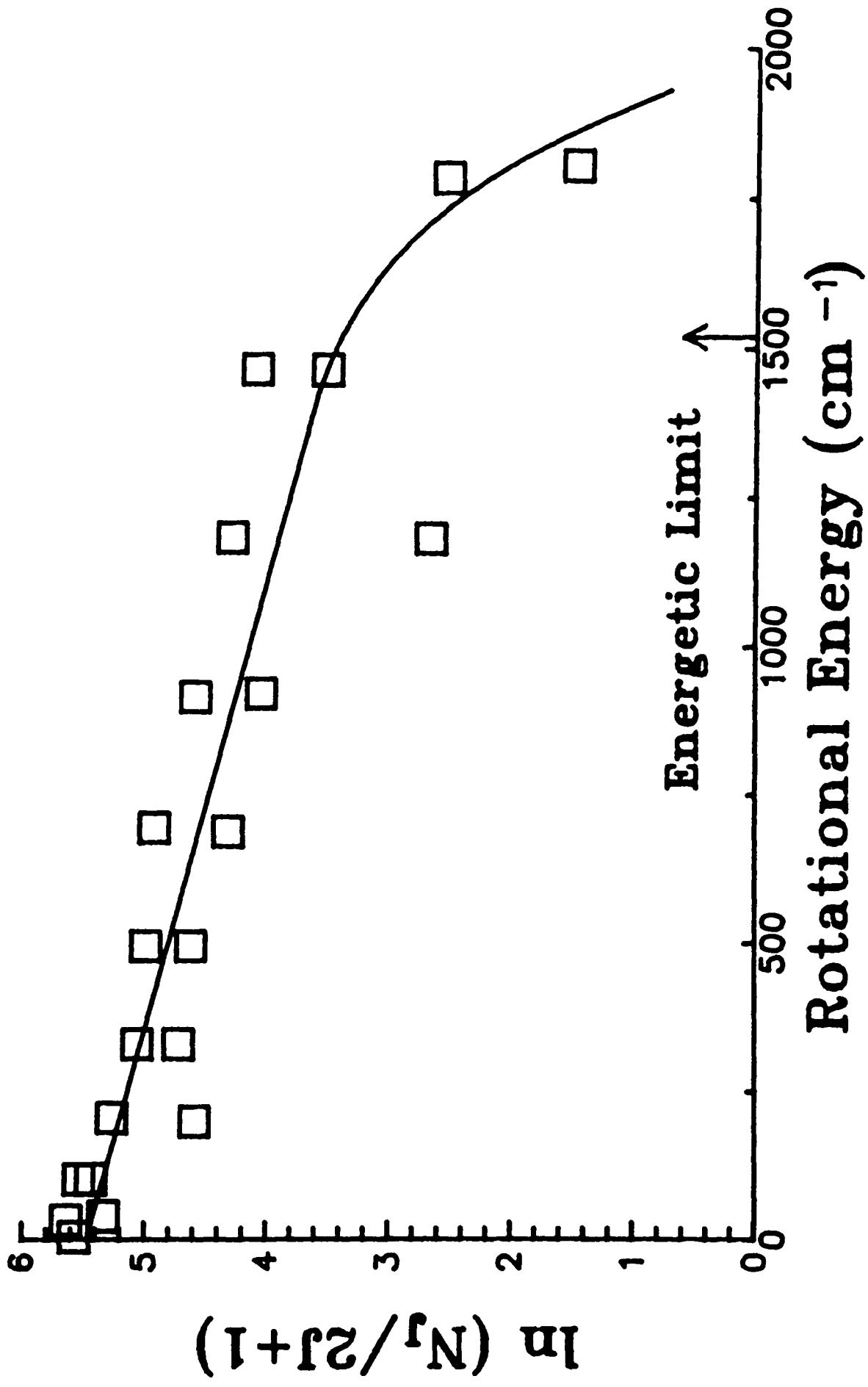

Figure 3.15. Population resulting from fitting procedure represented as a Boltzmann plot.

3.2.4 Production of Ground State OH The majority of the studies of photodissociation of H_2O in the VUV region of the spectrum have concentrated on the production of $OH(A^2\Sigma^+)$ [71] [69] [76] and much less attention has been paid to the electronic ground state, $OH(X^2\Pi_i)$ [6]. Laser Induced Fluorescence has succesfully been used for some years to investigate ground electronic state species formed in photodissociation or reactions. In the present case the second harmonic of dye laser radiation pumped by the second harmonic of the Nd:YAG laser was used to investigate the $A^2\Sigma^+ \leftarrow X^2\Pi_i$ transition in OH via LIF near 283nm. Unfortunately the subsequent emission is in the same spectral region as the direct emission from $OH(A^2\Sigma^+)$ as a result of the photodissociation making quantitative spectroscopy difficult.

LIF signal from $OH(X^2\Pi_i)$ was initially observed at water pressure of 8 Torr when the dye laser probe beam crossed the photolysis beam in the centre of the stainless steel cell, emission being observed vertically, at right angles to both beams. A preliminary LIF spectrum showed a rotational distribution corresponding closely to one expected for a 300K Boltzmann distribution. The dependance of the LIF signal upon the pressure of H_2O, for three lines in the Q_{11} branch of the spectrum, is shown in Fig. 3.16. It is apparent, from comparison with Fig. 3.10, which shows the dependance of the OH(A-X) emission upon pressure, that the signal varies in an entirely different manner. At pressures at which LIF could be detected ($\geq$500 mTorr) collisional quenching of excited state $OH(A^2\Sigma^+)$ by H_2O dominates over radiative decay (see Fig. 3.10) and thus if the ground state OH concentration

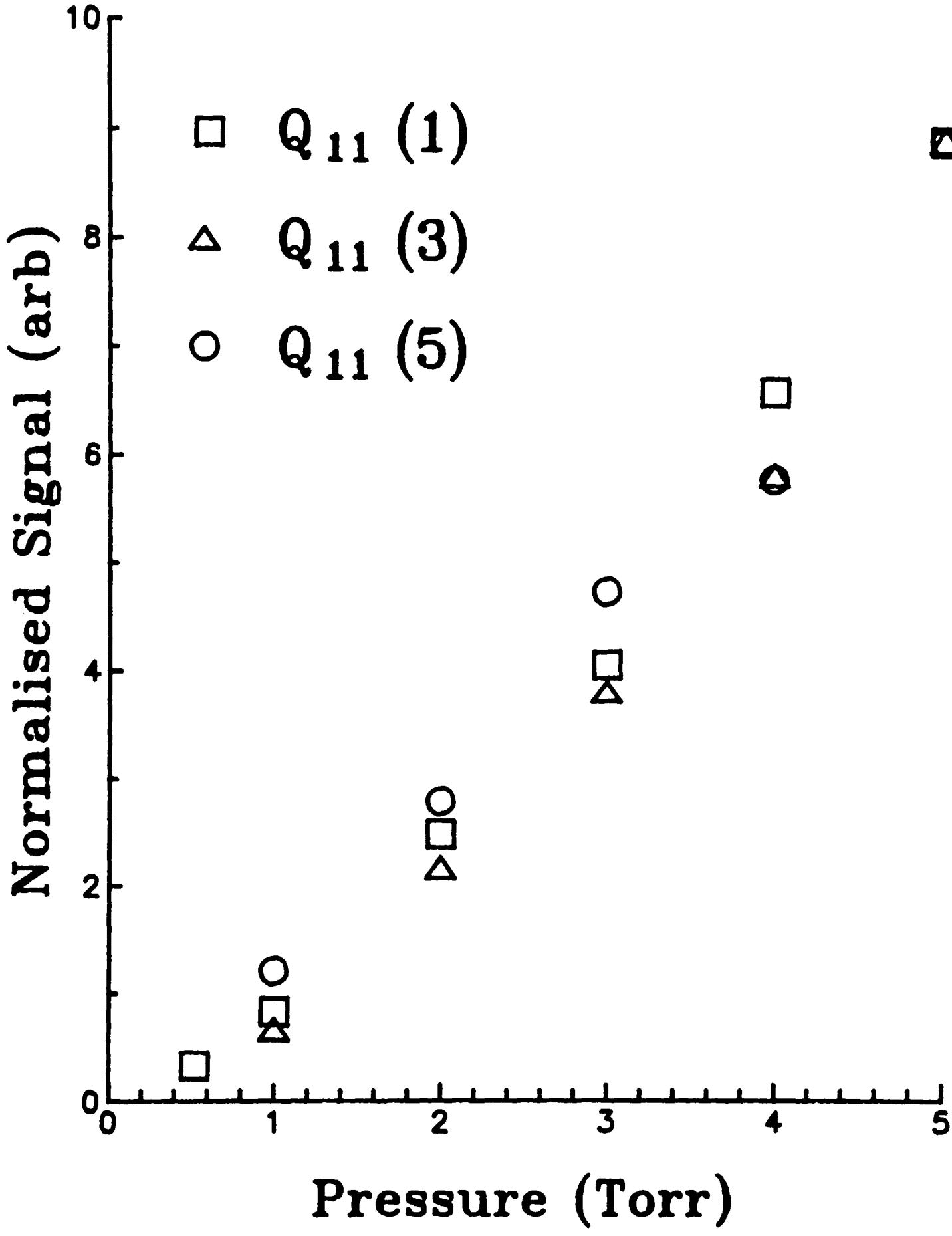

Figure 3.16. Intensity of three lines in LIF spectrum as a function of total pressure.

increases linearly with with H_2O pressure, as expected for the photolytic production step, then the LIF signal should remain constant, in the same way the $OH(A^2\Sigma^+)$ fluorescence signal in Fig. 3.10 does. The data of Fig. 3.16 show a monotonic increase in LIF signal with H_2O pressure, with values extrapolating close to zero at the lowest pressures. This can be explained if rapid vibrational relaxation of $OH(X^2\Pi_i)$ formed in levels v">0 contributes to the signal at increasing pressure: the data show that this must dominate OH(v"=0) production, with a vanishingly small fraction formed directly in v"=0. Although the vibrational quenching rate constant for OH(v"=1) by H_2O has been measured [106] uncertainties in cascade quenching from higher levels, in rotational relaxation processes, and in the products of $OH(A^2\Sigma^+)$ quenching preclude extraction of quantitative data from these LIF pressure plots. A LIF spectrum of $OH(X^2\Pi_i)$ v"=0 at the lowest possible H_2O pressure, 1 Torr, is shown in Fig. 3.17. Normally it would be argued that under these conditions of pressure and delay between photolysis and probe pulses (effectively equal to the 10ns pulse width, as both laser pulses were coincident in time) the distribution in rotational states should be close to the nascent one. However, as Fig. 3.16 shows, the LIF signal is rising with pressure in this range showing that although only one molecule in ten undergoes a gas kinetic collision before the observation time, the production is still dominated by collisional effects. No effort was made to extract populations from these data.

The ratio of populations of v"=0 to v"=1 could, in principle, be

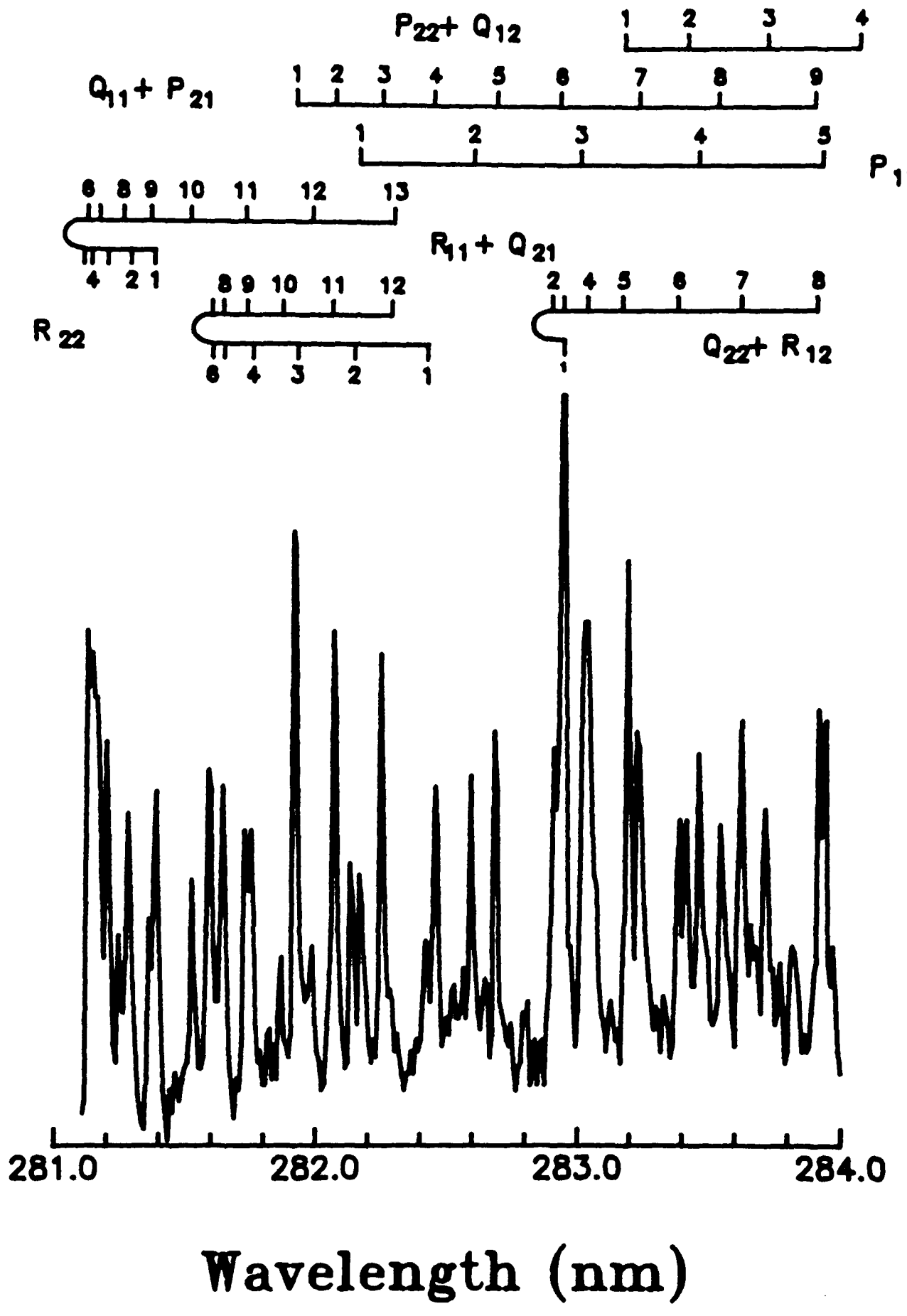

Figure 3.17. Part of the LIF spectrum of $OH(X^2\Pi_i)$ following two photon dissociation of H_2O at 266nm.

probed by Laser Induced Fluorescence of, for instance, the (0,0) and (1,1) bands of the OH(A-X) system which are very close to each other in wavelength. Unfortunately a suitable frequency doubling crystal for operation over a range which spanned both bands was unavailable. Vibrational levels v"≥2 of $OH(X^2\Pi_i)$ are not easily accessible by LIF due to the rapid predissociation of vibrational levels v'≥2 in the excited $A^2\Sigma^+$ state and very poor Frank-Condon factors linking levels v"≥2 in the $X^2\Pi_i$ state with v'=1,2 in the $A^2\Sigma^+$ state, the vibrational overlap having only strong diagonal terms. The $A^2\Sigma^+ \leftarrow X^2\Pi_i$ v"≥2 transition of OH might be examined by Multi-Photon Ionisation in which the $OH(A^2\Sigma^+)$ v'≥2 molecule might be able to absorb a further photon, within the short lifetime of the predissociating levels, leading to ionisation, if a sufficiently high laser intensity was used. This interesting experiment, which would require considerable preliminary spectroscopic study, was not attempted in the present work.

Another possible method of examining the high vibrational levels of $OH(X^2\Pi_i)$ is via high overtone vibration-rotation bands within the $X^2\Pi_i$ state, the Meinel bands, which have been observed in emission in the visible and near-IR region and are weak with a long radiative lifetime [107] [108] [109] [110]. An attempt was made to observe emission from $OH(X^2\Pi_i)$ using a small monochromator with ~20nm resolution, in 1st and 2nd order. The results of this experiment are shown in Fig. 3.18, uncorrected for photomultiplier response which is indicated in the Figure. Also shown are the positions of the Meinel bands of OH taken from the literature cited above and the emission bands of the $\tilde{A}$-$\tilde{X}$ system

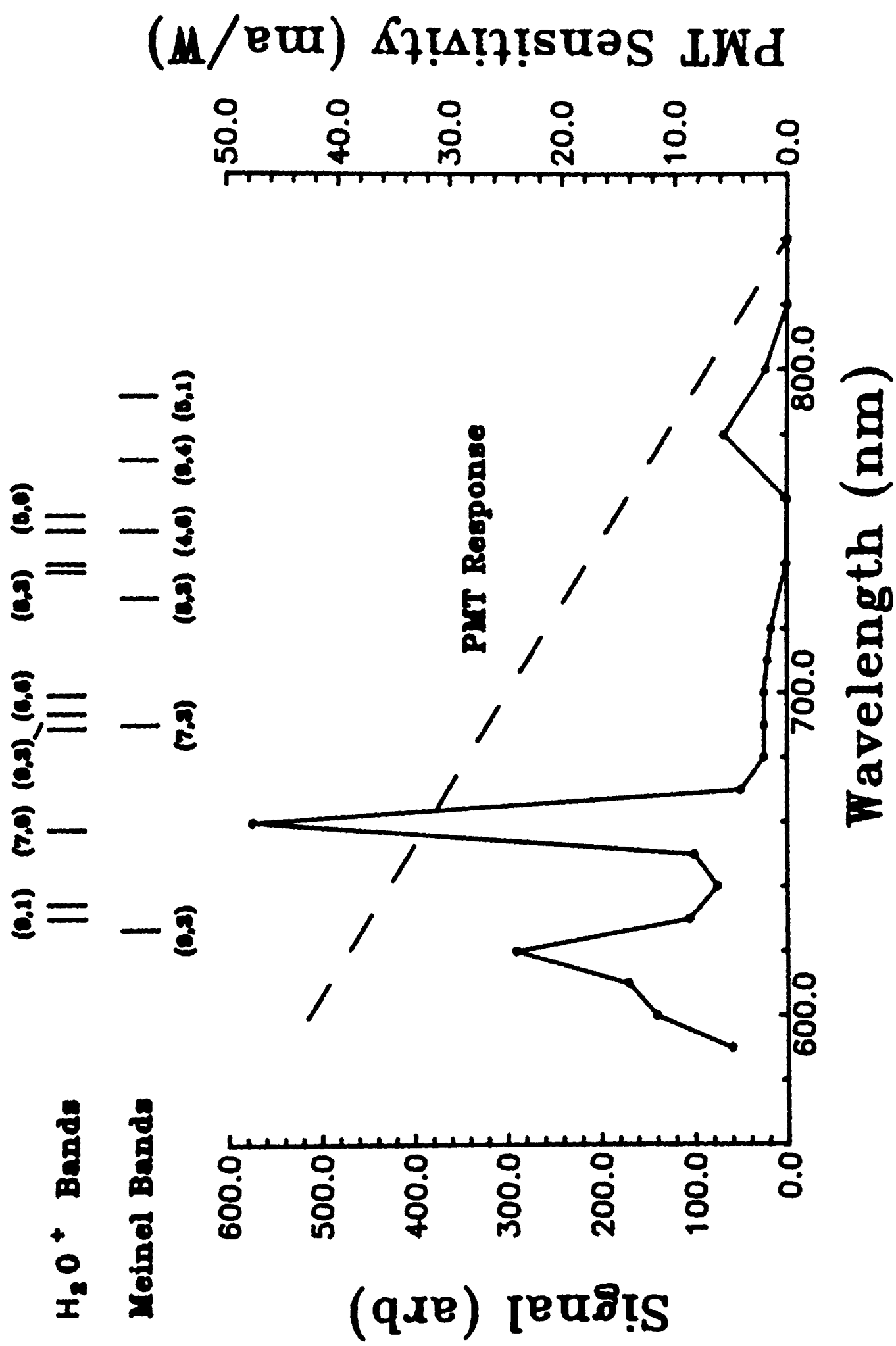

Figure 3.18. Emission spectrum in the region 560-860nm, uncorrected for PMT response which is indicated on the right abcissa. Possible sources of emission in this region are indicated at the top of the figure.

of H_2O^+, another possible source of red emission [95]. The very low signal just permitted an estimate of the zero pressure lifetime of the emission at ~660nm which was ~1.5μs. There does not appear to be any correlation between the observed bands and those expected for OH^* or H_2O^+ and further work is required in this area. A brief attempt to examine the Meinel bands via LIF also proved fruitless. The long lifetimes of the vibrational states involved makes LIF an unfavourable method of study in this case.

3.2.5 Discussion A discussion of the rotational distribution arising in $OH(A^2\Sigma^+)$ $v'=0$ following two photon dissociation of water at 266nm must concentrate on two major points. Firstly what electronic state (or states) is (are) initially populated following photoexcitation and secondly what features of the final repulsive surface account for the observed rotational distribution. Theoretical calculations and experimental observations, discussed in the introduction to this chapter, suggest that there are two possible electronic states which may be initially populated; the $\tilde{B}^1A_1$ which is allowed in both 1 and 2 photon absorption and has been postulated to explain the abnormal rotational distributions arising in $OH(A^2\Sigma^+)$ following single photon dissociation of H_2O in the VUV region, and the as yet unobserved $^1A_2$ state which is 2 photon allowed and has been calculated to lie in this region.

At the start of the present work it was hoped that a distinction between absorption to the $^1A_1$ and $^1A_2$ states could be made from the rotational distributions, following the first reports of 2 photon dissociation of H_2O at 248nm where a much cooler rotational distribution

was found [51] compared to that observed by Carrington [71] in the early single photon dissociation measurements.

The excitation wavelength used in this study is shown on Fig. 3.5, in which the results of theoretical calculations of the rotational distribution arising in OH are presented. It can be seen that this wavelength corresponds to a resonance and, according to the discussion earlier, should therefore lead to a cold rotational distribution. It must be noted that the theoretical predictions are for H_2O in its ground rotational state so that the sharp features of the Figure should not nessecarily be as pronounced although the general form might be expected.

It is not neccesary to invoke the two photon allowed $^1A_2$ state to explain the rotational distribution. It is interesting to note that, because the transition has been assigned as arising from a non-bonding $1b_1$ orbital and terminating in a non-bonding $3pb_2$ Rydberg orbital that there should be little geometric change upon excitation to the $^1A_2$ state. Theory [55] suggests an equilibrium geometry of ~120°. As the $^1A_2$ state does not correlate with $OH(A^2\Sigma^+)$ a crossing to the $\tilde{B}^1A_1$ state must occur. This can happen at long OH-H distances which suggests that dissociation along the antisymmetric stretch which, along with the small geometric change, would lead to low rotational excitation.

More recently, energy distributions have been measured in $OH(A^2\Sigma^+)$ $v'=0$ from the dissociation of H_2O known to be initially excited into the $\tilde{B}^1A_1$ state by both one and two photon procceses and which produce

noticeably cooler rotational distributions than those observed by Carrington, and which are not dissimilar to those of the present study. Fig. 3.19 shows the present data for F_2 OH (which is the "hotter" of the two components) compared with the single photon absorption measurements of Simons et al at 130.4nm [80] and with the two photon data of Simons et al using narrow band excitation near 248nm in the continuum region underlying the $\tilde{C}\leftarrow\tilde{X}$ transition. In the first case the $\tilde{B}\ ^1A_1$ state is the only single photon state avaliable: in the second case polarisation studies establish the initial state as $^1A_1$ rather than $^1A_2$. Although it might be argued that there are differences between the rotational distributions in Fig. 3.19, in particular the two-photon data where the F_1 distribution shows lower rotational excitation, theory shows that either low or high rotational excitation can occur upon the $\tilde{B}\ ^1A_1$ surface, dependant critically upon the point accesed on the surface and hence upon dissociation wavelength.

At 133nm Segev and Shapiro's calculations [84] [85] indicate low rotational energy in the OH^* product, peaking at N~2 (although both the Nd:YAG bandwidth and the room temperature distribution in the parent H_2O molecules used in the present experiments will tend to smear this effect). However Dixon [111] has recently shown that long lived trajectories on the $\tilde{B}\ ^1A_1$ surface, which would give rise to low rotational excitation in the theory of Segev and Shapiro, have a higher probability of crossing to the $\tilde{A}^1B_1$ surface, giving rise to ground electronic state OH, than do those following a direct dissociative trajectory. Low rotational excitation in $OH(A^2\Sigma^+)$ should thus not be

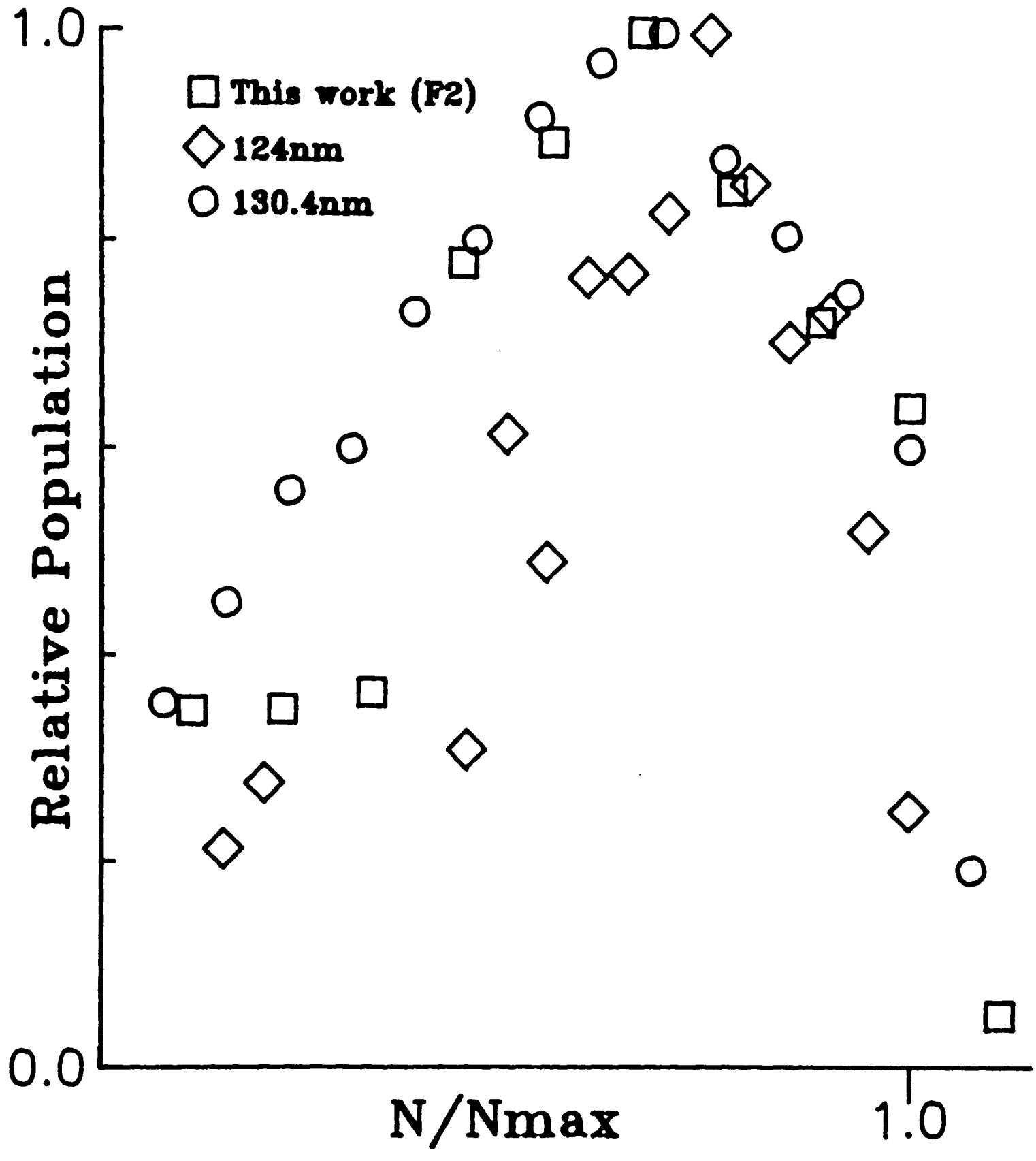

Figure 3.19. Comparison of the population distribution for the F_2 levels of $OH(A^2\Sigma^+)$ determined in this study with single and two photon dissociations of Simons and co-workers, all normalised to the same N max.

favoured. An exception is the special case in which H_2O with $j=0$ is excited to a long lived trajectory in which crossing to the $\tilde{A}^1B_1$ surface is forbidden [111].

We conclude from this section that, when F_1 and F_2 distributions are taken together, the present measurements appear to represent the least rotationally excited OH observed in either one or two photon excitation of H_2O. This cannot be used as unambiguous evidence supporting absorption to the $^1A_2$ state rather than the $^1B_1$ because of the very varied distributions possible in the latter case. The clear method of distinction between these two possibilities is in the polarisation of the OH emission [76]. Attempts were made in the present experiments to measure the polarisation and hence obtain the fragment alignment, but the polarising optics available reduced the already weak signal to unacceptable levels.

Fig. 3.14 shows the surprising result of unequal populations in the F_1 and F_2 levels of $OH(A^2\Sigma^+)$, implying that the unpaired electron has its spin preferentailly aligned with respect to the axis of OH rotation. Such an effect has been observed in the $CN(X^2\Sigma^+)$ fragment produced in photolysis of ICN and BrCN [112]. In these cases it is presumed to arise because, during fragmentation, the electron spins remain correlated, and strong spin orbit interactions in the ^2P halogen atom couple electronic spin and orbital angular momenta with the latter somehow correlated to the molecular frame. A similar explanation cannot apply to the departing $H(^2S)$ atom: such effects are not apparent in the OH^* distribution from one and two photon dissociations of H_2O [76]. The

present spectra require considerable deconvolution to produce the rotational population distribution and there is always the possibility of experimental error: until better resolution is available in these experiments the results must be treated with some cuation.

Finally in this section some of the other results are discussed briefly.

- As described in the introduction, the $^1A_2$ state of H_2O correlates with $O(^1D) + H_2$. The results presented above do not eliminate the $^1A_2$ state from being the major channel. However if $O(^1D)$ is the major product emission on the weak $O(^1D-^3P)$ transition at ~530nm might be expected. This was not observed.

- Experimantal evidence has been presented to show that both ion and $OH(A^2\Sigma^+)$ production depend on the square of the laser intensity. This could be explained if the $^1A_2$ state, produced by two photon excitation, is further excited in a saturated step, giving rise to ions, whilst rapid predissociation of the $\tilde{B}^1A_1$ state at the two photon level prevents futher excitation. This implies that the $^1A_2$ state must live longer than the $\tilde{B}^1A_1$. If this were so then it would be expected that features due to the $^1A_2$ state should be evident in MPI spectroscopy. No such features have been reported to date.

- The low quantum yield for the production of $OH(A^2\Sigma^+)$ suggests that the majority of OH is produced in the ground electronic state. LIF data has been presented which suggests that the $OH(X^2\Pi_i)$ produced

is vibrationally excited. The H atom kinetic energy following 266nm photodissociation of H_2O has been studied recently by Doppler techniques using Lyman-α radiation [113]. The kinetic energy is low, compared to the available energy, confirming the evidence presented here for high vibrational excitation in $OH(X^2\Pi_i)$. In addition the same results following single photon dissociation are observed.

3.3 EXPERIMENTAL RESULTS : 355nm

3.3.1 Introduction In an attempt to gain more information on the photodissociation of H_2O as a function of wavelength (two photon tunable radiation not having sufficient energy to produce any signal in the present experiments) irradiation of water using the third harmonic of the Nd:YAG laser at 355nm has been used and shown to give rise to both ground and electronically excited OH fragments and to ions. Energetically these processes require 2, 3 and 4 photons respectively, and thus a discussion of the potential intermediates at the two and three photon level is nesseccary. At the two photon level, single photon absorption populates the $\tilde{A}^1B_1$ state from which dissociation to give ground state OH occurs, as discussed earlier. At the three photon level (118.2nm) single photon absorption is to a valley between two Rydberg peaks [52] and has recently been assigned [70] as largely to a $3a_1 \rightarrow 3pb_2 : 2b_2$ transition from a bonding orbital to a mixed Rydberg/valence state of symmetry $^1B_2$ which is theoretically predicted to lie in this region [114] although not previously assigned. The $^1B_2$ state is dissociative: some structure can be seen in the spectrum near

118nm and the presence of a different state, $\tilde{D}'^{1}B_1$ has been inferred from Multi-Photon Ionisation spectroscopy [27]. The $\tilde{D}'^{1}B_1$ state lives long enough to show rotational structure in the MPI spectrum and is homogeneously predissociated, presumably by the $\tilde{A}^{1}B_1$ state, correlating with ground electronic state OH. Ion production via the $\tilde{D}'^{1}B_1$ state shows a cubic intensity dependance [27] consistent with three photon excitation to the intermediate state followed by a saturated step from this relatively long lived state. Predissociation products are presumed to be ground state OH fragments due to dissociation on the $\tilde{A}^{1}B_1$ potential surface. The mechanism for the production of $OH(A^{2}\Sigma^{+})$ from single photon dissociation in low quantum yield (2.6%) [114] is presumed [70] to arise by predissociation via the $\tilde{B}^{1}A_1$ state, despite the fact that no crossing between the $^{1}B_2$ and the $^{1}A_1$ states has been predicted theoretically [59]. The quantum yield for ground state OH production is unknown: $O^{1}D$ foramation has been estimated at 25% at 123.6nm [56] [59].

3.3.2 Experimental

3.3.2.1 Emission from Electronically Excited OH Emission in the region 308-315nm was observed when water was irradiated using the third harmonic of the Nd:YAG laser at 355nm, using the same experimental arrangement as that described earlier in this chapter. The signal levels were smaller than those observed for irradiation at 266nm. The resolved spectrum, recorded at a pressure of 200mTorr, is shown on Fig 3.20. Fig. 3.21 shows a plot of reciprocal lifetime of the emission as a function of pressure from which a radiative lifetime of 616 ± 140ns was obtained. The unresolved emission as a function of pressure showed

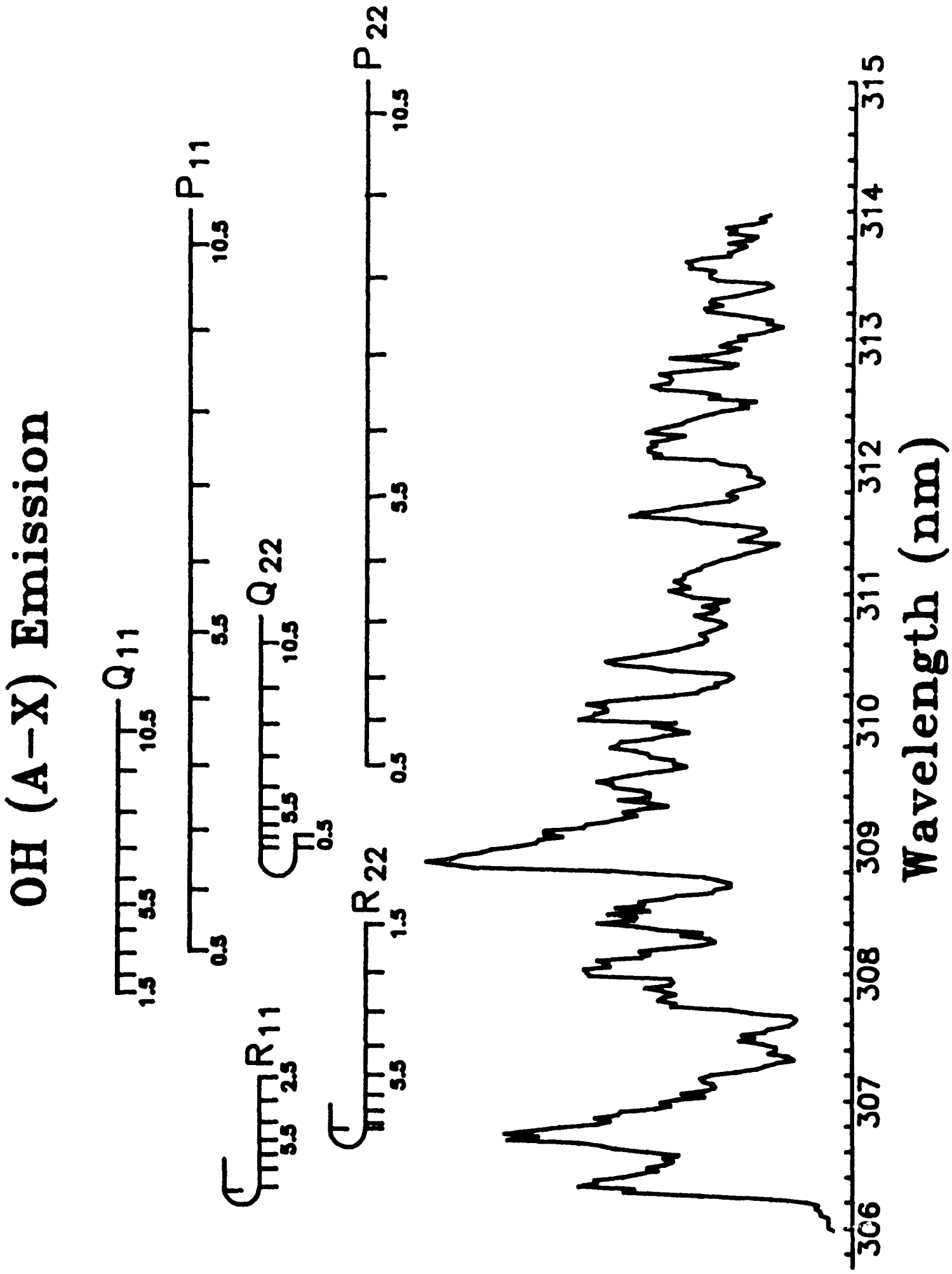

Figure 3.20. Emission spectrum of $OH(A^2\Sigma^+)$ following dissociation of H_2O using 355nm laser radiation.

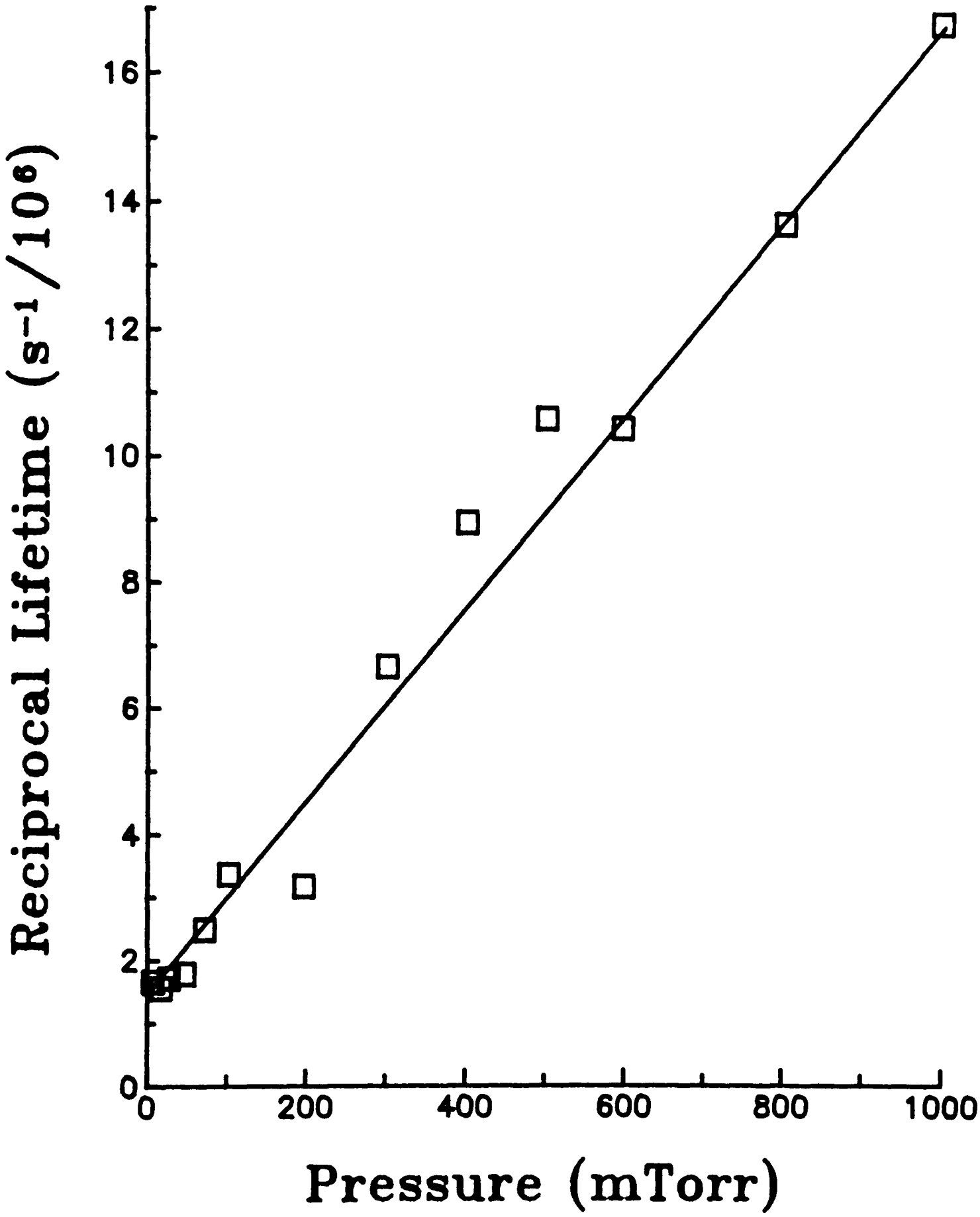

Figure 3.21. Reciprocal radiative lifetime of emission as a function of total pressure.

exactly the same form as that observed under 266nm irradiation. The appearence of the spectrum, along with the corroborative lifetime measurements clearly identify the emitting fragment as $OH(A^2\Sigma^+)$. Energetic considerations show that at least three photons must be absorbed to give rise to electronically excited OH. However the dependance of the emission upon the laser intensity, shown on a log-log scale in Fig. 3.22, shows a quadratic dependance.

3.3.2.2 Production of Ionic Species Ion production was observed, in a similar manner to that described earlier. Fig. 3.23 shows the ion signal as a function of laser intensity, on a logarithmic scale. Over most of the region covered there is a cubic dependance although this is clearly reduced at high laser intensity, possibly due to geometric saturation. Although the slope is noticably lower than three at low laser intensities (to be discussed in more detail shortly) the cubic dependance is consistent with MPI Spectroscopy of water at this wavelength [27].

3.3.2.3 Ground Electronic State OH In an attempt to obtain complimentary information to that described earlier for 266nm irradiation of water, an attempt was made to investigate ground electronic state OH via Laser Induced Fluorescence. The signal was, however very weak so that it was not possible to record a resolved LIF Spectrum. The LIF signal intensity as a function of pressure was recorded for three identifiable lines in the spectrum and shows the same form as before (see Fig. 3.16) but with a marked difference in the value of the intercept. It is clear from this that there is now much more

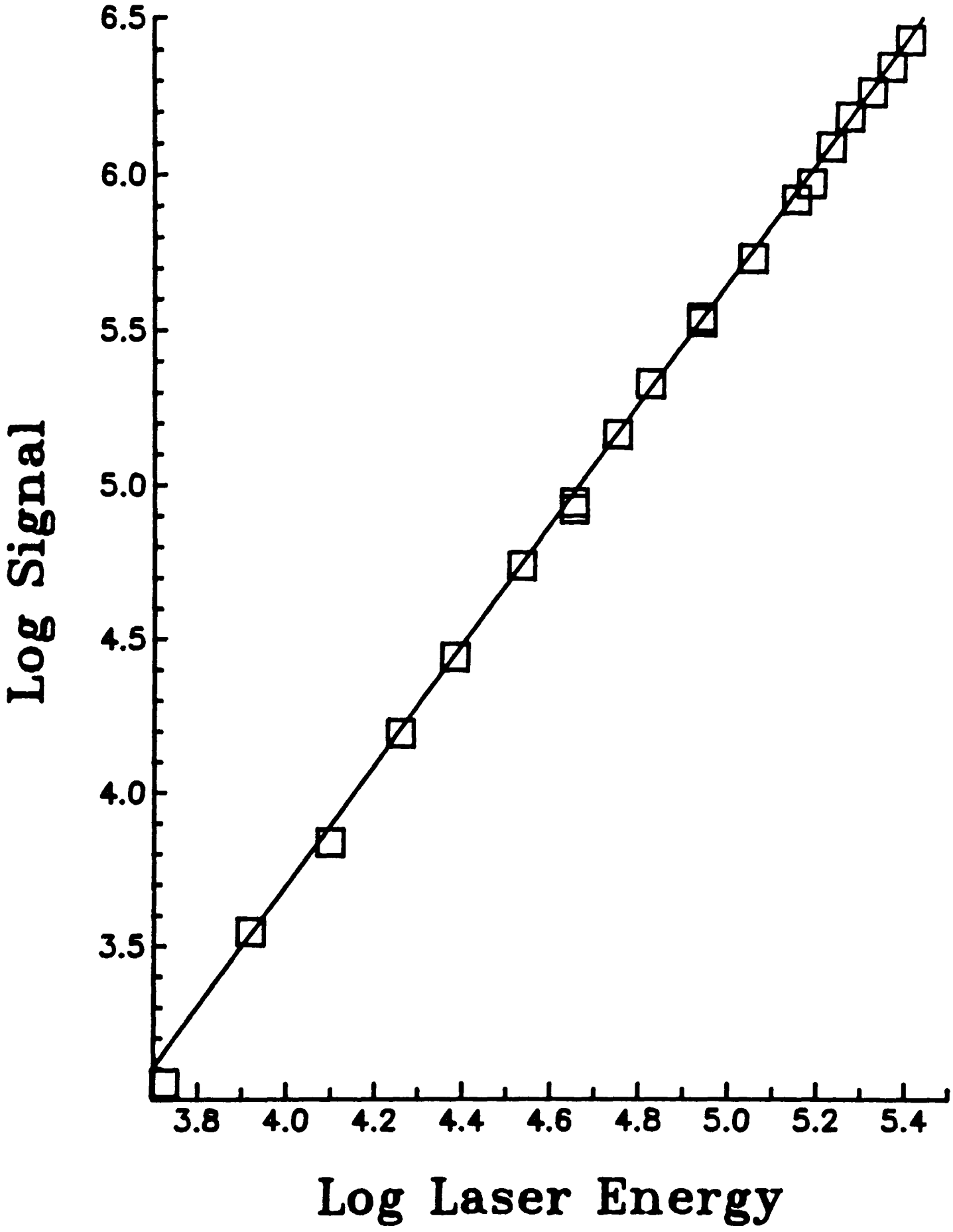

Figure 3.22. Emission intensity as a function of laser energy, both axes being represented on logarithmic scales.

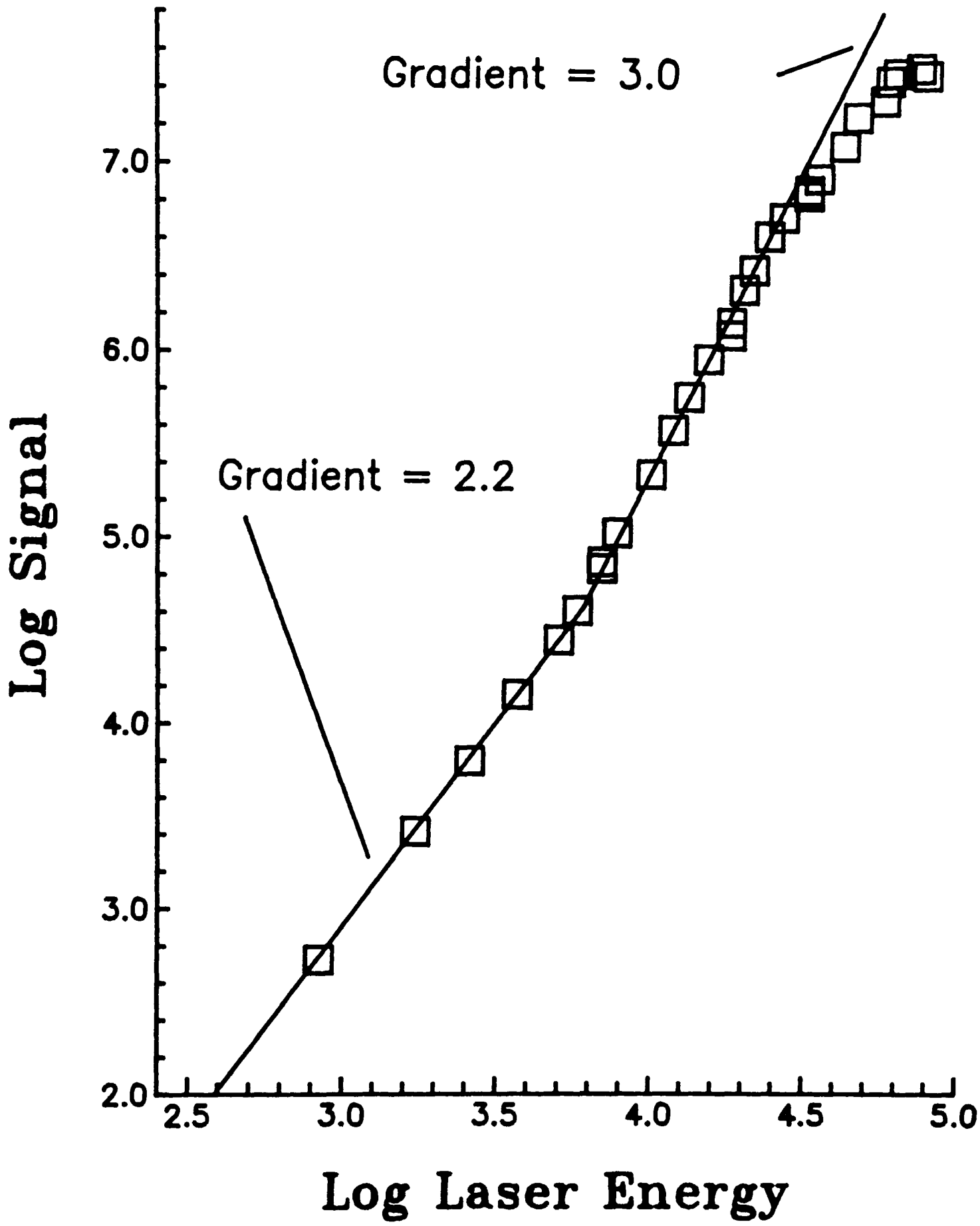

Figure 3.23. Ion signal as a function of laser energy, both axes are logarthmic scales.

$OH(X^2\Pi_i)$ formed directly in v"=0 than in the 266nm experiments described earlier. Despite the weak signal levels it was possible to estimate the dependance of the LIF signal upon the dissociating laser intensity which was close to cubic.

3.3.3 Discussion Formation of electronically excited OH fragments requires at least three photon excitation of the parent water molecules at 355nm. On the basis of the discussion given above for the two photon dissociation, this gives 10900.7cm^{-1} for partitioning in the fragments; enough to populate all of the non-predissociating levels of $OH(A^2\Sigma^+)$ ie. v'=0,1, and up to N≤23 in the ground vibrational level. The emission spectrum shown in Fig. 3.20 suggests that higher rotational levels are populated in this case than for excitation at 266nm: comparison with Fig. 3.7 shows a less pronounced band head at at 309nm, corresponding to $Q_{22}(2.5)$, and a more pronounced band head at 306.8nm, caused by levels around $R_{22}(10.5)$ in the present case. No increase in signal was observed as the spectrum was continued out to longer wavelength suggesting that, although rotational excitation is greater than given under 266nm excitation, there is not excessive rotational energy in the fragment, such as that observed under single photon excitation. There is no evidence for a pronounced band head at 312.2nm, which would be expected for emission from $OH(A^2\Sigma^+)$ v'=1.

Due to the lower signal levels, resulting in a decreased signal/noise ratio, and the increased number of contributing rotational levels it was not possible to obtain an estimate of the rotational distribution using the fitting technique described earlier in this

chapter. It is clear however, from the qualitative discussion given above, that $OH(A^2\Sigma^+)$ does not seem to carry a large fraction of the available energy in internal excitation.

A consistent picture of the data obtained under 355nm excitation must explain the following facts:

- Ion production $\propto I^3$.
- $OH(A^2\Sigma^+)$ production $\propto I^2$.
- $OH(X^2\Pi_i)$ production $\propto I^3$, although the data is of very low quality and this must be treated with caution.
- The $OH(X^2\Pi_i)$ shows greater population in v"=0 than in the case of excitation at 266nm.
- $OH(A^2\Sigma^+)$ shows relatively low internal excitation.

Firstly the kinetics of the possible excitation paths will be discussed. These are shown in Fig. 3.24 for both cases described in the introduction to this section: direct three photon excitation to the intermediate state and also enhancement at the two photon level. Both cases can be treated separately.

1. Direct three photon excitation.

   Applying the steady state approximation to the intermediate level we obtain:

$$dy/dt = k_1 I^3 x - (k_2 I + k_3) y = 0 \qquad (3.14)$$

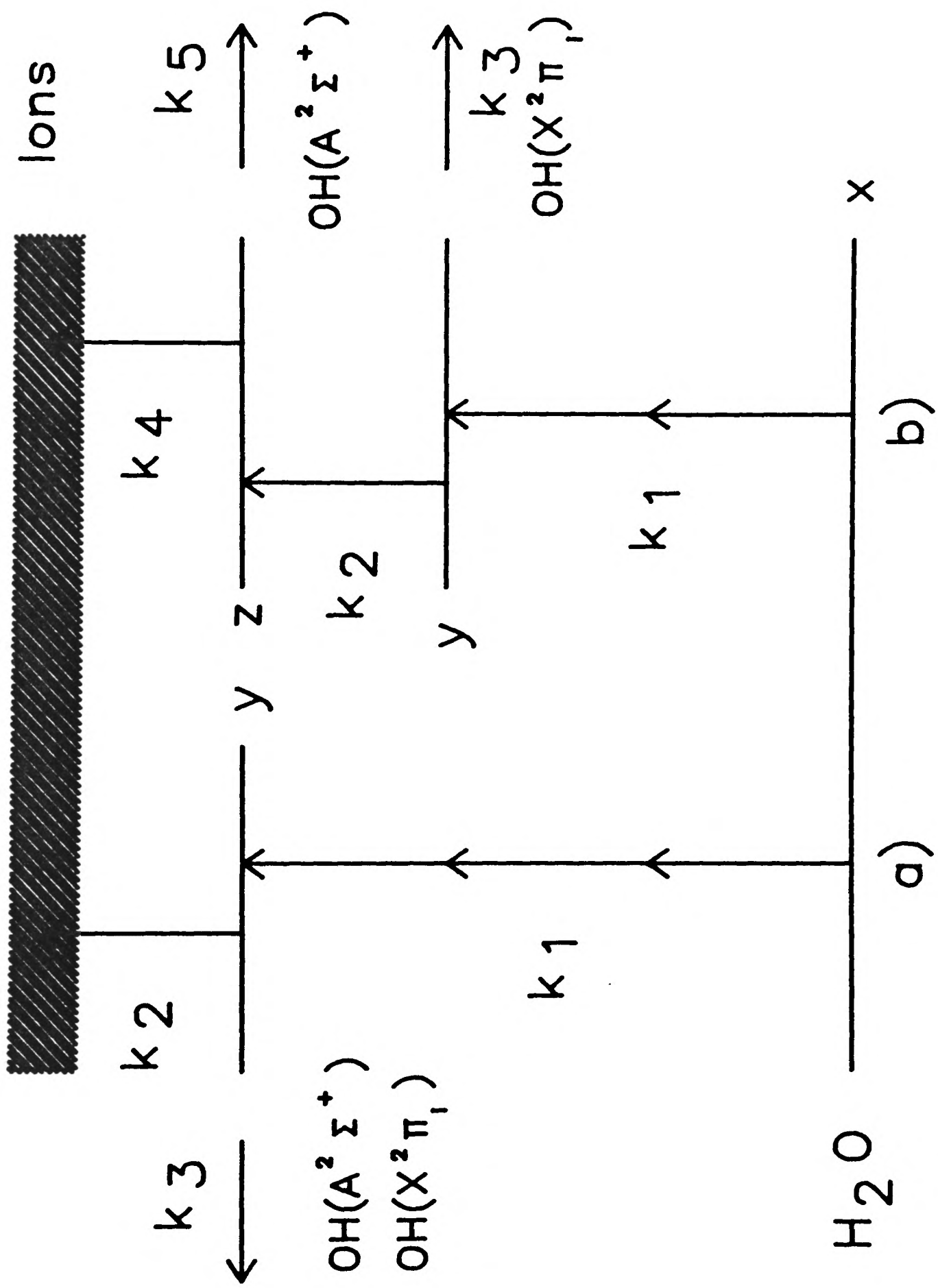

Figure 3.24. Possible kinetic schemes for dissociation of H_2O using 355nm radiation.

$$d[ions]/dt = k_2yI - k_1k_2I^4x \;/\; (k_2I+k_3) \qquad (3.15)$$

$$d[OH^*]/dt - d[OH]/dt - k_3y - k_1k_3I^3x/(k_2I+k_3) \qquad (3.16)$$

Assuming the ionisation step saturates, ie $k_2I \gg k_3$ we obtain:

$$d[ions]/dt \propto I^3 \qquad (3.17)$$

$$d[OH^*]/dt \propto I^2 \qquad (3.18)$$

$$d[OH]/dt \propto I^2 \qquad (3.19)$$

2. Enhancement at the two photon level:

Assuming a steady state at both the two and three photon level we obtain:

$$d[ions]/dt = k_1k_2k_4I^4x \;/\; (k_3+k_2I).(k_5+k_4I) \qquad (3.20)$$

$$d[OH^*]/dt - k_1k_2k_5I^3x \;/\; (k_3+k_2I).(k_5+k_4I) \qquad (3.21)$$

$$d[OH]/dt - k_1k_3I^2x \;/\; (k_3+k_2I) \qquad (3.22)$$

assuming that all the ground electronic state OH arises via the two photon intermediate state. Experimentally we observe $d[OH^*]/dt \propto I^2$ which implies:

$$(k_3+k_2I)(k_5+k_4I) \propto I \qquad (3.23)$$

in which case either

$$k_4 I > k_5 \text{ and } k_3 > k_2 I \qquad (3.24)$$

or

$$k_5 > k_4 I \text{ and } k_2 I > k_3 \qquad (3.25)$$

must be true.

Equations 3.20 and 3.23, above, imply:

$$d[\text{ions}]/dt \propto I^3 \qquad (3.26)$$

whilst equation 3.24 gives:

$$d[OH]/dt \propto I^2 \qquad (3.27)$$

and the alternative, equation 3.25, gives:

$$d[OH]/dt \propto I \qquad (3.28)$$

The first alternative for the rate of production of ground state OH is in agreement with the model for the three photon intermediate state, but neither predict the observed behaviour. It might be argued that this first alternative, Equation 3.24, is the more likely since the $\tilde{D}'^1B_1$ state is longer lived than the $\tilde{A}^1B_1$ state (it shows resolvable rotational structure) so that both models predict the same kinetic behaviour.

There are several observations that can be made in the light

of the analysis presented above.

- The production of ions is consistent with the obsevations of Ashfold et al [27] and takes place via the long lived, structured, $\tilde{D}'\,^1B_1$ state. It does not seem likely that ions are formed to any extent by excitation through the recently assigned $^1B_2$ state. There are two reasons for this: firstly it appears to be unbound and hence has a much shorter lifetime than the $\tilde{D}'$ state and secondly there is no chance of resonance enhancement by the $\tilde{A}^1B_1$ state as can the $\tilde{D}'$ state.

- Ground electronic state OH cannot be predominantly formed by two photon excitation to the dissociative $\tilde{A}^1B_1$ state as the dependance on laser intensity is too steep.

- Formation of ground state OH from the $^1B_2$, presumably via the $\tilde{A}^1B_1$ surface, could explain the observed cubic dependance on the laser intensity: different dynamics, giving rise to less vibrationally excited OH than following two photon excitation at 266nm, must clearly occur.

- The production of electronically excited OH via the $\tilde{D}'$ state is kinetically consistent but it is expected that this would be a minor channel since homogeneous predissociation via the $\tilde{A}^1B_1$ state, which correlates with ground electronic state OH, was found to predominate by Ashfold.

- The relatively low internal excitation observed within the

$OH(A^2\Sigma^+)$ may, again, reflect long lived trajectories upon the $\tilde{B}^1A_1$ potential surface [84].

In conclusion it must be stated that, since several electronic states are involved and each process has an unknown quantum yield, more detailed information, such as polarisation measurements, which can identify the symmetry of the states and better resolved emission and LIF spectra are required to clarify the various possibilities at this wavelength.

CHAPTER FOUR

4.1 INTRODUCTION

This chapter describes an investigation of the rotational and vibrational distribution arising in the ground electronic state of the NO molecule, $NO(X^2\Pi_i)$, following single photon dissociation of methyl nitrite, CH_3ONO, using the third harmonic of a Nd:YAG laser at 355nm. The ease of detection of NO by a variety of laser methods has made the study of photodissociation of NO containing molecules popular in recent years. For example, both single photon Laser Induced Fluorescence [115] [116] [117] and Multi-Photon Ionisation [28] have been used to examine the rotational and vibrational product distribution in $NO(X^2\Pi_i)$ following dissociation of NO_2 at a variety of wavelengths. Houston and co-workers used two photon LIF to investigate the ~700nm photodissociation of CF_3NO cooled to an initial rotational energy of $\sim 10cm^{-1}$ via a supersonic expansion [118]. Some of the most detailed photodissociation studies reported to date have involved four atom molecules dissociating into diatomic fragments, one of which is NO: in the case of NCNO both $CN(X^2\Sigma^+)$ and $NO(X^2\Pi_i)$ products have been probed by one and two photon LIF respectively [119]. For the case of HONO [21] [120] (of obvious comparative interest for the present study of CH_3ONO) only the OH fragment could be observed due to the unavoidable contamination of the sample with ground state NO. This [120] study outlined one of the most interesting recent developments of LIF detection of photofragments - namely that information on the energetics of dissociation (translational and internal energy distributions) can be

complemented by information on the vector quantities of dissociation, eg. spatial anisotropy of products with respect to the transition dipole moment, and in the case of the $OH(X^2\Pi_i)$ state, orbital anisotropy revealed by measurements of Λ doubling.

In principle the photodissociation of methyl nitrite can be studied in similar detail since both NO and MeO [121] [122] can be investigated by LIF - although such a complete study has not yet been performed.

The absorption spectrum of CH_3ONO is shown in Fig. 4.1, with the dissociation wavelength used in the present study also indicated. The transition has been assigned as $\pi^* \rightarrow n$ type, localised in the -N=O unit of CH_3ONO, the separation of the vibrational bands corresponding to the vibrational frequency of NO in CH_3ONO; ~1100cm^{-1}. Methyl nitrite exists in both cis and trans conformers, as shown by NMR studies as a function of temperature [123] [124]. The cis form is slightly more stable. Each vibrational level in the absorption spectrum contains contributions from each conformer with the absorption due to the trans conformer at slightly longer wavelength [125]. It is likely that excitation at 355nm will preferentially excite ν=2 of the NO progression in the trans conformer of methyl nitrite.

The primary products of photodissociation in the wavelength region 240-360nm was first studied in an Ar matrix by Brown and Pimentel [126]. The observed products were H_2CO and HNO which did not distinguish between:

$$CH_3ONO \rightarrow CH_3O + NO \qquad (4.1)$$

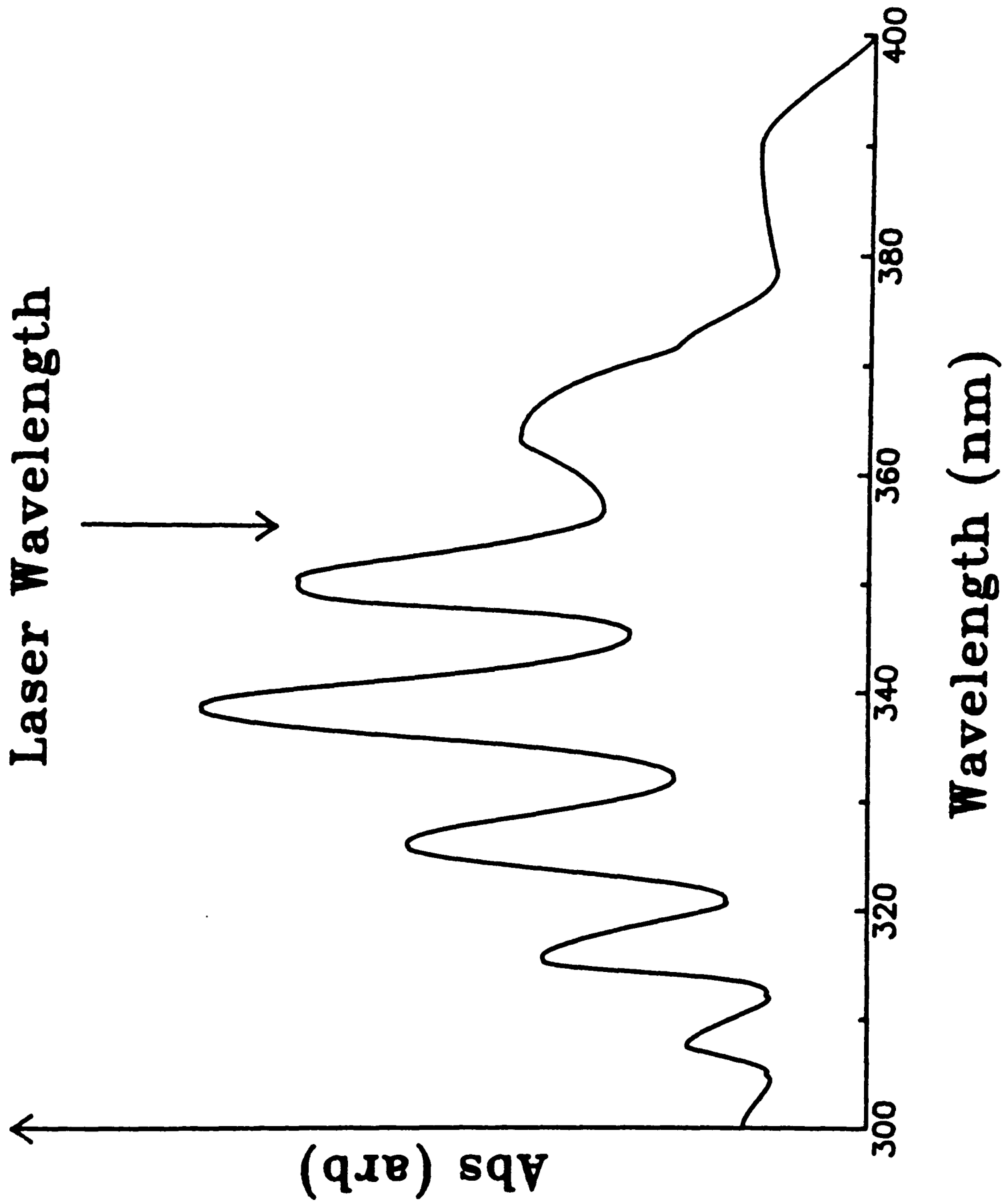

Figure 4.1. Absorption spectrum of CH_3ONO, taken from Lahmani and co-workers. The dissociation wavelength in the present work is indicated.

$$CH_3O + NO \rightarrow CH_2O + HNO \qquad (4.2)$$

and

$$CH_3ONO \rightarrow CH_2O + HNO \qquad (4.3)$$

Flash photolysis studies [127] observed absorption bands which were attributed to CH_3O and also to NO in vibrational levels of the ground state [128] thus establishing these as the primary photolysis products. Cox et al [129] find a quantum yield of unity for this process for broad band excitation in the near UV region.

The dynamics of alkyl nitrite photolysis was first investigated by Tuck who used photofragment spectroscopy to study the dissociation of ethyl nitrite at 347nm [130]. The primary products in this case were CH_3CH_2O and NO and the angular distribution suggested an excited state lifetime of $\leq 2\times10^{-13}$s. Time-of-flight measurements showed that translational motion accounted for ~36% of the energy above that required to break the O-N bond. No information was obtained on the internal energy distribution since the resolution of the apparatus was not sufficiently high to show any structure. The results of this study were compared with a simple impulsive model, to be discussed later, with a modification of the available energy due to the initial absorption into v=3 of the NO chromophore; the available energy being decreased by this amount. The model was able to rationalise successfully the experimental results.

Photodissociation of CH_3ONO at a variety of wavelengths has been reported. Lahmani and co-workers have excited CH_3ONO in the VUV region

using synchrotron radiation [131] [132] and observed the production of $NO(A^2\Sigma^+$ $v'=0,1,2,3)$, $(C^2\Pi_i$ $v'=0)$ and $(D^2\Sigma^+$ $v'=0)$. The vibrational distribution arising in the $NO(A^2\Sigma^+)$ state was shown to be close to a statistical one and anomalous population in $v'=3$ of the $A^2\Sigma^+$ state was shown to be due to collisional interaction of the $C^2\Pi_i, v'=0$ and $D^2\Sigma^+, v'=0$ states with the CH_3O fragment. A close agreement between the threshold wavelength for production of the various electronic states of NO and their thermodynamically allowed values suggested a predissociation rather than direct dissociation mechanism.

Radhakrishnan has investigated the photodissociation of a series of alkyl nitrites RONO; $R=CH_3$, C_2H_5, C_3H_7 [29] at a wavelength of ~383nm in a single colour experiment in which the dissociation wavelength changed whilst the MPI spectrum of the NO fragment was recorded. Consequently, to avoid altering the dissociation energy significantly, only a small portion of the MPI spectrum was recorded. The results of these experiments showed that the rotational distributions arising in $NO(X^2\Pi_i)$ from ethyl and propyl nitrite were statistical with "temperatures" corresponding to 350±35K and 250±25K respectively whilst that from methyl nitrite was considerably rotationally excited and non-statistical in nature.

Only one experimental investigation has been made of the photodissociation of methyl nitrite in which the $CH_3O(\tilde{X}^2E)$ fragment has been probed. Sanders et al [121] dissociated CH_3ONO at 266nm and observed LIF of the $\nu_3'=2\rightarrow0$ and $\nu_3'=3\rightarrow0$ of the $\tilde{A}^2A_1\rightarrow\tilde{X}^2E$ system of CH_3O at 302nm and 299nm respectively. They observed no LIF attributable to

the hot bands of $CH_3O(\tilde{X}^2E)$ suggesting no vibrational excitation. No rotational distribution was reported.

The experimental investigation most pertinent to the present discussion was reported by Lahmani et al [133], whilst the current study was in the final experimental stages. The rotational distribution arising in $NO(X^2\Pi_i)$ is monitored by two photon LIF following dissociation of CH_3ONO at 355nm. The relative vibrational distribution in the four vibrational levels observed was: v"=0:1:2:3 = 1:4:0.8:0.2. The rotational distribution arising in v"=1 is shown in Fig. 4.2. "Similar" distributions were found for the other vibrational levels populated. The translational energy of the NO fragment was determined by measuring the linewidth of the $O_{12}(J=16.5)$ line in the spectrum arising from v"=0 giving $0.68\pm0.03cm^{-1}$ (FWHM) compared to a 300K sample of NO which yielded $0.46\pm0.01cm^{-1}$. A deconvolution of the laser linewidth led to a Doppler width of $0.51cm^{-1}$ which suggests the translational energy of NO is $3800\pm600cm^{-1}$ for v"=0 and a mean translational energy of $2600\pm600cm^{-1}$. Conservation of linear momentum implied a mean translational energy in CH_3O of $\sim2500\pm600cm^{-1}$ which gives 36% of the available energy appearing as product translation, the same value as found for ethyl nitrite [133]. The results of this experiment were compared with both the simple and modified impulsive models used by Tuck in the analysis of ethyl nitrite dissociation [130] and significant disagreement was found, particularly in the vibrational and rotational energy content of the NO fragment.

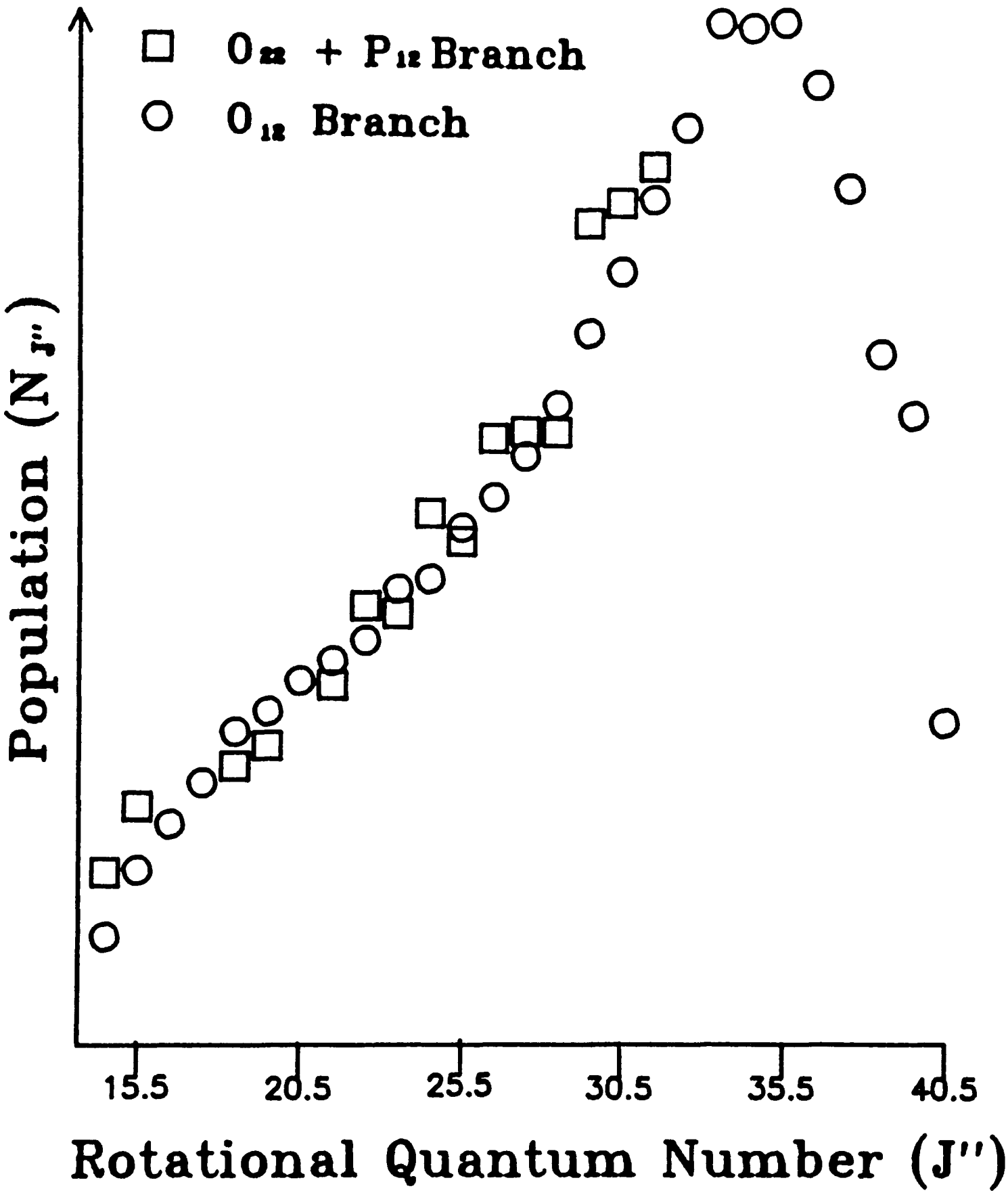

Figure 4.2. Rotational distribution resulting in NO($X^2\Pi_i$, v"=0) following 355nm dissociation of CH_3ONO. Nomenclature refers to two photon LIF spectra.

In a further study [134] the same workers varied the dissociation wavelength to match the -N=O vibrational peaks observed on the absorption spectrum of CH_3ONO (Fig. 4.1) and measured the rotational distributions in v"=0-4. The vibrational populations in NO were found to vary with dissociation wavelength whilst the rotational distributions showed little change. This suggested that the vibrational energy present in the CH_3O-N=O is retained as vibration in the NO fragment. More recent time-of-flight measurements show the translational energy of NO and CH_3O to be 4070±180cm^{-1} and 3930±170cm^{-1} respectively [135].

4.2 EXPERIMENTAL

4.2.1 Methyl Nitrite Preparation Methyl Nitrite was prepared by a transesterification reaction of octyl nitrite and methanol [136]:

$$C_8H_{17}ONO + CH_3OH \rightarrow C_8H_{17}OH + CH_3ONO \qquad (4.4)$$

An excess of methanol ensures a high yield of methyl nitrite which is carried from the reaction vessel on a flow of dry nitrogen gas and condensed via a liquid nitrogen trap.

After transfer to the experimental vacuum line residual air was removed by repeated freeze-pump-thaw cycles using a liquid nitrogen bath. Contamination by NO was then reduced by freeze-pump-thaw cycles at 163K using an ethanol/liquid nitrogen slurry. The purified methyl nitrite was stored in a darkened bulb to prevent photochemical decomposition.

Purity was established by recording IR absorption spectrum and mass spectrum of a small sample. Table 4.1 summarises the results of these tests.

IR spectrum

	energy/cm^{-1}	Assignment
Peaks at	3100-2900	O-CH_3 CH Stretch
	1780,1660	O-N=O cis,trans CH_3ONO
	1350	NO bound to NaCl window
	1080-1000	C-O stretch
	880-800	N-O stretch
	650	O-N=O bend
No Peaks at	3600	OH stretch in CH_3O
	1650,1600	O-N=O cis,trans octyl nitrite

Mass Spectrum

Mass	Ion	Mass	Ion
61	CH_3ONO^+	29	CHO^+
60	CH_2ONO^+	28	CO^+, CH_2N^+
46	NO_2^+	16	O^+
32	NH_2O^+	15	CH_3^+
31	CH_3O^+	14	CH_2^+
30	NO^+, CH_2O^+	13	CH^+

Table 4.1

In the case of the IR absorption spectrum the absence of peaks at $3600cm^{-1}$ from the OH stretch of methanol and at 1650 and $1600cm^{-1}$ from

the cis and trans forms of octyl nitrite indicate good purity. On the mass spectrum good agreement was found between the observed mass peaks and the literature values [137]. In particular the absence of peaks at m/e>61 confirmed that there was no contamination from octyl nitrite. A LIF spectrum of a small sample of the methyl nitrite confirmed that there was slight contamination by NO.

4.2.2 Preliminary Experiments Initial experiments revealed Laser Induced Fluorescence signals from NO($X^2\Pi_i$) in vibrational levels v"=0-3. The bands observed were the (0,0) and (0,2) using the 2nd and 1st Anti-Stokes Stimulated Raman transitions of frequency doubled Rhodamine 6G near 225 and 247nm respectively and (0,1) and (0,3) bands using the corresponding Raman transitions of frequency doubled Rhodamine B near 234 and 259nm respectively. The use of a common vibrational level of the $A^2\Sigma^+$ state of NO ensured that the detectivity for each band was the same and only absorption factors had to be accounted for. The LIF signal was shown to depend linearly on the intensity of the probe laser, showing that saturation was not occurring and allowing the computer spectral data acquisition system to be used, and also in a linear manner on the dissociation laser intensity. Although the methyl nitrite was found to absorb the probe laser radiation slightly, no LIF signal was observed in the absence of the 355nm radiation under the conditions used to record the LIF spectra, thus confirming the dissociation wavelength. The magnitude of the LIF signal was found to be linear with the pressure of methyl nitrite at low pressures up to ~100mTorr. Because both dissociation and probe laser pulses originated from the same laser the

delay between pulses was approximately 5-10ns ensuring that, at the pressures used (40mTorr), no relaxation of rotational levels or of their orientation could have occured between dissociation and subsequent probing by LIF.

Before a detailed description of the rotational and vibrational distribution in $NO(X^2\Pi_i)$ is given, another feature of the photodissociation will be discussed. This is the observation of direct emission following 355nm excitation of methyl nitrite. Emission in the region 300-540nm was observed when a sample of methyl nitrite was subjected to 355nm radiation alone. The time behaviour of this signal over a period of ~1hr indicated that the emission was due to a stable species; the intensity rose in a linear manner and eventually saturated at a constant level when a bulk sample of CH_3ONO was constantly photolysed. The emission spectrum, recorded under low resolution using a small monochromator (Baush and Lamb 33-86-07, 20nm resolution) and a small steady flow of methyl nitrite, is presented in Fig 4.3. Also shown are the positions of lines observed in emission from the $\tilde{A}^1A_2$ state of formaldehyde in cool flames [138]. The agreement is very good. The IR absorption spectrum of the products after ~1hr irradiation is presented in Fig. 4.4. In addition to the peaks reported earlier for CH_3ONO a sharp peak at $1750cm^{-1}$ is observed which is consistent with the C=O stretch in an aldehyde. Time resolved emission , as examined on the transient digitiser, was found to be bi-exponential with a fast component of ~20±20ns and a slow component with a lifetime of 300±100ns. The large uncertainty reflects the small signal levels observed. The

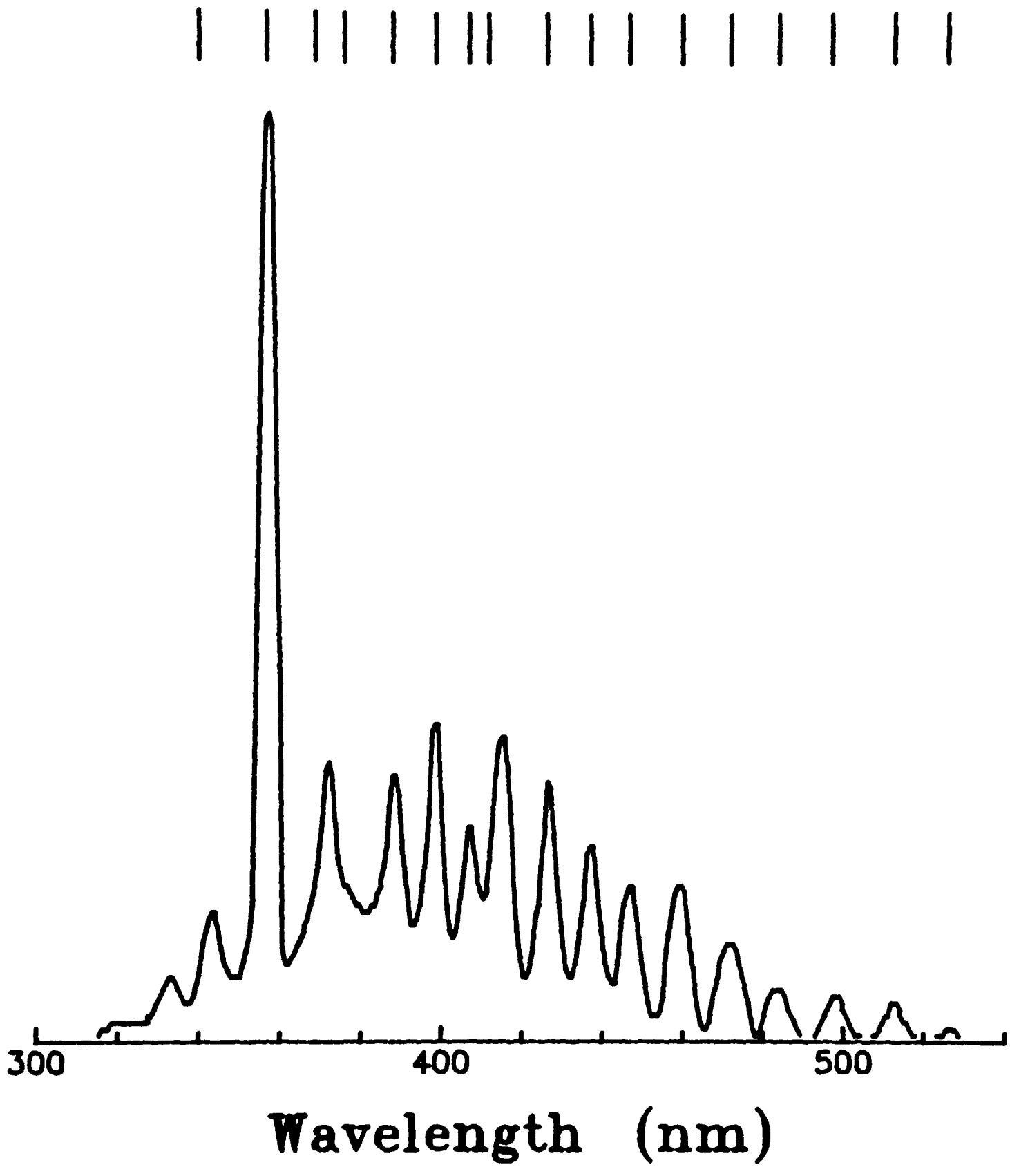

Figure 4.3. Emission spectrum following 355nm irradiation of CH_3ONO. Observed emission lines of CH_2O in cool flames are also shown.

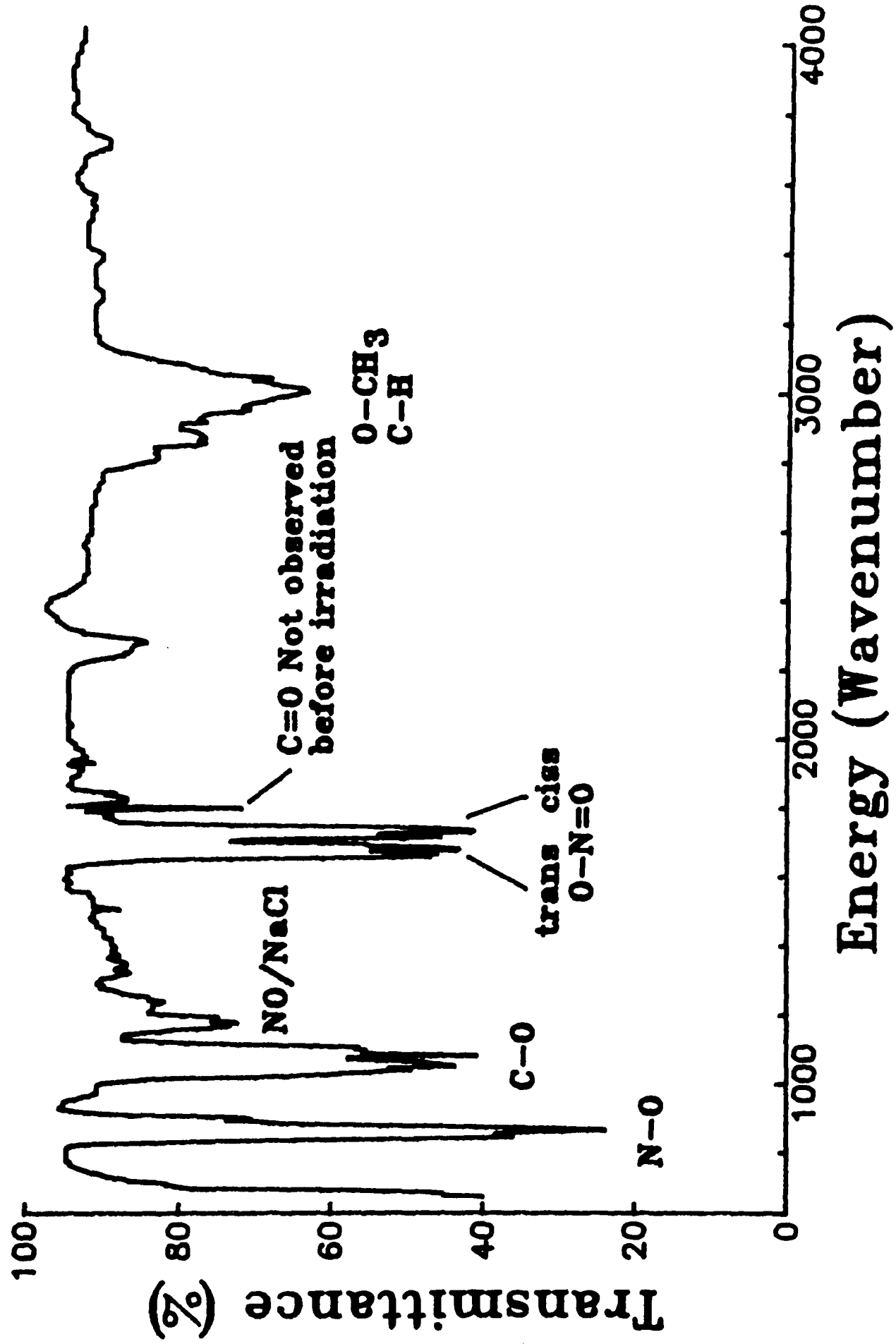

Figure 4.4. IR absorption spectrum of the products following 1hr irradiation of CH_3ONO at 355nm.

fast component decays in a time short compared to the effective bandwidth of the transient digitiser making an accurate determination impossible. The ratio of the intensities of the fast to slow decay was found to be ~2.5 but was found to depend critically on the pressure, flowrate and the wavelength of the radiation observed. A Stern-Volmer analysis of the slow component is presented in Fig. 4.5. As can be seen there is pronounced curvature at low pressures. All the features of the emission described above have been observed by Moore and co-workers following 355nm excitation of formaldehyde [139]. A comparison of the results is given in Table 4.2.

	τ_{fast}	τ_{slow}	I_{fast}/I_{slow}
This work	20 ± 20 ns	300 ± 100 ns	~2.5
Moore	69 ± 7 ns	435 ± 15 ns	2.6 ± 0.5

Table 4.2.

Two features of the data which are not reproduced by the study of Moore et al are the two small, but reproducable, peaks to the blue of the excitation wavelength and the anomalous intensity of the peak at the excitation wavelength.

As described in the introduction to this chapter the production of formaldehyde following photolysis of methyl nitrite takes place by a radical abstraction following the primary photolysis step of main interest to this study [129]:

$$CH_3ONO \rightarrow CH_3O + NO \qquad (4.5)$$

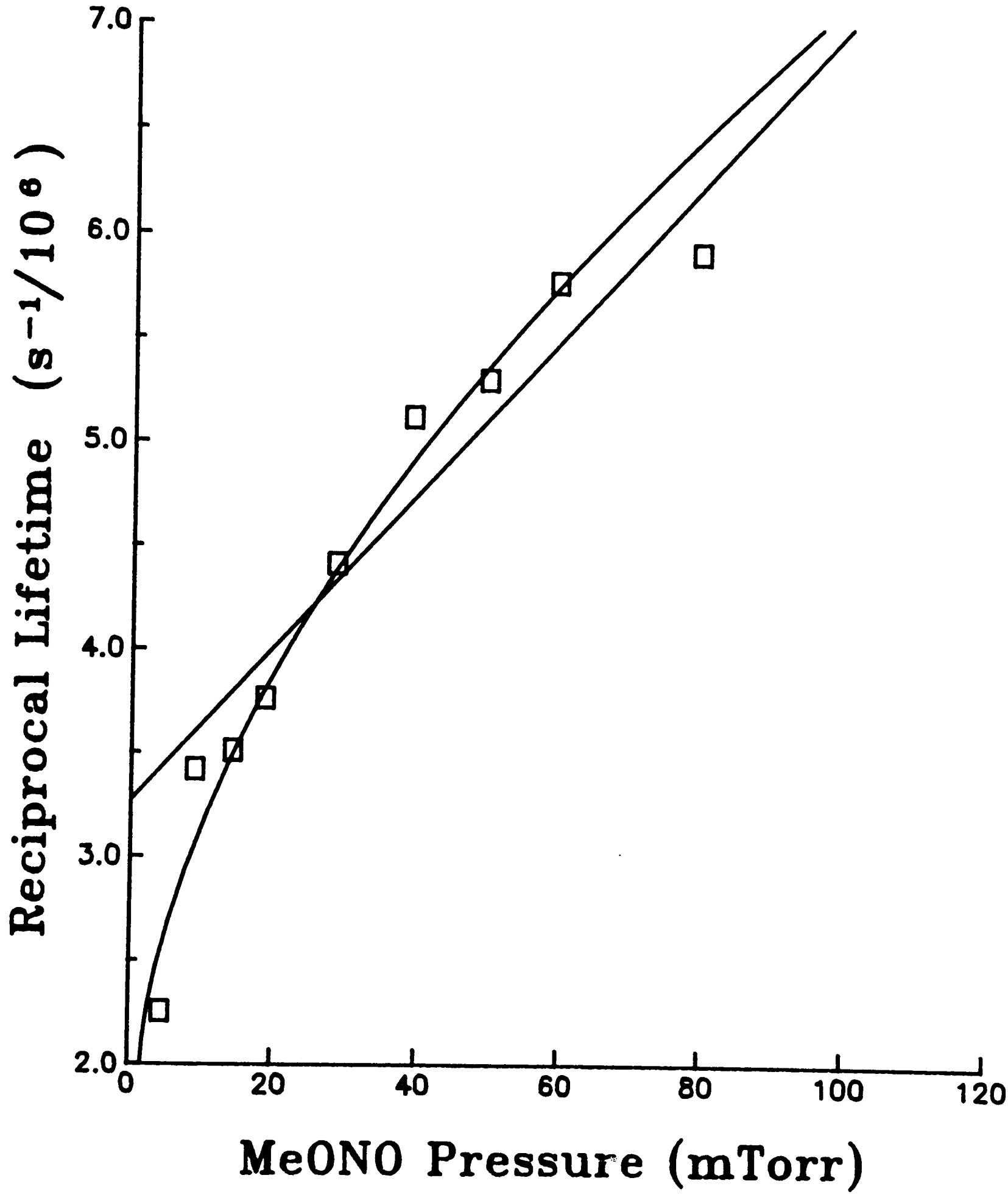

Figure 4.5. Reciprocal radiative lifetime of direct emission following 355nm irradiation of CH_3ONO vs. total pressure.

$$CH_3O + NO \rightarrow CH_2O + HNO \qquad (4.6)$$

Reaction 4.6 has insufficient energy associated with it to produce the $\tilde{A}^1A_2$ state of formaldehyde and hence further photon absorption must occur to give rise to the observed emission. However, the peaks observed to the blue of the dissociation wavelength can only be explained by the excitation of vibrationally hot formaldehyde which would have to occur within the same laser pulse as the dissociation step (bands to the red of the excitation wavelength could be due to formaldehyde produced from previous photolysis pulses and vibrationally equilibrated at 300K). The former case would result in a non-linear dependance on the excitation laser intensity whilst the latter would not. At a pressure of 25mTorr of CH_3ONO the intensity dependance (exponent) was 1.2 at an observation wavelength 355nm and 1.6 at 425nm. Thus it appears that an unknown fraction of CH_3ONO photolysis at 355nm leads directly to CH_2O production in contrast to the results of [129] but in agreement with the original suggestions of [126].

The anomalous intensity of the resonance excitation at 355nm can not be explained on the basis of the known Franck-Condon factors for formaldehyde [140]. It is possible that the emission is due to several vibrational bands of a transition which has very strong diagonal terms in the Franck-Condon factors but no suitable candidate can be proposed. Alternatively Rayleigh scattering or aerosol formation could explain the effect but neither of these possibilities were investigated.

CH_3O was not considered as a candidate for the source of the

emission since the spectral characteristics of the observed emission were incompatible with those reported for CH_3O [121] and the radiative lifetime is 1.5μs, again in contrast to that determined here. As the determination of the vibrational and rotational distribution in $NO(X^2\Pi_i)$ arising as a result of 355nm photodissociation of methyl nitrite was the main aim of this work the study of the emission from formaldehyde was not pursued any further.

4.2.3 Quantum State Distributions Laser Induced Fluorescence spectra were recorded at a pressure of 40mTorr of methyl nitrite using the computer data acquisition system which corrected for variations in probe laser intensity. Typically 10 laser shots were recorded at each point in the spectrum. Approximately 20mJpulse^{-1} of unfocussed 355nm radiation was used to dissociate the methyl nitrite and, as this was not found to vary during the course of an experiment, no correction was necessary for variation in dissociation energy. A slow, steady flow of methyl nitrite was established prior to each experiment and, for determination of the rotational distribution arising in $NO(X^2\Pi_i$ v"=0), the background NO concentration, which was not completely removed by the pumping system between laser pulses, was allowed to stabilise by dissociating the methyl nitrite for 10-15 minutes before commencing a LIF spectrum. It was possible to record an extensive spectrum from v"=1 of $NO(X^2\Pi_i)$ but, due to computer memory restrictions, this had to be recorded in overlapping sections of 1000 data points. In other cases however, wavelength restrictions of the laser system prevented the full LIF spectra from being recorded.

4.2.3.1 v"=0 Fig 4.6 shows a portion of the LIF spectrum arising from $NO(X^2\Pi_i$ v"=0). Comparison with a LIF spectrum of pure NO in the same region showed that some, but by no means all, of the lines were due to NO produced by previous dissociation pulses and not subsequently removed from the reaction cell. However, many of the features are due to direct photodissociation products only. In an attempt to remove the background signal the pumping speed was increased greatly but the problem was not completely alleviated.

4.2.3.2 v"=1 Part of the LIF spectrum arising from $NO(X^2\Pi_i$ v"=1) is presented in Fig. 4.7. It was possible to record an extensive region of this spectrum covering the range 232.19-235.6nm. The entire recorded spectrum includes lines from levels with $J" \leq 49.5$ indicating that the distribution is considerably hotter than a 300K thermal distribution within this vibrational level.

4.2.3.3 v"=2 The LIF spectrum arising in $NO(X^2\Pi_i$ v"=2) is shown in Fig. 4.8 and compared to a simulation of a 300K sample of $NO(X^2\Pi_i)$ within this vibrational level. It is clear that the experimental distribution is different from the thermal one. Unfortunately the tuning range of the laser system did not allow the higher rotational levels of this band to be investigated.

4.2.3.4 v"=3 Finally, a section of the LIF spectrum from $NO(X^2\Pi_i$ v"=3) is shown in Fig. 4.9.

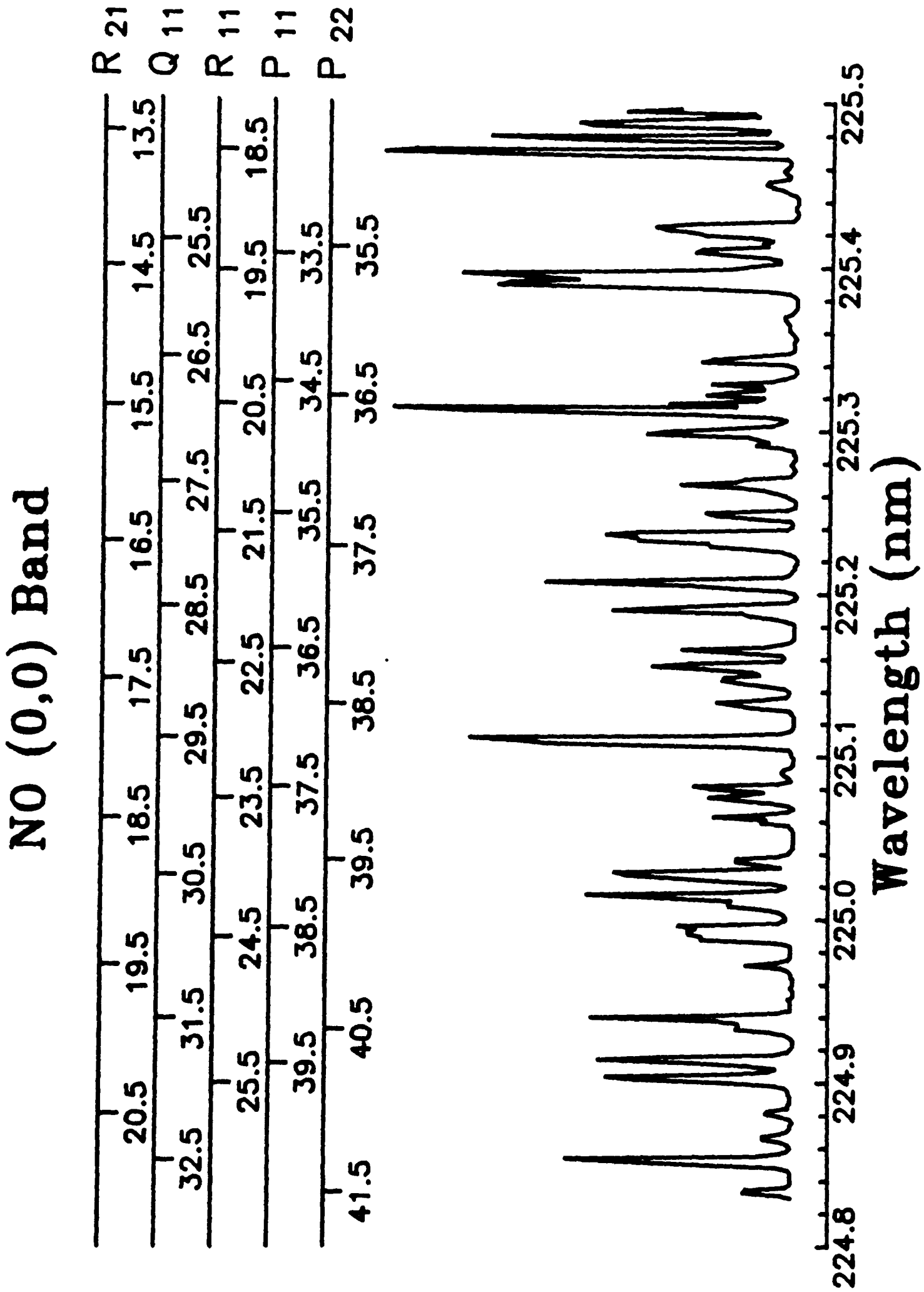

Figure 4.6. Part of the LIF spectrum of NO($X^2\Pi_i$ v"=0).

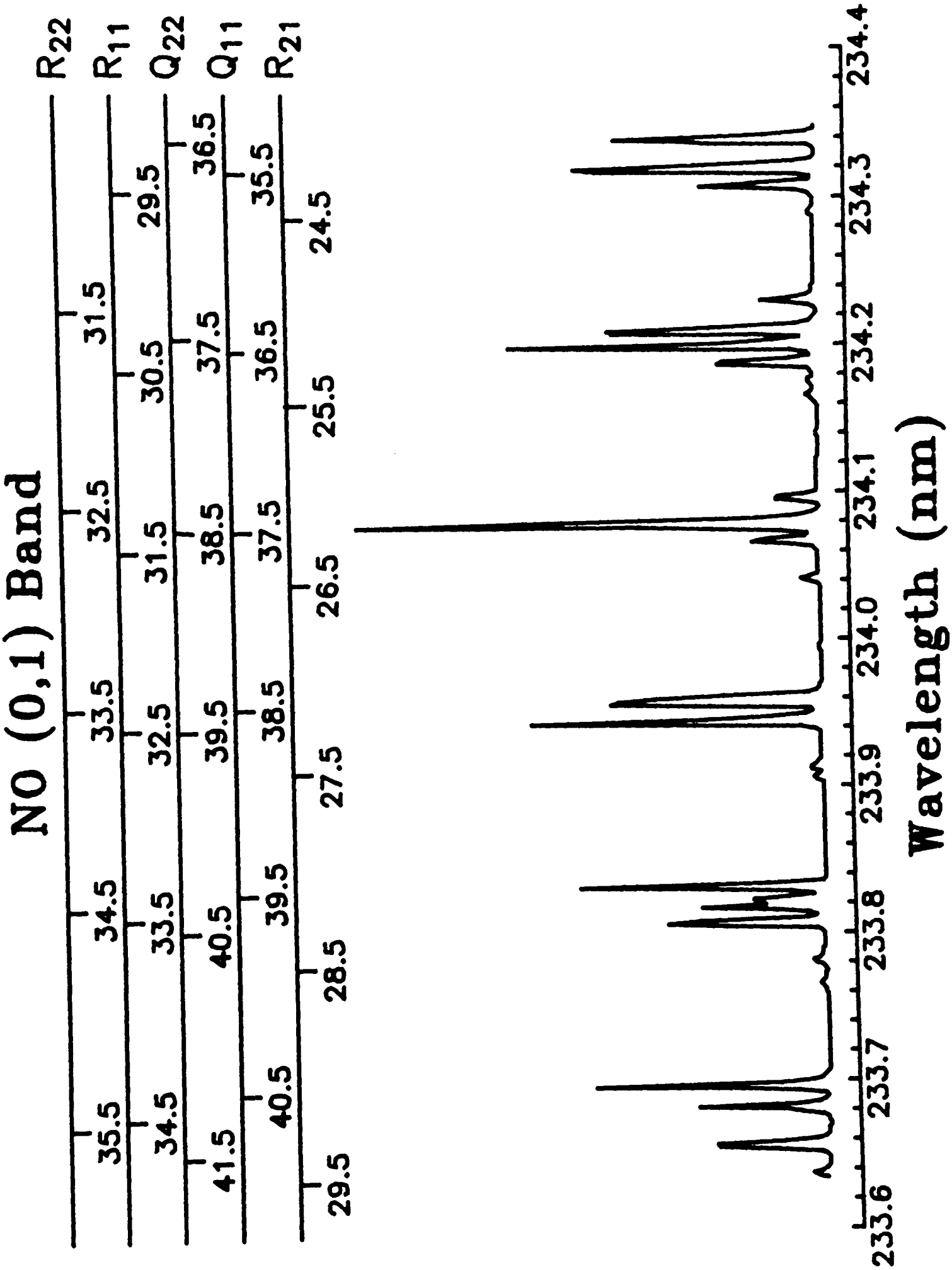

Figure 4.7. Part of the LIF spectrum arising from NO($X^2\Pi_i$ v"=1).

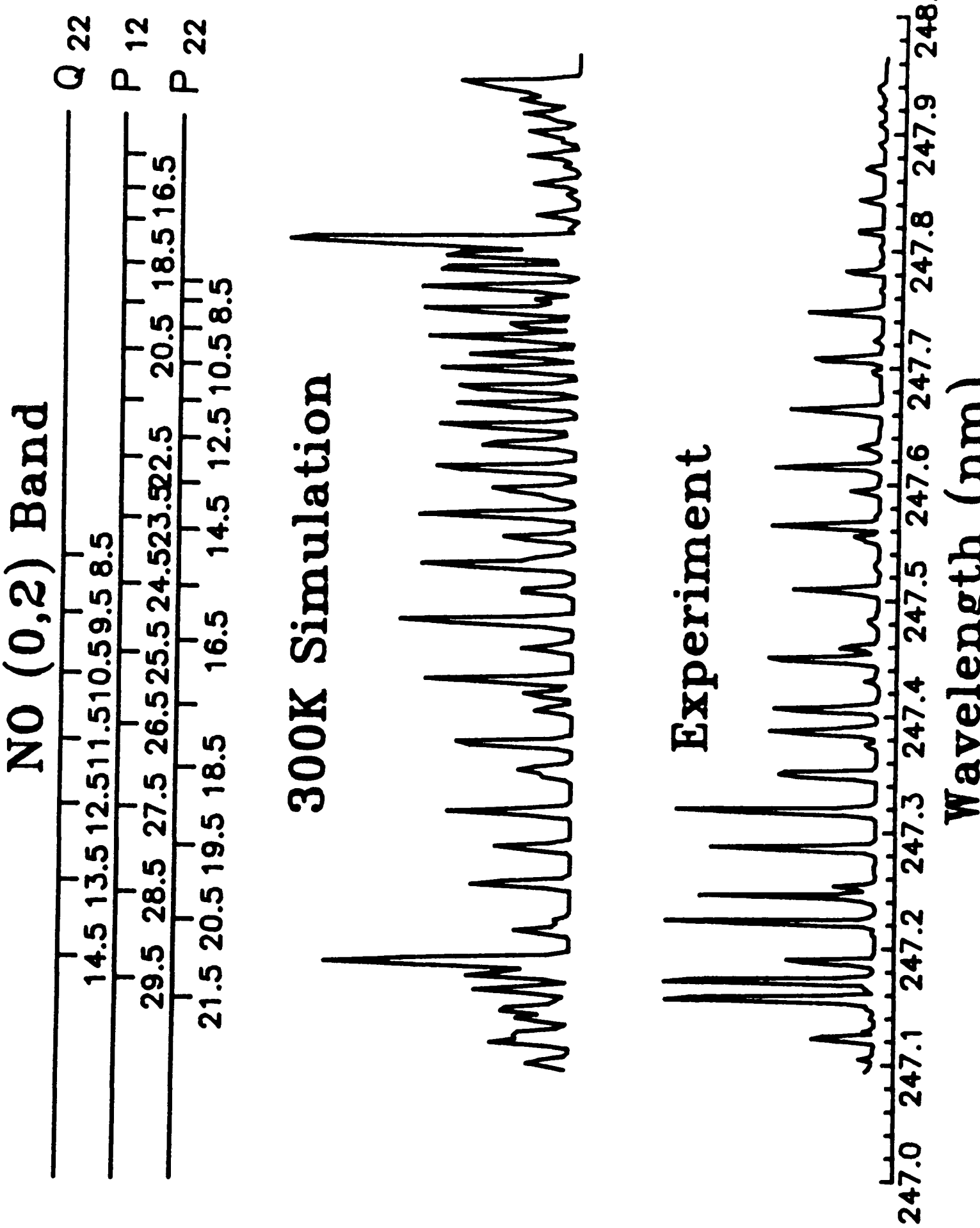

Figure 4.8. LIF spectrum arising from NO($X^2\Pi_i$, v"=2) compared with a simulation of the same region using a 300K rotational temperature.

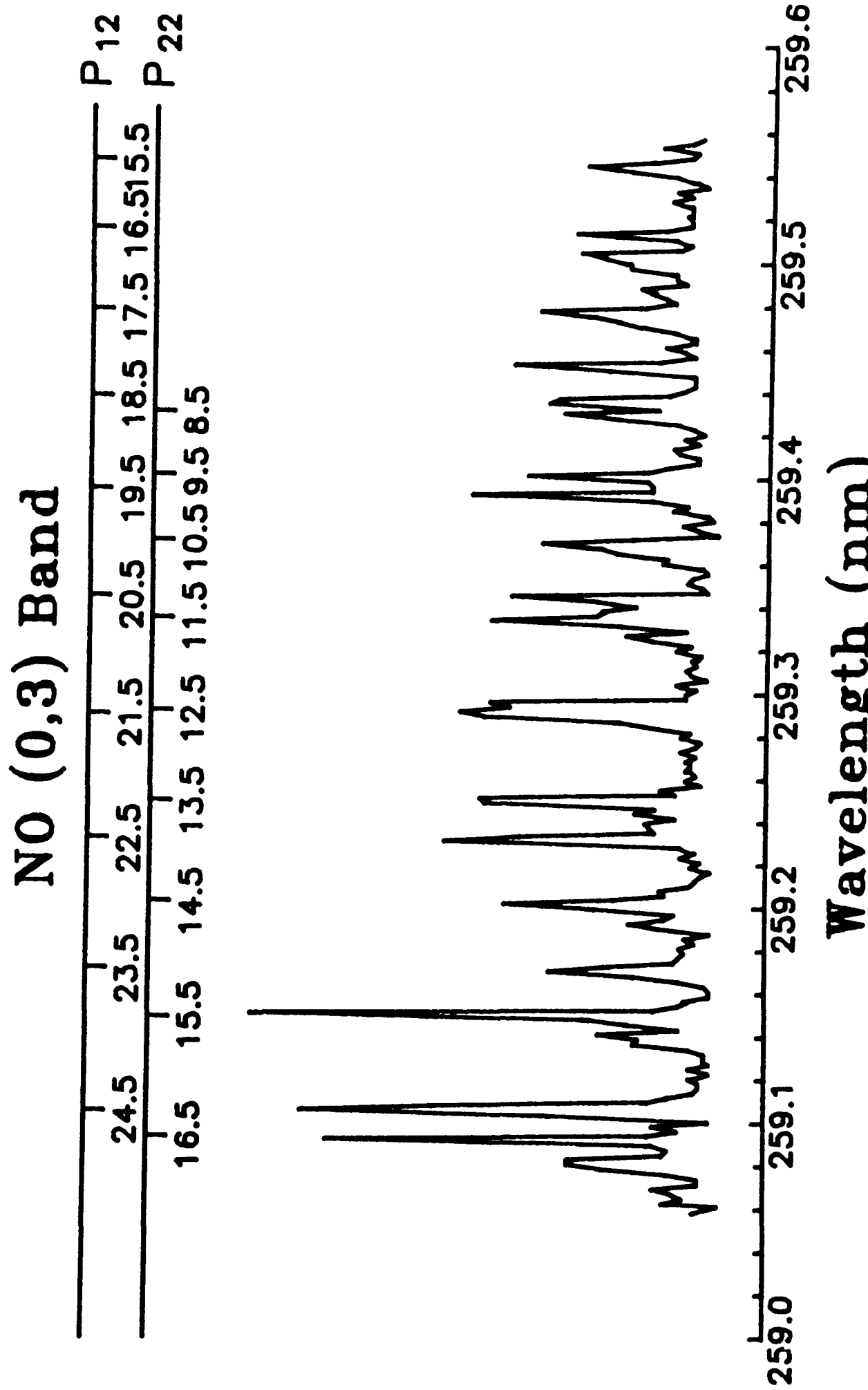

Figure 4.9. LIF spectrum resulting from NO($X^2\Pi$, v"=3). The noise reflects the lower signal levels available.

4.2.4 Spectral Assignment It was found to be impossible to assign the LIF spectra described above on the basis of formulae (given in Appendix 2) for the energy levels given by Mallard et al [141] and the best available molecular constants from the literature [96]. This was particularly noticeable in the NO($A^2\Sigma^+ \leftarrow X^2\Pi_i$) (0,1) band where the effects of centrifugal distortion will be most apparent in the high rotational levels observed. To overcome this difficulty improved molecular constants were obtained by an examination of accurate experimental determinations of the ground electronic, $X^2\Pi_i$, state energy levels of Amiot et al [142] and NO(A-X) band line positions of Englemann et al [143] The procedure used was as follows. The formulae for the $X^2\Pi_i$ state term values of Mallard et al [141] were used in a non-linear least squares fitting method developed on the laboratory microcomputer and taken from Bevington [144]. The values of the rotational constants B and D and the vibrational origin G_v were allowed to vary to give the best fit to the $X^2\Pi_i$ state term values given by Amiot et al [142] for v"=0-2. The improved calculated $X^2\Pi_i$ state term values were then combined with the formulae for the $A^2\Sigma^+$ state term values and improved molecular constants for the $A^2\Sigma^+$ state were obtained by varying the rotational constants B and D and the electronic origin term T_e and fitting the resulting line positions to the experimentally determined line positions of the ($A^2\Sigma^+$ v"=0 - $X^2\Pi_i$ v"=0) band given by Englemann et al [143]. The results of this minimisation procedure are given in Tables 4.3 and 4.4.

NO($X^2\Pi_i$) Molecular Constants

$X^2\Pi_i$		B/cm^{-1}	10^6D/cm^{-1}	G_v/cm^{-1}
v"=0	F_1	1.69588	5.44	1.69×10^{-2}
	F_2	1.69595	5.83	5.79×10^{-3}
v"=1	F_1	1.67827	5.43	1876.013
	F_2	1.67834	5.82	1875.971
v"=2	F_1	1.66072	5.48	3723.895
	F_2	1.66076	5.86	3723.837
v"=3	F_1	1.64323	5.59	5543.663
	F_2	1.64321	5.95	5543.604

Table 4.3.

NO($A^2\Sigma^+$) Molecular Constants

$A^2\Sigma^+$		B/cm^{-1}	10^6D/cm^{-1}	T_e/cm^{-1}
v'=0	F_1	1.98617	5.45	44139.09
	F_2	1.98623	5.56	44139.09

Table 4.4.

When the improved molecular constants were used in the formulae for the $X^2\Pi_i$ and $A^2\Sigma^+$ state term values (given in Appendix 2) a very good fit to the experimentally determined lines was given allowing the spectra to be assigned easily.

Rotational distributions within the four observed vibrational levels were them obtained by plotting the natural logarithm of the line intensity divided by the line strength, as determined using formulae in Appendix 2, against the energy of the rotational levels in the $X^2\Pi_i$

state. The results of this for the $NO(X^2\Pi_i$ v"=0) rotational distribution is shown in Fig. 4.10. As can be seen the distribution falls into two parts. At an energy less than $1500cm^{-1}$ a linear dependance is observed. A linear least squares fit to this portion of the data yields a rotational "temperature" of 310±15K. It is clear that the data in this region corresponds to a thermal sample of $NO(X^2\Pi_i$ v"=0). The remainder of the distribution does not correspond to a thermal temperature and thus represents the nascent rotational distribution arising from the photodissociation.

Figs. 4.11a and 4.11b show the results for the rotational distribution within the $X^2\Pi_i$ v"=1 state, again plotted in such a way that a straight line of negative slope would indicate a Boltzmann distribution. The distribution peaks at ~$2000cm^{-1}$ (Fig. 4.11b), similar to that for v"=0, but the more complete set of data available for v"=1 shows additional information. On Fig. 4.11a the data appears to fall into two distinct groups, with Q_{11} and Q_{22} lines enhanced over R_{11} and R_{22} lines by a factor of approximately 2, and this is repeated (although clearly there is less overlap) in Fig. 4.11b. Furthermore, lines from the R_{21} branch (J=29.5-38.5) appear on Fig. 4.11a, and they appear also to be enhanced, lying above the corresponding R_{11} and R_{22} lines with the same value of J. This effect will be discussed in the next section. It was not possible to obtain information on levels ≤$1000cm^{-1}$ due to laser limitations.

The partial rotational distribution deduced for $NO(X^2\Pi_i$ v"=2) is presented in Fig. 4.12. Again, due to limitations in the wavelength

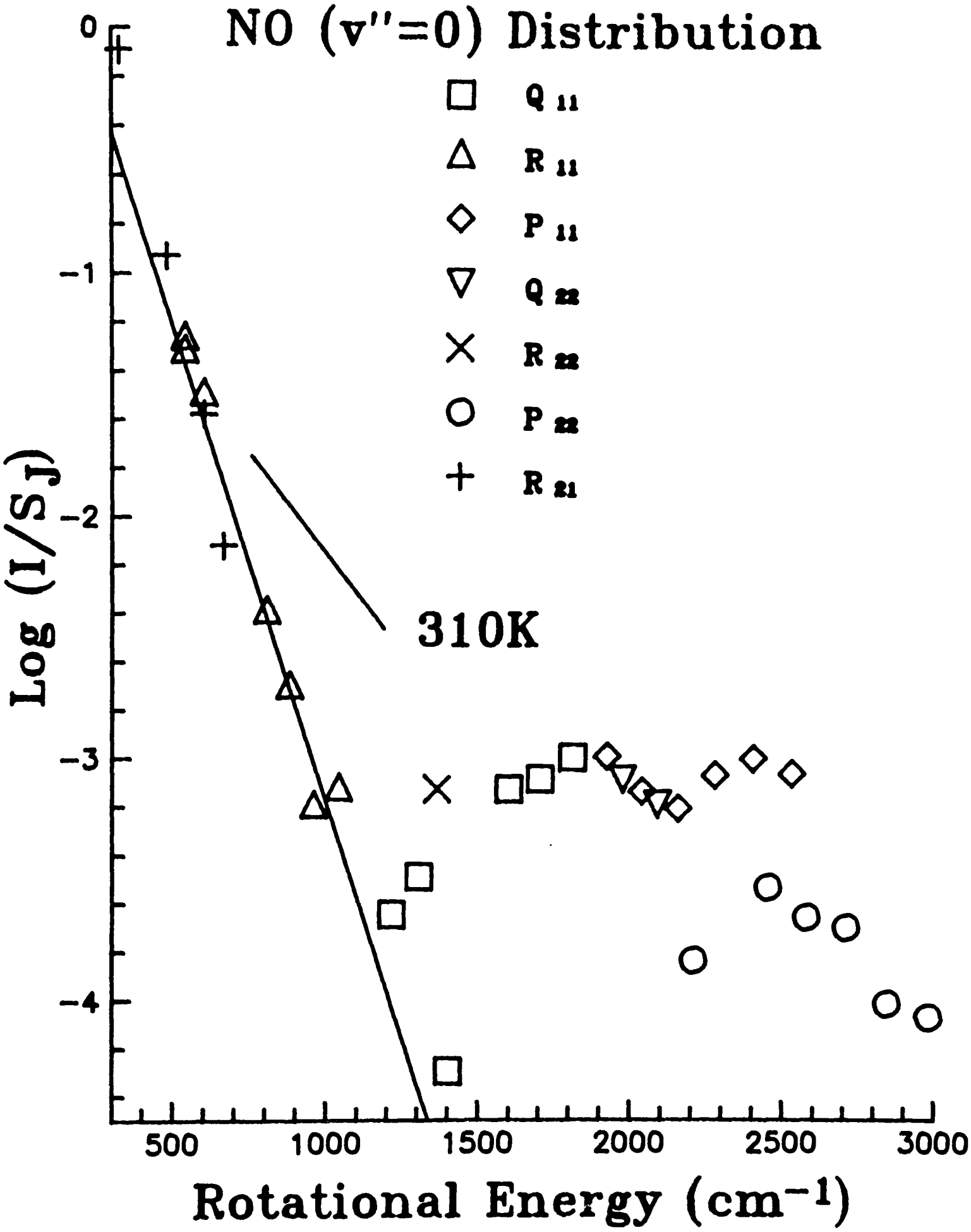

Figure 4.10. Rotational distribution resulting in NO($X^2\Pi_i$ v"=0). Each spectroscopic band is separately identified. The low energy region fits a room temperature rotational distribution closely.

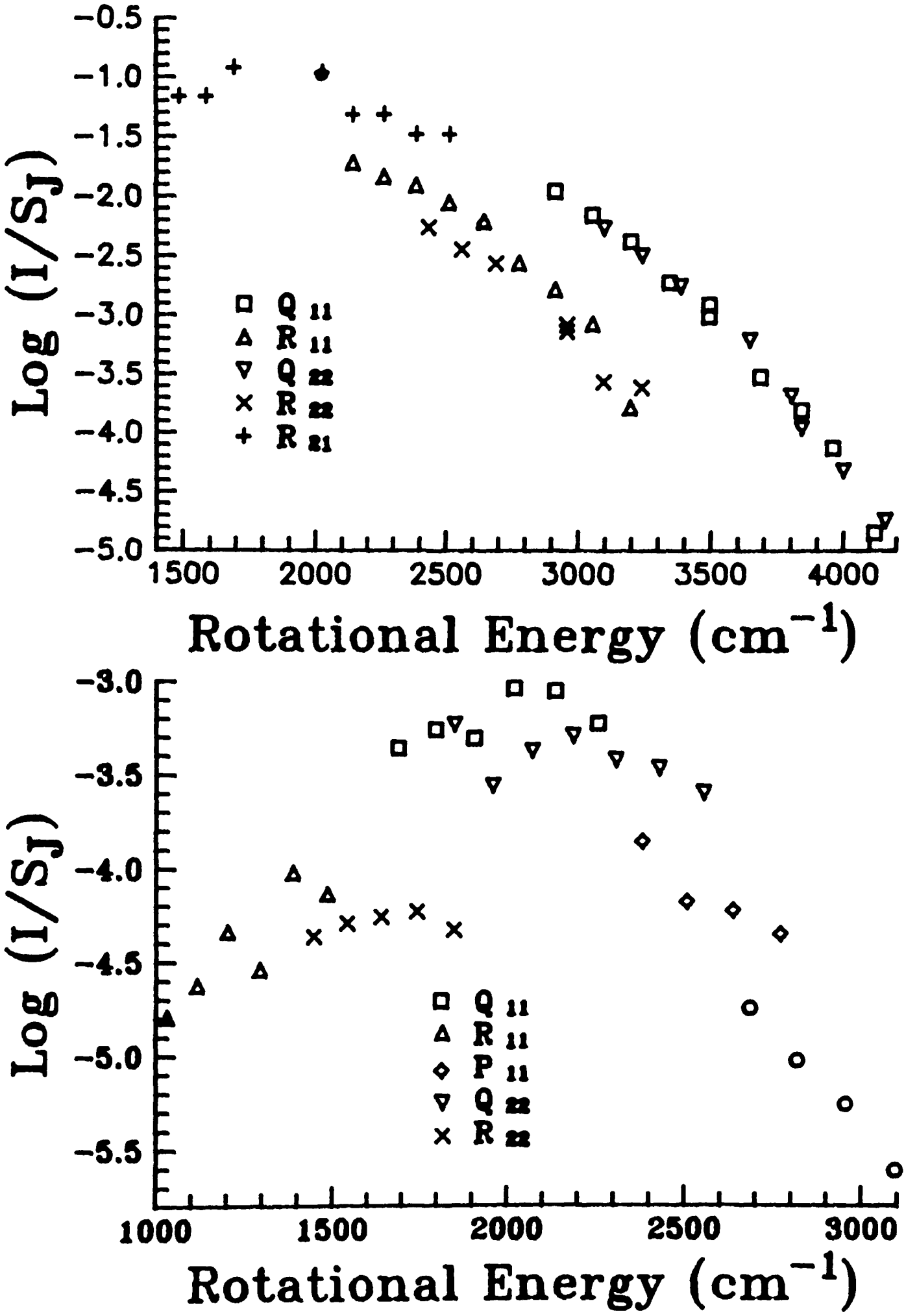

Figure 4.11. Rotational distribution in NO($X^2\Pi_i$, v"=1). Top (a) shows region 1500-4000cm^{-1}. Bottom (b) shows 1000-3000cm^{-1} recorded on a different LIF spectrum. All observed band are identified.

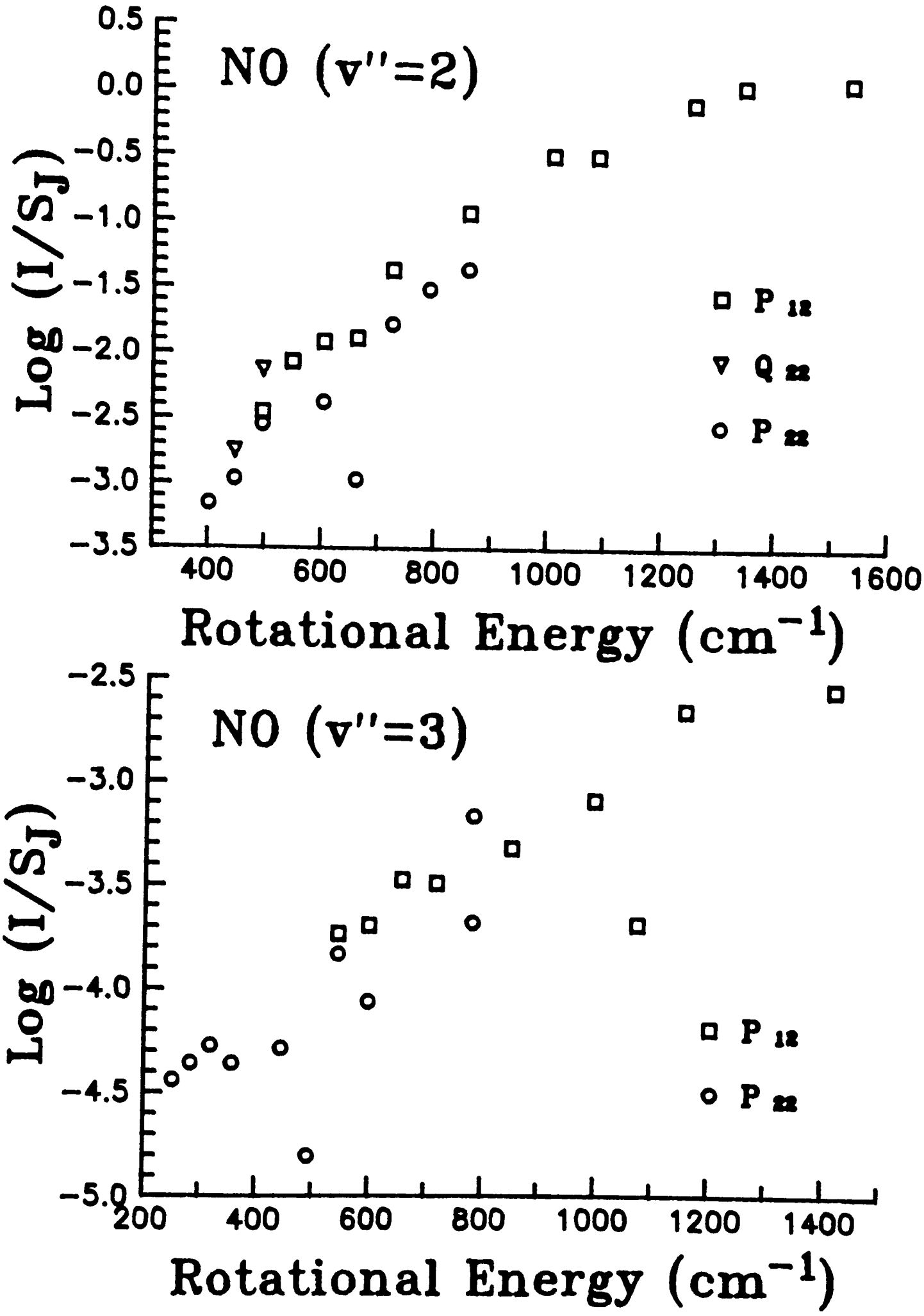

Top: Figure 4.12. Rotational distribution within NO($X^2\Pi_i$ v"=2).
Bottom: Figure 4.13. Rotational distribution resulting in NO($X^2\Pi_i$ v"=3)
In both figures the contributing bands are identified.

available from the laser, only a small part of the distribution can be shown but it provides complimentary information to the v"=1 data, which shows the high rotational energy part of the distribution, whilst the v"=2 data shows the distribution resulting at low rotational energy. No effects similar to those described above for v"=1 are apparent in this data. However, only P branches are represented on the graph.

A similar part of the rotational distribution is observed for $NO(X^2\Pi_i$ v"=3) and this is presented in Fig. 4.13. Again only P branch lines contribute to the observed distribution.

4.2.5 Anisotropy Information from LIF

4.2.5.1 Molecular Alignment As described in Chapter 3, the interaction of a polarised light beam with a molecule will give rise to fragments which are aligned with respect to both the molecular framework, determined by the dissociation dynamics, and to the laboratory, due to the aligned electric vector of the light. If the fragments are produced in an electronically excited state, then their fluorescence polarisation allows the anisotropy of the absorption and dissociation steps to be examined. If the fragments are formed in their ground electronic state then such information can be determined, in principle, by LIF. Although the formalism for such an analysis has existed for some years [145] [146] it has only recently been made more accessible to experimental workers by the work of Greene and Zare [4] [147]. Before the application of their results to the present data, we consider the following simple example applied to the dissociation dynamics of CH_3ONO.

We consider the C-O-NO framework to be planar, from IR spectroscopic evidence [148] [130], and the transition dipole moment μ_p must therefore lie either in or perpendicular to the molecular plane. LIF measurements of the anisotropy in the OH fragment arising from the photodissociation of HONO shows that μ_p lies perpendicular to its molecular framework [120]. Let us assume that the same applies to methyl nitrite. If dissociation takes place in this plane then, in the limit of high J, this will also be the plane of rotation of NO fragments, ie J will be parallel to μ_p. The experimental geometry used in the experiment is illustrated in Fig. 2.5. From this it can be seen that the 355nm beam causes alignment of J for NO to be along the electric vector of the 355nm beam and parallel to the probe beam. In the high J limit, the transition dipole moment for the (A-X) transition in NO, μ_f, will lie along J for Q band excitation and parallel to J for P and R branches [146]. Given the experimental geometry and the assumption about μ_p we would thus expect Q branches to be weak compared to P and R branches in the resulting LIF spectrum.

Quantitatively the enhancement, or otherwise, of P and R branches over Q branches may be evaluated from the work of Greene and Zare [147]. Assuming an isotropic distribution of parent molecules, taking the high J limit in all cases (an assumption justified by the experimentally observed levels: $J \geq 20.5$) and ignoring the effects of hyperfine structure, we consider two limiting cases of the alignment parameter, A_0^2. Firstly the case considered above where μ_p is parallel to J ($A_0^2=4/5$) and the alternative example where μ_p is perpendicular to J

(A_0^2=-2/5). The results are shown in Table 4.5 [149] and show, as expected, the weak Q branch compared with P and R branches for the example described above and for the other case approximately equal contributions, a consequence of the experimental geometry employed.

	(A_0^2=-2/5)	(A_0^2=4/5)
Transition	J Perpendicular μ_p	J Parallel μ_p
P,R Branch	1.52	2.15
Q Branch	1.87	1.00

Table 4.5.

Table 4.5 shows the ratio of intensities of P and R branch to Q branch excitation to range from approximately 2 to 1, depending on the direction of μ_p, and favouring a higher value if CH_3ONO behaves similarly to HONO [120]. In general the alignment factors will lie between the extremes quoted. The results shown in Fig. 4.11, where the Q branch is enhanced over the P and R branches can not be a consequence of such alignment.

4.2.5.2 Electronic Alignment The previous section has considered nuclear anisotropy in the molecular frame. The orbital angular momentum in the NO fragment, due to the unpaired electron, may give rise to electron anisotropy which can be examined via measurements of the Λ doublet ratios. Each rotational level, J, in NO($X^2\Pi_i$) is split into two components, designated Π^+ and Π^-, due to the lifting of the degeneracy by coupling of nuclear rotation and orbital angular momentum [150] (NO spectroscopy is described in Appendix 2). The Π^+ and Π^- refer to the

symmetry of the electronic wavefunction with respect to reflection in the plane containing the internuclear axis, and perpendicular to the total angular momentum, J. In the limit of high J Π^+ refers to the Π lobes being in the plane of the NO rotation (and therefore perpendicular to J) and Π^- refers to the Π lobes being perpendicular to the plane of rotation (and parallel to J). The parity of the levels are $(-1)^N$ for Π^+ and $(-1)^{N+1}$ for Π^- where N refers to the total angular momentum, excluding electron spin [120] [150]. The NO($A^2\Sigma^+$) state levels have parity $(-1)^N$ and so applying the selection rule + $\leftrightarrow$ - we see that transitions with $\Delta N=0$ will connect Π^- levels and those with $\Delta N=\pm 1$ connect Π^+ levels. As a consequence the following branches in the spectrum connect Π^- levels: $Q_{11}+P_{12}$, R_{21}, $Q_{22}+R_{12}$ and P_{12} whilst for the Π^+ we have: $R_{11}+Q_{21}$, P_{11}, $P_{22}+Q_{12}$ and R_{22}. It is now apparent that the distribution shown in Fig. 4.11a arises due to unequal population of the Λ doublet levels in NO($X^2\Pi_i$) with the Π^- component, the $Q_{11}+P_{12}$ and $Q_{22}+R_{12}$ branches, enhanced over the Π^+ component, the $R_{11}+Q_{21}$ and R_{22} branches. This trend is also seen in Fig. 4.11b, although the data is more scattered. For other vibrational levels the distinction between Π^+ and Π^- is less clear, although in Fig. 4.12 P_{12} lines appear stronger than $P_{22}+Q_{12}$, again indicating Π^- enhancement. The same trend is marginally visible for the v"=3 data of Fig. 4.13.

We conclude from this section that the observed enhancements of specific branches in the LIF spectra are due to Λ doublet effects with the Π^- levels enhanced over the Π^+ levels, implying that the half filled orbital has its lobe perpendicular to the plane of the NO fragment

rotation. The enhancement is by a factor of approximately 2 in the high J limit, and this must be seen as a lower limit since the effects of nuclear alignment, discussed above, tend to decrease the observed value. The experimental geometry employed did not allow the separation of these two effects and coaxial geometry, as used by Dixon et al [120] in which the relative polarisations could have been varied should, in hindsight, have been used.

4.3 SURPRISAL ANALYSIS OF ROTATIONAL DISTRIBUTIONS

The experimental determination of the rotational distributions resulting in v"=0-3 of $NO(X^2\Pi_i)$ yielded only partial distributions for each of the vibrational levels studied due to the wavelength restrictions of the laser system. In the absence of a complete rotational distribution it is not possible to determine the vibrational product distribution by the comparison of single rotational lines within the different vibrational levels. One method of surmounting this problem is the use of an inert buffer gas in the dissociation chamber. The correct choice of buffer gas pressure will cause complete rotational relaxation resulting in a 300K thermal distribution allowing the vibrational product distribution to be calculated by measuring the intensity of rotational lines within each vibrational level and correcting the results using the relevant line strengths, Franck-Condon factors etc. This approach has been used by Lahmani et al on the 355nm photodissociation of methyl nitrite [133]. A problem associated with this method is that vibrational relaxation may also occur, thus distorting the observed distribution. Clearly the correct choice of

buffer gas pressure is vital to the success of this method and a knowledge of both the rotational and vibrational relaxation rates of the molecule under study by the buffer gas should, ideally, be known. An alternative procedure, followed here, is to deduce. from the experimental distribution and statistical calculations, a best estimate of the full rotational distribution. This technique, developed by Levine and Bernstein using concepts from information theory, is known as surprisal analysis [46]. The first stage of such an analysis is the construction of a "prior" rotational distribution. The prior distribution arises from a statistical calculation based on the principle that all product states which are energetically allowed are equally probable and, hence, the probability of a particular outcome of a molecular event (photodissociation scattering etc.) depends on the total number of ways of realising this outcome. An equivalent description is that the prior distribution is the most entropic.

In the case of methyl nitrite the fragments are NO, having vibrational levels V_{NO} and rotational levels J_{NO}, and the methoxy radical, with vibrational levels V_{MeO} and rotational levels J_{MeO}, K_{MeO} (assuming symmetric top geometry). The probability of formation of a single ro-vibrational level in NO is proportional to the rotational degeneracies of NO and CH_3O and to the translational density of states, which can be expressed as the square root of the translational energy:

$$P(V_{NO},J_{NO}) \propto (2J_{NO}+1)(2J_{MeO}+1)^2 E_r^{\frac{1}{2}} \qquad (4.7)$$

The amount of translational energy depends on the product states of both

fragments. Given a total energy, E_{avail}, to be partitioned amongst the fragments, conservation of energy gives:

$$E_T = E_{avail} - E_{V_{NO}} - E_{J_{NO}} - E_{V_{MeO}} - E_{J,K_{MeO}} \qquad (4.8)$$

The probability of formation of a single level in NO depends on the total number of ways in which the residual available energy can be partitioned in the methoxy radical and the translational density of states, which accounts for energy not found internally in the fragments.

Simple expressions for $E_{J_{NO}}$:

$$E_{J_{NO}} = BJ(J+1) \qquad (4.9)$$

and similarly for $E_{J_{MeO}}$:

$$E_{J_{MeO}} = BJ(J+1) + (A-B)K^2 \qquad K=0,\pm1\ldots\pm J \qquad (4.10)$$

are substituted into the equation for the translational energy.

Most approaches of this nature integrate over the vibrational density of states to obtain the vibrational energy terms. The harmonic oscillator model [43], which underestimates the number of vibrational levels due to the neglect of anharmonic terms, gives:

$$N_v(E_v) = E_v^{S-1}/[(s-1)\Pi h\nu] \quad : S \equiv \text{No. Vibr. Freq.} \qquad (4.11)$$

whereas the Marcus-Rice approximation [43]:

$$N_v(E_v) = (E_v+E_z)^{S-1}/[(S-1)!\ \Pi h\nu] \quad : E_z \equiv \text{Zero Point Energy} \qquad (4.12)$$

overestimates N_v. Further approximations are then made to allow

analytic integration of the expression for the probability. To avoid these approximations the probability of formation of a particular state can be calculated numerically.

The surprisal, I_{vj}, represents the difference between the experimentally determined product distribution and the prior expectation distribution and is defined as:

$$I(v,j) = -\ln[P_{vj}/P^{0}_{vj}] \qquad (4.13)$$

where P_{vj} is the experimental distribution and P^{0}_{vj} the prior distribution. The surprisal shows how the actual distribution differs from one which would be expected on statistical grounds: in effect how "surprising" the distribution is!

It has been found in many cases that the surprisal , expressed as a function of v and j, when plotted against the fractional available energy, E_{vj}/E_{avail}, gives rise to a linear relationship: a so-called linear surprisal [7]. This has been interpreted as being due to the participation of a single dissociative potential surface in the photofragmentation process. In this case such an explanation is not invoked but the surprisal analysis of the experimental data is used to reconstruct, via an inversion of the surprisal, the full rotational distribution and hence give an estimate of the parts of the distribution not determined experimentally. This, in turn, allows an estimation of the vibrational product distribution from the incomplete, but entirely unrelaxed, rotational data.

4.3.1 Calculation of the Rotational Prior Distribution All three methods of calculating the rotational prior distribution discussed above were used, namely the Harmonic Oscillator Approximation (HO), the Marcus-Rice Approximation (MR) and a direct state count. The derivation of the expressions used are given in Appendix 4.

The HO method gives [151]:

$$P_{vj} \propto (2j+1)(E_{avail}-E_v-E_j)^{11} \qquad (4.14)$$

where v and j refer to the NO fragment while the MR treatment yields:

$$P_{vj} \propto (2j+1)[(E' + E_z)^{11} - E_x^9(55E'^2 + 11E'E_z + E_z^2)] \qquad (4.15)$$

where $E'=E_{avail}-E_v-E_r$, the residual energy, and E_z is the zero point energy of the CH_3O fragment; v and j having the same meaning as above. For the direct state count the fundamental vibrational frequencies of the CH_3O radical were taken from the literature [132] and the vibrational levels calculated. This gave very good agreement for both the number of states and the vibrational state density with a Whitten-Rabinovitch calculation [152] which was also performed. The rotational constants were taken from the literature [153] and a symmetric top assumed.

The results of these calculations for $NO(X^2\Pi_i\ v"=0)$ are presented in Fig. 4.14 which shows the prior distribution, calculated by each of the methods described above. The direct state count lies between the HO and MR approximations as expected. In this case there is a close agreement with the MR method but this will depend on the molecular

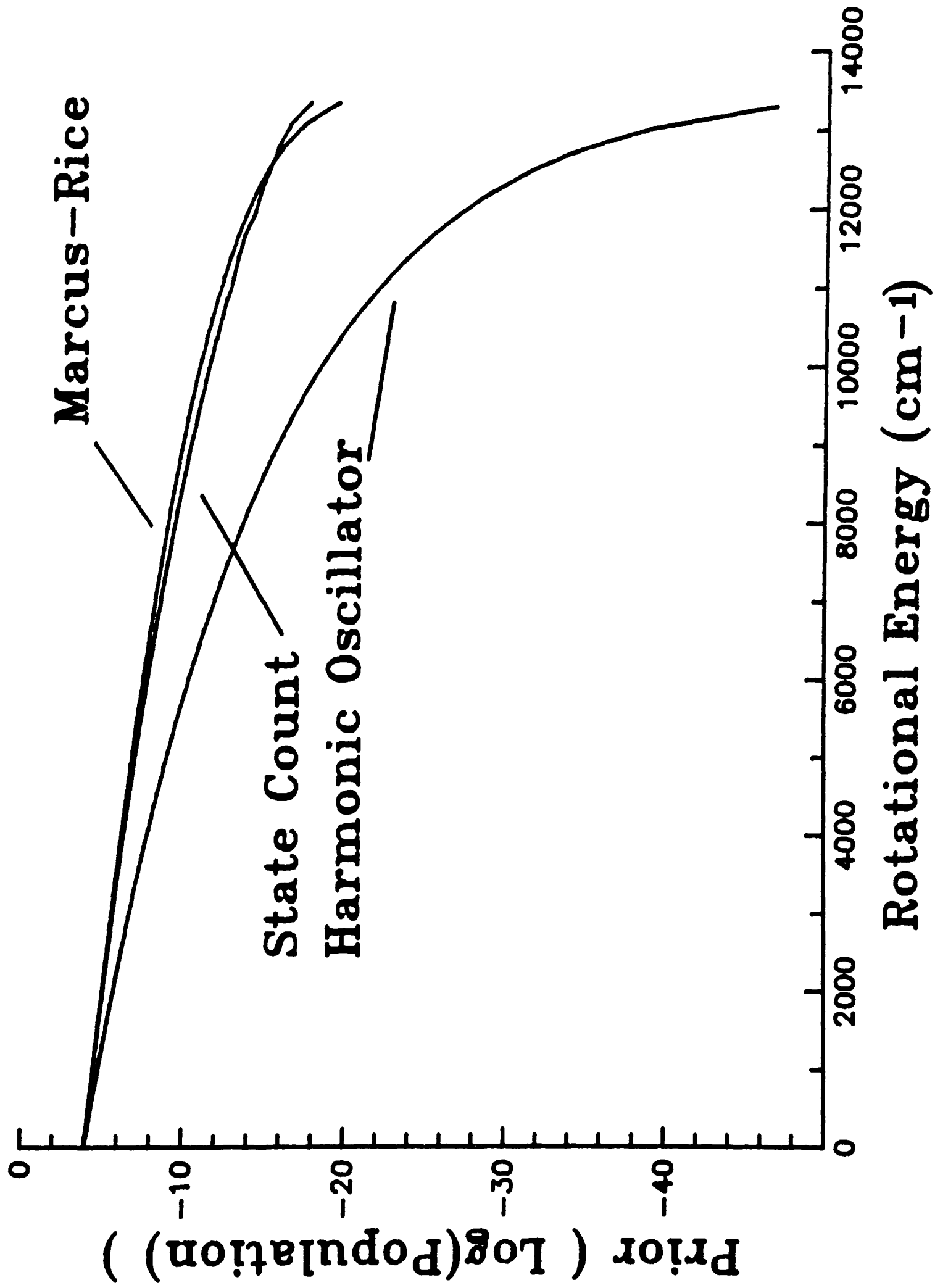

Figure 4.14. Prior rotational distribution for NO($X^2\Pi_i$, v"=0) calculated by the harmonic oscillator method, Marcus-Rice method and a direct state count. The state count corresponds closely to the MR method.

constants for a specific system.

Surprisal analysis of the experimental data for the rotational distributions arising in v"=0-3 of $NO(X^2\Pi_i)$ is presented in Figs. 4.15 to 4.18. For v"=1, the data is separated into two sections, reflecting the enhancement of spectral lines connecting Π^- levels over Π^+ levels, as described earlier. Two regions of approximately linear behaviour are apparent: a negative surprisal up to fractional energy, f_R, $\simeq 0.18$, corresponding to a rotational population inversion, and a positive surprisal at higher values of f_R. Data for v"=2 and 3, in which only low J levels could be probed, shows only the negative region of the surprisal, with a similar slope in each case. The results of the surprisal analysis are presented in Table 4.5.

v"	$I(f_R<0.18)$	$I(f_R>0.18)$
0	-19	-
1	-17	18
2	-17	-
3	-20	

Table 4.5.

The contamination of the v"=0 data by NO with a thermal rotational distribution makes analysis difficult, but selected levels between f_R=0.09 and 0.2 seem to indicate both negative and positive slopes.

In order to extract the vibrational distribution it was assumed that all the rotational distribution fitted the same surprisal, that

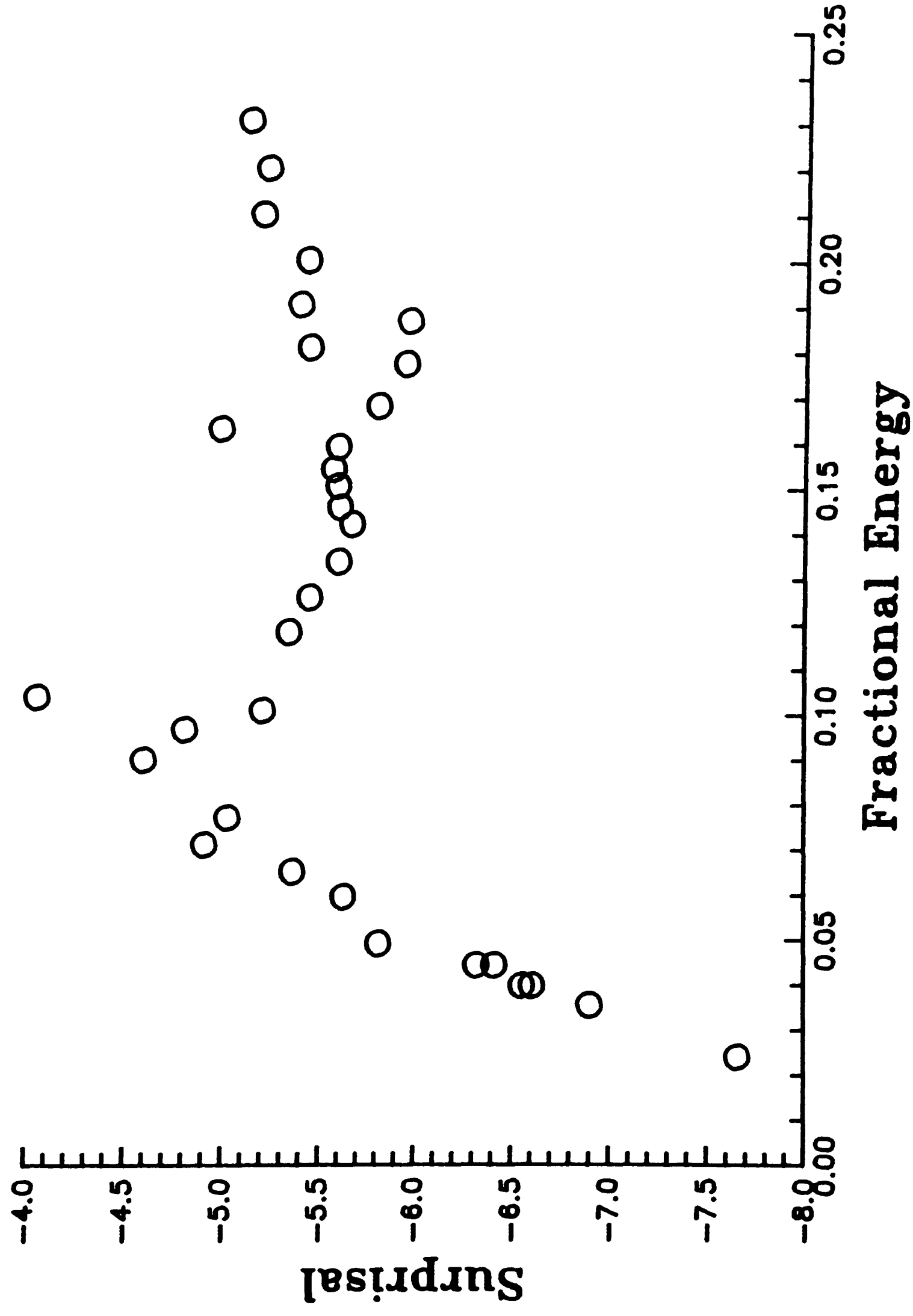

Figure 4.15. Surprisal plot for NO($X^2\Pi_i$ v"=0). The region at low fractional energy corresponds to the thermalised contribution.

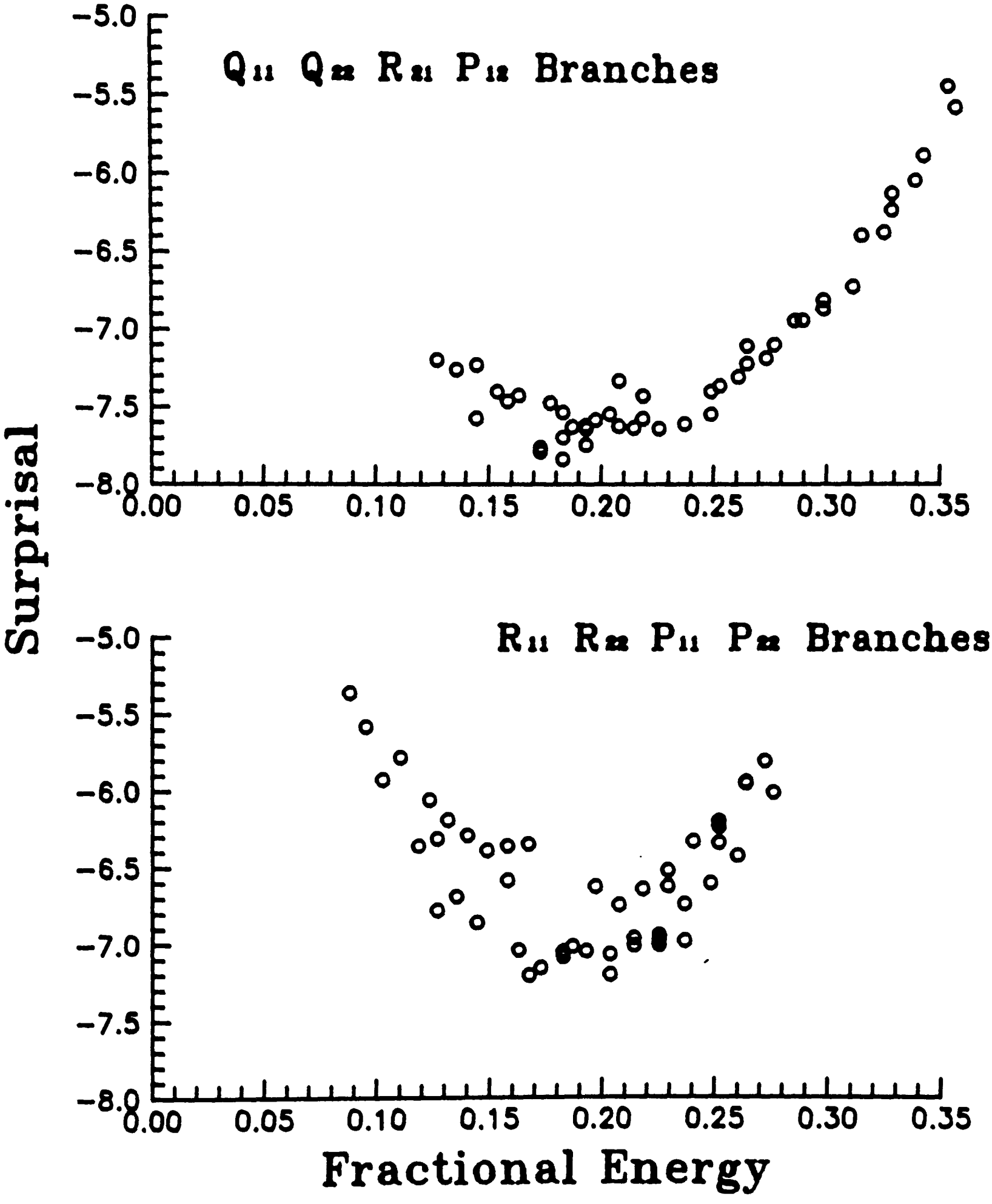

Figure 4.16. Surprisal analysis for NO($X^2\Pi$, v"=1). Top shows the results for the Π^- Λ doublet whilst the lower graph shows the Π^+ component.

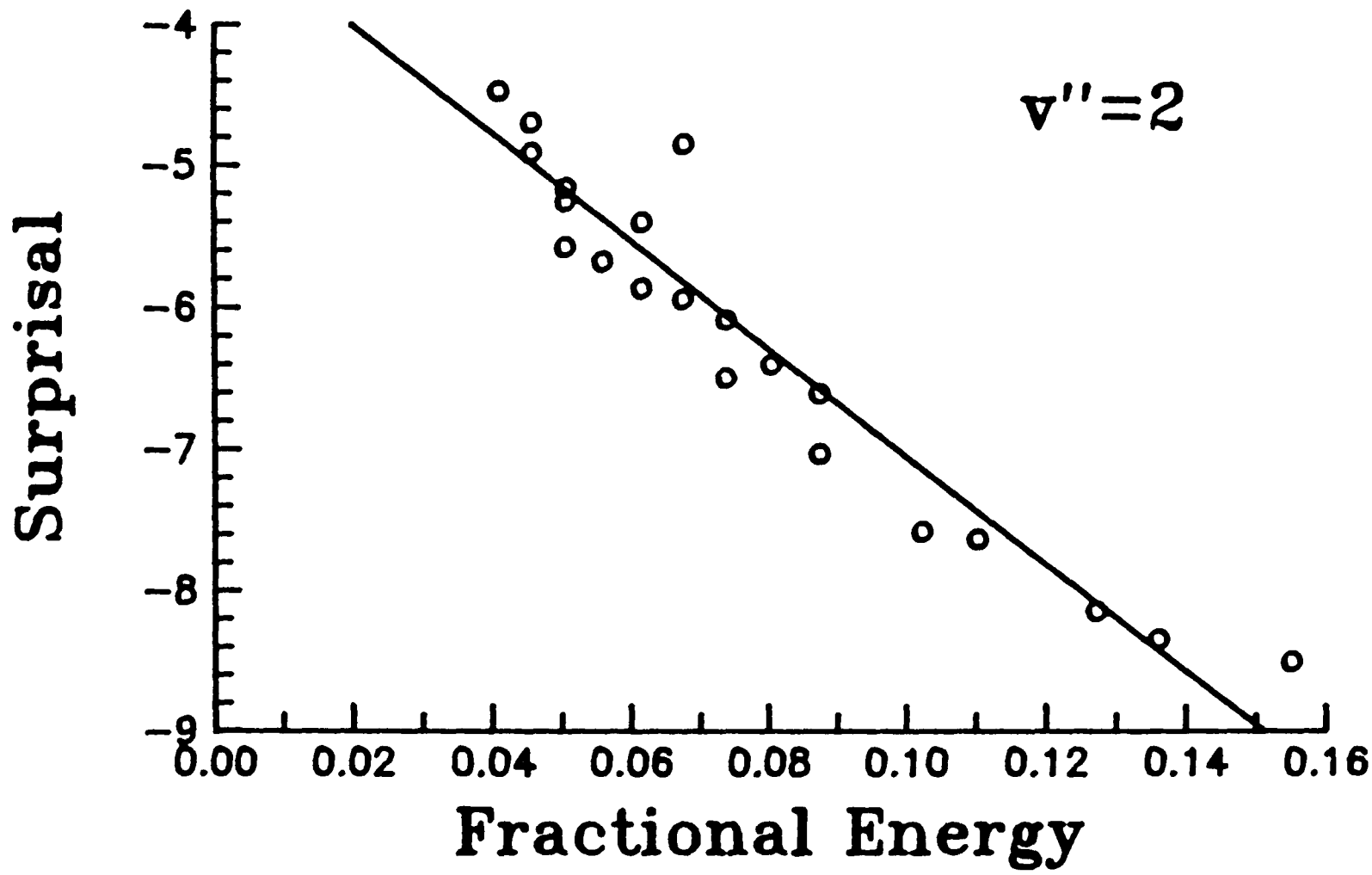

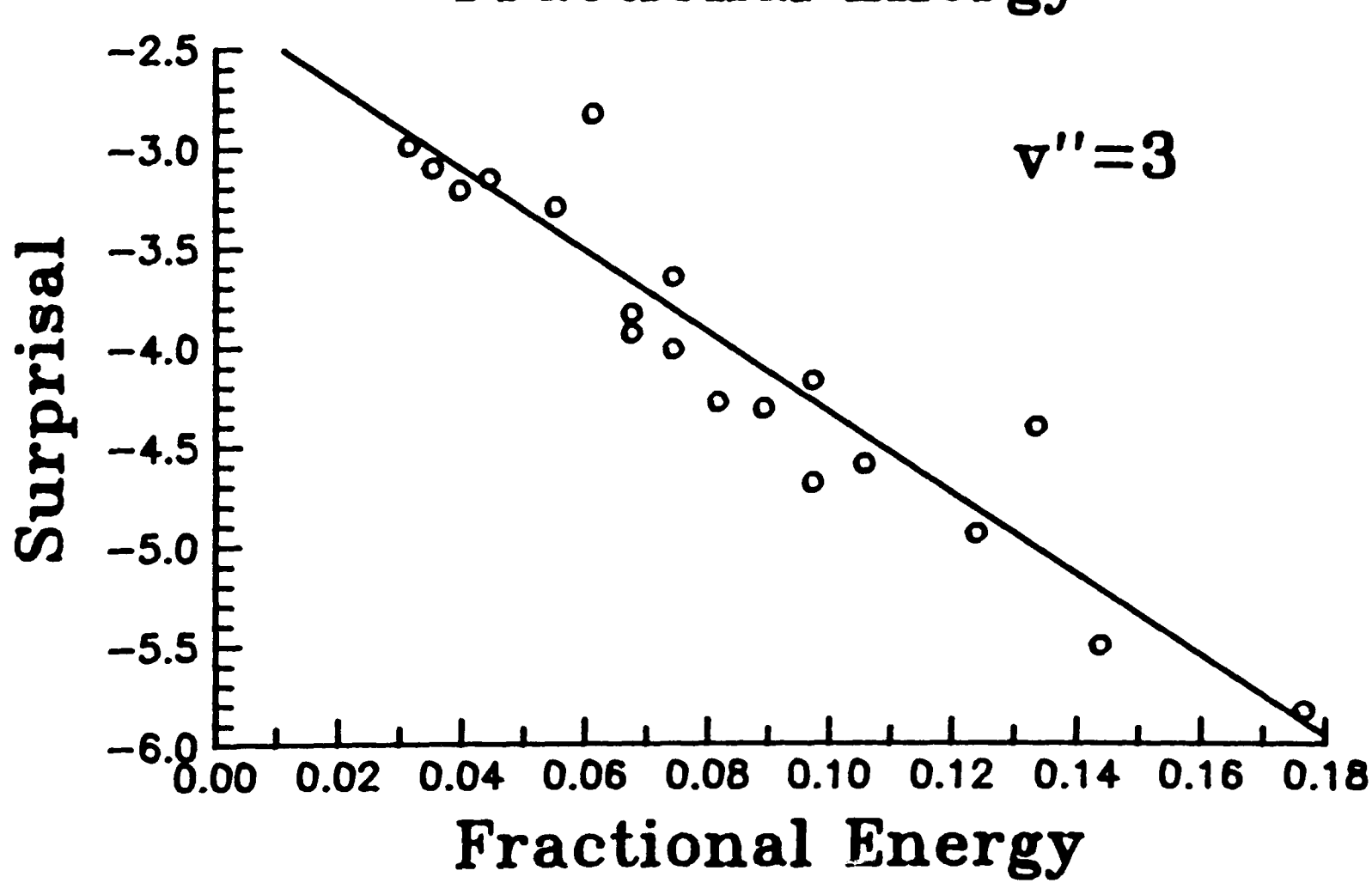

Top: Figure 4.17. Surprisal plot for $NO(X^2\Pi_i, v''=2)$.
Bottom: Figure 4.18. Surprisal analysis for $NO(X^2\Pi_i, v''=3)$.
In both figures a linear fit to the data is also shown.

given predominantly by v"=1 and confirmed at low f_R by the data for v"=2,3. The "full" rotational distributions were then obtained by inversion of the surprisal plots.

4.3.2 Determination of Vibrational Distribution Small regions of the LIF spectra for each vibrational level were recorded under carefully controlled conditions in which the CH_3ONO pressure, photomultiplier gain and laser power monitoring system were kept constant. In each case several well isolated rotational lines were recorded. The contribution of each of these lines to the extrapolated full rotational distribution, described above, allowed relative vibrational populations to be calculated, independant of the rotational levels recorded. These figures were then corrected for the signal recording input levels and the spectral response of the detection system. The Franck-Condon factors in absorption were taken into account but, since the same level of the $NO(A^2\Sigma^+)$ state, v'=0, was populated in each case, no emission corrections were needed. The results of these calculations are a relative vibrational population in $NO(X^2\Pi_i)$ for the photodissociation which is v"=0:1:2:3 = 0.367:0.547:0.064:0.022, in general agreement with the results of Lahmani et al [133].

4.4 DISCUSSION

The results presented above are in broad agreement with the independent series of experiments reported by Lahmani and co-workers [133] [134] using two photon LIF to detect the $NO(X^2\Pi_i)$. For v"=1, the only vibrational level for which the highest rotational levels populated

were probed, the current work finds population in up to J"=49.5, somewhat higher than reported by Lahmani et al [133] (see Fig. 4.2).

Perhaps the most striking feature of the dissociation is the unequal population of the Λ doublet levels giving rise to enhancement of spectral lines arising from the Π^- levels over those arising from the Π^+ levels. In, as yet, unpublished work Lahmani and co-workers also report such an enhancement by a factor of ~2, in agreement with the present results [154]. This effect can be explained in terms of symmetry conservation during the dissociation of the planar CH_3ONO as illustrated in Fig. 4.19. The excited, dissociating, state has the π orbitals on the terminal NO group perpendicular to the plane of the molecular frame. Assuming a planar dissociation, the impulsive force on the O-N bond will preferentially produce the Π^- orientation in the NO product. Since NO falls in between Hund's cases (a) and (b) this will only be true in the limit of high J where the two Π components are distinct. Lahmani et al find that the ratio of Π^-/Π^+ does not approach the theoretical maximum expected from the Λ doublet mixing ratio and attribute this to deviation from planarity in the dissociation, induced by torsional motion in the parent CH_3ONO.

4.4.1 Impulsive Model The impulsive model, developed by Holdy, Klotz and Wilson [32] to interpret the energy partitioning within the fragments of ICN photodissociation, was applied, in modified form to dissociation of ethyl nitrite by Tuck [130] and has been used recently on the 355nm dissociation of methyl nitrite by Lahmani et al [133] and on the 369nm photodissociation of HONO by Dixon and co-workers [21].

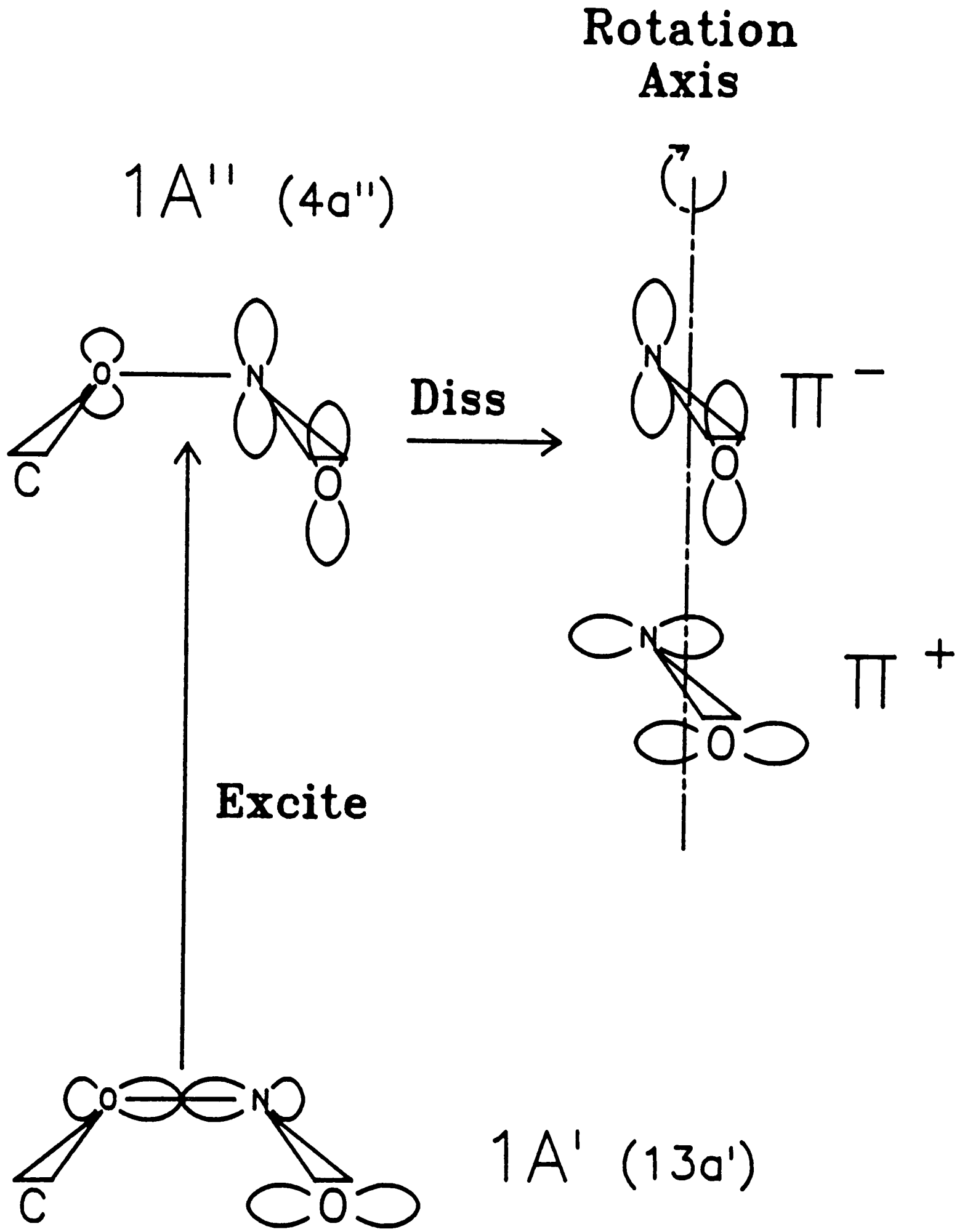

Figure 4.19. Schematic diagram of the dissociation process. The molecular orbitals of the ground and excited states of CH_3ONO are shown and the correlation with the two Λ doublet components in NO is indicated. Planar dissociation will give rise to the Π^- component.

The model assumes that all the energy in excess of that required to break the bond, the available energy, is produced initially as translational motion of the two atoms involved in the breaking bond in a direction along the line of centres. This may impart a torque upon each fragment if the line of action does not pass through the centre of mass of the fragment thus giving rise to rotational excitation. The translational energy of these atoms, which are deemed to be independant from the rest of the molecule, is partitioned amongst the available degrees of freedom of the fragments. The fragment translational energy partitioning is calculated by application of conservation of linear momentum to each fragment, rotational energies by conservation of angular momentum about their centre of mass of the fragments, and vibrational energy by conservation of energy.

To apply this model to the photodissociation of methyl nitrite the molecule can be considered to be a quasi tetra-atomic species with the hydrogen atoms condensed onto the carbon atom: The geometry and bond lengths shown are taken from the literature [155]. Since the O-N-O bond angle will be the same in both the cis and trans form (neglecting any hydrogen bonding in the cis conformer) the same dynamics will apply to both forms.

The gross energy partitioning is given by conservation of linear momentum of atoms β and γ and by conservation of energy.

$$E_t(\beta) = M_\gamma E_{avail}/(M_\gamma+M_\beta) \qquad (4.16)$$

$$E_t(\gamma) = M_\beta E_{avail}/(M_\gamma+M_\beta) \qquad (4.17)$$

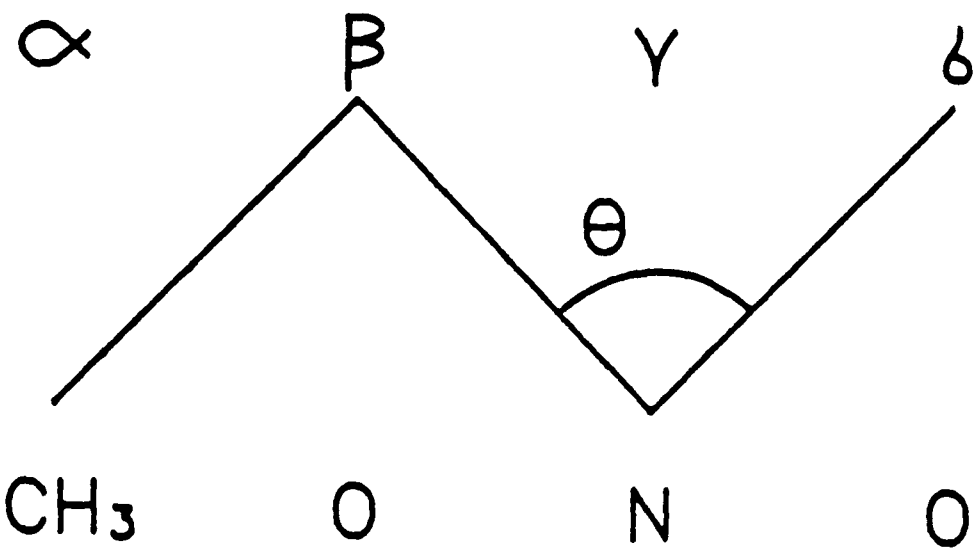

CH_3ONO Nomenclature used in the impulsive model.

Conservation of linear momentum to each of the fragments gives:

$$E_t(\alpha\beta) = M_{\gamma\delta}\mu_{\beta\gamma}E_{avail}/(M\mu_f) \qquad (4.18)$$

$$E_t(\gamma\delta) = M_{\alpha\beta}\mu_{\beta\gamma}E_{avail}/(M\mu_f) \qquad (4.19)$$

where M is the mass of the parent molecule and μ_f the reduced mass of the fragments. The angular momenta of the atoms β and γ about the centre of mass of $\alpha\beta$ and $\gamma\delta$ respectively are:

$$\bar{J}(\beta) = (2M_\beta E_t\beta)^{\frac{1}{2}} r_\beta \sin\theta \qquad (4.20)$$

$$\bar{J}(\gamma) = (2M_\gamma E_t\beta)^{\frac{1}{2}} r_\gamma \sin\theta \qquad (4.21)$$

where r_i is the distance of atom i from the centre of mass of the corresponding fragment and θ is the tetrahedral bond angle $109^o28'$. Applying conservation of angular momentum gives:

$$E_r(\alpha\beta) = J_\beta^2/2I_{\alpha\beta} \qquad (4.22)$$

$$E_r(\gamma\delta) = J_\gamma^2/2I_{\gamma\delta} \qquad (4.23)$$

where I_i is the moment of inertia of fragment i. Substitution of 4.16 and 4.20 into 4.22 gives:

$$E_r(\alpha\beta) = M_\beta M_\gamma r_\beta^2 \sin^2\theta E_{avail}/[(M_\gamma+M_\beta)\ I_{\alpha\beta}] \qquad (4.24)$$

Similarly equations 4.17, 4.21 and 4.23 give:

$$E_r(\gamma\delta) = M_\gamma M_\beta r_\gamma^2 \sin^2\theta E_{avail}/[(M_\gamma+M_\beta)\ I_{\gamma\delta}] \qquad (4.25)$$

Conservation of energy then gives the vibrational energies:

$$E_v(\alpha\beta) = E_t(\beta) - E_t(\alpha\beta) - E_r(\alpha\beta) \qquad (4.26)$$

$$E_v(\gamma\delta) = E_t(\gamma) - E_t(\gamma\delta) - E_r(\gamma\delta) \qquad (4.27)$$

assuming no electronic excitation (which is not possible in this case).

The dissociation energy of methyl nitrite into $CH_3O(\tilde{X}^2E)$ and $NO(X^2\Pi_i)$ has been determined thermodynamically to be 1.81ev = $14598.97cm^{-1}$. Taking $E_{avail} = h\nu - D_0^0$ gives $13593.83cm^{-1}$ as the available energy, neglecting any initial internal energy in the methyl nitrite.

The results of these calculations are shown in Table 4.6 using this value of the available energy. Also shown are values calculated using $14343.83cm^{-1}$ as the available energy, which allows for $750cm^{-1}$ of internal energy in the parent molecules, as used in similar calculations [133].

Tuck modified the basic impulsive model described above in an attempt to model the results of the photodissociation of ethyl nitrite [130]. He argued that the dissociation wavelength employed caused

excitation of 3 vibrational quanta of the -N=O stretch in ethyl nitrite and that this energy remained localised in the NO fragment as vibration. He therefore reduced the available energy by an amount corresponding to this excitation. This modification was found to give a good fit to the experimental data in the case of ethyl nitrite. Following this argument a similar modification might be made in the present case since, as discussed in the introduction, absorption by methyl nitrite at 355nm excites v'=2 of the dissociative state. The peaks in the absorption spectrum are separated by ~1000cm^{-1} so in this case the available energy is reduced by 2000cm^{-1}. Table 4.6 also includes results of this modification to the impulsive model using 12343.83cm^{-1} as the available energy and a comparison with the experimental results presented here, those of Lahmani et al [133], and of Keller and co-workers performed at 350nm [135].

E_{avail}	E_T	E_R	E_v
This work	-	~2150	1407
Lahmani et al	2600	1775	1960
Keller et al	4070	-	-
13593.83	3383.35	3437.25	429.44
14343.83	3570.02	3626.89	453.13
12343.83	3072.24	3121.18	2389.95

Impulsive model results for NO

E_{avail}	E_T	E_R	E_v
Keller et al	3930	-	-

13593.83	3274.21	2728.66	340.91
14343.83	3454.86	2879.21	359.72
12343.83	2973.14	2477.75	309.56

Impulsive model results for CH_3O

Table 4.6.

It can be seen from Table 4.6 that there is qualitatively good agreement between the modified impulsive model and the collected experimental results. In the absence of more detailed information on the excited state geometry and potential it does not seem beneficial to pursue such a model, or more complex models, further.

CHAPTER FIVE

5.1 INTRODUCTION

This chapter describes an investigation of the rotational distribution arising in various vibrational levels of $CO(X^1\Sigma^+)$ following the reaction of $O(^3P)$ with $CS(X^1\Sigma^+)$, a reaction which has received considerable attention as it is the basis of a chemical laser operating on the vibration-rotation transitions in CO. Laser action on this system was first reported when a mixture of O_2 and CS_2 was flash photolysed by Pollack [156]. In subsequent experiments [157] [158] the laser action was initiated by both electrical discharge and flash photolysis, and the effects of reagent concentration and discharge conditions were studied. Many reaction schemes were proposed to explain the production of vibrationally excited $CO(X^1\Sigma^+)$ responsible for laser action. Hancock and Smith [159] [160] demonstrated that, of the schemes proposed, the reaction between oxygen atoms, $O(^3P)$, and the $CS(X^1\Sigma^+)$ radical gave rise to vibrationally excited $CO(X^1\Sigma^+)$ in a population inversion. Further experiments by the same workers [161] [162] in which the IR chemiluminescence resulting from vibrationally excited $CO(X^1\Sigma^+)$ was resolved and the spectral data corrected for loss processes such as collisional relaxation gave rise to the nascent vibrational product distribution which is presented in Fig. 5.1. This shows a highly excited vibrational distribution with complete inversion below v"=13. The distribution has been subsequently confirmed in other studies employing a variety of experimental methods such as intracavity gain/loss measurements [163] and conventional absorption spectroscopy

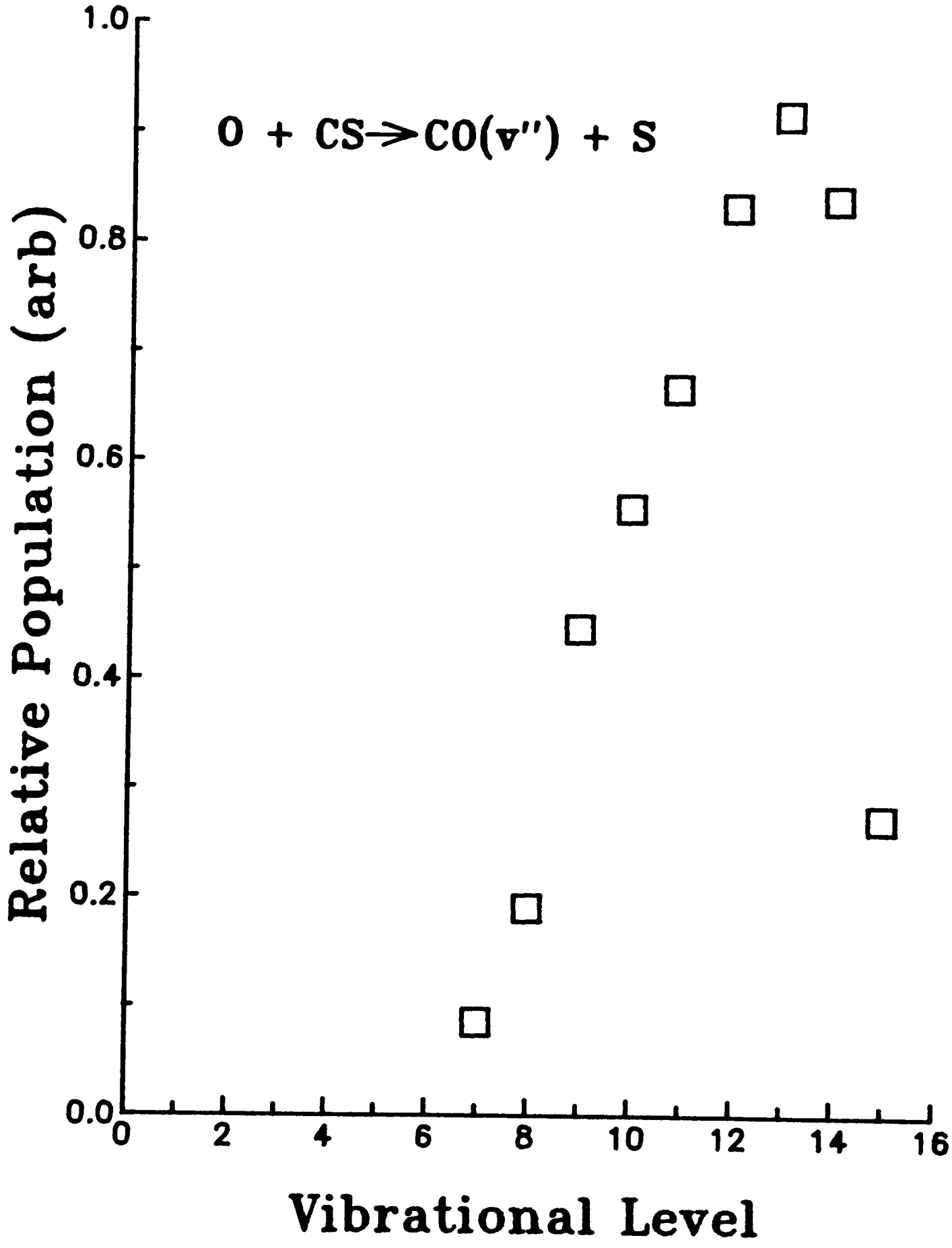

Figure 5.1. Vibrational distribution resulting in CO following the reaction between O and CS, taken from [161].

[164].

It is now generally accepted that the reaction scheme leading to high vibrational excitation of $CO(X^1\Sigma^+)$ is:

$$O(^3P) + CS_2(X^1\Sigma_g^+) \rightarrow CS(X^1\Sigma^+) + SO(X^3\Sigma^-) \qquad (5.1)$$

$$O(^3P) + CS(X^1\Sigma^+) \rightarrow CO(X^1\Sigma^+\ v") + S(^3P) \qquad (5.2)$$

Reaction 5.1 is only one of three possible channels for the reaction between $O(^3P)$ and $CS_2(X^1\Sigma_g^+)$. All three are shown below:

$$O + CS_2 \rightarrow CS + SO \qquad (5.3a)$$

$$CO + S_2 \qquad (5.3b)$$

$$OCS + S \qquad (5.3c)$$

The branching ratios for these processes have been measured as $0.7 \leq k_{3a} \leq 0.85$ [165] $k_{3b} = 0.014 \pm 0.002$ [166] and $k_{3c} = 0.098 \pm 0.004$ [164], showing that the production of $CS(X^1\Sigma^+)$ is the major channel of the reaction. Reaction 5.3b is a possible source of $CO(X^1\Sigma^+\ v")$ and, as such, may complicate the current investigation.

The vibrational distribution in $CO(X^1\Sigma^+)$ resulting from reaction 5.3b has been investigated [164] [167], and although complicated by residual traces of vibrational levels of $CO(X^1\Sigma^+)$ due to reaction 5.2 the resulting distribution is found to be considerably colder than that arising from the latter, with $v"=0$ the most populated level and essentially no population in levels $v"\geq 6$.

Since the ideal state-to-state reaction dynamics experiment specifies exactly the initial (and final) state of a reaction it is necessary to know the energy disposal in reaction 5.3a since the $CS(X^1\Sigma^+)$ produced from it is a participant in the reaction, 5.2, studied in this chapter. The vibrational product distribution of reaction 5.3a has been studied by Smith [168] via kinetic absorption spectroscopy. A vibrational "temperature" of 1755K was determined for $CS(X^1\Sigma^+)$ from observations of population up to v"=3. The vibrational energy in $CS(X^1\Sigma^+)$ has been proposed to explain vibrational excitation in $CO(X^1\Sigma^+$ v") above the allowed energetic limit of $O(^3P)$ + $CS(X^1\Sigma^+$ v"=0) as observed in several studies of this reaction [164].

Although the vibrational distribution arising in $CO(X^1\Sigma^+)$ following reaction 5.2 is well established there has been no previous determination of the nascent rotational distribution within the various vibrational levels. This was mainly due to the pressure (several Torr) and observation time (>1ms) combination employed in the majority of the experiments described above.

Laser Induced Fluorescence has been widely used to determine rotational distributions in the products of both reactions and photodissociations. In the present case this technique is difficult to apply since the $(A^1\Pi - X^1\Sigma^+)$ transition in CO falls in the VUV region of the spectrum; the (0,0) band origin is at 154.4nm. Non-linear optical mixing techniques have been used to produce radiation of a wavelength suitable for single photon excitation of the $A^1\Pi$-$X^1\Sigma^+$ transition in CO. The (0,0) band, at ~155nm, has been excited by radiation produced by

third order mixing of two visible dye lasers in Mg vapour [169], whilst third harmonic generation in Kr has been used to pump the (13,0) band at ~123nm [170].

The application of multi-photon techniques to overcome the difficulty of working in the VUV region has been applied to the CO($A^1\Pi$-$X^1\Sigma^+$) 4th positive system. Two photon absorption has been used by Filseth et al to record the (3,0) band [171] and by Bernheim and co-workers [172] to study transitions from v"=0 of the $X^1\Sigma^+$ state to v'=0-9 of the $A^1\Pi$ state. A three photon absorption has been used to access the v"=2 level of the $A^1\Pi$ state employing visible radiation of ~440nm as the excitation source [173]. The multi-photon processes described above all employed VUV fluorescence as the method of detection of the CO($A^1\Pi$ v') state. Resonantly Enhanced Multi-Photon Ionisation, discussed in chapter 3, has been applied to the CO($A^1\Pi$-$X^1\Sigma^+$) transition in a study in which the v'=3 level of the $A^1\Pi$ state was populated via a two photon absorption as the intermediate state in the ionisation process [174].

The VUV wavelengths required to promote CO($X^1\Sigma^+$) to the $A^1\Pi$ state can be changed to the more accessible UV region by initially preparing vibrationally excited CO($X^1\Sigma^+$). One method of achieving this is the use of a CO laser in resonance with the vibrational frequency of CO($X^1\Sigma^+$) [175]. An alternative method is via a chemical reaction and that described earlier in this chapter between O(^3P) and CS($X^1\Sigma^+$) is ideal in this respect, with ~80% of the reaction exothermicity appearing as CO vibrational excitation [161]. In a preliminary investigation to the work presented in this chapter Hancock and Zacharias [176] were able to

excite vibrational levels v"=11,12,14 and 15 of the $X^1\Sigma^+$ state of CO to various vibrational levels of the $A^1\Pi$ state using radiation in the range ~213-229nm under conditions in which complete rotational equilibration and some vibrational relaxation of the $CO(X^1\Sigma^+)$ had occurred. A schematic diagram of the optical pumping scheme is presented in Fig. 5.2 which shows the potential curves for the $X^1\Sigma^+$ and $A^1\Pi$ states of CO, the vibrational distribution arising in the $X^1\Sigma^+$ state as a result of the reaction of $O(^3P)$ with $CS(X^1\Sigma^+)$, the optical excitation wavelength and the resulting VUV laser induced fluorescence. The up-conversion of the UV excitation wavelength into the VUV region by the addition of the energy of the chemical reaction allows excellent sensitivity in the detection of $CO(X^1\Sigma^+)$ since a solar blind photomultiplier, not sensitive to the excitation wavelength, can be used. Hancock and Zacharias [176] estimated an upper limit for the concentration of $CO(X^1\Sigma^+$ v"=15) of 5×10^{-5} Torr and considerably lower concentrations can obviously be employed in the light of the very good signal/noise ratio they observed.

The very low population of $CO(X^1\Sigma^+)$ in vibrational levels v"<5 suggests that, once the $A^1\Pi$ state has been populated via optical pumping of $CO(X^1\Sigma^+$ v"≥7), a population inversion will exist on the $A^1\Pi$-$X^1\Sigma^+$ system of CO giving rise to the potential for a VUV CO electronic laser [176]. CO has shown laser action in the region 181-197nm from vibrational levels of the $A^1\Pi$ state, populated via high energy electron impact, to thermally unoccupied levels of the $X^1\Sigma^+$ state [177]. A pumping scheme such as that described earlier has not been demonstrated to date. Some comments on this proposal will be made later in this

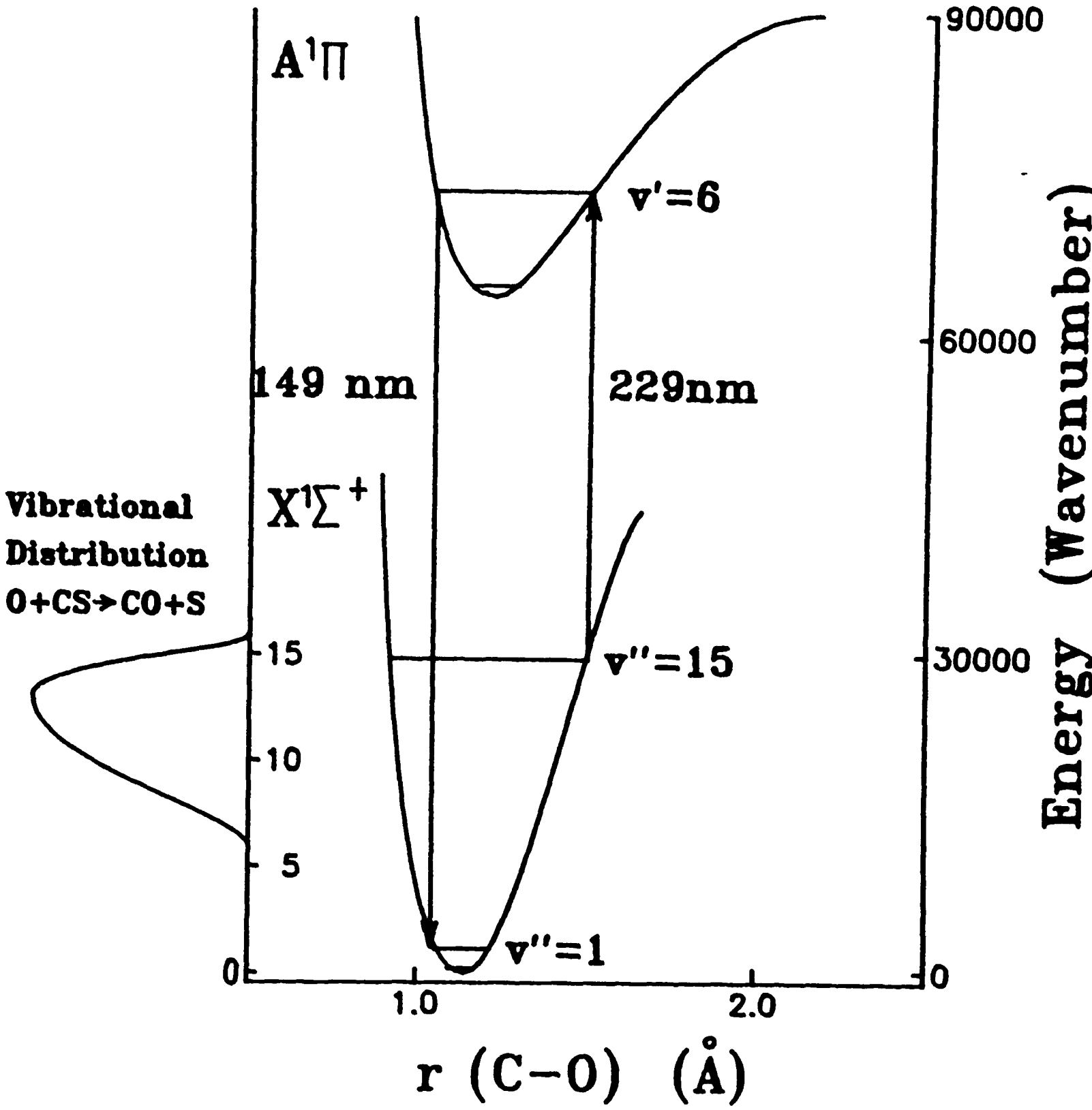

Figure 5.2. Experimental pumping scheme showing potential curves, vibrational distribution, absorption and emission lines.

chapter.

5.2 EXPERIMENTAL

5.2.1 Preliminary Investigations The apparatus used for the experiments has been described in Chapter 2. Initial experiments on the $CO(X^1\Sigma^+\ v")$ populated from the reaction between O and CS relied on the following scheme:

$$O(^3P) + CS_2(X^1\Sigma_g^+) \rightarrow CS(X^1\Sigma^+) + SO(X^3\Sigma^-) \qquad (5.4)$$

$$O(^3P) + CS(X^1\Sigma^+) \rightarrow CO(X^1\Sigma^+\ v") + S(^3P) \qquad (5.5)$$

A mixture of CS_2 in Ar of approximate ratio 1:5 was admitted to the reaction cell via a capillary leak. O_2 and Ar, mixed in ratio 1:20 passed through a microwave discharge and entered the cell through a large, ~3cm diameter, inlet. The pressure in the cell was maintained at 1Torr by a large rotary pump. Excitation of $CO(X^1\Sigma^+\ v")$ to the $A^1\Pi$ state was achieved using the 1st, 2nd and 3rd Anti-Stokes Stimulated Raman transitions of frequency doubled dye laser radiation (Rhodamine 6G). Initial experiments employing the full UV tuning range of the laser system revealed a large number of bands which were assigned from spectroscopic data detailed in Appendix 2 [178]. The observed bands are presented in Table 5.1.

AS Transition	Band	Wavelength/nm
1	(6,17)	248.8
	(2,14)	249.8
	(3,15)	252.2

	(7,18)	251.4
2	(8,16)	225.0
	(5,14)	226.5
	(9,17)	227.6
	(6,15)	228.9
3	(7,13)(10,15)	206.0
	(13,17)	206.6
	(4,11)	207.0
	(8,14)(11,16)	208.5
	(1,9)	209.0
	(5,12)	209.3

Table 5.1.

Of the bands observed the (5,14), (6,15), (4,11) and (5,12) were by far the strongest and it was upon these bands that most of the subsequent experiments were performed. Observation of bands arising from vibrational levels in $CO(X^1\Sigma^+)$ above that allowed on energetic grounds [161] may reflect two aspects of the experimental arrangement. Firstly incomplete vibrational relaxation of the $CS(X^1\Sigma^+)$ produced by reaction 5.4 will lead to an increase in the available energy of ~1285cm^{-1} for each vibrational quantum in $CS(X^1\Sigma^+)$. Secondly, vibrational energy transfer between $CO(X^1\Sigma^+)$ molecules may also produce apparent excitation above the energetic limit.

It is likely that, under the experimental conditions employed, complete rotational equilibration would occur in the various product

vibrational levels of the $CO(X^1\Sigma^+)$ formed in the reaction. To investigate this LIF spectra of the (4,11) and (5,12) bands were recorded in greater detail. Fig. 5.3 shows the resulting laser excitation spectrum for the (5,12) band. The LIF signal was found to increase linearly with the laser energy, indicating that no saturation was occurring. The rotational state population measured from the spectra are presented as a conventional Boltzmann plot in Fig 5.4. The gradient corresponds to a rotational temperature of 302±36K which confirms the complete rotational equilibration as expected [176]. A similar analysis for the (4,11) band also gave rise to a room temperature distribution.

As described in the introduction to this chapter, the vibrational distribution resulting in $CO(X^1\Sigma^+)$ following the reaction of $O(^3P)$ and $CS(X^1\Sigma^+)$ is well established. As complete rotational equilibration was observed under the conditions used in the preliminary experiments described here, some vibrational relaxation, despite being a slower process, might be expected. A series of experiments were carried out to determine the vibrational distribution under these conditions. The intensities of the band head region in the transitions listed in Table 5.1 were recorded and related to the population in the lower vibrational levels by assuming a Boltzmann rotational temperature of 300K, allowing for the number of individual transitions contributing to the band head and making use of the known Franck-Condon factors [179] and the fluorescence detection efficiencies. The results of this analysis are presented in Fig. 5.5 and compared to the nascent vibrational

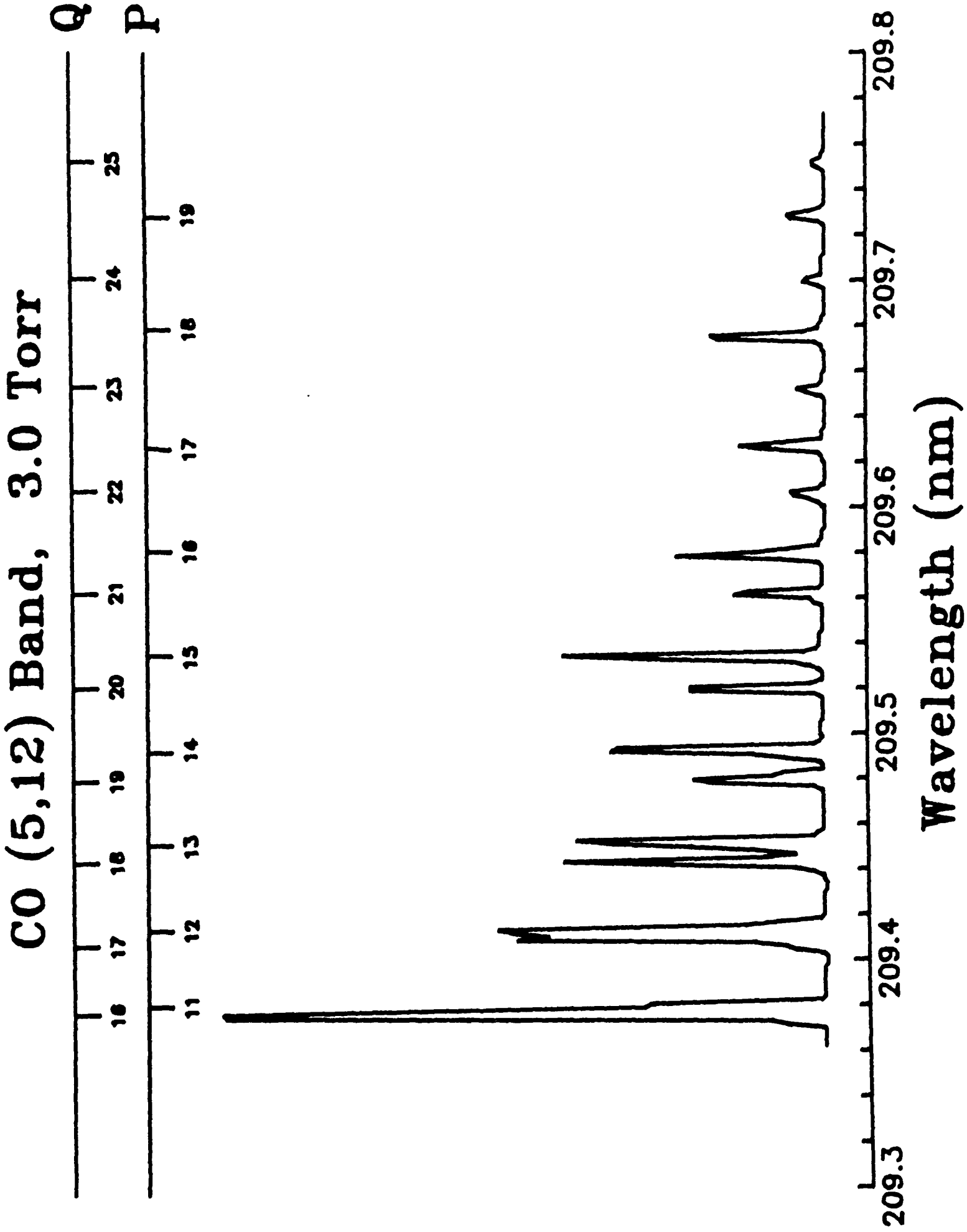

Figure 5.3. LIF spectrum of the (5,12) band of CO(A-X) recorded under high (3 Torr) pressure conditions.

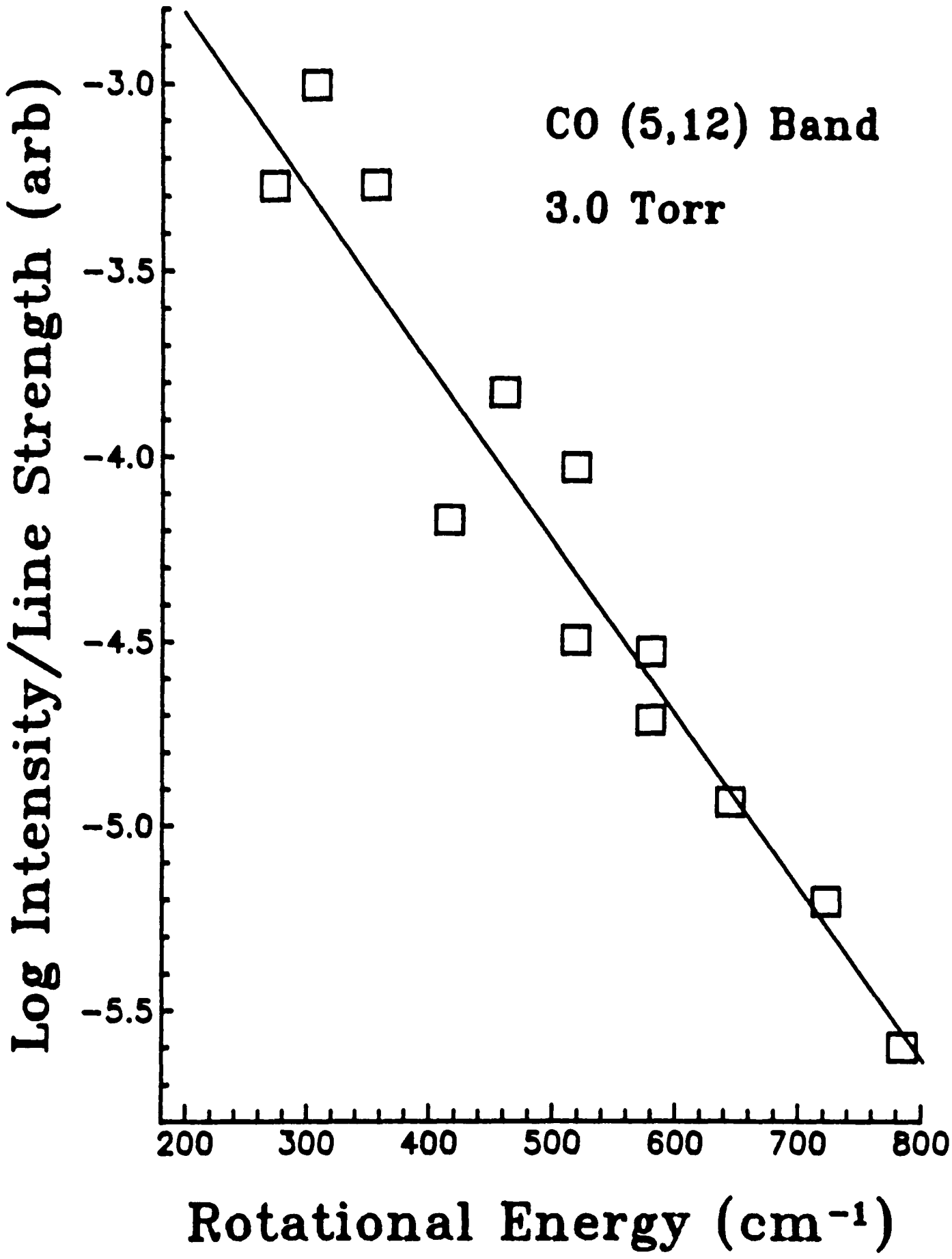

Figure 5.4. Rotational distribution for (5,12) band recorded under high (3 Torr) pressure conditions showing thermal distribution.

distribution of Smith et al [162]. The data shows evidence for both vibrational relaxation, since the population in v"=11 is greater than that in v"=12 (in contrast with the results of Smith et al), and also population of vibrational levels above the energetic limit of the reaction, by mechanisms described previously.

5.2.2 Rotational Distribution Under Low Pressure Conditions Results of the preceding section have shown that an investigation of the nascent rotational distribution resulting from the reaction must employ considerably lower pressures in the reaction vessel than those used. The pumping system employed in the initial experiments was replaced by a large oil vapour diffusion pump capable of a pumping rate of 750ls^{-1} at pressures $\leq 10^{-3}$Torr. A low power microwave discharge in CS_2/Ar was used to produce the $CS(X^1\Sigma^+)$ radicals: under high pressure conditions this measure was found to raise the LIF signal by a factor of more than 3, and thus helped to reduce the problem of low signal levels at the low total pressures used. This method has the additional advantage of allowing vibrational relaxation of the $CS(X^1\Sigma^+$ v") radicals to take place prior to entry into the reaction cell, thus reducing any possible problems associated with determination of the energy available to the reaction. Additional changes to the O_2/Ar microwave discharge, such as the increase of the proportion of O_2 to a ratio of 1:1 and the addition of traces of H_2O vapour in the gas mixture [180], contributed to the rise of the resulting $CO(X^1\Sigma^+$ v") concentration without raising the total reaction pressure.

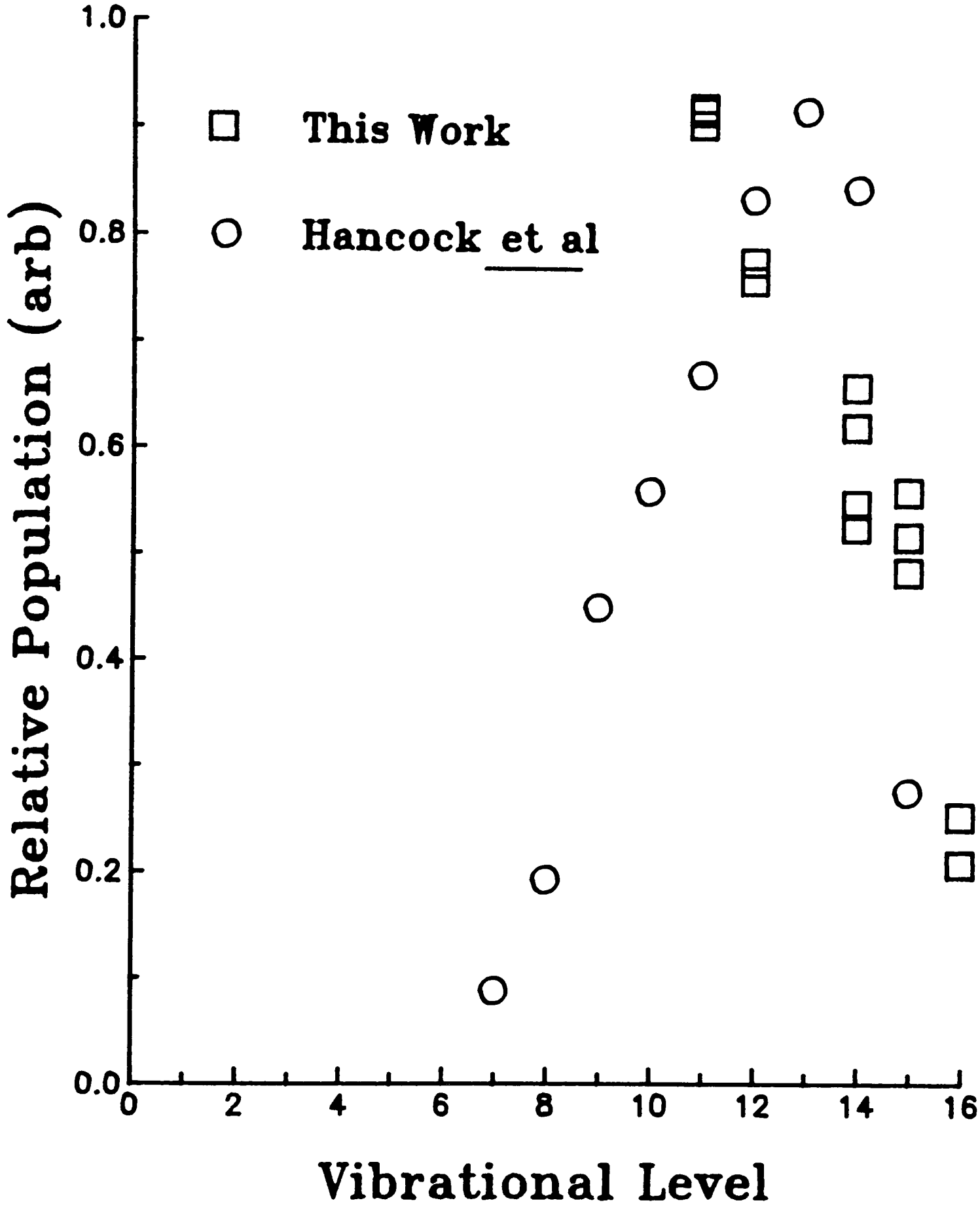

Figure 5.5. Experimentally determined vibrational distribution compared to that of Smith and co-workers [162].

The dissociated CS_2 and O_2 in Ar were admitted to the reaction cell via pinhole leaks, most of the gases being pumped away from the microwave discharge units via subsidiary rotary pumps which maintained the optimum 1 Torr pressure within the discharge volume. The pressure within the cell was varied by altering the size of the pinholes - full pumping by the large diffusion pump always being maintained. The inlets were within a few cm of each other and inclined at 60^{o}, as shown in Chapter 2 (Fig 2.6).

Despite these measures to raise the concentration of $CO(X^1\Sigma^+)$ within the reaction cell, very low signal levels were observed when a total pressure of 2×10^{-4} Torr was established. It was necessary to record 200 laser pulses at each point in the laser excitation spectrum to obtain reliable spectra. It was only possible to record spectra from the strongest bands which were the (5,14) and (6,15), using the 2nd Anti-Stokes Stimulated Raman transition, and the (4,11) and (5,12), using the 3rd Anti-Stokes transition giving rotational distributions for v"=11,12,14 and 15 in $CO(X^1\Sigma^+)$. Parts of the LIF spectra, recorded at a pressure of 2×10^{-4}Torr, for these bands are presented in Figures 5.6 - 5.9. The corresponding rotational distributions are shown in Figures 5.10-5.13, plotted in a conventional Boltzmann manner. All the distribution are similar showing a region which corresponds to a temperature at low rotational energy with a deviation from statistical behaviour at higher rotational energy apparent, where the rotational populations are higher than would be expected for a thermal distribution.

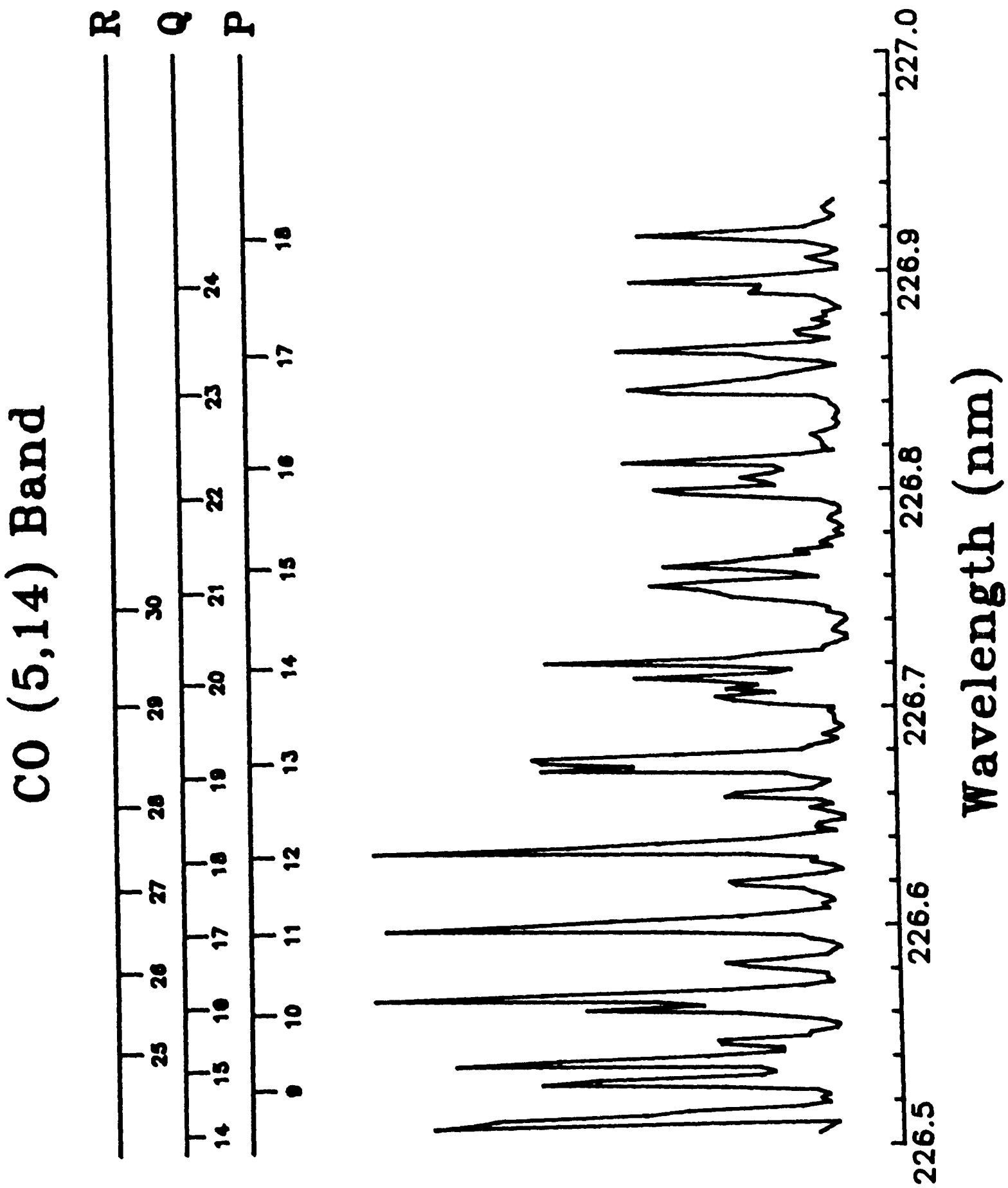

Figure 5.6. LIF spectrum of (5,14) band of CO recorded at 2×10^{-4}Torr.

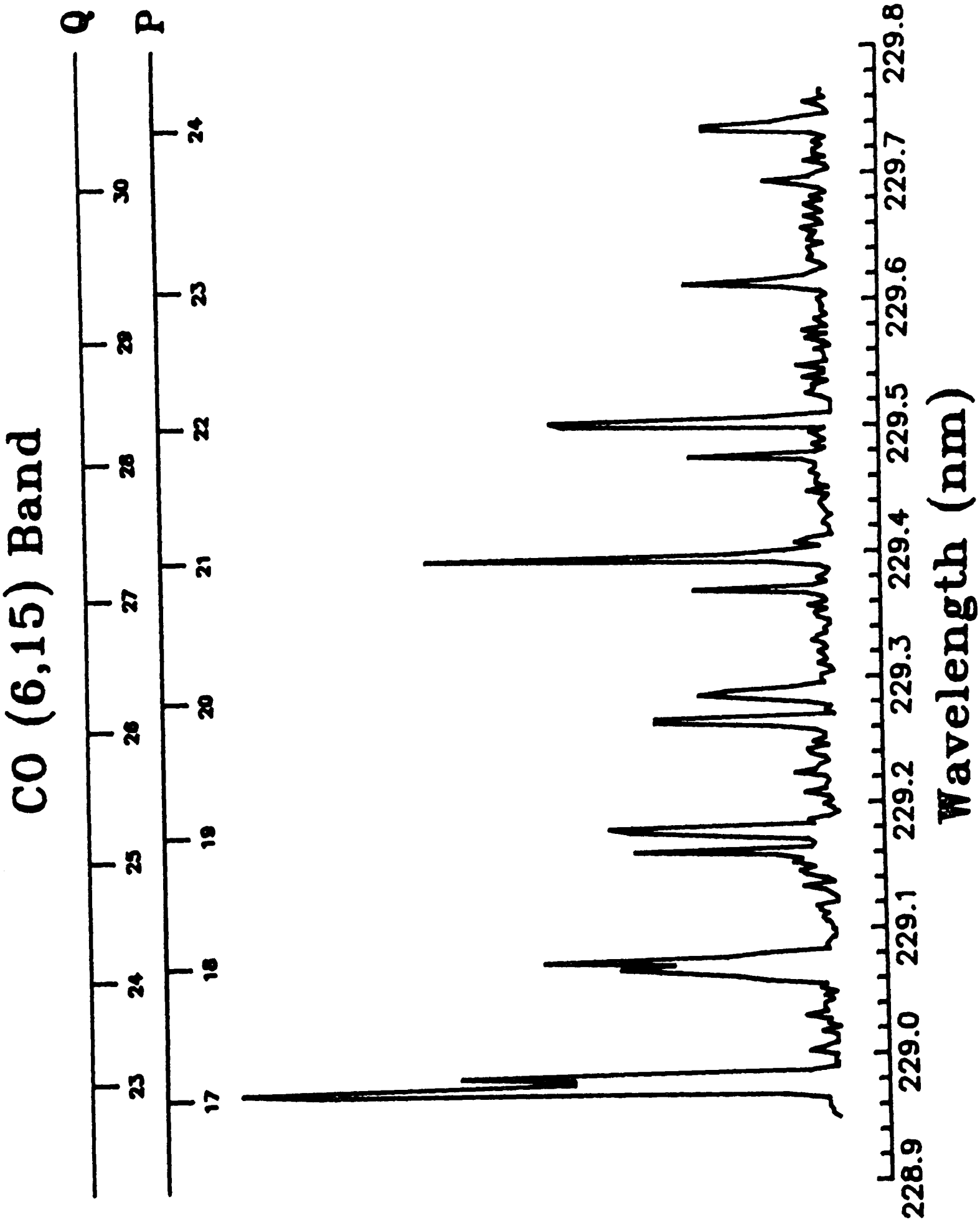

Figure 5.7. LIF spectrum of (6,15) band of CO recorded at 2×10^{-4}Torr.

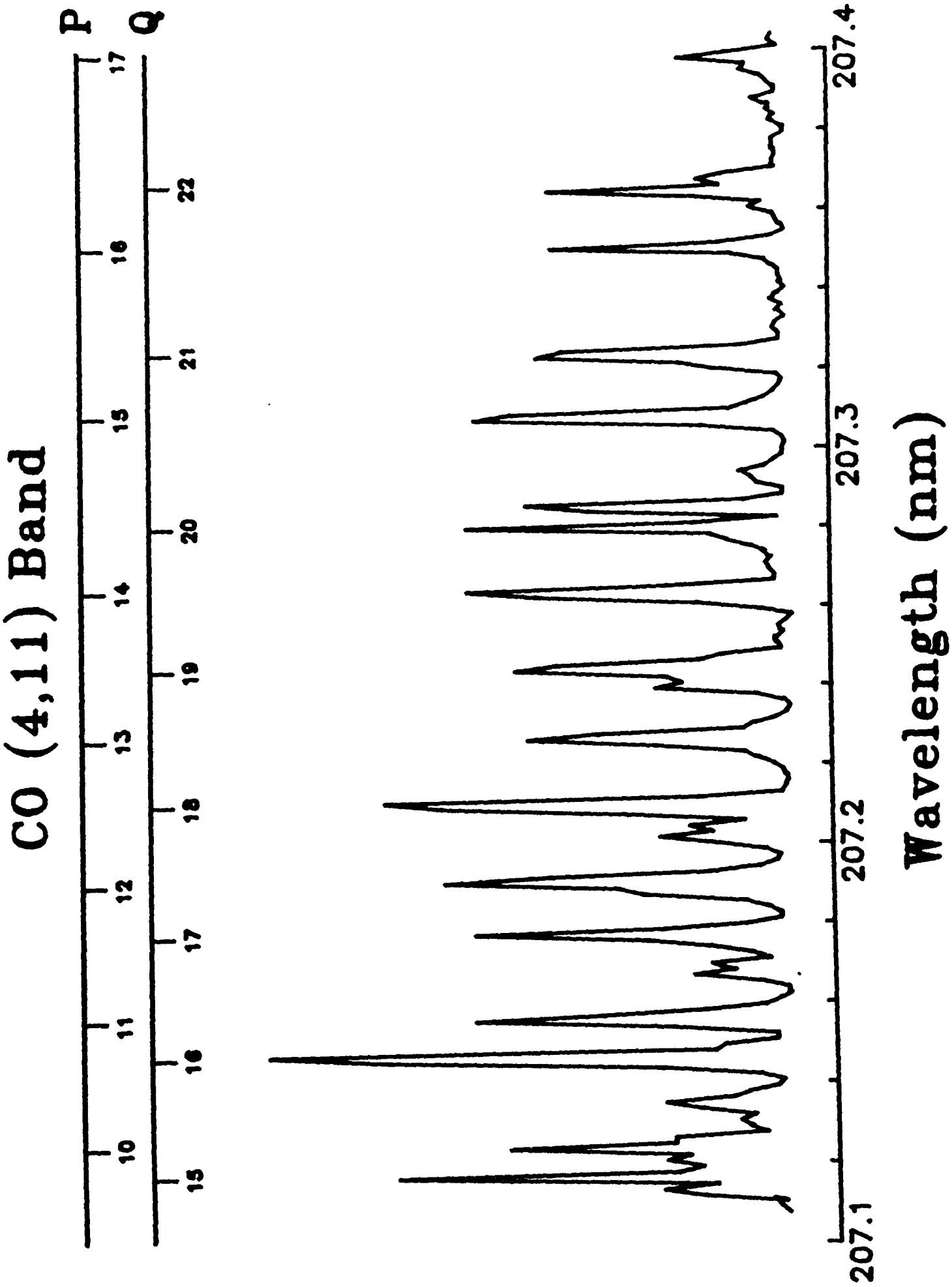

Figure 5.8. LIF spectrum of (4,11) band of CO recorded at 2×10^{-4}Torr.

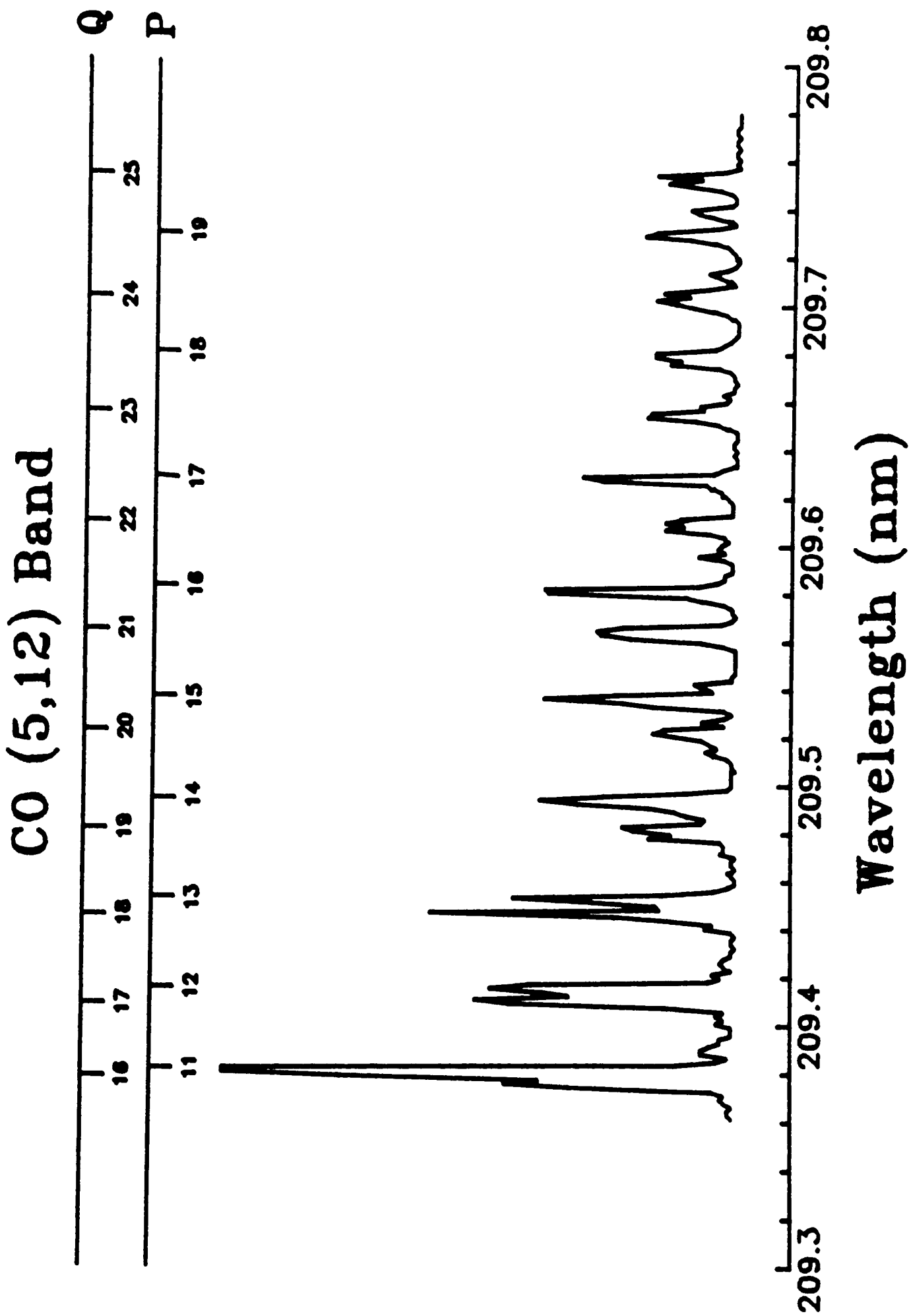

Figure 5.9. LIF spectrum of (5,12) band of CO recorded at 2×10^{-4}Torr.

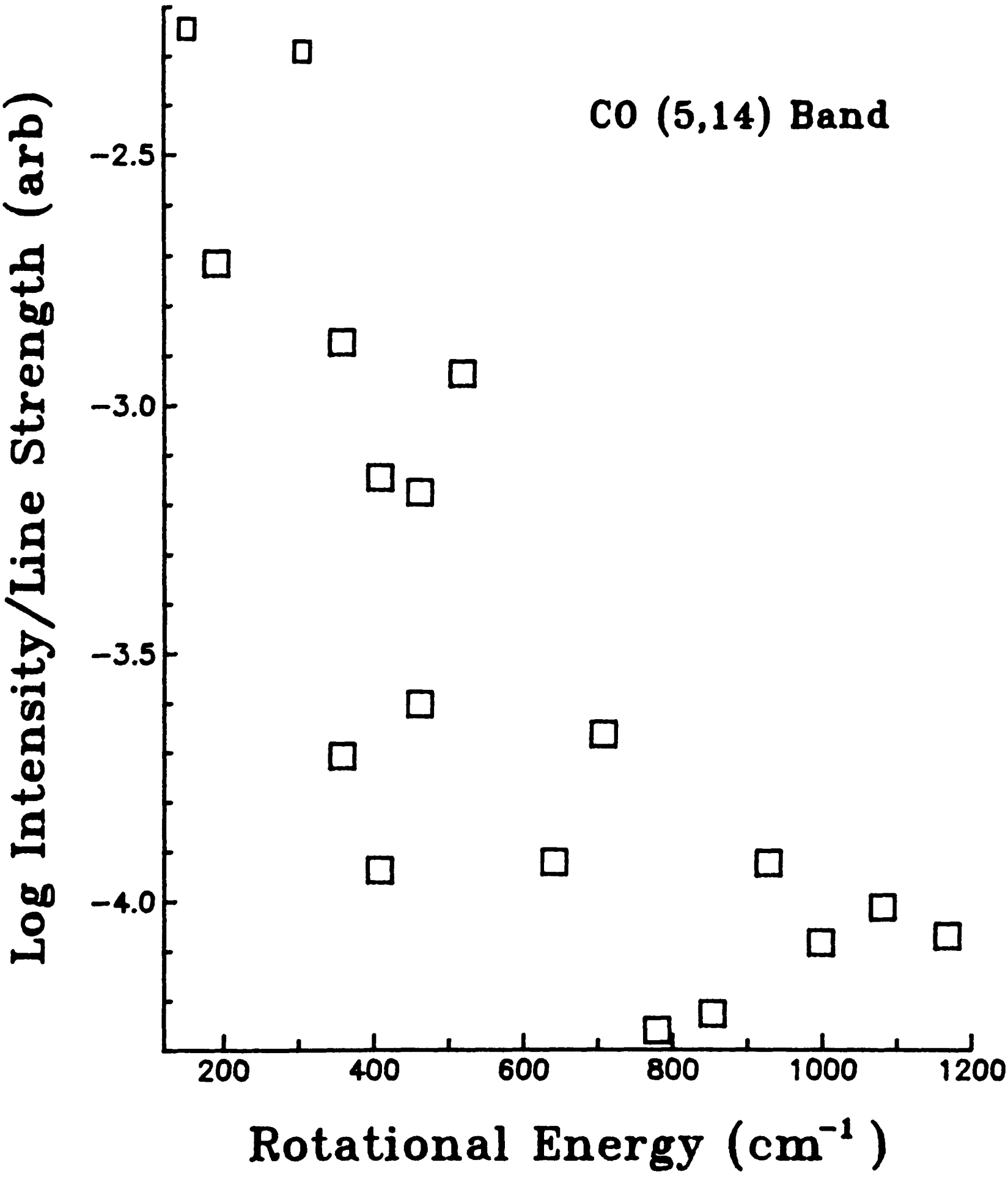

Figure 5.10. Boltzmann plot of rotational distribution from (5,14) band.

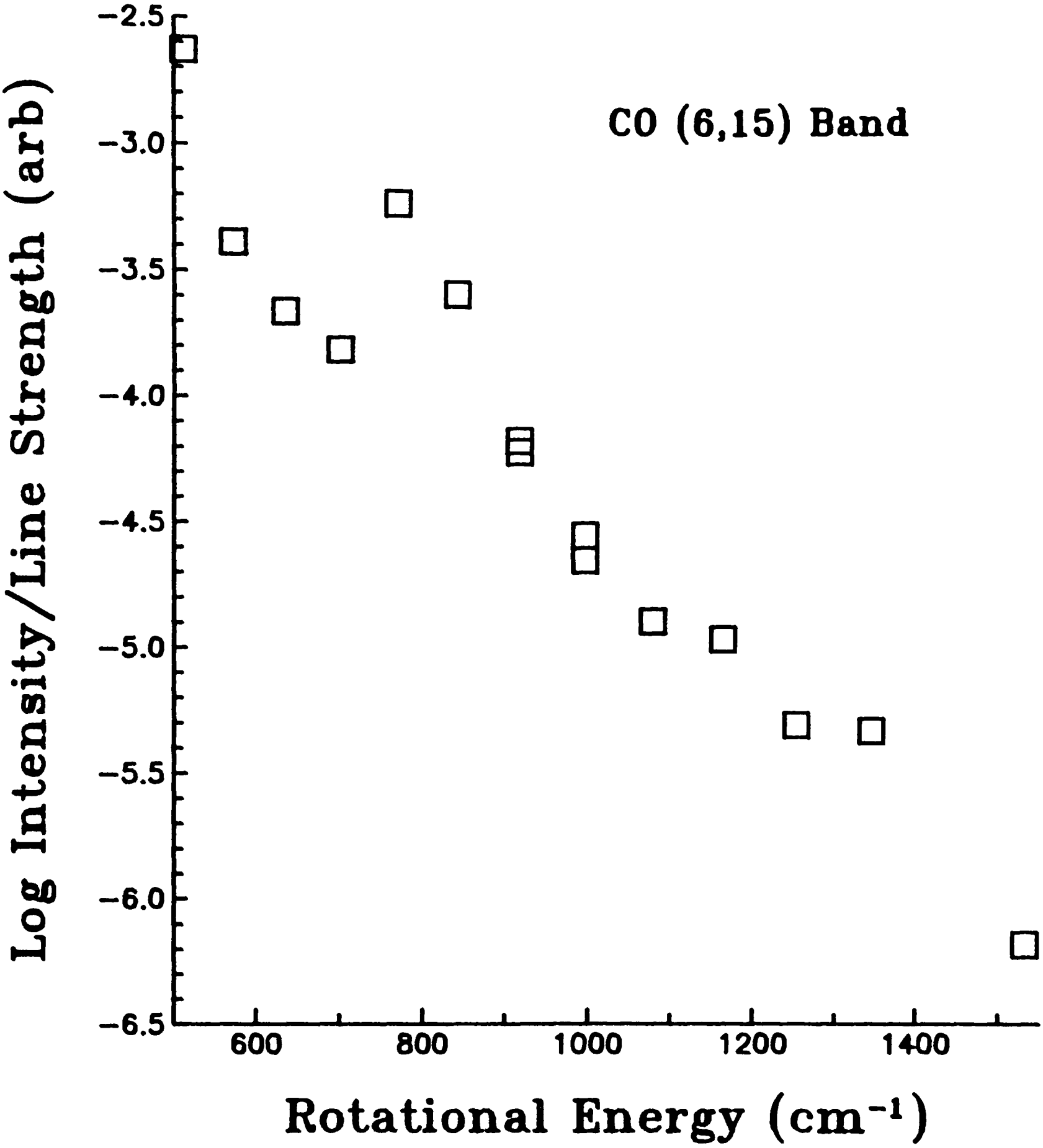

Figure 5.11. Boltzmann plot of rotational distribution from (6,15) band.

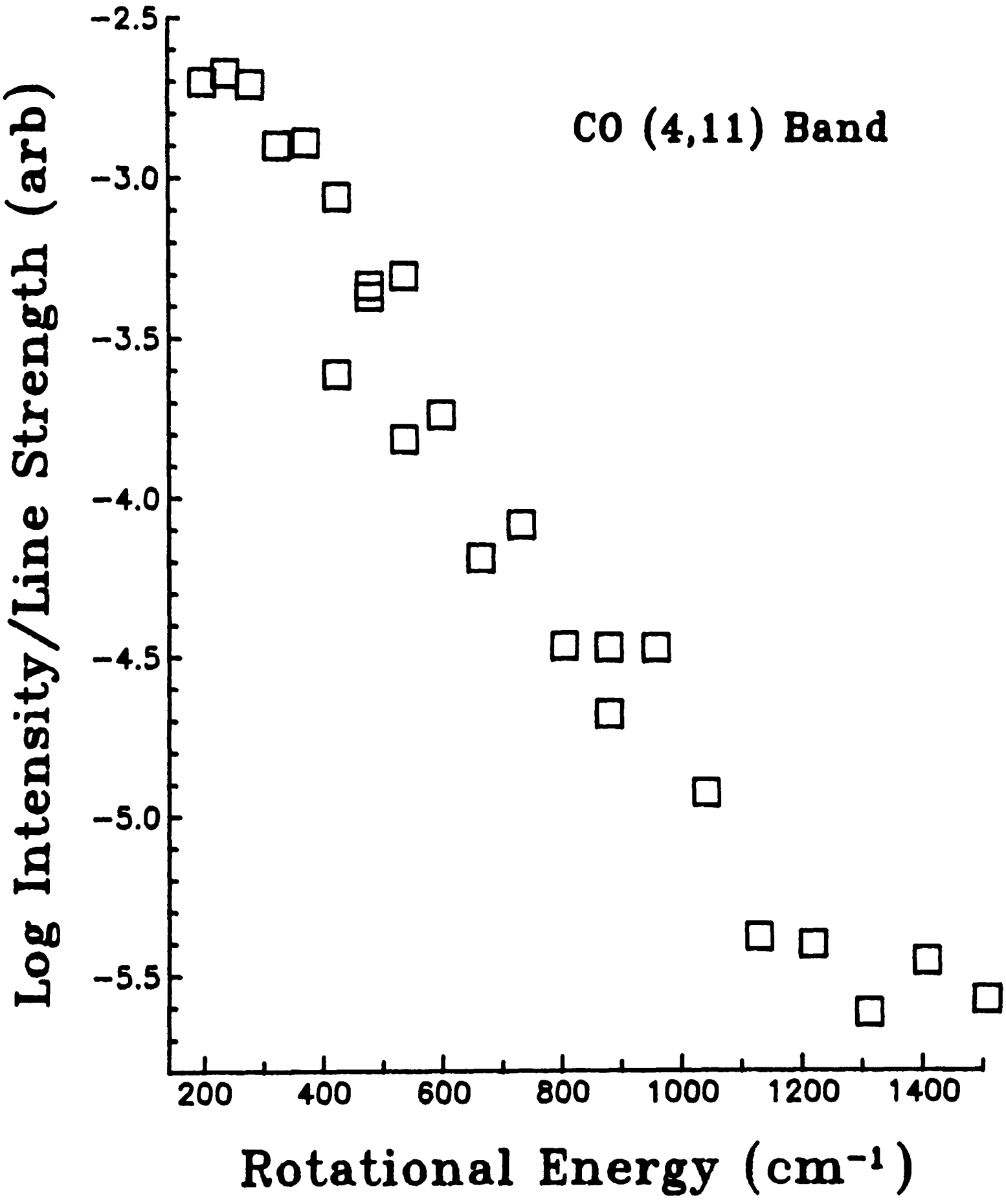

Figure 5.12. Boltzmann plot of rotational distribution from (4,11) band.

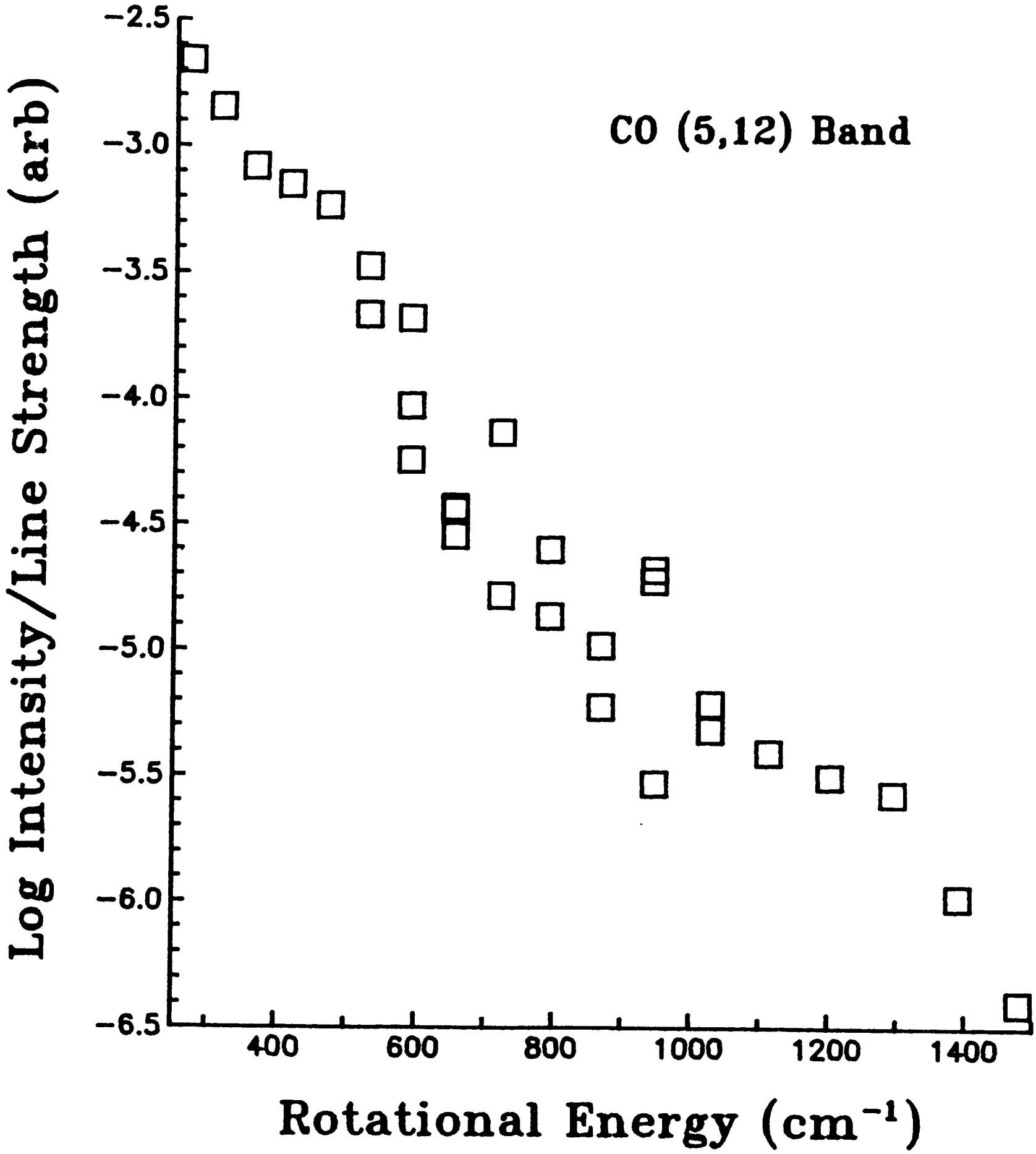

Figure 5.13. Boltzmann plot of rotational distribution from (5,12) band.

5.3 DISCUSSION

As discussed previously, rotational distributions which are used to investigate dynamics must be shown to be free of effects due to collisions. In the preceding chapters of this thesis the collisional, or otherwise, nature of the process being studied was relatively easy to establish, especially in the case of a pump-probe type experiment in which the time delay between the two laser pulses accurately determines if any collisional effects occur. In the present case there is a continual production of the $CO(X^1\Sigma^+)$ under study so it is not immediately clear what part, if any, collisions play in distorting the experimental results. Several comments can be made in relation to this problem.

- The pumping system maintained a pumping speed of $\geq 700 l s^{-1}$ at the pressure used, 2×10^{-4}Torr. This implies that the residence time of gas within the cell was $\sim 7\times10^{-3}$s. From simple collision theory it can be shown that, at the pressure used, a molecule will undergo an average of ~7 gas kinetic collisions in this time. From this it would appear that some collisional effects are probably occurring between the production of $CO(X^1\Sigma^+)$ and its detection. However, a calculation of the mean free path of the gas molecules under the conditions used shows that, on average, a molecule travels ~40cm between collisions. As this is larger that the dimensions of the reaction cell it is likely that a molecule will collide with a cell wall before it undergoes a gas kinetic collision. Assuming that a wall collision will not be elastic it seems likely that molecules

in collision with the reaction cell walls will be vibrationally deactivated and thus probably not contribute to the LIF signal. In conclusion it can be stated that collisional effects may not pose such a problem as might be expected from the residence time within the cell.

- If collisional rotational relaxation was occurring the observed distributions should change with the total pressure within the reaction cell. To investigate this possibility the LIF spectrum of the (5,14) band was recorded at total pressures of 0.2mTorr, 2.0mTorr and 10mTorr. The rotational distributions are presented in Fig. 5.14 with the data normalised to the average population in J"=9 and 10, as observed via the P(9) and P(10) transitions in the spectra. Also indicated is a line whose slope represents a 300K rotational distribution. The data recorded at 0.2mTorr and 2.0mTorr represent essentially the same distribution, although the 0.2mTorr data shows more scatter. However at 10mTorr it is clear that some collisional effects are changing the rotational distribution and this can be seen in both the low rotational levels, which lie on a steeper Boltzmann plot than at lower pressure, and in the reduction of the population at higher rotational levels. The fact that the rotational distribution shows little change when the pressure is increased by an order of magnitude is a good indication that collisional effects play only a small part in the process observed.

- If the distributions presented above were subject to collisional distortion then it is most likely that rotational energy transfer would be most rapid in the lower rotational levels. Higher rotational levels populated in the reaction should be removed more slowly than the lower rotational levels and hence should be visible under the conditions of the experiment conducted at the lowest pressure. Two comments can be made in relation to this.

  i. Although it was not possible to examine the long wavelength tail of the (5,12) and (6,15) bands, since they fell at the long wavelength end of the tuning range of the laser system, a careful observation of the corresponding regions in the (4,11) and (5,14) bands revealed no features due to high rotational levels in the P and Q branches of these spectra.

  ii. Because of the blue bandhead in the R branch of these spectra the high rotational levels of this branch fell in the observed region for all four bands recorded. No such lines were observed suggesting that no higher rotational levels were populated in the reaction.

These comments suggest that the observed rotational distributions are close to the nascent distributions from the reaction of O with CS although ideally one would have liked to performed the experiments at a much lower pressure to ensure that this was the case. Low signal levels prevented this and the distributions presented are the best that could be obtained with the apparatus available.

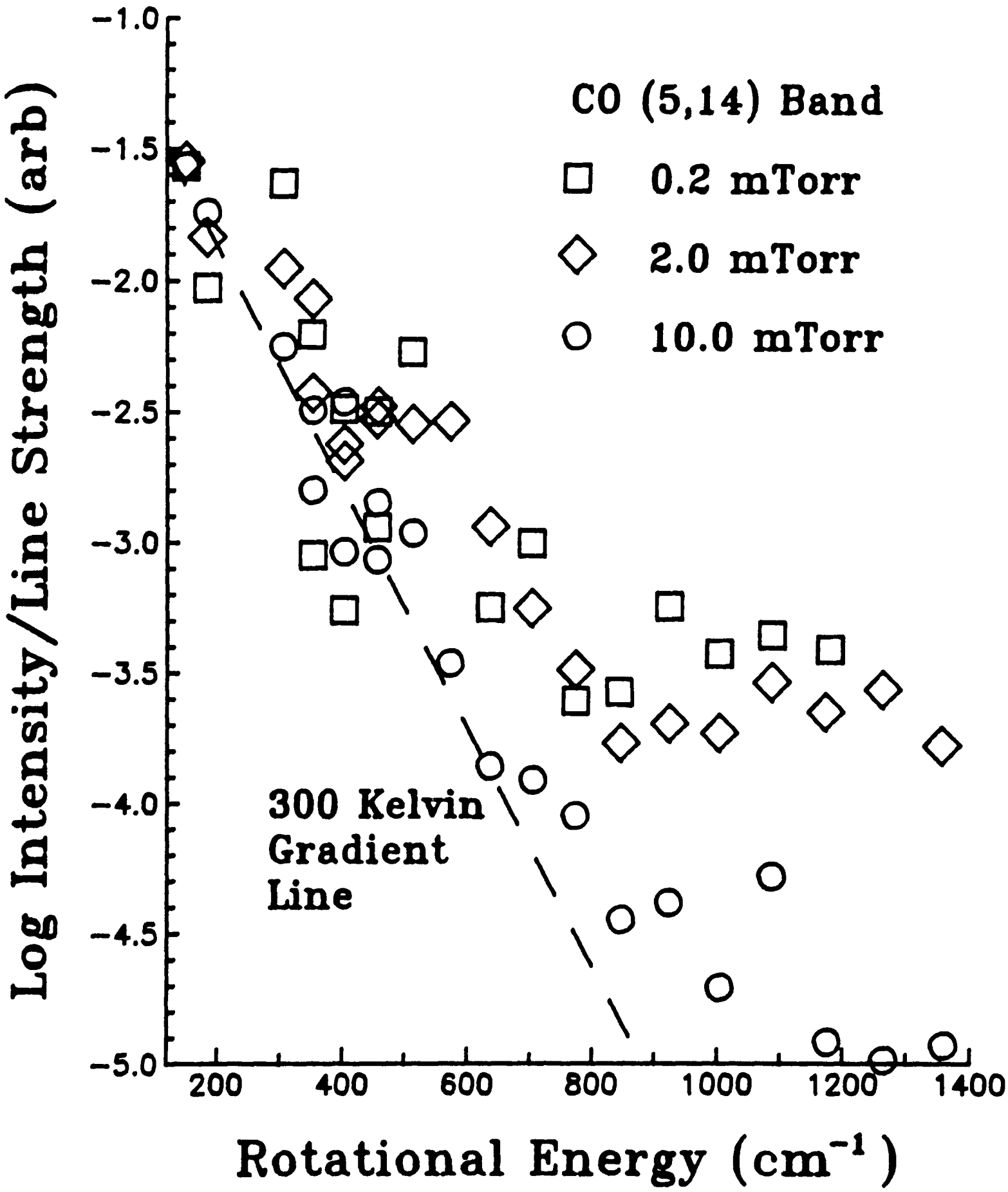

Figure 5.14. Rotational distribution from (5,14) band recorded at 2×10^{-4} Torr, 2.0mTorr and 10mTorr.

The reaction between $O(^{3}P)$ and $CS(X^{1}\Sigma^{+})$ gives rise to a highly excited vibrational distribution, as discussed previously, which suggests that the transition state, OCS^{*}, is linear with a large impulsive force between the departing S atom and the CO fragment giving rise to the high vibrational excitation. In accordance with the discussion on the impulsive model of photodissociation presented in Chapter 4 of this thesis, if the impulsive force between the departing fragments gives rise to high vibrational excitation, by virtue of the linear transition state, then only low rotational excitation in the fragments would be expected since no torque can be applied to such a linear system. This gives a rationalisation of the rotational distributions, presented in this chapter, within the CO product of the reaction. In the absence of any theoretical calculations on the potential surface governing the reaction no detailed modeling of the system was performed to attempt to quantify this rationalisation. The results must be considered as contributing to the body of experimental dynamics data which await consideration from theoretical workers in the field of molecular reaction and photodissociation dynamics.

5.3.1 A Potential CO Electronic Laser In the introduction to this chapter it was explained that the up-conversion of the vibrational energy resulting in the reaction of oxygen atoms with the CS radical, via pumping to the $A^{1}\Pi$ state, gives the potential for a VUV laser, since a population inversion exists between the $A^{1}\Pi$ state and the unoccupied levels of the $X^{1}\Sigma^{+}$ state [176]. As a conclusion to this chapter some general comments will be made about this scheme.

- Vibrational relaxation of $CO(X^1\Sigma^+ v")$ formed in the reaction will populate the lowest vibrational levels of $CO(X^1\Sigma^+)$, which are the proposed lower laser levels, thus depleting the population inversion.

- The formation of low vibrational levels in CO by other reactions (such as $O + CS_2$), as discussed in the introduction to this chapter, will have the same effect as that described above.

- A major loss mechanism within the laser cavity may be absorption of the VUV laser emission by reactants such as O_2 and CS_2. Clearly such absorbing species must be removed rapidly from the active region or not produced at all. For example O_2 within the laser system might be eliminated by forming the oxygen atoms required by a chemical reaction between nitrogen atoms and NO. Similarly CS might be produced by photodissociation of CS_2 using a ArF excimer laser at 193nm.

- The short radiative lifetime of $CO(A^1\Pi)$, ~10ns, suggests that fast optical pumping will be required to generate a sufficiently large population inversion. Possible coincidences of the (8,12) band with the 193nm ArF excimer laser line and the (3,12) band with the KrCl excimer laser line at 222nm might be used to pump such a system.

- Emission from the pumped vibrational level of the $A^1\Pi$ state of CO to high vibrational levels of the $X^1\Sigma^+$ state will compete with the desired transition to the lowest vibrational levels of this state

(see Fig. 5.2). Clearly some wavelength selective element within the laser cavity will be required.

Although laser action in CO has been demonstrated on the A-X transition [177] the output energy was very low, ~10nJ. It is hoped that the scheme described above might provide a more favourable VUV source although clearly further experimental effort is required to realise this aim.

APPENDIX 1 - DERIVATION OF ROTATIONAL POPULATION DISTRIBUTIONS FROM LIF

Consider a molecule in the ground electronic state v",J" being promoted to a level v'J'. The number of molecules promoted to the upper state can be written as:

$$N' = N'' \; I \; B$$

where N" is the ground state concentration, I the laser intensity and B the Einstein B factor, which can be written as:

$$B \propto S_J \; f_v^{abs} \; |R|^2 \; / \; (2J''+1)$$

where S_J is the line strength, f_v^{abs} the Franck-Condon factor and $|R|^2$ the transition dipole moment. Substitution gives:

$$N' \propto N'' \; I \; S_J \; f_v^{abs} \; |R|^2 \; / \; (2J''+1)$$

The signal ($\propto$ number of photons emitted) can be written as:

$$\text{Signal} = N' \; A \; q_v$$

where A is the Einstein A factor and q_v is the quantum efficiency of the detector. Summing over all possible lower state combinations of v" and J" we have:

$$\text{Signal} = \sum_{v''} \sum_{J''} N' \; A \; q_v$$

The Einstein emission factor can be written as:

$$A \propto \nu^3 \; S_J \; f_v^{em} \; |R|^2 \; / \; (2J'+1)$$

So that:

$$\text{Signal} \propto \sum_{v"} \sum_{J"} N' \, q_v \, \nu^3 \, S_J \, f_v^{em} \, / \, (2J'+1)$$

Over the J" summation, normally P, Q and R lines, q_v and ν are constant.

Therefore:

$$\text{Signal} \propto \sum_{v"} N' \, q_v \, \nu^3 \, f_v^{em} \sum_{J"} [S_J \, / \, (2J'+1)]$$

where the summation of the line strength factors is unity. This gives:

$$\text{Signal} \propto \sum_{v"} N" \, I \, S_J \, f_v^{abs} \, q_v \, \nu^3 \, f_v^{em} \, / \, (2J"+1)$$

Assuming only one upper state vibrational level is accessed and the rotational distribution only in v" is required we can write:

$$\text{Signal} \propto C \, N" \, I \, S_J \, f_v^{abs} \, / \, (2J"+1)$$

where $C = \sum_{v"} q_v \, \nu^3 \, f_v^{em}$

is constant for one vibrational level. Since the Franck-Condon factor in absorption is constant throughout the band we obtain:

$$\text{Signal} \propto N" \, I \, S_J \, / \, (2J"+1)$$

Assuming the laser intensity is constant and that N" can be represented as a Boltzmann distribution ie:

$$N" = (2J"+1) \exp (-E_J/kT)$$

we find:

$$\text{Signal} \propto S_J \exp (-E_J/kT)$$

So a plot of the signal divided by the line strength, on a logarithmic scale against the rotational energy will be a straight line for a Boltzmann distribution. This procedure is adopted throughout the thesis.

APPENDIX 2 - SPECTROSCOPY OF SPECIES STUDIED

The transitions studied in both OH and NO in the work reported in this thesis are of the type $A^2\Sigma^+$-$X^2\Pi_i$ whilst that for CO is $A^1\Pi$-$X^1\Sigma^+$.

7.1 OH and NO Spectroscopy

An energy level diagram for a $^2\Sigma^+$ - $^2\Pi_i$ is shown in Fig. A2.1. The $X^2\Pi_i$ state can be either Hund's case (a), large spin-orbit splitting, or case (b), negligable spin-orbit splitting, and for $NO(X^2\Pi_i)$ and $OH(X^2\Pi_i)$ is intermediate between the two limiting cases. At low values of rotational angular momentum case (a) is more appropriate since the splitting between the $2\Pi_{½}$ and $^2\Pi_{3/2}$ levels is ~100cm^{-1}. At higher values of the rotational angular momentum a transition to case (b) gradually takes place. In the work reported the $2\Pi_{½}$ and $^2\Pi_{3/2}$ states, designated F_1 and F_2, are considered to be essentially separate. Λ doubling splits each rotational level giving two states designated Π^+ and Π^-.

The $A^2\Sigma^+$ state is strictly Hund's case (b). Spin splitting gives rise to levels of + and - parity (even N +, odd N -).

The selection rules for $X^2\Pi_i$, Hund's case (a) to $A^2\Sigma^+$ are $\Delta J=\pm1,0$ and $+\leftrightarrow-$ leading to six branches in each of the two sub-bands. The notation is P_{11}, Q_{11}, R_{11}, P_{12}, Q_{12}, R_{12} with F_1 upper levels (first subscript) and either F_1 or F_2 lower levels (second subscript) as required by the selection rules, and P_{22}, Q_{22}, R_{22}, P_{21}, Q_{21}, R_{21} for the other sub-band (F_2 upper levels). The small splitting in the $A^2\Sigma^+$

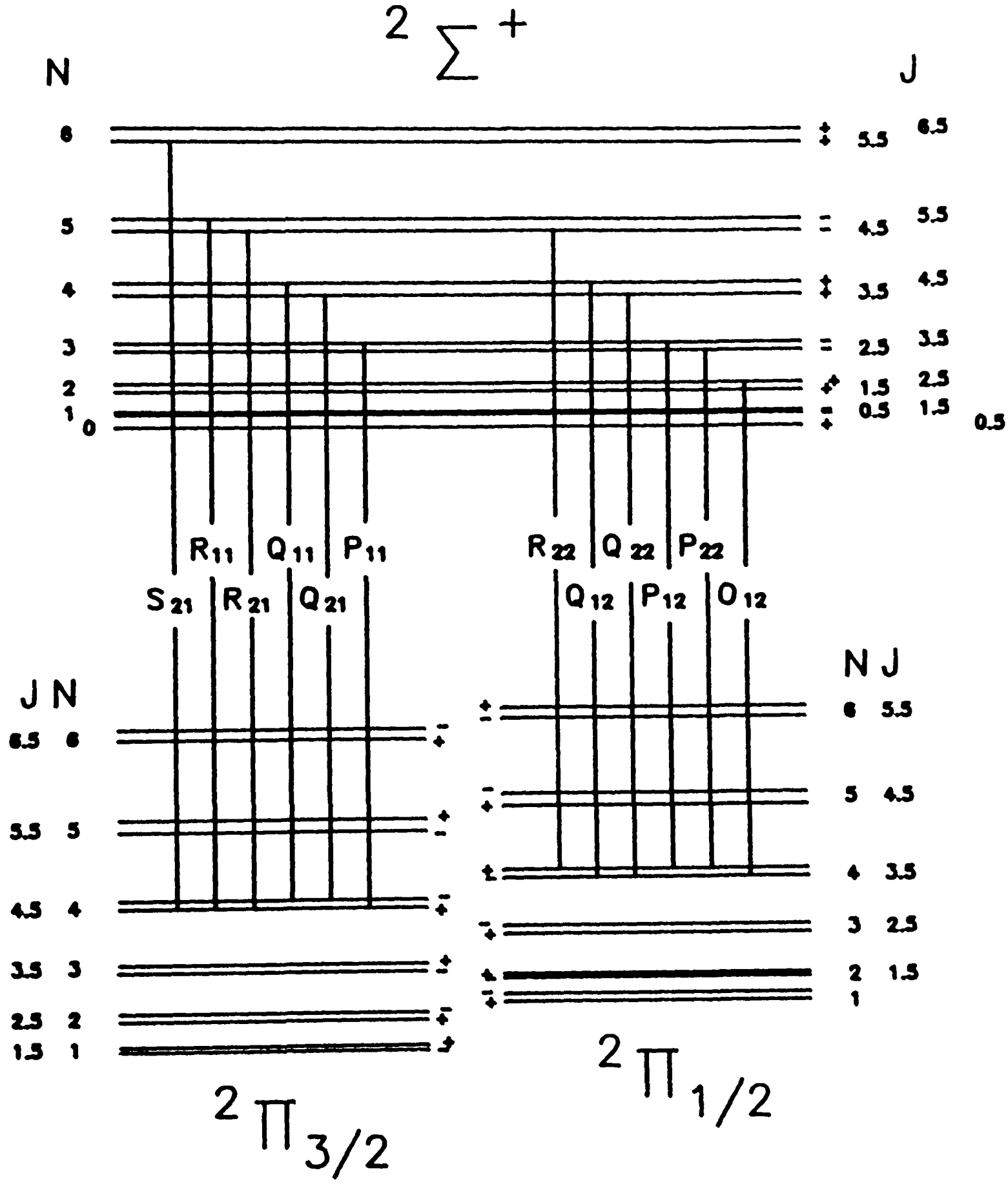

Figure A2.1. Energy level diagram for $X^2\Pi_i$-$A^2\Sigma^+$ systems.

state makes the pairs of branches (Q_{11}, P_{21}), (R_{11}, Q_{21}), (P_{22}, Q_{12}) and (Q_{22}, R_{21}) almost degenerate; cetainly within the experimental resolution employed, thus reducing the effective spectroscopy to eight branches, designated P_{11}, Q_{11}, R_{11}, P_{22}, Q_{22}, R_{22}, P_{12} and R_{21} in this work. The P_{12} and R_{21} bands have $\Delta N=\pm 2$ and are much weaker than the six remaining major branches.

7.1.1 Spectroscopic constants for OH Data used for analysis of experimental spectra and for simulation purposes was taken from Goldmann and Gillis [89], which tabulates line positions for all 12 branches and gives Einstein A factors required to deduce populations from the emission spectra. Additional data for analysis of LIF spectra were taken from Chidsey and Crosley [88].

7.1.2 Spectroscopic constants for NO No similar exhaustive database was found for NO and calculations were used to generate line positions and line strengths for the A-X system of NO. The formulae were taken from Mallard et al [141] and are reproduced here.

Term values for $X^2\Pi_i$ state.

$$T'' = G(v'') + F_i(v'',J'')$$

where:

$$F_{2,1} = B(v'') \{ (J''+\tfrac{1}{2})^2 - 1 \pm \tfrac{1}{2} [\lambda(v'')^2 - 4\,\lambda(v'') + 4(J''+\tfrac{1}{2})^2]^{\frac{1}{2}} \}$$

$$\lambda(v'') = A(v'') / B(v'')$$

$$G(v'') = 1904.405(v''+\tfrac{1}{2}) - 14.187(v''+\tfrac{1}{2})^2 + 0.0240(v''+\tfrac{1}{2})^3$$

$$A(v") = 123.26 - 0.1906(v"+½) - 0.0108(v"+½)^2$$

$$B(v") = 1.70427 - 0.01728(v"+½) - 0.000037(v"+½)^2$$

Term values for the $A^2\Sigma^+$ state.

$$T' = T_e + G(v') + F_i'(v',J')$$

where:

$$F_1'(v',J') = B(v')(J'-½)(J'+½) - D'(J'-½)^2(J'+½)^2$$

$$F_2'(v',J') = B(v')(J'+½)(J'+1½) - D'(J'+½)^2(J'+1½)^2$$

$$T_e = 43906.37cm^{-1}$$

$$G(v') = 2374.307(v'+½) - 16.106(v'+½)^2 - 0.04645(v'+½)^3$$

$$B(v') = 1.99478 - 0.018328(v'+½)$$

Line positions were calculated by subtraction: $T'(v',J',F_i')$ - $T"(v",J",F_i")$. In practice it was found that, although this method gave a good fit at low values of J for all branches studied it was impossible to assign spectra containing lines originating from high J levels on the basis of these formulae. Chapter 4 describes how better constants than those available in the literature were obtained allowing the spectra to be assigned, and lists the constants derived.

Line strengths were obtained by the following formulae:

$$\begin{matrix} R_{22}(+) \\ R_{21}(-) \end{matrix} : \frac{(2J"+1)^2 \pm (2J"+1)\ U\ (4J"^2+4J"-2\lambda)}{32(J"+1)}$$

$$R_{11}(+) : (2J"+1)^2 \pm (2J"+1)\ U\ (4J"^2+4J"-7+2\lambda)$$
$$R_{12}(-) \qquad\qquad 32(J"+1)$$

$$Q_{22}(+) : (2J"+1)\ [\ (4J"^2+4J"-1) \pm U\ (8J"^3+12J"^2-2J"+1-2\lambda)\ ]$$
$$Q_{21}(-) \qquad\qquad 32J"(J"+1)$$

$$Q_{11}(+) : (2J"+1)\ [\ (4J"^2+4J"-1) \pm U\ (8J"^3+12J"^2-2J"-7+2\lambda)\ ]$$
$$Q_{12}(-) \qquad\qquad 32J"(J"+1)$$

$$P_{22}(+) : (2J"+1)^2 \pm (2J"+1)\ U\ (4J"^2+4J"-7+2\lambda)$$
$$P_{21}(-) \qquad\qquad 32J"$$

$$P_{11}(+) : (2J"+1)^2 \pm (2J"+1)\ U\ (4J"^2+4J"+1-2\lambda)$$
$$P_{12}(-) \qquad\qquad 32J"$$

$$U = [\ \lambda(v") - 4\lambda(v") + (2J"+1)^2\ ]^{-\frac{1}{2}}$$

where $\lambda(v")$ is given above.

7.2 CO Spectroscopy

The transition studied in Chapter 5 is $CO(A^1\Pi\text{-}X^1\Sigma^+)$ and is relatively simple. Term values for the $X^1\Sigma^+$ state were calculated using constants from Huber and Herzberg [96] and formulae from Herzberg [150]. In principle the same can be done for a $^1\Pi$ state thus allowing a simple calculation of the line positions in the spectra. However in the case of $CO(A^1\Pi)$ perturbations occur due to mixing with triplet states close in energy. This makes calculation of line positions impossible. Term values for the $A^1\Pi$ state of CO were calculated by subtraction of the appropriate $X^1\Sigma^+$ v"=0 term values from the $CO(A^1\Pi\text{-}X^1\Sigma^+)$ absorption data of Tilford and Simmons [178]. These were then used to calculate the perturbed line positions.

Formulae for $X^1\Sigma^+$ state.

$$B(v") = 1.93128087 - 0.01750441(v+½) + 5.487\times10^{-7}(v+½)^2 + 2.54\times10^{-8}(v+½)^3$$

$$D(v") = 6.1214\times10^{-6} - 1.153\times10^{-9}(v+½) + 1.805\times10^{-10}(v+½)^2$$

$$G(v") = 2169.81358(v+½) - 13.28831(v+½)^2 + 0.010511(v+½)^3$$
$$+ 5.74\times10^{-5}(v+½)^4 + 9.83\times10^{-7}(v+½)^5 - 3.166\times10^{-8}(v+½)^6$$

$$T"(v") = G(v") + B(v")J"(J"+1) - D(v")J"^2(J"+1)^2 - G"(0)$$

Line strengths were calculated using the Honl-London formulae for an $A^1\Pi - X^1\Sigma^+$ transition:

$$S_J(P) = (J'-1)J' \;/\; 4J'$$

$$S_J(Q) = (J'+1)\;J'\;(2J'+1) \;/\; 4J'(J'+1)$$

$$S_J(R) = (J'+2)\;(J'+1) \;/\; 4(J'+1)$$

It is important to note that the line strengths of the perturbed lines will not follow these formulae and will depend on the degree of perturbation. Such effects are best determined experimentally. Where possible heavily perturbed lines were not used in the calculation of rotational distributions following analysis of the experimental spectra.

APPENDIX 3 - SPECTRAL SIMULATION PROGRAM

Widespread use has been made of spectral simulation, both for spectral assignment and calculation of rotational distributions, in the work presented in this thesis. The procedure used is described below. In most cases the oscillator strength and vibrational overlap terms can be ignored when simulating a single vibrational band of an electrionic transition as these are essentially constant throughout the band. The input to the program is therefore the rotational line positions, a rotational line strength term and a population distribution.

A Gaussian line shape was assumed; this was found to be very close to the experimentally determined line shape. The line profile was truncated at twice the full width at the 1/e points from the line centre.

An effective intensity for each line was calculated by combining the line strength term and the rotational population factor. The spectral region to be calculated was divided into 1000 steps. At each step the contribution from each line under the line shape function is calculated giving rise to a spectral intensity "score" for each step.

APPENDIX 4 - PRIOR DISTRIBUTION - DERIVATION OF EXPRESSIONS USED

Let NO have vibration and rotation quantum numbers v and j, and CH_3O have V and J. The probability of distribution into levels v, j, V, J is proportional to the rotational degeneracies of NO and CH_3O, and to the sqare root of the translational energy. Neglecting any electronic excitation we have:

$$P \propto (2j+1)\ (2J+1)^2\ (E - E_v - E_V - E_j - E_J)^{\frac{1}{2}}$$

where $E_j = B_j j(j+1)$ and $E_J = B_J J(J+1)$ which neglects the dependance of E_J on K.

Integration over all J gives:

$$P(V,v,j) = (2j+1) \int_0^{J_{max}} (2J+1)^2\ (E'-BJ(J+1))^{\frac{1}{2}}\ dJ$$

where $E' = E - E_V - E_v - E_j$. Neglecting the +1 terms allows simplification giving:

$$P(V,v,j) \propto (2j+1)\ (E - E_V - E_v - B_j j(j+1))^2$$

P(v,j), the density of vibrational states as a function of E_V can be obtained by either the harmonic oscillator model of the Marcus-Rice method. The HO treatment gives:

$$N_V(E_V) = E_V^{s-1} / (s-1)\ \Pi h\nu_i$$

where s is the number of vibrational frequencies. Substitution gives:

$$P(v,j) \propto \int_0^{E_{V\,max}} (2j+1)\ (E - E_V - E_v - B_j j(j+1))^2\ N_V\ dE_V$$

$$P(v,j) \propto (2j+1)\ (E - E_v - E_j)^{11}$$

Integration over j gives:

$$P(v) \propto (E - E_v)^{12}\ /12B$$

as derived by Zamire and Levine [151]. The HO treatment given above underestimates N_V whilst the Marcus-Rice method presented below overestimates N_V.

$$N_V(E_V) = (E_V + E_z)^{s-1}\ /\ (s-1)!.\Pi h\nu_i$$

where E_z is the zero point energy and s has the same meaning as above. Substitution gives:

$$P(v,j) \propto \int_0^{E_V max=E'} (2j+1)(E' - E_V)^2\ (E_V + E_z)^8\ dE_z$$

$$P(v,j) \propto (2j+1)\ [\ (E" + E_z)^{11} - E_z{}^9(55E"^2 + 11E"E_z + E_z{}^2)\ ]$$

where $E" = E - E_V - E_j$.

Integration of this expression over j gives:

$$P(v) \propto (E + E_z - E_V)^{12} - 220(E + E_z - E_V)^3E_z{}^9 - 66(E + E_z - E_V)^2E_z{}^{10}$$
$$-12(E + E_z - E_V)E_z{}^{11} + 297E_z{}^{12}.$$

The results of these two methods give a lower and upper limit respectively for P(v,j) and P(v), as shown in Chapter 4 for P(0,j).

References

1. J C Whitehead. Comprehensive Chemical Kinetics 24 358 (1983)

2. S R Leone. Dynamics of the excited state. 255 (1982). Ed. K P Lawley.

3. J P Simons. J Phys Chem 88 1287 (1984)

4. C H Greene R N Zare. Ann Rev Phys Chem 33 119 (1982)

5. E E Marinero C T Rettner R N Zare. J Chem Phys 80 4142 (1984)

6. P Anddresen G S Ondrey B Titze E W Rothe. J Chem Phys 80 2584 (9184)

7. R B Bernstein. Chemical Dynamics via Molecular Beam and Laser Techniques. Oxford University Press. (1982)

8. M Heaven T A Miller V E Bondybey. Chem Phys Lett 84 1 (1981)

9. B M Dekoven A P Baronavski. Chem Phys Lett 86 392 (1982)

10. R K Sparks K Shobatake L R Carlson Y T Lee. J Chem Phys 75 3838 (1981)

11. R J S Morrison E R Grant. J Chem Phys 77 5994 (1982)

12. K H Kramer R B Bernstein. J Chem Phys 42 767 (1965)

13. E E Bromberg A E Proctor R B Bernstein. J Chem Phys 63 3287 (1975)

14. R Altkorn F E Bartoszek J Dehaven G Hancock D S Perry. Chem Phys Lett 98 212 (1983)

15. Z Karny R N Zare. J Chem Phys 68 3360 (1978)

16. Z Karny R C Estler R N Zare. J Chem Phys 69 5199 (1978)

17. M N R Ashfold R N Dixon. Chem Phys Lett 93 5 (1982)

18. J H Glownia S J Riley S D Colson G C Nieman. J Chem Phys 73 4296 (1980)

19. A Hodgson J P Simons M N R Ashfold J M Bayley R N Dixon. Chem Phys Lett 107 1 (1984)

20. G E Busch J F Cornelius R T Mahoney R I Morse D W Schlosser K R Wilson Rev Sci Instr. 41 1066 (1970)

21. R Vasudev R N Zare R N Dixon. Chem Phys Lett 96 1349 (1983)

22. D R Herschbach G H Kwei J A Norris. J Chem Phys 34 1842 (1961)

23. R K Sparks L R Carlson K Shobatake M L Cowalczyk Y T Lee. J Chem Phys 72 1401 (1980)

24. D H Maylotte J C Polanyi K B Woodall. J Chem Phys 57 1547 (1972)

25. T Carrington J C Polanyi. Int Rev Sci: Phys Chem: Chemical Kinetics. 9 135 (1972)

26. H W Cruse P J Dagdigian R N Zare. Farad Disc Chem Soc: Molecular Beam Scattering. 55 277 (1973)

27. M N R Ashfold J M Bayley R N Dixon. Can J Phys 62 1806 (1984)

28. G Radhakrishnan R C Estler. Chem Phys Lett 84 260 (1981)

29. G Radhakrishnan. PhD Thesis. Univ of Southern California. (1982)

30. A P Baronavski R G Miller J R McDonald. Chem Phys 30 119 (1978)

31. J C Polanyi. Acc Chem Research 5 161 (1972)

32. K E Holdy L C Klotz K R Wilson. J Chem Phys 52 4588 (1970)

33. J P Simons P W Tasker. Mol Phys 26 1267 (1973)

34. M J Berry. Chem Phys Lett 27 73 (1974)

35. M J Berry. Chem Phys Lett 29 329 (1974)

36. a) Y B Band K H Freed. Chem Phys Lett 28 328 (1974)

b) Y B Band K H Freed J Chem Phys 63 3382 (1975)

c) Y B Band K H Freed. J Chem Phys 63 4479 (1975)

d) Y B Band K H Freed. J Chem Phys 64 4329 (1976)

e) M D Morse Y B Band K H Freed. Chem Phys Lett 49 399 (1977)

f) Y B Band K H Freed. J Chem Phys 67 1462 (1977)

g) M D Morse Y B Band K H Freed. Chem Phys Lett 44 125 (1976)

h) M D Morse Y B Band K H Freed. Farad Disc Chem Soc. 67 297 (1979)

i) M D Morse Y B Band K H Freed. J Chem Phys 70 3604 (1979)

j) M D Morse Y B Band K H Freed. J Chem Phys 70 3620 (1979)

k) M D Morse K H Freed. J Chem Phys 74 4395 (1981)

l) Y B Band K H Freed D J Kouri. J Chem Phys 74 4380 (1981)

37. M Shapiro R Bersohn. Ann Rev Phys Chem 33 409 (1982)

38. J N L Connor. Computer Phys Commun 17 117 (1979)

39. E Zamir R D Levine R B Bernstein. Chem Phys Lett 107 217 (1984)

40. P Siegbahn B Lio. J Chem Phys 68 2457 (1978)

41. W M Gelbart. Ann Rev Phys Chem 28 323 (1977)

42. M S Child. Atomic and Molecular Collision Theory. Chapter 13. (1978)

43. P A Robinson K A Holbrook. Unimoleculr Reactions. Wiley Interscience (1972)

44. P Pechukas J C Light. J Chem Phys 42 3281 (1965)

45. See for example: M Quack. Chem Phys 51 353 (1980)

46. R B Bernstein R D Levine. J Chem Phys 57 434 (1972)

47. V Wilke W Shmidt. Appl Phys 18 177 (1979)

48. H Schomburg H F Dobele B Buckle. Appl Phys B. 30 131 (1981)

49. W Demtroder. Laser Spectroscoy. Springer Series in Chemical Physics. 5 (1981)

50. R L Byer. Electro-Optical System Design. (Feb. 1980)

51. C Fotakis C B McKendrick R J Donovan. Chem Phys Lett 80 598 (1981)

52. H Wang W S Felps S P McGlynn. J Chem Phys 67 2614 (1977)

53. M N R Ashfold M T Macpherson J P Simons. Topics in Curr Chem 18 1 (1979)

54. R N Dixon G Duxbury J W Rabalais L Asbrink. Mol Phys 31 423 (1976)

55. R J Buenker S D Peyerimhoff. Chem Phys Lett 29 253 (1974)

56. G Theodorakopoulus C A Nicolaides R J Buenker S D Peyerimhoff. Chem Phys Lett 89 164 (1982)

57. D H Katayama R E Huffman C L O'Bryan. J Chem Phys 59 4309 (1973)

58. M B Robin. Higher Excited States of Polyatomic Molecules. Academic Press, New York (1974)

59. G Theodorakopoulus D Petsalkis R J Buenker S D Peyerimhoff. Chem Phys Lett 105 253 (1984)

60. M T Macpherson J P Simons. Chem Phys Lett 51 261 (1977)

61. J W C Johns. Can J Phys 41 209 (1963)

62. M N R Ashfold J M Bayley R N Dixon. Chem Phys 84 35 (1984)

63. K Watanabe A S Jursa. J Chem Phys 41 1650 (1964)

64. S Tsurubuchi. Chem Phys 10 335 (1975)

65. L J Stief W A Payne R B Klemm. J Chem Phys 62 4000 (1975)

66. K H Welge F Stuhl. J Chem Phys 46 2440 (1967)

67. P Andresen E W Rothe. Chem Phys Lett 86 270 (1982)

68. O Oldenberg. Phys Rev. 46 210 (1934)

69. L C Lee L Oren E Phillips D L Judge. J Phys B 11 47 (1978)

70. O Dutuit A Tabche-Fouhaile I Nenner H Frohlich P M Guyon. J Chem Phys 83 584 (1985)

71. T Carrington. J Chem Phys 41 2012 (1964)

72. H Okabe. J Chem Phys 72 6642 (1980)

73. J P Simons P W Tasker. Mol Phys. 27 1961 (1974)

74. R J Donovan C Fotakis A Hopkirk C B McKendrick A Torre. Can J Chem 61 1023 (1983)

75. C Fotakis. Optical Eng 22 554 (1983)

76. A Hodgson J P Simons M N R Ashfold J M Bayley R N Dixon. Mol Phys 54 351 (1985)

77. G A Chamberlain J P Simons. Chem Phys Lett 32 355 (1975)

78. M T Macpherson J P Simons R N Zare. Mol Phys 38 2049 (1979)

79. J P Simons A J Smith. Chem Phys Lett 97 1 (1983)

80. J P Simons A J Smith R N Dixon. J Chem Soc Faraday Trans II 80 1489 (1984)

81. M T Macpherson J P Simons. Chem Phys Lett 51 261 (1977)

82. K S Sorbie J N Murrell. Mol Phys 29 1387 (1975)

83. F Floquet J A Horsley. J Chem Phys 60 3767 (1974)

84. E Segev M Shapiro. J Chem Phys 73 2001 (1980)

85. E Segev M Shapiro. J Chem Phys 77 5604 (1982)

86. I P Vinogradov F I Vilesov. Opt Spectr USSR. 44 653 (1978)

87. R N Dixon. Mol Phys 54 333 (1985)

88. I L Chidsey D R Crosley. JQSRT 23 187 (1980)

89. A Goldmann J R Gillis. JQSRT 25 111 (1984)

90. R A Copeland D R Crosley. Chem Phys Lett 107 295 (1984)

91. S Speiser J Jortner. Chem Phys Lett 44 399 (1976)

92. D S Zakheim P M Johnson. Chem Phys 46 263 (1980)

93. I Hanazaki. Appl Phys B 26 111 (1981)

94. A L'Huillier G Mainfray P M Johnson. Chem Phys Lett 103 447 (1984)

95. H Lew. Can J Phys 54 2028 (1976)

96. K P Huber G Herzberg. Molecular Spectra and Molecular Structure. Vol 4. Constants of Diatomic Molecules. Van Nostrand (1979)

97. G W Loge J R Wiesenfeld. J Chem Phys 75 2795 (1981)

98. K H Welge S V Filseth J Davenport. J Chem Phys 53 502 (1970)

99. P W Fairchild G P Smith D R Crosley. J Chem Phys 79 1975 (1983)

100. R K Lengel D R Crosley. J Chem Phys 2085 (1977)

101. D Stepowski M J Cottereau. J Chem Phys 74 6674 (1981)

102. S Brandt. Statistical and Computational Methods in Data Analysis. 2nd ed. North Holland. (1976)

103. W Koechner. Solid State Laser Engineering. Springer Verlag Series in Optical Sciences 1 (1976)

104. H Okabe. Photochemistry of Small Molecules. Wiley-Interscience, New York (1978)

105. Fortran Library Mark 11. Numerical Algorithms Group. Oxford (1984)

106. I W M Smith M D Williams. J Chem Soc Faraday Trans II. In press

107. A B Meinel. Astrophys J 111 555 (1950)

108. J D McKinley Jr. D Garvin M J Boodart. J Chem Phys 23 784 (1955)

109. P A Freedman W J Jones. J Chem Soc Faraday Trans II 72 207 (1967)

110. J A Coxon S C Foster. Can J Phys 60 41 (1982)

111. R N Dixon. Mol Phys 54 333 (1985)

112. F Shokoohi S Hay C Wittig. Chem Phys Lett 110 1 (1984)

113. M N R Ashfold. Private communication.

114. G H F Dierksen W P Kramer T N Resigno C F Bender B V McKoy S R Langhoff P W Langhoff. J Chem Phys 76 1043 (1982)

115. H Zacharias M Geilhaupt K Meier K H Welge. J Chem Phys 74 218 (1981)

116. A P Baranovski. Conference abstract. (1982)

117. T G Slanger M J Dyer W K Bishel. Bull Soc Chim Belg 92 637 (1983)

118. R W Jones R D Bower P L Houston. J Chem Phys 76 3339 (1982)

119. I Nadler M Noble H Reisler C Wittig. J Chem Phys 82 2608 (1985) and references therein.

120. R Vasudev R N Zare R N Dixon. J Chem Phys 80 4863 (1984)

121. N Sanders J E Butler L R Pasternak J R McDonald. Chem Phys 48 203 (1980)

122. G Inoue H Akimoto M Okuda. J Chem Phys 72 1769 (1980)

123. J P Chauvael Jn. C B Conboy W M Chen G B Matson C A Spring B D Ross N S True. J Chem Phys 80 1469 (1984)

124. P Gray M W T Pratt. J Chem Soc 54 3403 (1958)

125. P Tarte. J Chem Phys 20 1570 (1952)

126. H W Brown G C Pimentel. J Chem Phys 29 883 (1958)

127. J J McGarvey W D McGarth. Trans Farad Soc 60 2196 (1964)

128. I M Napier R G W Norrish. Proc Roy Soc A299 317 (1967)

129. R A Cox R G Derwent S V Kearsey L Batt K G Patrick. J Photochem 13 149 (1980)

130. A F Tuck. J Chem Soc Faraday Trans II 73 689 (1977)

131. F Lahmani C Lardeux M Lavoler D Solgadi. J Chem Phys 73 1187 (1980)

132. F Lahmani C Lardeux D Solgadi. J Chem Phys 73 4433 (1980)

133. F Lahmani C Lardeux D Solgadi. Chem Phys Lett 102 523 (1983)

134. O Benoist D'Azy F Lahmani C Lardeux D Solgadi. Chem Phys 94 247 (1985)

135. B A Keller P Felder J R Huber. Chem Phys Lett 124 135 (1986)

136. N Rose. Part II Thesis. Oxford University. (1979)

137. Eight Peak Index of Mass Spectra. Mass Spectrometry Centre. Vols I and II

138. P W B Pearse A G Gaydon. The Identification of Molecular Spectra.

139. C B Moore J C Weissmarr A P Baranovski A Cabello. J Chem Phys 69 4720 (1978)

140. E K C Lee K Shibuya R A Margem. J Chem Phys 69 751 (1978)

141. W G Mallard J H Miller K C Smyth. J Chem Phys 76 3483 (1982)

142. C Amiot R Bacis G Guelachuili. Can J Phys 56 251 (1978)

143. R Engeleman P E Rouse H M Peck V D Baiamonte. Los Alamos Nat Lab Scientific Lab Report LA 4364 (1969)

144. P R Bevington. Data Reduction and Error Analysis for the Physical Sciences. McGraw-Hill (1969).

145. U Fano G Racha. Irreducable Tensonal Sets. Academic Press New York (1959)

146. D A Case G M McClelland D R Herschbach. Mol Phys 35 541 (1978)

147. C H Greene R N Zare. J Chem Phys 78 6741 (1983)

148. P Klaeboes. Spectrochim Acta A23 2957 (1967)

149. G Hancock. Private Communication

150. G Herzberg. Molecular Spectra and Molecular Structure Vol I,

Diatomic Molecules. (1950). Van Nostrand.

151. E Zamire R D Levine. Chem Phys 52 253 (1980)

152. S E Stein B S Rabinovitch. J Chem Phys 58 2438 (1973)

153. D K Russell H E Bradford. J Chem Phys 72 2750 (1980)

154. F Lahmani C Lardeux D Solgadi. In Press

155. M Tanaka J Tanaka S Nagakura. Bull Chem Soc Jap 39 776 (1966)

156. M A Pollack. Appl Phys Lett 8 237 (1966)

157. R D Suart P H Dawson G H Kimbell. J Appl Phys 43 1022 (1972)

158. S Tsuchiya N Nielsen S H Bauer. J Phys Chem 77 2455 (1973)

159. G Hancock I W M Smith. Chem Phys Lett 3 573 (1969)

160. G Hancock I W M Smith. J Chem Soc Faraday Trans II 67 2586 (1971)

161. G Hancock C Morley I W M Smith. Chem Phys Lett 12 193 (1971)

162. G Hancock B A Ridley I W M Smith. J Chem Soc Faraday Trans II 68 2117 (1972)

163. N Djeu. J Chem Phys 60 4109 (1974)

164. D S Y Hsu W M Shaub T L Burks M C Lin. Chem Phys 44 143 (1979)

165. I R Slagle D Gutman J R Gilbert. 15th Symp Combustion. Combustion Inst. Pittsburgh PA 785 (1974)

166. R E Graham D Gutman. J Phys Chem 81 207 (1977)

167. J W Hudgens J T Cleaves J D McDonald. J Chem Phys 64 2528 (1976)

168. I W M Smith. Disc Faraday Soc 44 194 (1967)

169. A C Provorov B P Stoicheff S Wallace. J Chem Phys 67 5393 (1977)

170. H Zacharias H Rottke K H Welge. Opt Commun 35 185 (1980)

171. S V Filseth R Wallenstein H Zacharias. Opt Commun 23 231 (1977)

172. R A Bernheim C Kittrell D K Viers. Chem Phys Lett 51 325 (1977)

173. F H M Faisal R Wallenstein H Zacharias. Phys Rev Lett 39 1138 (1977)

174. R W Jones M Sivakumar B H Rockney P L Houston E R Grant. Chem Phys Lett 91 271 (1982)

175. G L Wolk J W Rich. Chem Phys Lett 87 117 (1982)

176. G Hancock H Zacharias. Chem Phys Lett 82 402 (1981)

177. R T Hodgson. J Chem Phys 55 5378 (1971)

178. S G Tilford J D Simmons. J Phys Chem Ref Data 1 147 (1972)

179. R W Nicholls. JQSRT 2 433 (1962)

180. P Andressen A C Luntz. J Chem Phys 72 5842 (1980)